2012

Optimising the packaging of semiconductor detectors to improve their energy response to gamma and neutron radiation for radiation protection: a GEANT4 Monte Carlo study

Mohd Amir Radhi Othman

OPTIMISING THE PACKAGING OF SEMICONDUCTOR DETECTORS TO IMPROVE THEIR ENERGY RESPONSE TO GAMMA AND NEUTRON RADIATION FOR RADIATION PROTECTION: A GEANT4 MONTE CARLO STUDY

A thesis submitted in partial fulfilment of the requirements for the award of the degree

DOCTOR OF PHILOSOPHY

from

UNIVERSITY OF WOLLONGONG

by

M. A. R. OTHMAN

BACHELOR OF SCIENCE WITH HONOURS (PHYSICS)

CENTRE FOR MEDICAL RADIATION PHYSICS

DEPARTMENT OF ENGINEERING PHYSICS

2012

CERTIFICATION

I, Mohd Amir Radhi Othman, declare that this thesis, submitted in partial fulfilment of the requirements for the award of Doctor of Philosophy, in the Centre for Medical Radiation Physics, Department of Engineering Physics, University of Wollongong, is wholly my own work unless otherwise referenced or acknowledged. The document has not been submitted for qualification at any other academic institution.

____

Mohd Amir Radhi Othman

17 August 2012

ABSTRACT

There are many types of semiconductor detectors used in radiation detection and dosimetry. A common problem of these detectors under a wide energy spectrum is that their response in a radiation field depends on energy. In radiation protection-applications, gamma and neutron are the most common primary radiation. Other forms of radiation, such as hadronic particles, are important in space applications, but are not included in the scope of this study because they deserve a separate examination. This study mainly focuses on the development of semiconductor dosimeters for mixed gamma-neutron, with an improved energy response achieved by an innovative design and packaging that can adjust the energy response of the detector for each application. Two detectors – were the metal-oxide-semiconductor field-effect transistor (MOSFET) for gamma dosimetry and the pixelated silicon diode detector, Medipix2 [1] for fast neutron dosimetry – were modelled using a Monte Carlo simulation developed in the GEometry ANd Tracking (GEANT4) application toolkit to improve their energy response.

Since the MOSFET was introduced to the field of radiation detection, its packaging has undergone many evolutions to satisfy its intended working conditions. This study focuses on the optimisation of MOSFET packaging to adjust its energy response for personnel dosimeter applications. The aim of this optimisation was to reduce its tendency to over-respond at photon energy less than 100 keV.

Medipix2 was first developed as a tracker of high-energy charged particles in HEP applications; it subsequently found a use as an X-ray imaging detector. In later developments Medipix2 demonstrated its ability in neutron imaging and detection [2], thereby showing its potential as a neutron dosimeter. This research proposed and developed a structured hydrogen-rich neutron converter coupled with Medipix2 to achieve an independent energy response. The converter was designed to allow Medipix2 to measure the ambient dose equivalent of neutrons [3]. The GEANT4 simulation results were then compared to the preliminary experimental results on fast-neutron sources. These promising results will help pave the way for future development of a novel fast-neutron detector.

ACKNOWLEDGEMENTS

I would like to thank Professor Anatoly B. Rosenfeld for his constant support and guidance throughout my enrolment in this degree. His competence in research helped him to teach me well, even though he manages many research students. The flexibility he offered in conducting my research made me feel very comfortable. His professionalism when contacting research colleagues and maintaining and expanding a research network is outstanding, and is something I would like to emulate. I would like to thank him for the research skills that I learned from him.

Although Dr. Dean Cutajar was not my official co-supervisor, his helps – particularly Monte Carlo simulations – was invaluable. I would like to thank him for introducing me to the GEANT4 simulation toolkit, and to cluster development and setup. He also introduced me to other researchers, many of whom became my friends. Thanks also to Dr. Bradley M. Oborn for useful discussions on GEANT4 and aspects of the computer simulations. I thank Dr. Nick Hardcastle for his comments and discussion on writing a good scientific paper. I have learned from Dean, Brad and Nick that doing Ph.D. research is also a candidate’s contribution to the team’s work, as it constitutes part of the strong research program at CMRP.

I would like to thank Dr. Susanna Guatelli for useful discussion and guidance in advanced GEANT4 programming, and for her help in the simulation of Medipix2 detector. I would like to thank Dr. Marco Petasecca, Dr. Damian Marinaro, Dr. Joseph Uher, Dr. Dale Prokopovich and Dr. Mark Reinhard for their help during my final project study on the Medipix2. I want to acknowledge the friendly people in my research centre, Dr. Micheal Lerch, Dr. Jeannie Wong, Dr. Scott Penfold, Dr. Lakshal Parera, Amy Ziebell, Laili Abd. Kabir, Alise Pogson, Cheryl Lian, Nandika Thapar and Marion Bug. I also acknowledge the editorial assistance of Laura E. Goodin.

I would like to thank my wife Izazuliati and my family for their patience and support throughout my study in Wollongong.

Finally, I would like to thank all the people I met during my study at the Centre for Medical Radiation Physics for being very friendly and helpful.

TABLE OF CONTENTS

Chapter 5

Chapter 6

LIST OF FIGURES

LIST OF TABLES

PUBLICATIONS

The author contributed to the following peer-reviewed publications:

- M.A.R. Othman, D.L. Cutajar, N. Hardcastle, S. Guatelli, A.B. Rosenfeld. *Monte Carlo study of MOSFET packaging, optimised for improved energy response: Single MOSFET filtration.* Radiation Protection. Dosimetry, 141(1):10-17. 2010.

- M.A.R. Othman, D.G. Marinaro, M. Petasecca, S. Guatelli, D.L. Cutajar, M.L.F. Lerch, D.A. Prokopovich, M.I. Reinhard, J. Uher, J. Jakubek, S. Pospisil, A.B. Rosenfeld. *From imaging to dosimetry: GEANT4-based study on the application of Medipix to neutron dosimetry*. Radiation Measurements 45(10): 1355-1358. 2010.

- Othman, M.A.R.; Petasecca, M.; Guatelli, S.; Uher, J.; Marinaro, D.G.; Prokopovich, D.A.; Reinhard, M.I.; Lerch, M.L.F.; Jakubek, J.; Pospisil, S.; Rosenfeld, A.B. *Neutron Dosimeter Development Based on Medipix2*. IEEE Transactions on Nuclear Science 57(6): 3456-3462. 2010.

CONFERENCES

The author's work has been presented at the following conferences:

- M.A.R. Othman, D.G. Marinaro, M. Petasecca, S. Guatelli, J. Uher, D.A. Prokopovich, M.I. Reinhard, J. Jakubek, S. Pospisil, D.L. Cutajar, M.L.F. Lerch, A.B. Rosenfeld. *From imaging to dosimetry: GEANT4-based study on the application of Medipix to neutron personnel dosimetry*. 11^{th} Neutron and Ion Dosimetry Symposium, NEUDOS-11. October, 2009. Cape Town, South Africa.

- M.A.R. Othman, D.G. Marinaro, M. Petasecca, S. Guatelli, J. Uher, D.A. Prokopovich, M.I. Reinhard, J. Jakubek, S. Pospisil, D.L. Cutajar, M.L.F. Lerch, A.B. Rosenfeld. *From imaging to dosimetry: GEANT4-based study on the application of Medipix to neutron personnel dosimetry and experimental application*. Nuclear Science Symposium and Medical Imaging Conference, NSS/MIC IEEE. October, 2009. Orlando, USA.

- M.A.R. Othman, D.G. Marinaro, M. Petasecca, S. Guatelli, J. Uher, D.A. Prokopovich, M.I. Reinhard, J. Jakubek, S. Pospisil, D.L. Cutajar, M.L.F. Lerch, A.B. Rosenfeld. *From imaging to dosimetry: GEANT4-based study on the application of Medipix to neutron personnel dosimetry*. GEANT4 User Workshop. October, 2009. Catania, Italy.

- D.G. Marinaro, M.A.R. Othman, S. Guatelli, J. Jakubek, S. Pospisil, A.B. Rosenfeld. *The application of pixelated detectors to neutron personnel dosimetry*. Joint 6^{th} Singapore International Symposium On Protection Against Toxic Substances (6^{th} SISPAT) and 2^{nd} International Chemical, Biological, Radiological & Explosives Operations Conference (2^{nd} ICOC). Dicember, 2009. Singapore.

- Mohd A. R. Othman, M. Petasecca, S. Guatelli, J. Uher, Damian G. Marinaro, Dale A. Prokopovich, Mark I. Reinhard, Michael L. F. Lerch, J. Jakubek, S. Pospisil, and Anatoly B. Rosenfeld. *Neutron Dosimeter Development Based on Medipix2*. IEEE Nuclear and Space Radiation Effects Conference, NSREC. July, 2010. Denver, Colorado, USA.

- Mohd A. R. Othman, M. Petasecca, S. Guatelli, J. Uher, Damian G. Marinaro, Dale A. Prokopovich, Mark I. Reinhard, Michael L. F. Lerch, J. Jakubek, S. Pospisil, and Anatoly B. Rosenfeld. *Development of a Neutron Energy Independence Solid State Dosimeter Based on Multi Converter on Medipix2*. 16th International Conference on Solid State Dosimetry. September, 2010. Sydney, Australia.

CHAPTER 1

INTRODUCTION

1. 1 Dosimetry of ionising radiation

The quanta of moving particles (with or without mass) that carry a distinct amount of energy have the ability to interact through electro-weak or hadronic interactions with the matter they traverse. Through this interaction they will ionise the matter either immediately or at a delayed time (decay). Thus they are regarded as ionising radiation. The two types of primary ionising radiation on which this study focuses are gamma and neutron. Gamma and neutron radiation, being uncharged particles, have a longer mean-free-path, and are thus of primary concern in most fields requiring radiation protection. A detector that detects ionising radiation, measures the energy deposited and translates the output proportional to the deterministic biological risk is called a dosimeter.

1.1.1 *Unit for measuring energy imparted by ionising radiation*

The basic *physical quantity* for measuring energy imparted by ionising radiation is absorbed dose. The ICRU Report 85 [4] defines the absorbed dose, *D*, as the quotient of $d\bar{\varepsilon}$ by *dm*, where $d\bar{\varepsilon}$ is the mean energy imparted by ionising radiation to matter of mass *dm*; thus:

$$D = \frac{d\bar{\varepsilon}}{dm} \tag{1.1}$$

where *D* is in unit of gray (Gy) or J kg^{-1}.

1.1.2 *Photon detection*

A photon is a quantum of electromagnetic energy. The quantum energy of photons is measured in *electron volts* (eV). X-ray and gamma radiation are photons with their quantum energies in the range above 120 eV and 100 keV, respectively. Both X-ray and gamma radiation could cause ionisation in matter with which they interact. With gamma it is understood that electromagnetic radiation usually originates from the nucleus due to a relaxation of the nucleus from an exited state to the ground state; in routine situations, gammas can come from Bremsstrahlung (e.g at the LHC), whereas X-rays can originate from the energy transition of electrons in an atom or from electrons accelerating (the Bremsstrahlung effect). In this thesis a photon will be regarded as having enough energy to cause ionisation in matter. Photons are detected through secondary electrons generated by the interaction of radiation with matter. These secondary electrons are generated from the photoelectric effect, Compton scattering and pair-production (a complete discussion on these interactions appears in Attix's book [5]).

The photoelectric effect is the process whereby an incident photon is absorbed by an atom, resulting in the emission of one of its previously bound electrons; this is then referred to as a photoelectron. The absorption of the photon with an energy E_{pe} can cause the atom to eject an electron of inner atomic shells with bounding energy $E_b < E_{pe}$. The kinetic energy T_{pe} given to the photoelectron is represented by:

$$T_{pe} = E_{pe} - E_b \tag{1.2}$$

The equation assumes that no kinetic energy is given to the atom from which the photon was absorbed. If the previously bound electron was from K- or L-shell, there will be a possibility for a second photon emission through the prompt filling of this inner shell vacancy from other bound electrons from a less tightly bound shell. The secondary photon emission also can produce another photoelectron. The energy deposited by the photoelectron in matter contributes to the absorbed dose. This interaction is depicted in Figure 1.1.

The resulting vacancy in the K-shell is promptly filled by an electron from outer shells, in this case from L-shell, as shown in Figure 1.1. This filling process is accompanied by the disposal of excessive energy from the different $hv_K - hv_L$ of the K-shell and the L-shell bounding energy level, respectively. It is disposed through either the emission of fluorescent X-rays or the ejection of Auger electrons.

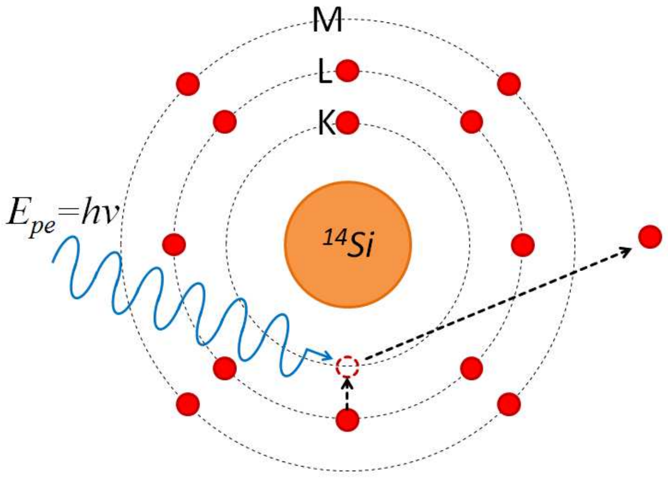

Figure 1.1: The photoelectric effect on a K-shell of a silicon atom. The silicon nucleus and the electrons are denoted by amber and red circles, respectively.

The photoelectric interaction cross-section per atom ${}_a\tau$ at incident energy of photons less than 0.1 MeV is represented by:

$$ {}_a\tau \propto \frac{Z^4}{\left(E_{pe}\right)^3} \;\; (cm^2/atom) \tag{1.3} $$

where Z is the atomic number. The photoelectric effect is a dominant process in silicon for energy of incident photons below 70 keV, as shown in Figure 1.2.

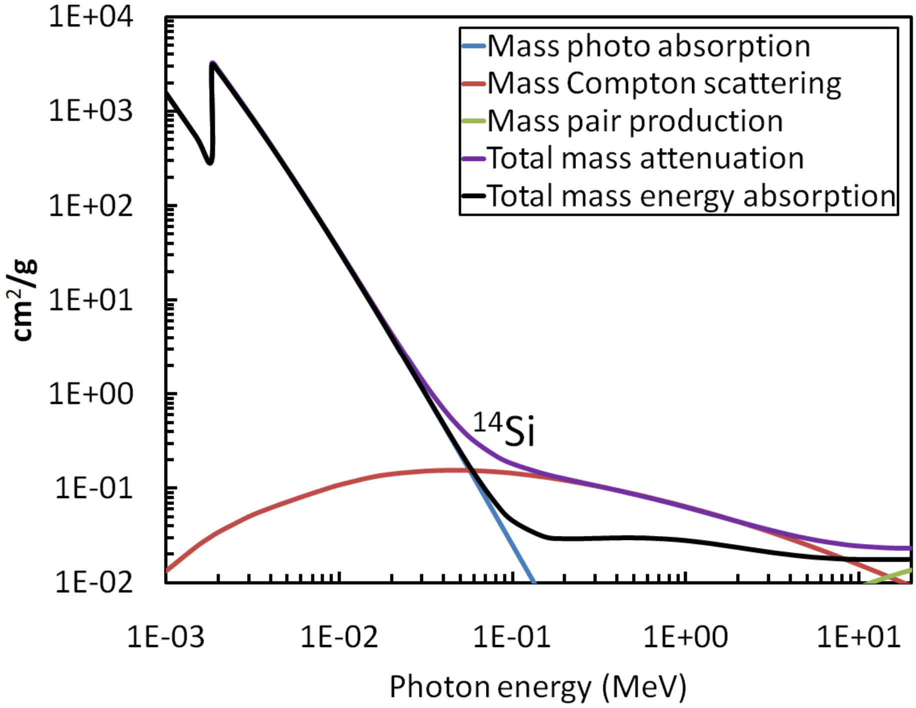

Figure 1.2: The contribution of photoelectric effect, Compton effect and pair-production to the coefficient of total mass attenuation of photons in silicon for energy of incident photons from 1 keV to 20 MeV [6].

The Compton effect is derived from the interaction of photons with free electrons that are assumed to be unbound and stationary. For silicon, the Compton effect is the dominant effect on the energy of incident photon > 70 keV, as shown in Figure 1.2. In this interaction, the energy E_{cs} of the incident photon is partly given as kinetic energy T_{cs} to the stationary electron, and the other part to a scattered photon with energy E_s, as shown in Figure 1.3.

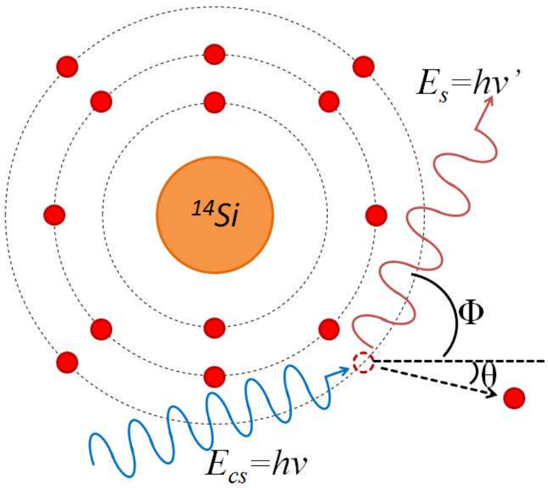

Figure 1.3: The Compton effect on a valence shell of a silicon atom. The angles of scattered electron and photon are denoted by θ and Φ respectively. The silicon nucleus and the electrons are denoted by amber and red circles, respectively.

Assuming bounding energy of the valence electron $E_b << E_s$,

$$T_{cs} = E_{cs} - (E_s + E_b) \approx E_{cs} - E_s \tag{1.4}$$

The energy deposited by the scattered Compton electron in matter contributes to the absorbed dose. The Klein-Nishina cross-section for the Compton effect per atom ${}_a\sigma$ is represented by:

$${}_a\sigma = Z \cdot \ {}_e\sigma \ \ (cm^2/atom) \tag{1.5}$$

where ${}_e\sigma$ is the Klein-Nishina cross-section per electron per unit solid angle. The ${}_e\sigma$ is dependent on the energy of incidence photon. The differential form of ${}_e\sigma$ is given below.

$$\frac{d_e\sigma}{d\Omega_\Phi} = \frac{r_0^2}{2}\left(\frac{hv'}{hv}\right)^2\left(\frac{hv}{hv'} + \frac{hv'}{hv} - sin^2\varphi\right) \tag{1.6}$$

where $E_{cs} = hv$, $E_s = hv'$, Φ is photon scattering angle and r_0 is the classical electron radius, with a value of 2.818×10^{-13} cm.

Pair-production is an absorption process whereby an incident photon is converted into an electron-positron pair, as shown in Figure 1.4. This process takes place in a Coulomb force field near either an atomic nucleus or an electron. The probability of pair-production occuring in the Coulomb force field of an electron is lower than near that of the atomic nucleus; thus, it is not discussed here. Therefore the threshold energy for this process is equal to the rest mass energy of those products, which is $2m_oc^2$ = 1.02 MeV, where m_o is a rest mass of electron and c is the speed of light in vacuum.

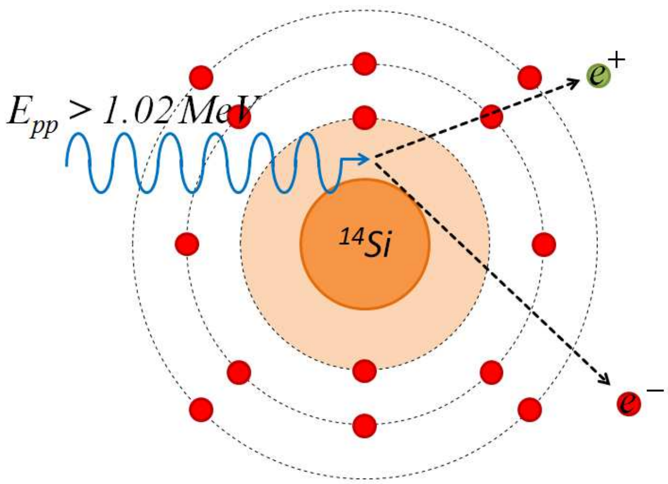

Figure 1.4: The pair-production interaction in a field of a silicon nucleus. The silicon nucleus and the electrons are denoted by amber and red circles, respectively.

The kinetic energies given to the electron and positron pair on average are:

$$\bar{T} = \frac{E_{pp} - 1.02\ MeV}{2} \quad (1.7)$$

where $\bar{T}$ is the average kinetic energy. The energies deposited by the scattered pair in matter contribute to the absorbed dose. The cross-section per atom ${}_a\kappa$ of the pair-production is represented by:

$$ {}_a\kappa = \sigma_o Z^2 \bar{P} \ \ (cm^2/atom) \tag{1.8} $$

where σ_o = 5.8 × 10^{-28} cm^2/electron, $\bar{P}$ is a function of E_{pp} and Z. For a silicon atom, the contribution of the pair-production is only significant (> 10^{-2} cm^2/g) at an incident-photon energy > 10 MeV, as shown in Figure 1.2.

The cross-section of the interaction between those effects varies according to the energy of the photons and the material. As an example, at photon energy < 100 keV, the semiconductor detector has a greater photoelectric absorption than water, which can cause an over-response in terms of dose in tissue or water(Figure 1.10). Thus, for photons, a dosimeter made from tissue-equivalent (TE) material is better in a spectrum of unknown photons, despite its being more difficult to realise. TE material has an effective atomic number Z_{eff} near or equal to the effective atomic number of the corresponding tissue; thus, it responds to photon interaction in the same way as the tissue.

1.1.3 *Neutron detection*

Like photons, neutrons are indirectly ionising radiation that deposit ionising energy from secondary charged particles that are generated by the interaction of neutrons with a nucleus. Neutrons are categorised according to their kinetic energies, which from a dosimetry aspect are either fast, intermediate-energy or thermal neutrons. The energy range for these types of neutrons are > 10 keV, 0.5 eV – 10 keV and < 0.5 eV [5], respectively. A cross-section of their interaction depends on the energy of the neutrons in a particular medium.

These cross-sections, which can be either elastic or inelastic interactions, are not always smooth; they can show resonances, as shown for silicon in Figure 1.5. Elastic scattering is an interaction where the incident neutrons transfer small part of their kinetic energy to the recoil nucleus, with the internal energy states of both colliding entities unchanged and both kinetic energy and momentum conserved in the final state, as shown in Figure 1.6(a). In inelastic interactions of neutrons, the incident neutron is temporarily absorbed and the nucleus is excited [7]. This prompts an emission of one neutron with lower energy and a gamma ray, as shown in Figure 1.6(b).

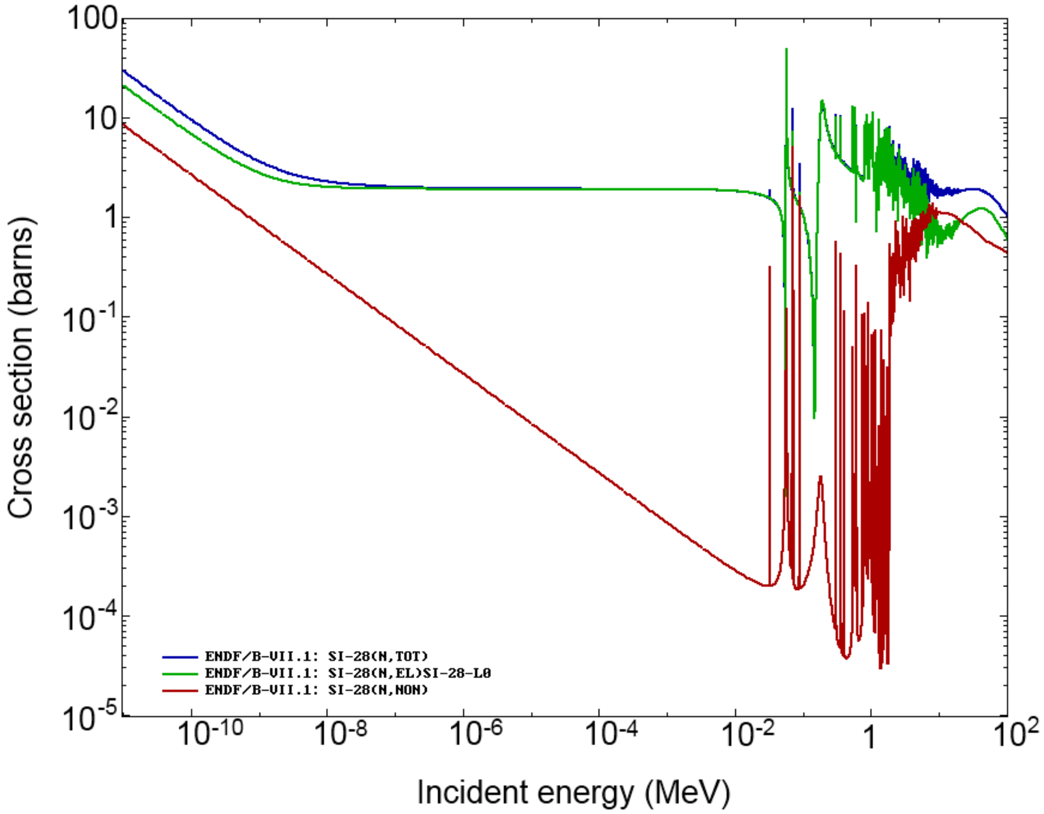

Figure 1.5: The interaction cross-sections of neutrons in ^{28}Si: total (blue line), elastic (green line), and inelastic (red line) cross-sections [8].

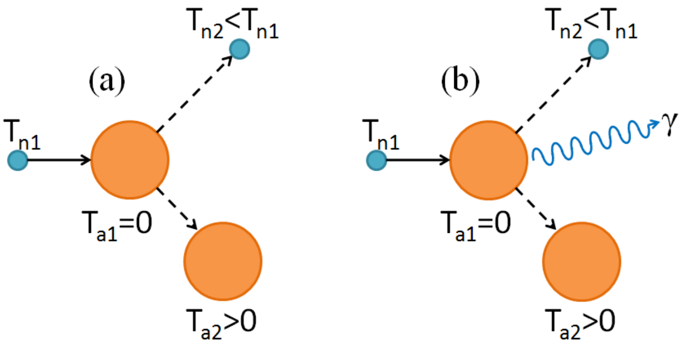

Figure 1.6: Neutrons in (a) elastic interaction and (b) inelastic interaction. T_{n1}, T_{n2}, T_{a1}, and T_{a2} are the kinetic energies of the incident neutrons, scattered neutrons, stationary target nucleus and recoil nucleus, respectively. γ is the gamma ray emitted in an inelastic interaction.

The elastic scattering of neutrons in silicon is a dominant interaction for energy of incident neutrons from 10^{-5} eV to 5 MeV (Figure 1.5). The inelastic interaction is solely represented by a radiative capture for the energy of incident neutrons from 10^{-5} eV to 1.8 MeV. In radiative capture, a neutron is absorbed and the nucleus is excited. The excited nucleus decays through an emission of a gamma ray and becomes a different isotope with the addition of one atomic weight from its predecessor, in this case, ^{28}Si(n,γ)^{29}Si.

For an incident-neutron energy from 1.8 to 20 MeV, neutron interaction is represented partially by radiative capture, inelastic interaction, ^{28}Si(n,2n)^{27}Si, ^{28}Si(n,n+α)^{24}Mg, ^{28}Si(n,n+proton)^{27}Al, ^{28}Si(n,proton)^{28}Al, ^{28}Si(n,deuteron)^{27}Al and ^{28}Si(n,α)^{25}Mg interactions. All these interaction cross-sections are as shown in Figure 1.7. The interactions types that have not been plotted are ^{28}Si(n,triton), ^{28}Si(n,^{3}He) and ^{28}Si(n,2proton). Above 20 MeV energy of incident neutrons, neutron interaction is represented by a simplified term of ^{28}Si(n,anything) which is used by the Evaluated Neutron Data File [8].

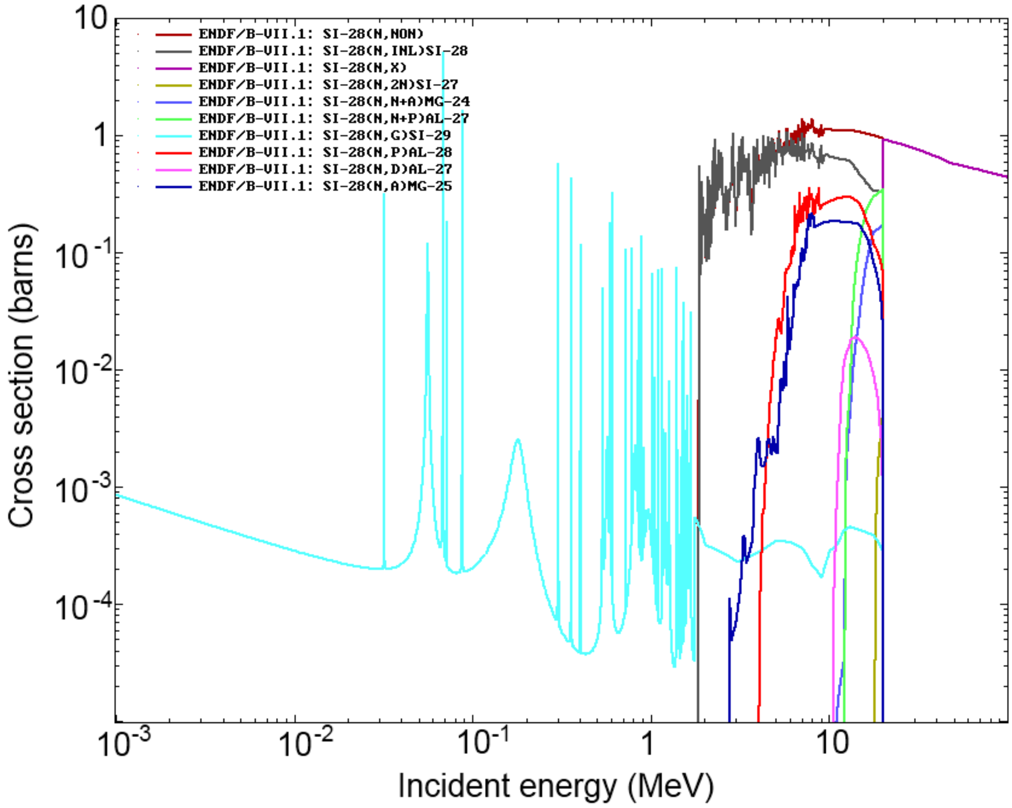

Figure 1.7: The partial contribution of the neutron interaction [8]. The non-elastic, inelastic, radiative capture, ^{28}Si(n,2n)^{27}Si, ^{28}Si(n,n+α)^{24}Mg, ^{28}Si(n,n+proton)^{27}Al, ^{28}Si(n,proton)^{28}Al, ^{28}Si(n,deuteron)^{27}Al and ^{28}Si(n,α)^{25}Mg interactions are denoted as SI-28(N,NON), SI-28(N,INL)SI-28, SI-28(N,G)SI-29, SI-28(N,2N)SI-27, SI-28(N,N+A)MG-24, SI-28(N,N+P)AL-27, SI-28(N,P)AL-28, SI-28(N,D)AL-27 and SI-28(N,A)MG-25, respectively. The simplified term of ^{28}Si(n, anything) interaction is denoted as SI-28(N,X) [8].

A semiconductor detector for neutron dosimetry is generally coupled to a material that contains a concentration of isotope for converting the incident neutron into detectable charged particles. It has rarely been used without a converter because its energy response in term of kinetic energy released per mass (KERMA) differs to that in tissue (Figure 1.8).

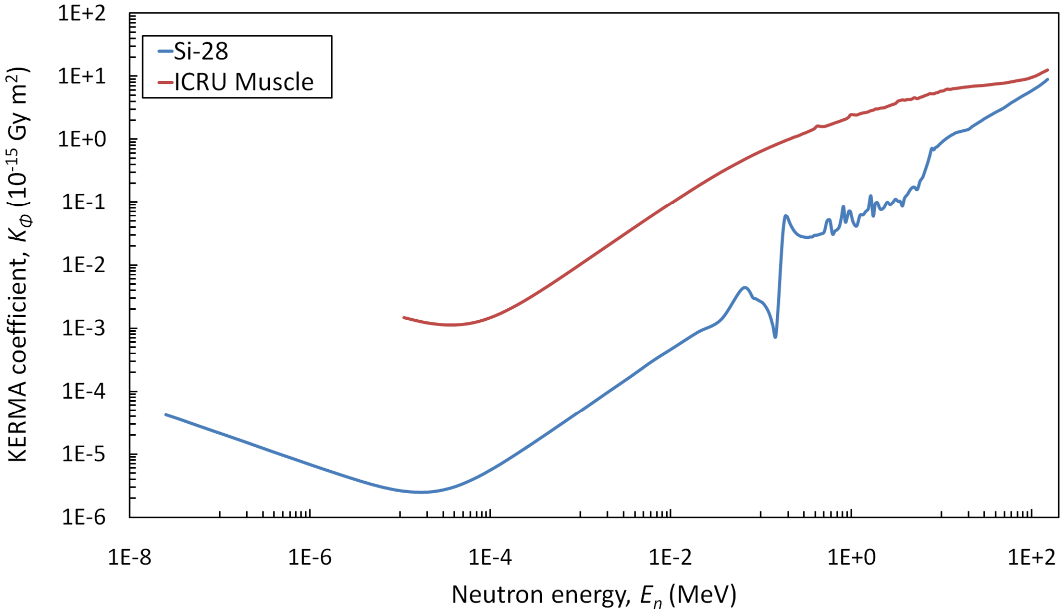

Figure 1.8: The coefficients of KERMA for ^{28}Si and ICRU muscle versus the energy of incident neutron [9].

Neutrons undergo multiple elastic scatterings in a moderator before they become thermalised; increase its probability to be absorbed by a nucleus. The cross-section of such a process is proportional to 1/*v*, where *v* is the velocity of the neutron. ^{10}B and ^{6}Li are examples of a good converter for this type of detection, particularly in association with semiconductor neutron detectors.

A charged alpha particle is produced from thermal neutron absorption in a converter that contains either a ^{10}B or ^{6}Li isotope resulting from ^{10}B(n,α)^{7}Li and ^{6}Li(n,α)^{3}H reactions, respectively. These interactions have larger cross-sections than an inelastic cross-section in silicon at an energy range of incident neutron below 1 MeV (Figure 1.9). The alpha particle from these interactions has an energy of either 1.47 MeV (^{10}B) or 2.05 MeV (^{6}Li) [10]. The neutrons are detected through electronic signal generated in the semiconductor detector when it is traversed by the charged alpha particle.

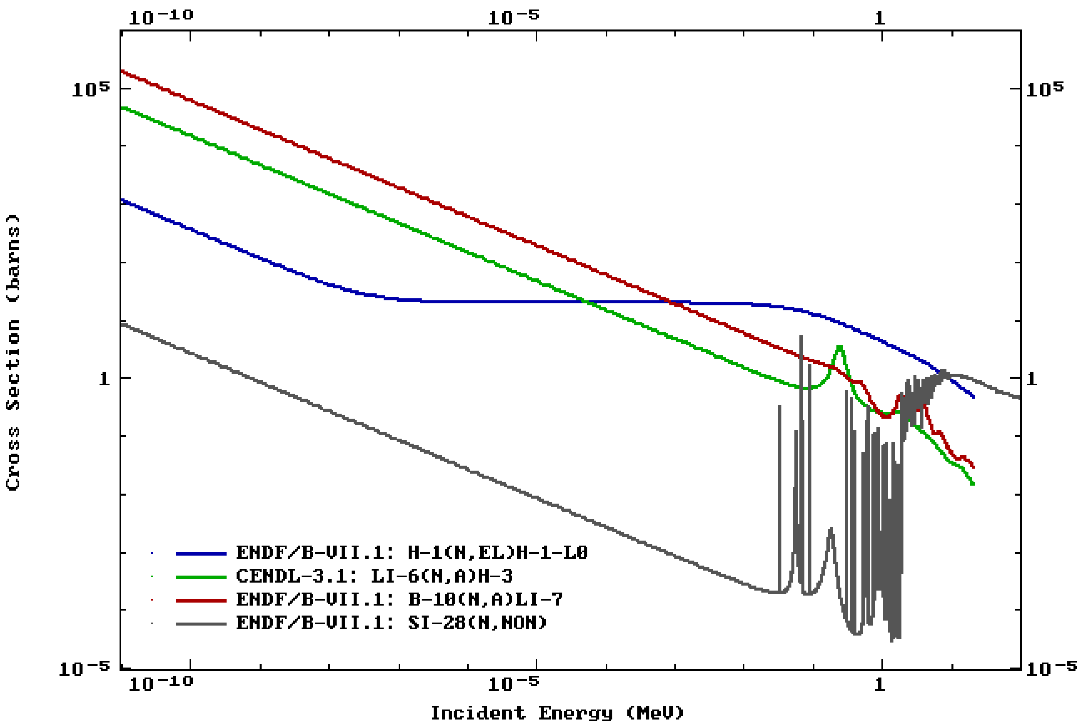

Figure 1.9: The comparison of cross-sections of ^{1}H elastic (blue line), ^{6}Li(n,α)^{3}H (green line) and ^{10}B(n,α)^{7}Li (red line) to inelastic interaction of silicon (grey line) [8].

^{10}B has a natural isotopic abundance of 19.8%, whereas ^{6}Li has a natural isotopic abundance of 7.4% [10]. ^{10}B is usually found in a semiconductor detector as a dopant in a *p*-type silicon or as a layer of *p+* silicon on top of the semiconductor detector simultaneously serving as a p-n junction and converter. A ^{6}Li converter can also be deposited on a semiconductor detector in the form of LiF, or be present in a thermo-luminesence LiF dosimeter (TLD); this is widely used for thermal neutron dosimetry. The ^{6}Li isotope inside a TLD 600 has up to 95.6% concentration [11].

Other way to detect fast neutrons is by using a hydrogen-rich converter such as polyethylene (PE) to convert neutrons into recoil protons resulting from elastic scattering. The energy of the recoil protons is represented by:

$$E_p = E_n cos^2\theta \tag{1.9}$$

where E_p is the energy of the recoil proton, E_n is the energy of the incident neutron and θ is the recoil angle in a laboratory frame. From Figure 1.9, it is clear that the hydrogen-rich converter, due to its large cross-section of interaction (which contributes to a higher detection efficiency of neutrons), is favourable in fast-neutron dosimetry applications.

1.1.4 *The relevance of the Bragg-Gray cavity theory to semiconductor detectors*

The advantage of semiconductor detectors in medical radiation dosimetry lies in their small sensitive volume (SV), whereas most secondary electrons produced by photons in water or tissues have a range that is larger than the average chord of sensitive volume. The response of the detector with a small sensitive volume is driven by the Bragg-Gray relation:

$$\frac{D_w}{D_s} = \frac{\bar{S}_w}{\bar{S}_s} = \bar{S}_s^w \tag{1.10}$$

where D_w is the dose in surrounding water, D_s is the dose in the silicon, $\bar{S}_w$ and $\bar{S}_s$ are the mass collision stopping power averaged over charge particle spectrum, for water and silicon respectively and $\bar{S}_s^w$ is the ratio of $\bar{S}_w$ over $\bar{S}_s$.

It is assumed that a semiconductor detector satisfies the Bragg-Gray cavity condition such as it does not perturb the charged-particle field and the absorbed dose in the sensitive volume is deposited entirely by the charged particles that are crossing it [5]. Even if a situation where charged-particle equilibrium (CPE) is absent, Equation (1.10) is still valid.

The sensitive volume considered in this thesis for a semiconductor detector is made from either silicon or silicon oxide (SiO_2). In the photon field, the secondary charged particles are mostly secondary electrons; this could cause ionisation in the sensitive volume if they have a minimum energy of 3.6 eV in silicon and either 18.4 eV [12], 18 eV [13] or 17 eV [14] in SiO_2. The advantage of a silicon detector is that the ratio of the mass stopping power of water to silicon and silicon oxide, $\bar{S}_s^w$ as presented in Figure 1.10, is quite constant over a wide electron-energy range, which leads to a small correction in the application of the semiconductor detector in the megavoltage (MV) X-ray field. Thus in the region where Compton scattering dominates, the energy deposition in a semiconductor detector is proportional to that in water. Hence even if the semiconductor detector is not composed of TE material, it can still be used as a relative dosimeter to measure an absorbed dose in water. However, where the energy of secondary electrons is lower, and where the size of a sensitive volume is comparable with a range of secondary electrons, dose enhancement can essentially be due to the contribution of photons absorbed in a sensitive volume; that is, the effect of the ratio of mass energy absorption coefficient of silicon to that of water is strongly dependent on the energy of the photon (Figure 1.10).

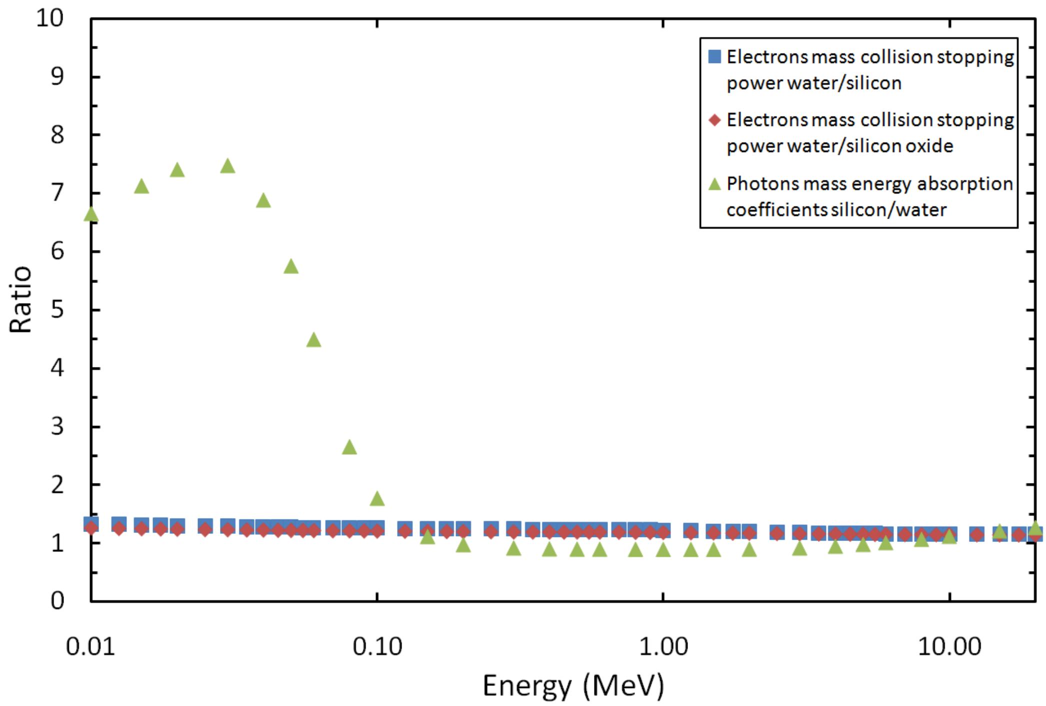

Figure 1.10: The ratios of electron’s mass stopping power of water to silicon and water to silicon oxide are almost constant over the energy of electrons from 10 keV to 20 MeV. The ratio of photon mass energy absorption coefficient of silicon to water shows an increase at lower photon energies due to higher photoelectric absorption in silicon than in water.

1. 2 Dosimetry in radiation protection

Radiation protection, sometimes known as radiological protection, is the science of protecting people and the environment from the harmful effects of ionising radiation, which includes both particle radiation and high-energy electromagnetic radiation [15]. In practical terms, radiation protection is the adoption of policies regarding exposure and providing shielding if necessary. Dosimetry is the act of monitoring the effectiveness of radiation-protection policies, and if done in real time can itself be incorporated into the policies. Four major international bodies develop standards for radiation protection:

- *International Commission on Radiation Units and Measurements* (ICRU).
  The ICRU is responsible for developing internationally accepted quantities and units for radiation and radioactivity, suitable procedures for measuring and applying quantities of radiation and providing conversion factors for electron, photon and neutron radiation into the dosimetry unit of interest [16].
- *International Commission on Radiological Protection* (ICRP).
  The ICRP is an advisory body that provides guidance and recommendations for radiation protection [17]. The ICRP works closely with the ICRU to develop recommendations for radiation protection. The ICRP and ICRU produce complementary reports for application in radiation protection.
- *International Organization for Standardization* (ISO).
  Under the ISO technical committee for Nuclear Energy, ISO/TC 85, and in the subcommittee for Radiation Protection, ISO/TC 85/SC 2, there are currently thirteen Working Groups (ISO/TC 85/SC 2/WG) developing a standard for radiation protection [18]. This standard will differ from those from the ICRU and ICRP in that it will aid the international exchange of radioactive goods and services, and develop a cooperative approach to radiation protection in the spheres of intellectual, scientific, technological and economic activity [19]. The ISO standard implements fundamental quantities and units defined by the ICRU and ICRP with respect to the availability of resources and apparatus used in real-world practice.

- *International Atomic Energy Agency* (IAEA).
  Practically, the IAEA uses standards from the ISO, ICRP, and ICRU to provide services and produce their Technical Report Series (IAEA TRS). They run the Primary Standard Laboratory (PSL) and Secondary Standard Dosimetry Laboratory (SSDL) to provide national reference standards based on those of the ISO, ICRP, and ICRU.

1.2.1 *Operational quantities*

The same dose of radiation from different particles has different effects on a biological tissue. To take this into account, new quantities of dose are defined as:

$$H_T = w_R D_{T,R} \tag{1.11}$$

where H_T is the dose equivalent in tissue T, $D_{T,R}$ is the average absorbed dose and w_R is the weighting factor for radiation R. The H_T SI unit is J kg^{-1}, but its special name is *Sievert* (Sv) [20]. The H_T is a *protection quantity* used to predict the radiobiological effect of ionising radiation. The effects depend on the *Linear Energy Transfer* (LET) of the particle in the biological tissue.

The *operational quantities* in radiation protection are in two categories: the operational quantities for area monitoring and individual monitoring. The dose equivalent, *H*, for *operational quantities*, is defined as:

$$H = \int_L Q(L) \cdot \frac{dD}{dL} \cdot dL \tag{1.12}$$

where $Q(L)$ is the quality factor for the particle with a linear energy transfer (LET), L, and the $(dD/dL) \cdot dL$ is the absorbed dose produced by charged particles with LET between L and $L+dL$. The *operational quantities* are described at depth d in a phantom, as $H(d)$.

The *operational quantities* for area monitoring are specified by the ambient dose equivalent, $H^*(d)$ and the directional dose equivalent, $H'(d,\Omega)$, where Ω is the incident radiation angle from the normal axis on the phantom surface. The *operational quantities* for individual monitoring are described by $H_p(d)$. The depths commonly use in radiation protection for individual monitoring are $H_p(0.07)$ for a skin dose and $H_p(10)$ for an organ dose [3].

1.2.2 *The use of phantoms in radiation protection*

The phantoms used in radiation protection serve two main purposes: first, as a theoretical medium to derive a conversion coefficient from *physical quantities* to *operational quantities*; and second, as the place to calibrate the dosimeter. The ICRU recommends a sphere phantom with a 30 cm diameter to calculate $H^*(d)$ and $H'(d,\Omega)$, and a slab phantom with 30 x 30 x 15 cm^3 to measure and calculate $H_p(d)$ [21]. Theoretically, phantoms should use ICRU tissue equivalent material with a density of 1 g cm^{-3} and a mass composition of 76.2% oxygen, 11.1% carbon, 10.1% hydrogen and 2.6% nitrogen.

In practice, the materials for the ICRU slab phantom can be made from polymethyl methacrylate (PMMA); in simulations they can be approximated by water. Backscatter from water as a material is similar to ICRU tissue [22, 23] at photon energies < 1 MeV. The ICRU slab phantom is the best practical approximation for a human trunk.

Other mathematical anthropomorphic phantoms are also used to derive the conversion coefficient of photon and neutron-dose equivalent [24-26].

1.2.3 *The* $H_p(0.07)$ *and* $H_p(10)$ *operational quantities for individual monitoring*

The quantities of $H_p(0.07)$ and $H_p(10)$ referred in this study are those recommended by the ICRP report 60 [27] for external dose protection. The special case of $H_p(d)$ is that it defined a dose equivalent at *d millimetres* deep in tissue from the surface at the point where the dosimeter was worn. Thus the absolute value of $H_p(d)$ depends on the the dosimeter's particular location on the human body, the size of the cross-sectional scoring volume for measuring $H_p(d)$ compared to the cross-section of the body surface, the size of the incident-radiation field and the incident-radiation angle. The standard procedures for deriving $H_p(0.07)$ and $H_p(10)$ use conversion factors to convert the air KERMA or exposure measured at the surface of the phantom at the point of interest to the dose equivalent at a particular depth in a specified phantom. These conversion factors also take the build-up dose and attenuation into account. For normally incident photon beams with energies more than 30 keV, the difference in dose between $H_p(0.07)$ and $H_p(10)$ under CPE is less than 10%, while for low-energy photons $H_p(0.07)$ can be essentially larger than $H_p(10)$ [28].

Previously, the measurement of *operational quantities* for area monitoring of $H_p(0.07)$ and $H_p(10)$ by Busuoli *et al.* [29] was performed using a 20 x 20 x 15 cm^3 slab of PMMA, as a standard phantom for measuring these quantities was unavailable until 1992 [21]. To avoid uncertainty in $H_p(0.07)$ and $H_p(10)$ related to different phantom geometry and KERMA approximation issues for $H_p(0.07)$ [24-26], this study further substituted them with $D_w(0.07)$ and $D_w(10)$, respectively. These quantities conservatively represent the absorbed photon dose at depths of 0.07 mm and 10 mm in the 30 x 30 x 30 cm^3 water phantom as used in Chapter 3 and Chapter 4, respectively (close to that recommended in the ICRU Report 47 [21] of 30 x 30 x 15 cm^3). Although the quantities $D_w(0.07)$ and $D_w(10)$ were used as surrogates for $H_p(0.07)$ and $H_p(10)$, they are still a close approximation.

1. 3 The MOSFET as a dosimeter

The Metal-Oxide-Semiconductor Field-Effect Transistor (MOSFET) device was introduced to the radiation detection community by Holmes-Siedel in 1974 for use in space dosimetry [30]. Since then, MOSFET has found its way as a dosimeter in radiotherapy [31-33], radiation monitoring in mixed gamma and neutron fields [34, 35], and space radiation monitoring [36-38]. The advantage of MOSFET as a dosimeter is its small sensitive volume, represented by 1 µm-thick gate oxide; this allows, for an active or passive mode of operation with and without gate bias [39] respectively, which can give a real-time [40, 41] or off-line [42-44] readout.

1.3.1 *Fundamental dosimetric characteristics of the MOSFET*

MOSFETs consist of a drain, source and gate on a silicon substrate (Figure 1.11). A thin layer of SiO_2 is grown on the top surface of the silicon substrate. Polysilicon or metal such as aluminium is deposited on top of the SiO_2 to form the gate.

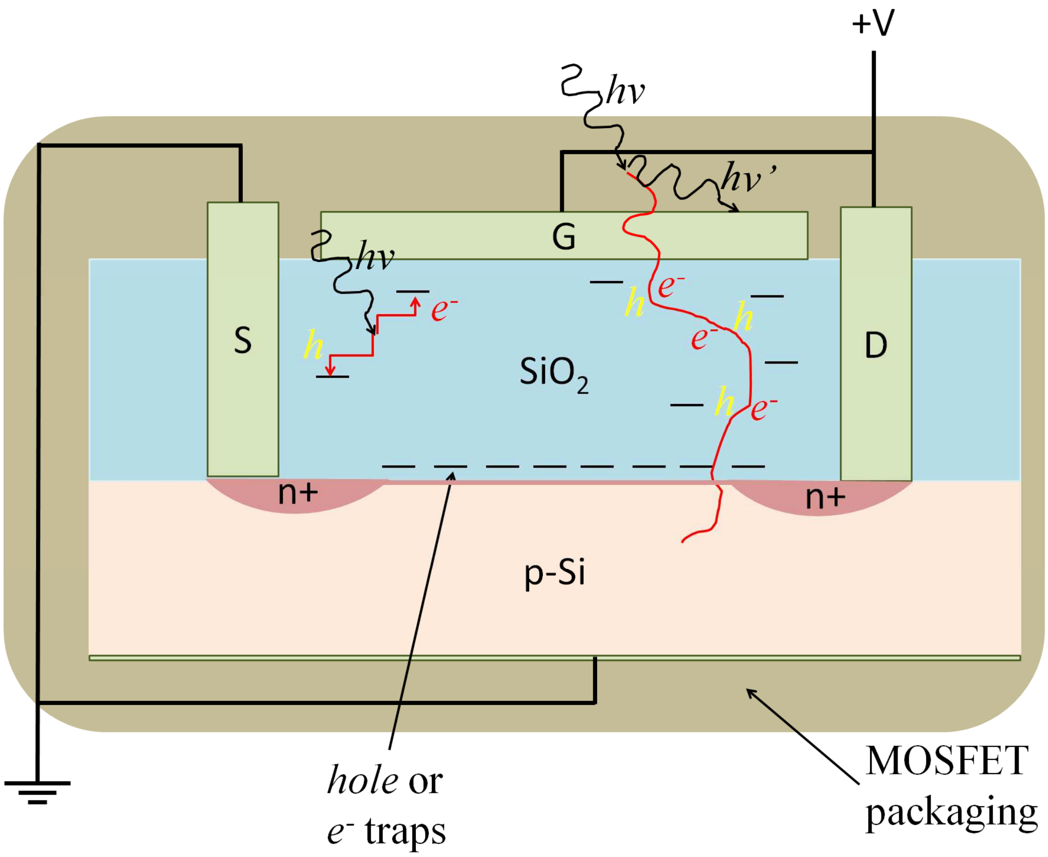

Figure 1.11: The basic structure of the n-MOSFET, where D is the drain, S is the source and G is the gate. Shown above is when the MOSFET is positively biased with a photoelectric interaction inside the sensitive volume and Compton scattering from the MOSFET packaging. Adapted from [45].

Figure 1.12 shows a diagram of the energy band for an ideal n-MOSFET. Without bias on the gate, the Fermi energy level E_F, of the metal gate aligns to the Fermi energy level in p-Si. When a negative bias is applied to the gate, the E_F of the metal increases. This causes the levels of p-silicon conductance energy, intrinsic energy and valence energy (represented by E_c, E_i and E_v, respectively) to bend upwards near the interface between Si-SiO_2. The resulting concentration of holes near the Si-SiO_2 interface increases and the concentration of electrons decreases; this condition is called accumulation. Inversely, under a small positive bias, the E_c, E_i and E_v bend downwards, and the concentration of holes decreases near the Si-SiO_2 interface while the concentration of electrons increases; this condition is called depletion. If the bias voltage keeps increasing, the concentration of electrons near the Si-SiO_2 interface will eventually be higher than the concentration of holes (a condition called inversion), forming a very thin layer of n-Si. In an inversion state, if a potential difference exists between source and drain, a current will flow between them. The magnitude of the current depends on the thickness of the inversion layer, which depends on the bias applied to the gate.

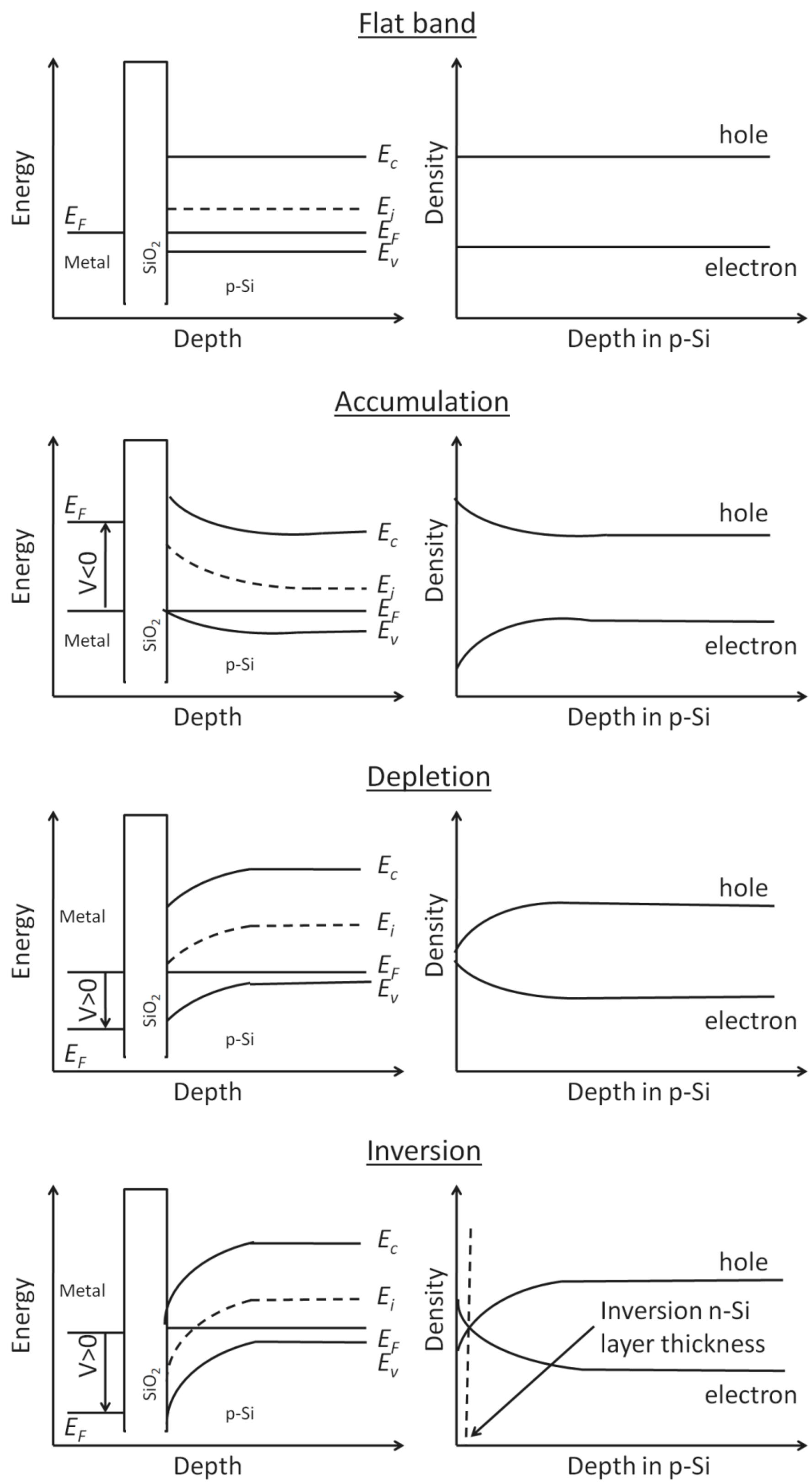

Figure 1.12: n-MOSFET energy band diagrams: i) under no gate voltage bias (flatband), ii) negative gate bias (accumulation), iii) small positive gate bias (depletion) and iv) large positive gate bias (inversion) (adapted from [46]).

As a dosimeter, the MOSFET operates under either no applied gate voltage (passive mode) or with a bias voltage applied to the gate (active mode). Active mode with a positive bias on the gate offers greater sensitivity in radiation detection than passive mode due to less recombination of electron-hole pairs in the gate oxide [39]. MOSFETs record the dose of ionising radiation in the silicon oxide in the manner of charge trapping in the SiO_2 and interface charge build up. When ionising radiation interacts with the SiO_2 gate, electron-hole pairs are formed. With or without positive bias on the gate respectively, the holes produced by ionising radiation are swept towards the Si-SiO_2 interface, where they are captured on traps and produce a positive sheet of charge. This charge leads to a negative shift in the gate voltage (ΔV_{th}) in p-MOSFET required to maintain a fixed current in the order of µA in a MOSFET channel [47]. The shift in threshold voltage is proportional to the absorbed dose in the SiO_2. (More detailed theory of MOSFET dosimetry can be found in [46]). The change in threshold voltage (ΔV_{th}) in a MOSFET is almost linear with low accumulated *D*, and can be described as:

$$\Delta V_{th} = \alpha \cdot D \tag{1.13}$$

where α is an experimental parameter [48]. Equation (1.13) held true for a simulation done in this study which considered that in most applications of interest in radiation protection, the expected accidental dose is less than 2-3 Gy; this is within the linear range of the passive p-MOSFET (developed at CMRP). For higher accumulated doses in the SiO_2, the saturation effect takes place that makes $\Delta V_{th} = \alpha\ (1 - e^{-\beta D})$, or alternatively, $\Delta V_{th} = kD^n$ [39], where α, β, k and n are parameters determined experimentally. The response of the absorbed-dose linear range and sensitivity can be increased by positive bias on a gate during irradiation that reduces the recombination of electron-hole pairs produced in the gate oxide due to a stronger electric field [49].

1.3.2 *Types of MOSFET dosimeters*

As reported in the literature, some major manufacturers are producing MOSFET dosimeters:

- RadFET [50] – This name, coined by Robert Hughes in 1985, is an abbreviation of Radiation-Sensing Field-Effect Transistor [51]. The dosimeter, which was invented by Andrew Holmes-Siedle, is produced by his company, REM Oxford Ltd. It is made from p-MOSFET with aluminium gate. The RadFET silicon substrate is 1 x 1 x 0.5 mm^3 and contains four MOSFETs. The SiO_2 is from 0.1 to 1.25 µm-thick. The MOSFET chip is mounted on the polymeric substrate and encapsulated by black epoxy resin. The RadFET REM TOT-501C was reported in a simulation study with a 950 x 950 x 0.25 μm^3 [52] of SiO_2. The silicon substrate for the REM TOT-501C is 405 µm-thick.
- TN-RD-70-W and TN-RD-90 [53, 54] – These dosimeters are built by Best Medical Canada. The old version of the TN-502RD, sold under the brand name Thomson and Nielsen Electronic Ltd, was equivalent to the Best Medical Canada's TN-RD-70-W and it was simulated without dimensions given in a proton-dose measurement [55]. The TN-502RD was reported to have 1 x 1 x 0.5 mm^3 of silicon substrate, and 200 x 200 x 1 μm^3 of SiO_2 [56]. Other literature reports a simulation of the TN-502RD done with 50 µm-thick SiO_2 [57]. A simulation on the other Thomson and Nielsen MOSFET, TN-1002RD, used 1 x 1 x 0.525 mm^3 of silicon substrate, 1 mm-thick epoxy, a 0.25 mm-thick by 2-mm wide Kapton base and 200 x 200 x 1 μm^3 of SiO_2 [58-61].
- LAAS 1600 – Manufactured by the Laboratory of Analysis and Architecture of System of CNRS in France, the LAAS 1600 was reported in a simulation study to have 1900 x 1900 x 1.6 μm^3 of SiO_2 [52]. The silicon substrate for the LAAS 1600 has the same area as SiO_2, but with a thickness of 405 µm.
- ESAPMOS4 – Manufactured by Tyndall National Institutes, this was formerly known as NMRC. The thickness of SiO_2 in the literature reports is 0.4 µm, and the cross-sectional area is 0.015 mm^2 [39, 40, 62].
- CMRP has extensive experience in clinical MOSFET dosimetry, and developed different versions of MOSFET-based dosimeters for photon- and neutron-radiation dosimetry. The CMRP MO*Skin* [63-65] dosimeter was designed and

built at the Centre for Medical Radiation Physics, University of Wollongong. The MO*Skin* readout has a special computerised reader that was also built at CMRP [66]. This dosimeter was specially developed for skin dosimetry; it has oxide thicknesses of 0.55 – 1 µm and a substrate only 350 µm-thick. The chip is covered by a thin, reproducible layer of material equivalent to water, which provides a water-equivalent depth (WED) of 0.07 mm. The MO*Skin* has a special "drop in" packaging in a thin 2.5 mm-wide Kapton carrier.

- Other MOSFETs include the SNL MOSFET, with 0.37 µm-thick oxide [67]; the RadFET-type MOSFET, for which simulation has been reported with a 1 µm aluminium gate, 1 µm SiO_2 and 500 µm-thick substrate [68]; Sicel Technologies' implantable MOSFET [45] and OneDose [44, 69].

1.3.3 *The effects of MOSFET configurations on dosimeter response*

Many configurations can affect the response of the MOSFET dosimeter in practice. Some of those will be described in this section.

The sensitivity of the MOSFET depends on the thickness of SiO_2, t_{oxide}. The ΔV_{th} changes proportionally according to t^2_{oxide} [70, 71]. This dependence is important in the application of the MOSFET as a dosimeter. For an example, a MOSFET with t_{oxide} = 1 µm and positive gate bias of 30 to 50 V is able to give a reading in steps of mGy of dose [72]. Thus the MOSFET can provide a reliable reading under low dose measurement.

The application of a voltage bias on the gate when the MOSFET is being irradiated tends to increase its sensitivity. A higher applied voltage bias means a higher electric field in the SiO_2 and Si-SiO_2 interface, which reduces the recombination of electron-hole, which in turn increases the sensitivity of the MOSFET. Also, the eventual build-up of traps at the Si-SiO_2 interface of the MOSFET during irradiation known as radiation-induced interface traps [73], increases with applied positive bias on p-MOSFET during irradiation. More details of this effect have been compiled by Oldham [74]. However, because the traps in the SiO_2 and Si-SiO_2 interface are likely to fill up quicker than when in a non-bias condition, the lifespan of the MOSFET becomes shorter. The rates at which the traps fill up differ for different photon irradiation energy at the same gate bias. When irradiated with high-energy photons (order of MeV), the

MOSFET would have a longer lifespan than if irradiated with photons at lowerenergy (order of keV) for the same dose in tissue or water [43]. This is because there is a stronger photoelectric effect for lower-energy photons (below 120 keV) and a large deposited energy in SiO_2 for the same tissue dose. However, the additional effect is a stronger charge recombination; this is due to a larger plasma density produced by lower energy electrons, which leads in turn to a stronger columnar recombination that depends on the electric field in a gate oxide.

If the time between irradiation and readout is prolonged, a MOSFET dosimeter could lose some of its trapped charge when stored at room temperature, due to a random process of thermally induced excitation [75]. The fading of the zero gate bias MOSFET is negligible in comparison with that for an active mode MOSFET, which tends to show a slight increase in fading after irradiation [39].

The responses of the MOSFET are influenced by the LET of charged particles. Near a track of high LET particles, the densities of electron-hole pairs are very high. This effect increases the chances of a recombination between the pairs, and thus reduces the response of the MOSFET. The high LET particles are either charged particles with a high-atomic-number, low energy MeV range protons or low-energy electrons [76].

1.3.4 *The challenge for the MOSFET as personnel dosimeter in the photon field*

The MOSFET is an excellent candidate for personal dosimetry, particularly for an instantaneous assessment of a gamma dose in an accident, and in military dosimetry, where radiation can be of a pulsed nature. The challenges in using the MOSFET for personnel dosimetry are its low sensitivity compared to TLD detectors, and energy dependence relative to its response to tissue dose. The former problem can be addressed with stacked MOSFETs [77, 78], and is not as important for accident and military dosimetry, where the absorbed doses of interest are more than 0.01 Gy. With regards to the latter, MOSFET dosimeters have been successfully used for military dosimetry, for example, in the United States army; the wristwatch dosimeter RADIACS AN/PDR-75 [79] is used in conjunction with a p-i-n diode neutron dosimeter in RADIACS AN/UDR-13 [80]. In these applications, the MOSFET dosimeter is being used in close to free-air geometry because it can be worn on a belt, wrist or tie-clip, or placed in free air around nuclear facilities. In such applications, optimising the energy response of a MOSFET dosimeter suitable for operational quantities for personal monitoring of $H_p(007)$ and $H_p(10)$ in a photon field is not a trivial task.

In previous work, MOSFET chips were packed in commercially available microelectronic packages of DIL, TO-5 and TO-8, which are less suitable for achieving a TE-penetrating dose response while being irradiated in free-air geometry [81, 82]. An early attempt to characterise the energy response of MOSFET for use as a military personal dosimeter with independent photon energy over the range of 80 keV to 1 MeV was undertaken by Brucker *et al.* [83]. In order for the MOSFET to be viable as a personal accidents dosimeter, particularly for detecting skin-absorbed doses from low-energy photons, the minimum measureable photon energy should be around 15 keV. Thus, 15 keV was considered as a minimum photon energy when designing the MOSFET package and simulating its energy response.

MOSFET detectors have been shown to over-respond to low-energy photons in free-air geometry, particularly below 100 keV [60]. This over-response stems from of the dose enhancement due to packaging materials with a high-atomic-number, and to stronger photoelectric interactions in SiO_2 than in tissue. This over-response has been ascertained previously either experimentally [84-86] or with Monte Carlo simulation [58-60]. Initial experimental results by Rosenfeld *et al.* [34], and Brucker *et al.* [82, 83] showed a correlation between the packaging of MOSFET detectors and energy response for effective X-ray energies (an average energy in the X-ray spectrum) below 250 keV. The essential dose-enhancement effect was related to an excessive creation of secondary electrons from commercial packaging's materials, which had high-atomic-number, and from the aluminium gate electrode of the MOSFET. The experimental attempt to characterise and adjust the energy response of the MOSFET in free-air geometry for photon fields was undertaken for TO-5-packed n-MOSFETs with the kovar lead removed and the MOSFET chip covered with epoxy [34]. In all previous work, the comparison of the MOSFET responses was performed relative to the absorbed dose in tissue or water in the case of full electronic equilibrium.

1.3.5 *Exploration of the MOSFET for personal accident dosimetry*

From the literature review and analysis of the existing MOSFET system, it is clear that the application of MOSFET for personal dosimetry has not been fully exploited, even though the MOSFET is very attractive substitution for TLD, optically stimulated luminescence (OSL) and radio-fotoluminescent (RFL) dosimeters for accident and military dosimetry. One of the aims of this work is to develop a MOSFET personal accident dosimeter for use in free-air (approximated with a vacuum) geometry, with a response that corresponds to wearing the detector as a dosimeter badge, rather than within a phantom application where full CPE is in place. The dosimeter should have an energy response proportional to the tissue energy response in terms of personal dose equivalent [87] for a large dynamic range of photon energies. Monte Carlo simulation was used to study the energy responses of the MOSFET under different configurations, as described in Chapter 2. The experience gained helped in the proposal of new MOSFET packaging designs, as described in Chapter 3 and Chapter 4, for improved MOSFET energy responses. The proposed methods include optimising the packaging for incident-photon energy above 15 keV and imitating backscatter as if the dosimeter were worn on the body.

1. 4 The Medipix2 as a neutron dosimeter

The Medipix2 [1] was the mutual outcome of 10 years of technological improvements in detector designs and knowledge gained through ongoing Medipix collaboration in scientific field instrumentation prior to Medipix1 [88]. As per Medipix1, Medipix2 was originally developed for X-ray radiography [89-91]. Later, Medipix2 was studied as an imaging device for electrons [92, 93], neutrons [94-98] and alpha radiation [99]. Medipix2 is actually a hybrid detector where a pixelated semiconductor detector is bump-bonded to the application-specific integrated circuit (ASIC) readout chip using flip-chip technology (Figure 1.13) [100, 101].

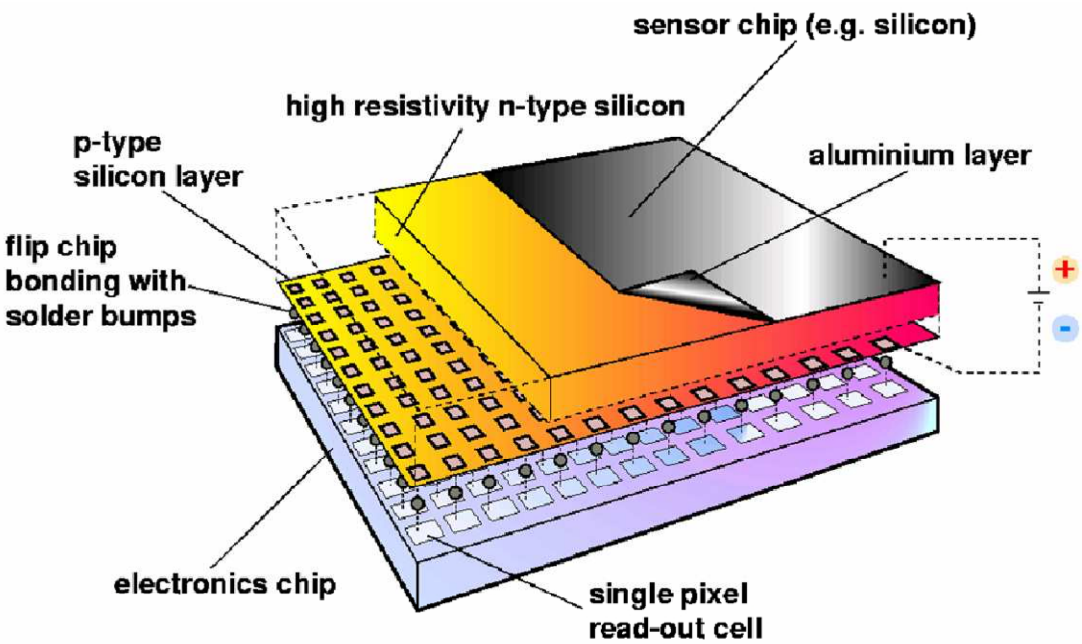

Figure 1.13: Construction of the hybrid detector where the pixelated silicon detector is based on high-resistivity n-Si with p+ implanted pixels (sensor) is connected to an ASIC multi-channel readout chip matched to p+ pixels (from [101]).

1.4.1 *The Medipix2 system*

The Medipix2 has an array of 256 x 256 pixels of 0.25 µm CMOS ASIC readout chips, to which the over-layer silicon sensor with the same array of diode segments can be mounted. Small readout chips with 55 µm pitch incorporate charge-sensitive amplifiers (CSA), a digital-to-analog converter (DAC), two discriminator thresholds, a pixel configuration register (PCR), a shift register and counter (SR/C) and double-discriminator logic [101]. The sensor over-layers can be any pixelated semiconductor made of Si, GaAs or CdTe and as thick as 1 mm. Figure 1.14 shows the detector used in this study, where the 300 µm-thick high-resistivity silicon was bump-bonded to the ASIC chips.

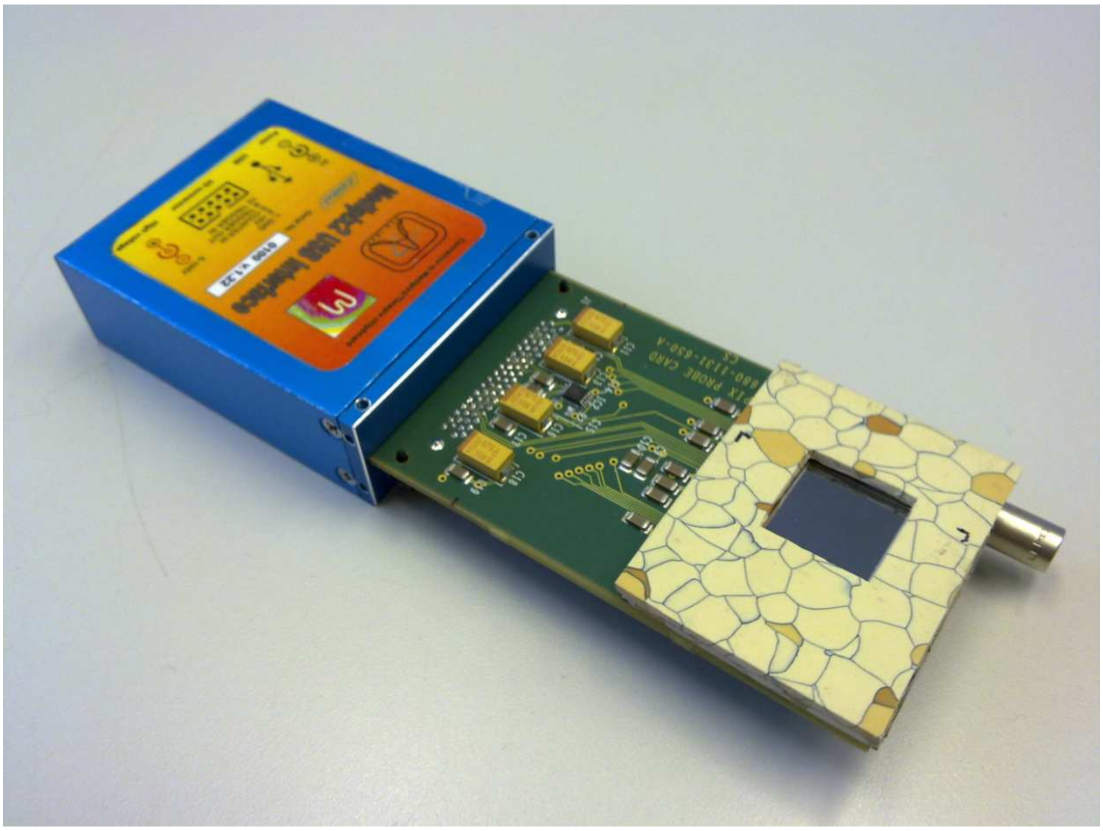

Figure 1.14: The Medipix2 detector used in this study. Shown on the blue box is the USB symbol indicating that this device can use a USB connection for data acquisition.

The active area of the Medipix2 is 14 x 14 mm^2. The Medipix2 can achieve 1 GHz of count rate at full array readout [97] and >1 kHz frame rate [98, 102]. The data acquisition is sent by USB to a personal computer, then processed by Pixelman software [103]. Figure 1.15 shows one of the Pixelman applications used to record clusters of pixels of collected charge formed from charged particles interacting in the silicon sensor. Simple analyses such as minimum and maximum size cluster filtration, minimum cluster roundness and cluster linearity are handled through this software. Details and explanation of cluster forming and handling relevant to neutron detection will be presented in Chapter 6.

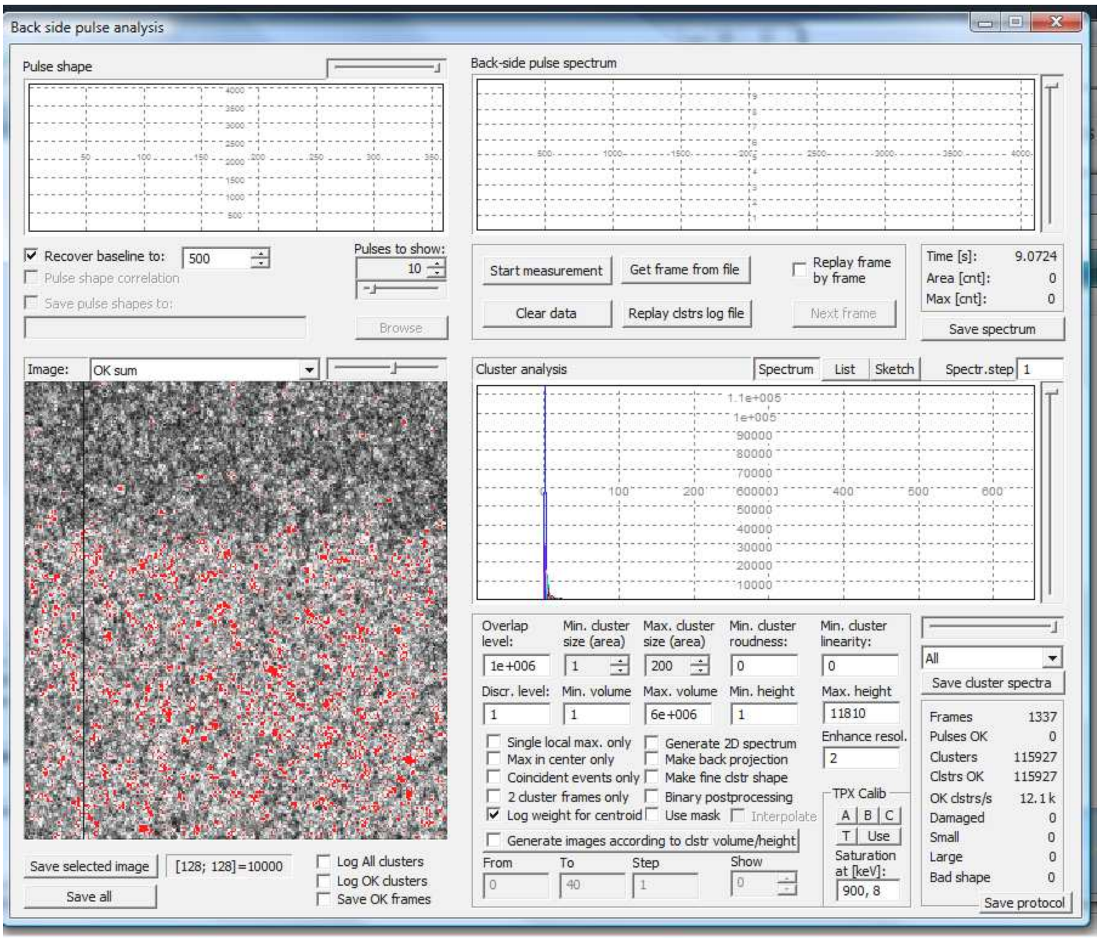

Figure 1.15: The Pixelman data acquisition for Medipix2 shows data acquired from the 14 MeV D-T neutrons, of which two-thirds of the Medipix2 is covered by 1 mm-thick PE. The red spots show higher counts obtained in the region where the converter is placed on the Medipix2 sensitive area.

1.4.2 *Fundamental dosimetric characteristics of the Medipix2*

When charged particles hit the sensor layer of a pixelated detector, they create electron-hole pairs along their tracks. The density of the pairs depends on the radial distance from the track and the effective charge and velocity of the charged particle. The electron-hole pairs along the track are eventually separated by the electric field established in the sensor layer. The hole will drift to the pixels of negative electrodes and the electron will drift to the positive electrode (Figure 1.16). Holes will experience lateral diffusion on their drift to the negative electrodes. The total magnitude of this diffusion depends on the initial distance from a particular point on the track to the collecting electrodes. The further the holes originate from the collecting electrodes, the more collecting electrodes they will spread over, as shown by (a) as compared to (b) in Figure 1.16.

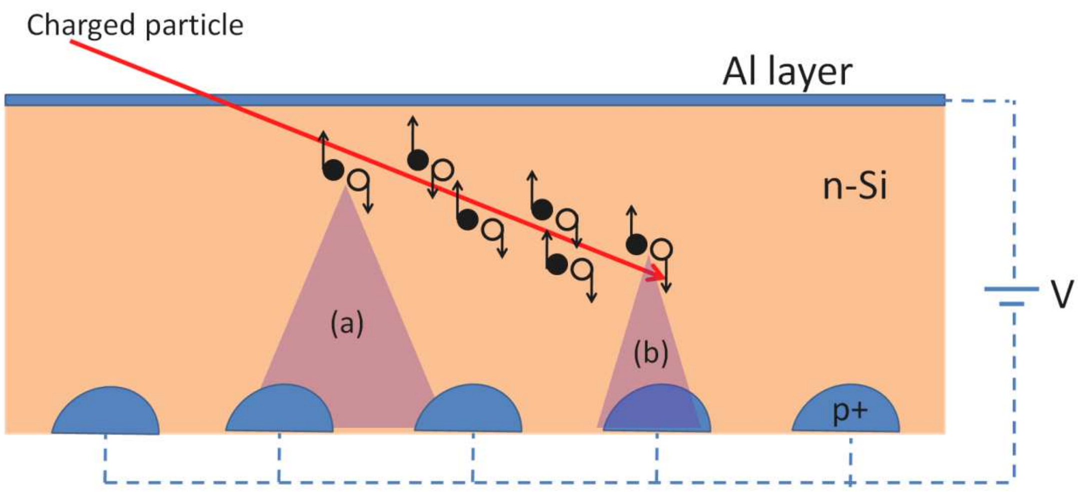

Figure 1.16: A charged particle track creates electron-hole pairs denoted as black filled (electrons) and open (holes) circles.

The Medipix detector was first accessed for its capability as a dosimeter in photon fields as the Medipix1 [104]. The technique of counting photons was used in the study, with 60 and 70 kilovolt peak (kV_p) X-ray sources. The drawback of counting photons is the loss of counts through dead time in the detector. The minimum dead time achievable in Medipix1 was 0.8 ms, which corresponds to a 1.2 kHz counting rate. The uncorrected counts at 200 kHz would give 32% less than actual counts. This can has implications for the limit of the dose rate, specifically for low-energy photons, where the count rate increases due to the domination of the photoelectric effect.

The applicability of the second generation of Medipix detectors, Medipix2, in photon field dosimetry using the photon counting technique was investigated [105]. The study used low-energy X-ray, from 40 to 150 kV_p, where the $H_p(0.07)$ and $H_p(10)$ per-photon fluences are relatively constant on this energy range. The report assumed that the absorbed dose is proportional to the number of counts. Thus, they showed that, using eight defined readout segments on the Medipix2 active area, the personal dose equivalent can be made proportional to the total weighted count of those segments, as shown in Equation (1.14). These eight segments have an equal area and are predefined with eight energy thresholds.

$$H_p^j = \sum_{i=1}^{8} \beta_i \, N_i^j \tag{1.14}$$

where H_p^j is the personnel dose equivalent at mono-energetic photons, E^j, β_i is the calibration factor for i^{th} segment and N_i^j is the accumulated counts from i^{th} segment after irradiation with photon energy, E^j. The eight β_i values were obtained from calibration to five filtered (RQA) and four unfiltered (RQR) X-ray radiation qualities [106]. Hence, the β_i depends on the experiment setup, detector characteristics and calibration energies. In photon-spectrum applications one would regard the spectrum as a superposition of mono-energetic photons; thus:

$$H_p^{spectrum} = \sum_{j=1}^{j_{max}} H_p^j \tag{1.15}$$

$$H_p^{spectrum} = \sum_{j=1}^{j_{max}} \sum_{i=1}^{8} \beta_i \, N_i^j \tag{1.16}$$

where $H_p^{spectrum}$ is the personnel dose equivalent at a spectrum of photons, and $\sum_{j=1}^{j_{max}} E^j$, j_{max} indicates the highest mono-energetic photons in the spectrum.

For dosimetry in neutron fields, the charged-particle-counting technique was used; this is analogous to the photon-counting technique described in Chapter 5. A converter layer on the surface of the Medipix2 was used to convert the incident neutrons to charged particles. This can be a hydrogen-rich converter for fast neutrons, a converter enriched with ^{6}Li and ^{10}B for thermal neutrons or a combination. Selection of the converter depends on neutron-energy spectra and the physics of neutron interaction with matter, as described in Section 1.1.3. The next section will describe in detail the converters used in this study. The 100% efficiency of the Medipix2 sensor in detecting charged particles makes it the best candidate for neutron dosimetry.

1.4.3 *The challenge for neutron dosimetry with a silicon detector*

In a radiation field of mixed gamma-neutron, separation of the components of the field in terms of dose is always challenging. In fast-neutron dosimetry, a silicon detector is used to detect charged particles that are escaping from the layered converter to the depletion layer of the detector at reverse biased p-n junctions. The amounts of energy deposited by the charged particles (protons in the case of a polyethylene converter) depend on the charged-particle energy and thickness of the depleted layer. In most neutron dosimetry applications, the detector is fully depleted.

There are two options for measuring neutron dose purely by counting the recoil protons. In the first option, the incident neutron spectrum can be unfolded by measuring the microdosimetric energy spectrum of the recoil protons measured from ΔE-E stages silicon detector. The accuracy of this technique depends strongly on estimating the average distribution of chord lengths of the charged particles inside the detector [107-109]. This spectrum is then convolved with coefficients that depend on neutron energy to determine a neutron dose for a given neutron fluence.

In the second option, the neutron dose is simply measured by counting the recoil-proton events. However, direct interactions of gammas and neutrons inside silicon also produce background counts. The Compton and photoelectric interaction by gammas produce continuous spectrum at low-energy channels in a multi-channel analyser, which can easily be discriminated from the events of the recoil proton at high-energy channels. This is not the case at increasing rate of gamma dose, because the pile-up effect raises the pulses of the gamma events. The inelastic interaction of fast neutrons in the detector produces different types of charged particles. These background events are mixed with the events from recoil protons in silicon. This implies that separation of gamma and neutron components in a mixed-radiation field is impossible below around the 1 MeV threshold in neutron spectra [110-112].

Figure 1.17 shows the spectrum of deposited energy events in a Medipix detector with 14 × 14 mm^2 area and 300 μm-thick from energy of ^{60}Co radiation simulated in GEANT4. This result is in good agreement with experimental results that show about 800 keV maximum deposited energy [112]; this indicates the significant of background counts from high-energy gamma inside a silicon detector.

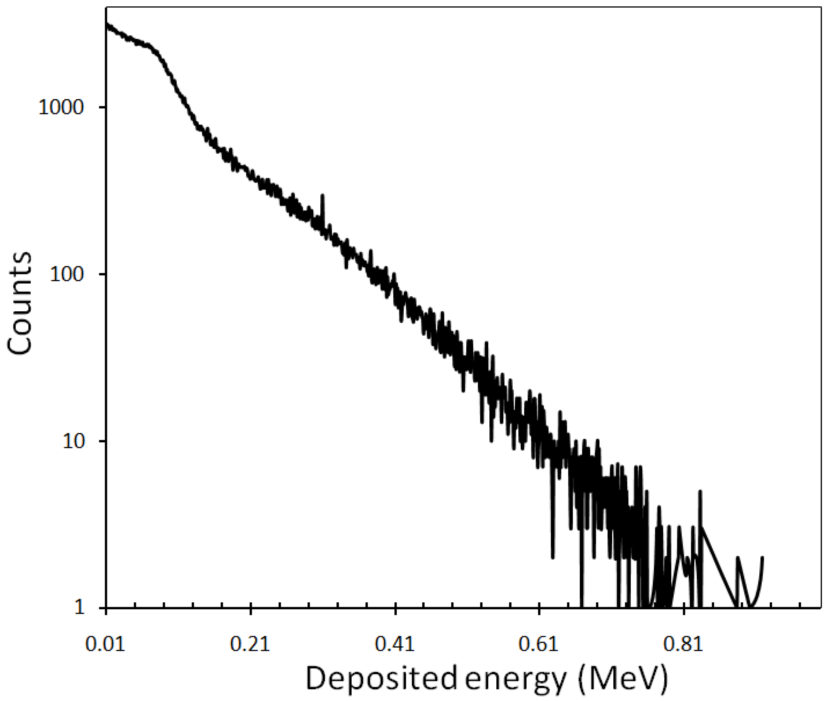

Figure 1.17: A GEANT4 (the Monte Carlo tool is described in Section 1. 5) simulated count of the multi-channel analyser in a silicon detector for ^{60}Co energy gamma-ray. Energy bins 1 keV wide were used.

For the purpose of military emergency-response dosimetry applications, the typical radiation field expected is likely to comprise a mixed field of neutrons, with maximum E_n= 14 MeV and 15 keV to 662 keV energies gamma-ray components, typical of radioisotopic sources. Low-energy (< 100 keV) photons have a higher cross-section ratio of photoelectric to Compton scattering than the ^{60}Co gamma-rays; thus a higher background count is anticipated than the one shown in Figure 1.17. It is again emphasised that dosimetry of fast neutrons by counting recoil protons in a single silicon detector requires a high-energy threshold to avoid pile-up effects.

For isolating the response of neutrons in a mixed gamma-neutron field, Barelaud *et al.* [113] used a subtraction method from two passivated ion implanted silicon (PIPS) detectors, where one of the PIPS detectors was covered with 1 mm-thick polyethylene and the other was left uncovered. The study was performed for *H*(10)*= 1.9 mSv under an Am-Be neutron source. Figure 1.18 shows that the ratio of neutron response to gamma and background response depends on the thickness of the depleted region in the silicon detector. This demonstrates a benefit of having thinner detectors to reduce gamma and background counts. However, in this case the number of events from the recoil protons that deposit full energy (stopper in depleted region) was reduced, which put a limit on unfolding the spectra of high-energy neutrons.

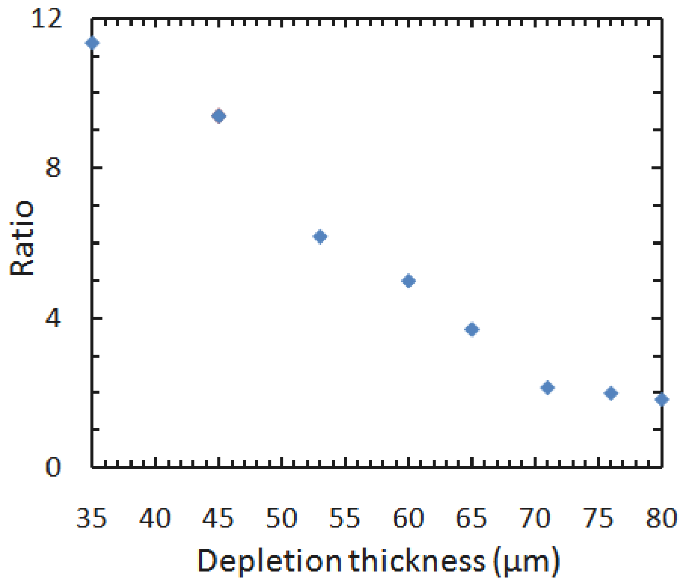

Figure 1.18: The ratio of neutron responses to gammas and background responses inside the depleted region of varying thicknesses [113].

Additionally, an even higher threshold value is required to discriminate charged particles produced by elastic and inelastic neutron interactions directly with the silicon nuclei. Elastically scattered silicon atoms produced continuous spectra with a maximum energy 0.133E_n:

$$E_s = \frac{4mM}{(M+m)^2} E_n cos^2\theta \quad (1.17)$$

where E_n is the incident energy of the neutron, E_s is the kinetic energy of the scattered silicon atom, m is the neutron rest mass, M is the silicon-atom rest mass and θ is the scattered angle of the silicon atom. In the case of the spectra of fission neutrons, most relevant to military and accidental neutron dosimetry, this background demands a threshold energy of about 1.8 MeV, and is mostly independent of the thickness of the detector due to the short range of the recoil silicon atoms. Figure 1.5 shows the elastic and non-nelastic cross-sections of neutron interaction in silicon. The inelastic interaction starts to produce heavy charged particles at around 4 MeV to 20 MeV from ^{28}Si(n,charged particles) interaction, as shown in Figure 1.7. In contrast, the elastic interaction remains significant up to 15 MeV, which is the maximum neutron energy considered in this study. Thus, a very high-energy threshold is further required for incident neutrons above 4 MeV, as both neutron interactions produce high-energy charged particles.

Figure 1.19 and Figure 1.20 show a GEANT4 Monte Carlo simulated spectrum of elastic and non-nelastic events from 14.5 MeV parallel neutron beam incident normal to a silicon slab with thicknesses of 10 µm (Figure 1.19) and 100 µm (Figure 1.20). The maximum energy gained by secondary particles depends on neutron energy, regardless of the thickness of the silicon slab. Contribution from the elastically recoiled silicon atoms is most essential, followed by contribution from inelastic reactions, which produce atom isotopes, alpha particles and protons. Contribution of alpha particles is less pronounced for the 10 µm slab, but increase for the 100 µm slab for deposited energies above 5 MeV. The important conclusion from these simulations is that the parasitic events from both gamma and neutron direct interactions with silicon can be achieved by reducing the thickness of the depletion layer of the silicon detector. Furthermore, the threshold energy must be equal to the maximum energy deposited by the charged particles, which for 10 and 100 µm-thick silicon are about 10 MeV and 20 MeV, respectively; a similar analysis using 10 µm-thick silicon was presented in [114].

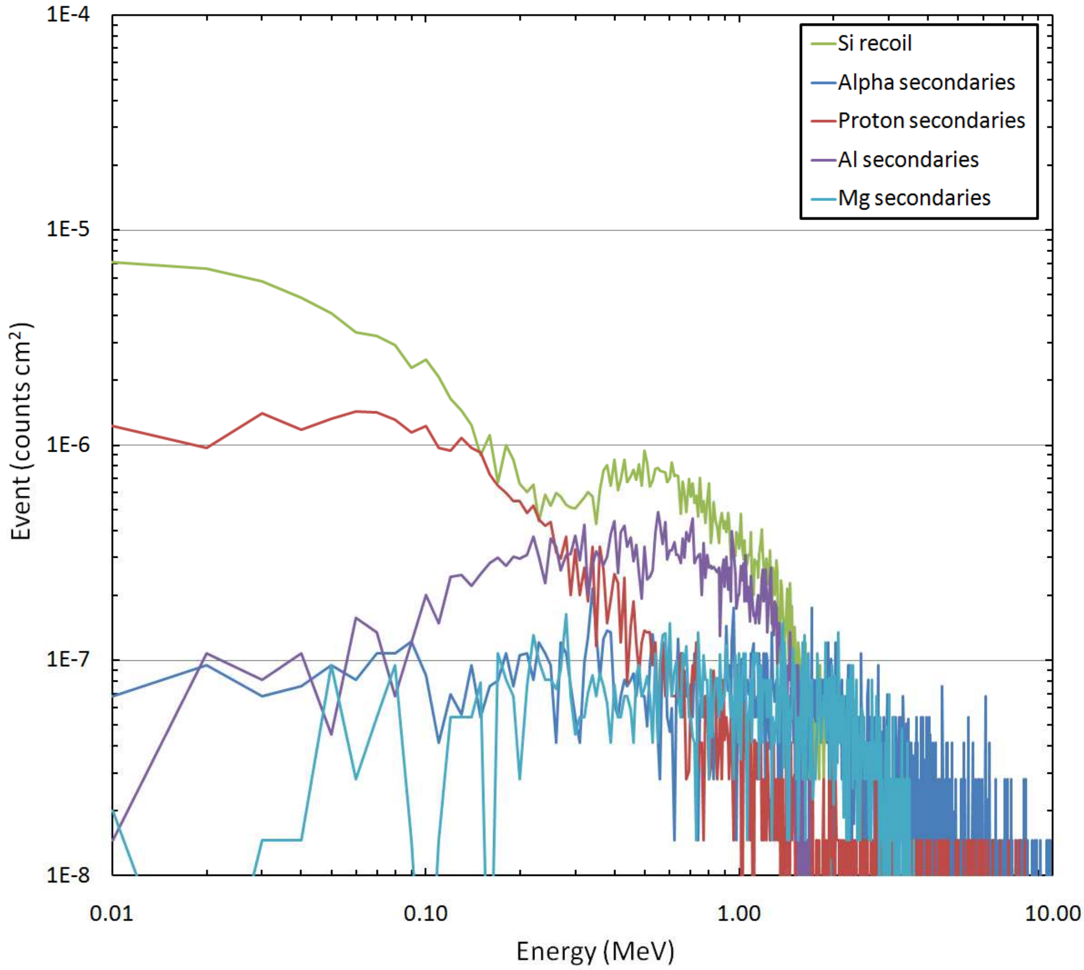

Figure 1.19: The recoil silicon and selected secondary particle counts inside 10 µm-thick silicon irradiated by 14.5 MeV neutrons.

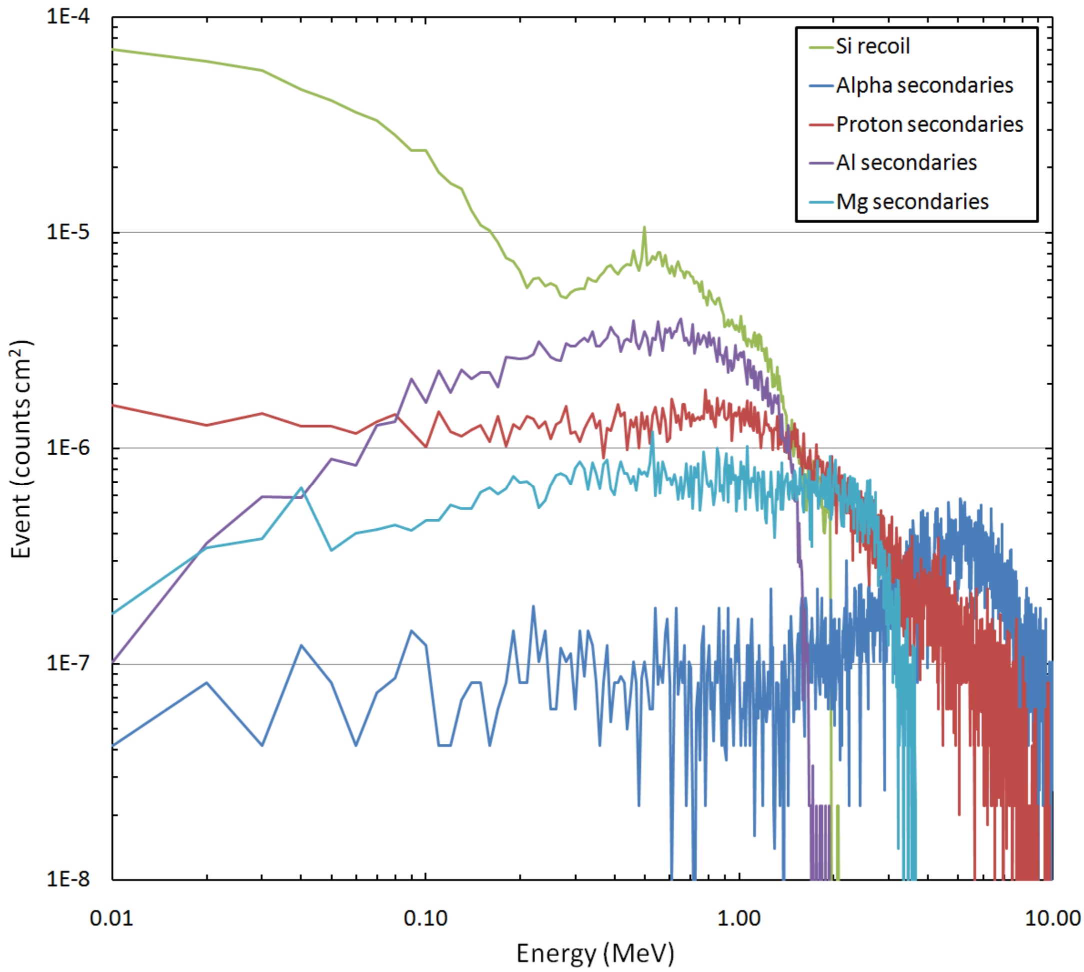

Figure 1.20: The recoil silicon and selected secondary particle counts inside 100 μm-thick silicon irradiated by 14.5 MeV neutrons.

Apart from the problems mentioned above, the response of a silicon detector with a polyethylene converter in count mode should be independent of neutron energy in terms of an ambient dose equivalent. It demands that a detector response (counts/fluence) should be proportional to the fluence-to-dose conversion coefficient suggested by ICRP, as shown in Figure 1.21 [115]. The recommended precision for an active neutron detector is 20% at dose detection increment steps of 10 μSv [116].

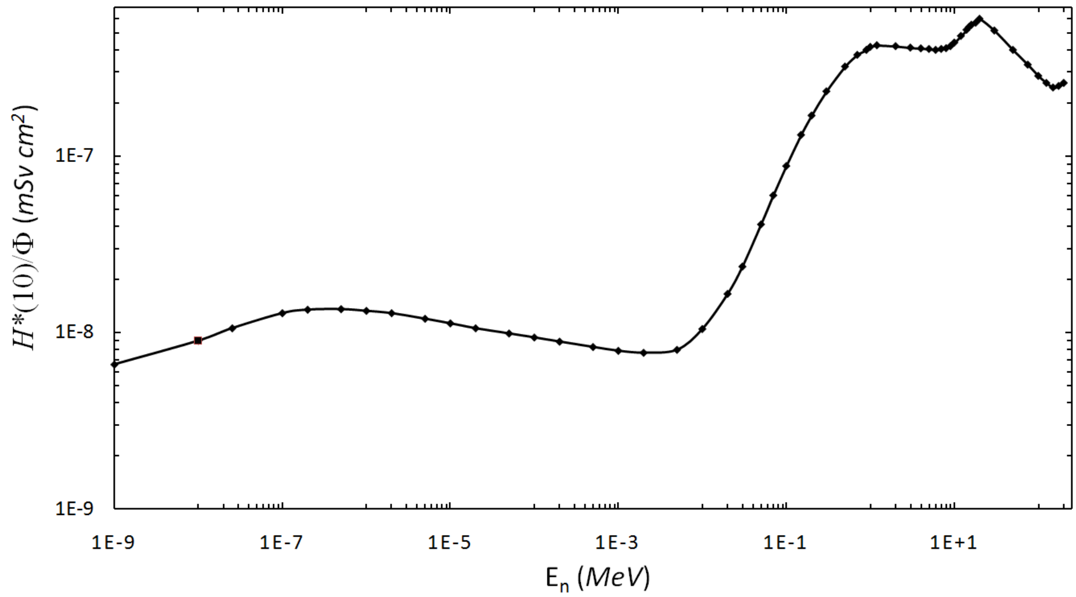

Figure 1.21: The equivalent ambient dose conversion coefficient reproduced from the Table A.42 ICRP Report 74 for mono-energetic neutrons.

1.4.4 *Proposed approach to neutron dosimetry with a pixelated silicon detector*

Previously, Eisen *et al.* [117] analytically analysed a single silicon detector with a uniform polyethylene converter in a count mode for measuring neutron-dose equivalent. Their results showed that a uniform thickness of polyethylene converter is unable to produce an energy-independent response for a neutron dosimeter, as shown in Figure 1.22a, c, and e. Improvement of the response variation by a factor of two over an energy range of 1 to 15 MeV was achieved by placing dual-thickness layers of polyethylene converter onto a silicon detector as shown in Figure 1.22d. The contribution of counts associated with direct interaction of neutrons with energy below 0.7 MeV in silicon was not considered. Although the energy response improved, the single silicon detector could neither further reduce the variation in the energy response nor lower the threshold energy. This is due to the unsolved problem of the direct interaction of gamma and neutron silicon.

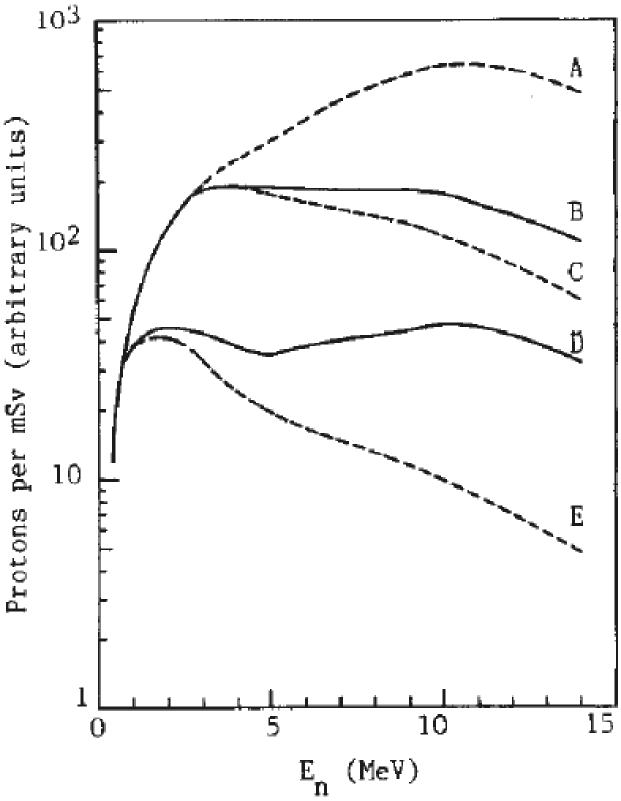

Figure 1.22: The calculations from Eisen *et al.* [117] show the response of the detectors under a combination of PE thicknesses: (a) 1 mm, (b) 0.1 mm (89%) + 1mm (11%), (c) 0.1 mm, (d) 0.01 mm (94%) + 1 mm (6%) and (e) 0.01 mm.

To address the limitation of the single-readout detector, we proposed using a pixelated silicon detector coupled with multi-thicknesses of structured polyethylene converter on top of the detector. This approach is equivalent to multiple single silicon detectors with different thicknesses of uniform polyethylene converters, which leads to flexibility in refining the energy response of the dosimeter and in subtracting parasitic background counts. Further chapters will describe the design and optimisation of a fast-neutron pixelated detector based on the Medipix2 with an active area of 14 x 14 mm^2, which allows a high detection efficiency, as required for radiation protection related to neutron dosimetry applications.

1. 5 The GEANT4 Monte Carlo simulation

GEANT4 is a free software package composed of tools that can be used to accurately simulate the passage of particles through matter [118]. The two major publications that summarise its development are published by Agostinelli *et al.*[119] and Allison *et al.*[120]. GEANT4, developed by the European Organization for Nuclear Research (CERN), was initially intended for use in high-energy (~ GeV) physics experiments such as the CERN Large Hadron Collider (LHC), the Main Injector Neutrino Oscillation Search (MINOS) at Fermilab and the BaBar experiment at SLAC. The first version of GEANT was written in the FORTRAN programming language. Current GEANT4 development is through international collaboration [121]. GEANT4 has become established as a reliable simulation tool in space-radiation physics, medical -radiation physics and examinations of nuclear and accelerator radiation sources [122].

There are other Monte Carlo simulations for charged-particle tracking, such as PENetration and Energy LOss of Positron and Electron (Penelope), Electron Gamma Shower (EGSnrc) and Monte Carlo N-Particle (MCNP), which are all written in FORTRAN. In contrast, the open-source GEANT4 is written in C++, which has an object-oriented design structure. GEANT4 uses the Class Library for High Energy Physics (CLHEP) for its C++ utility libraries, which control the random-number generators, physics vectors, geometry, and linear algebra [123].

Because a large number of events ($>10^8$) must be simulated to get good statistical results, these GEANT4 simulations were executed on a multi-core of 2.4 GHz Intel Core 2 Quad PCs from hours to weeks. This means the workloads were distributed in a cluster of OpenSuse 10.3 Linux computers. The workloads distributed from the same simulation required the use of a random-number generator to initiate the run , which in this study was CLHEP *RanecuEngine*. This random-number generator has been reviewed in reference [124]. On each iteration of the same simulation, the random-number generator was seeded with a different number. A seeded random number was used for two reasons: first, an intense computational simulation can be run with smaller events in multiple computer cores, which reduces the simulation time; second, GEANT4 can only support up to 2^{31} events, or about 2.15×10^9. Thus, a simulation that needs events $> 2.15 \times 10^9$ to achieve better statistics can run while multiplying with different random-number seeds. GEANT4 versions 9.1 and 9.2 were used in this study.

GEANT4 defines the secondary particle production energy threshold as a range cut for high-precision spatial energy deposition. This range cut is valid for secondary electron, positron and gamma production. As for photons, an approximate *absorption cross-section* of photons in a material is defined as, σ_{abs}. This σ_{abs} is the sum of the cross-section from pair-production, Compton scattering and the photoelectric effect, as these interactions change the photon energy. Then, an *absorption length* is defined as $L_{abs} = 5/\sigma_{abs}$. This L_{abs} is used as an approximation when converting the range cut into energy for dose deposition of photons in a material.

The GEANT4 charged-particle physics processes are defined under the physics list. The two main physics processes are electromagnetic and hadronic. The physics list for the electromagnetic process has two specialised models: the standard electromagnetic and low-energy electromagnetic processes. The hadronic process has two major physics process models: the parameterised and string models. In this study, GEANT4 low-energy electromagnetic process was used for the work in Chapter 2, Chapter 3, and Chapter 4, and hadronic string modelling was used for the work in Chapter 5, and Chapter 6.

1.5.1 *Low-energy electromagnetic processes*

The low-energy electromagnetic process considered the importance of the atomic shell structure at low energy by applying shell cross-section data. These data sets were obtained from the Evaluated Photon Data Library (EPDL97) [125], the Evaluated Electron Data Library (EEDL) [126] and the Evaluated Atomic Data Library (EADL) [127], while the stopping-power data sets were from reference [128-131] and Scofield binding energy data [132]. The data sets were used to calculate the total cross-section and to generate the final state for particles with energy from 250 eV to 100 GeV (covering elements with atomic numbers from 1 to 99).

Table 1-1 gives the list of physics processes included in the low-energy electromagnetic process.

Table 1-1: Physics processes under the low-energy electromagnetic physics list

Photons	Electrons	Hadrons and ions
Compton scattering *G4LowEnergyCompton*	Bremsstrahlung *G4LowEnergyBremsstrahlung*	Ionisation and delta-ray production *G4hLowEnergyIonisation*
Polarized Compton scattering *G4LowEnergyPolarizedCompton*	Ionisation and delta-ray production *G4LowEnergyIonisation*	
Rayleigh scattering *G4LowEnergyRayleigh*		
Pair-production *G4LowEnergyGammaConversion*		
Photoelectric effect *G4LowEnergyPhotoElectric*		

1.5.2 *String-model processes*

The string model used in this study was *G4QGSP_BIC_HP*, which stands for Quark-Gluon String Physics, Binary Cascade and High Precision Neutron model. This model used the string model for hadrons with energy 5 to 25 GeV, and the binary cascade model for primary protons and neutrons with energy < 10 GeV.

The *G4QGSP_BIC_HP* cross-section for neutrons with energy <20 MeV is based on high-precision experimental data from the *G4NDL3.13* data package that comes with the GEANT4 installation packages. The low-energy neutron interactions (< 20 MeV) considered in the GEANT4 were elastic scattering, non-elastic scattering, inelastic scattering, radiative capture and fission. These interactions were treated as independent models. The evaluated neutron data libraries that come with the GEANT4 installation packages are shown in Table 1-2.

Table 1-2: The evaluated neutron data libraries

Evaluated library	Description	Reference
Fusion Evaluated Nuclear Data Library, FENDL/E2.0	This library is maintained by IAEA.	[133]
Evaluated Nuclear Data File, ENDF/B-VI	This library is maintained by the National Nuclear Data Center, Brookhaven National Laboratory, USA.	[134]
Japanese Evaluated Nuclear Data Library, JENDL – 3.2	This library is maintained by the Nuclear Data Center, Japan Atomic Energy Agency (JAEA).	[135]
Russian Evaluated Neutron Data Library, BROND – 2.1	This library is maintained by the Russian Nuclear Data Centre (CJD) of the A.I. Leipunski Institute of Physics and Power Engineering (IPPE).	[136]
Joint Evaluated Fission and Fusion, JEF – 2.2 and EFF – 3	This library is maintained by the OECD Nuclear Energy Agency (NEA).	[137]
Chinese Evaluated Neutron Data Library, CENDL – 2.2	This library is maintained by the Chinese Nuclear Data Center, Institute of Atomic Energy	[138]
Medium Energy Nuclear Data Library, MENDL – 2	This is the report produced by the Nuclear Data Services, IAEA.	[139]

The photon and electron physics processes in the *G4QGSP_BIC_HP* used the standard electromagnetic process physics list. The major sources for the physics process and the structure of GEANT4 package tools can be found in references [122], [140] and [141] and the documentation provided with the GEANT4 extended C++ libraries package.

1.6 GEANT4 Monte Carlo simulation for design and optimisation of semiconductor gamma and neutron personnel dosimeters: Outline

Until now this study has discussed an approach to designing a gamma-neutron personal dosimeter with a MOSFET detector for gamma dosimetry and a silicon detector with polyethylene converter for neuron dosimetry. An approach to the problems related to MOSFET dosimeter and silicon detectors coupled with polyethylene converters with technical specifications suitable for personal ambient dosimetry were proposed in Sections 1.3.4 and 1.3.5 for a gamma detector and Sections 1.4.3 and 1.4.4 for a neutron detector.

The following chapters relate to the extensive GEANT4 Monte Carlo modelling of gamma and neutron detectors based on the solutions proposed. Chapter 2 discusses GEANT4 modelling of the energy response of the conventional MOSFET for mono-energetic gamma fields in a free-air geometry. This chapter introduces possible optimisations to improve the MOSFET energy response with filters on top of the aluminium gate of the MOSFET. Chapter 3 describes further optimisation of the conventional MOSFET packaging to obtain an energy response in free air that matches the MOSFET response on a water phantom surface. The multi-layer filter concept gained from the simulations described in Chapter 2 is used to improve the MOSFET response to mono-energetic gamma for energy < 100 keV. Chapter 4 further extends the simulation for optimising MOSFET packaging in Chapter 3, in the case of a dual-MOSFET chip. This new approach improves the energy response of the MOSFET-based personnel dosimeter by using a combination of responses of filtered and unfiltered MOSFETs.

Chapter 5 discusses a new approach to fast-neutron personnel dosimetry using a pixelated silicon detector with a structured polyethylene converter solution. The neutron-detector design is optimised to replicate response correspondence with the neutron fluence-to-dose equivalent conversion factor. Optimising the structured converter to produce such an energy response was achieved using GEANT4 simulations. The chapter also describes the algorithm proposed to lead to independence of energy response of the neutron-dose equivalent in a broad range of fast-neutron energy.

Chapter 6 deals with the experimental validation of the optimised neutron dosimeter reported in Chapter 5.

The studies on development of gamma-neutron personnel dosimeter are concluded in Chapter 7, including remarks on future work with the MOSFET and Medipix2 detectors.

CHAPTER 2

CONVENTIONAL MOSFET ENERGY-RESPONSE SIMULATIONS

2. 1 Introduction

The conventional MOSFET dosimeter is usually covered by about a 1 mm-thick epoxy bubble. This chapter examines the energy response of a conventional MOSFET detector to photons in free-air geometry. A MOSFET with a layer of silicon oxide (sensitive volume) of 180 x 270 x 1 μm^3 on top of a 1000 x 1000 x 500 μm^3 layer of silicon substrate was modelled. The energy response of the MOSFET with a combination of different packaging setups was studied. In every case the energy response of the MOSFET with filter was studied in free-air geometry, with the aim of developing a personnel accidental dosimeter with a dose response in free-air geometry matching the absorbed dose in a standard phantom for *operational quantities* (described in Section 1. 2).

2. 2 Simulation methods

Conventional MOSFET packaging was first modelled with a simple geometry as described in Section 2. 1, with an additional 180 x 270 x 1 μm^3 aluminium gate contact layer above the silicon oxide, a semi-spherical 1 mm-radius epoxy bubble covering the entire substrate, and Kapton carrier, 228 μm-thick by 2.5 x 2.5 mm^2 cross-sectional area (Figure 2.1). This was a symmetrical geometry. The compositions of all the materials were taken from reference [142], while the definitions of their elements were taken from reference [143]. The material composition for the epoxy bubble was taken from reference [144].

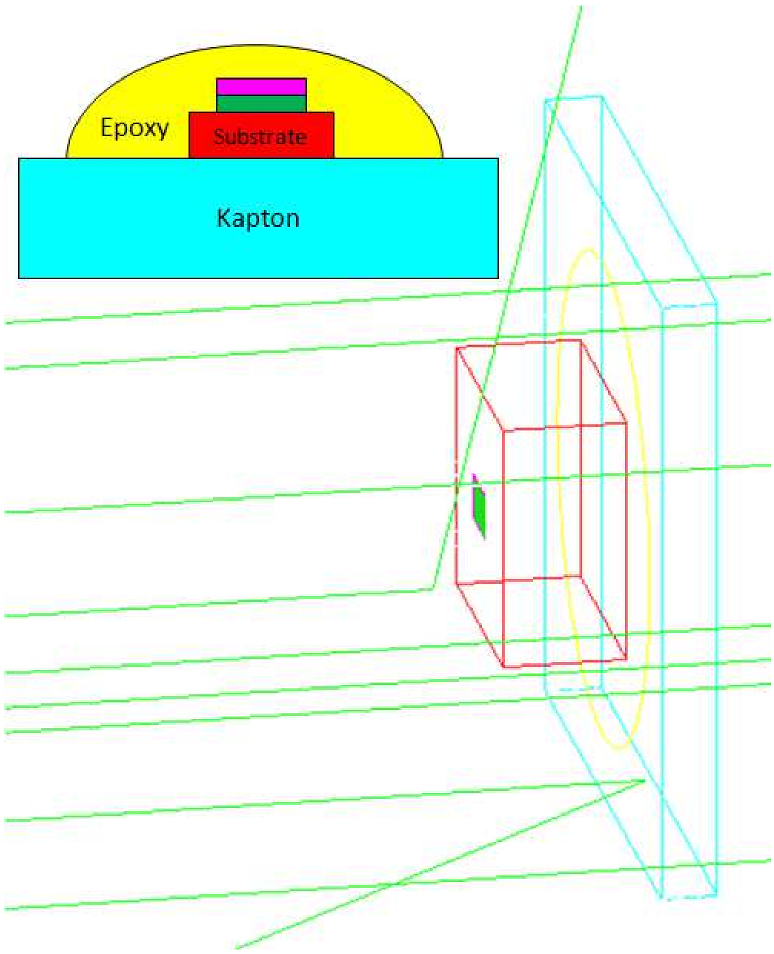

Figure 2.1: The conventional MOSFET geometry under GEANT4 simulation. The red and light-blue boxes are the silicon substrate and Kapton carrier, respectively. On top of the silicon substrate are layers of SiO_2 sensitive volume and aluminium gate, denoted by green and magenta boxes, respectively. An epoxy bubble (yellow semi-spherical) covers the entire silicon substrate. Shown above are nine events of photon incident perpendicular to the Kapton plane, coming from the left.

In the GEANT4 simulations, the electron-range cut-off was different for the different regions of the MOSFET detector. The smallest 0.1 μm electron range cut-off was defined inside the sensitive volume and increased outside the sensitive volume proportionally to the distance from it. These techniques help reduce computational time. GEANT4 version 9.1 was used for this simulation.

The numbers of simulated events were from 1 x 10^8 to 6 x 10^9 to get > 95% statistical confidence level of two standard deviations (2σ). The simulations were done in free air approximated by a vacuum. Primary mono-energetic photon energies from 10 keV to 2 MeV were considered. The physics list used, low-energy electromagnetic interactions, included the Bremsstrahlung effect, Rayleigh scattering, Compton scattering, photoelectric absorption, pair-production and positron annihilation.

2.2.1 *Energy response of the MOSFET with and without an epoxy bubble*

In this model, the epoxy-bubble material was first defined as air. The parallel beam of photons was incident on the MOSFET, as shown in Figure 2.1. The deposited dose was scored in the sensitive volume, the aluminium gate and 1 µm-thick layer of silicon substrate immediately below the sensitive volume. This silicon substrate scoring volume has the same cross-section as the sensitive volume.

Second, the MOSFET energy responses with different materials of semi-spherical bubble were studied. The materials used were epoxy, water and Kapton. The chosen materials used the same 1 mm-radius of the bubble on top of the MOSFET, while an additional 0.9 mm-radius of the bubble was used for the epoxy bubble. Absorbed doses were scored in the sensitive volume of the MOSFET on all the packages for mono-energetic photons from 10 keV to 2 MeV.

2.2.2 *Effects of the photon angle of incidence*

The MOSFET with a 1 mm epoxy bubble, as above, was used for the simulation. The energy responses of the MOSFET at photon incident angles θ of 45^o, 90^o, 135^o and 180^o (photon incidence from the Kapton plane) were simulated using the GEANT4 code (Figure 2.2). All the doses were scored in the sensitive volume of the MOSFET for mono-energetic photons from 10 keV to 2 MeV. The angular responses of the MOSFET from 0^o to 180^o in steps of 15^o were simulated for mono-energetic photons with 70 keV, 200 keV and 1.25 MeV energy.

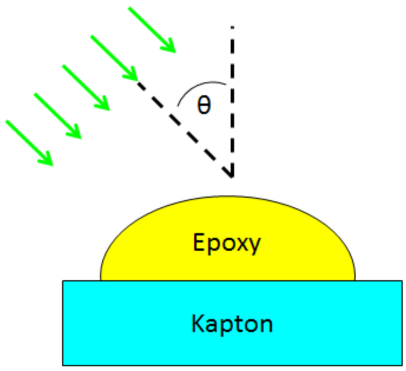

Figure 2.2: The incidence angle of the photon θ, on the MOSFET.

2.2.3 *The particle and dose origin regions*

To understand the nature of electron scattering within MOSFET packaging, additional simulations were performed to track the origin of the electrons that deposit a dose in the sensitive volume. GEANT4 provided tools such as the *G4Step* class to track the electron, and provide the user with all information to track down event-by-event energy deposition by each electron.

The total dose deposited by secondary electrons for 2 x 10^9 photon events was also scored according to their region of origin. Information about the secondary particle physics processes through each step of the *G4UserSteppingAction* class was extracted for their parent ID, dose deposition and current region. Then the *G4UserEventAction* class recorded the sequence of each event, such as the level of secondary particles (e.g, 0, 1 and 2 were assigned to primary photon, secondary electron/positron and delta ray respectively), and the region of origin for secondary particles that deposit their dose in a sensitive volume. The *G4UserRunAction* class tallied the number of electrons for each region and recorded the contribution of each secondary electron to the dose of the sensitive volume.

2.2.4 *The MOSFET response covered by filters*

The filtrations applied on the gate of the MOSFET are shown in Figure 2.3. The three combinations of filters consist of (1) a single layer of copper, (2) a combination of copper, aluminium and graphite, and (3) a combination of lead, aluminium and graphite. The simulations were done with mono-energetic photons from 15 keV to 2 MeV. The absorbed dose was scored in the sensitive volume of the MOSFET.

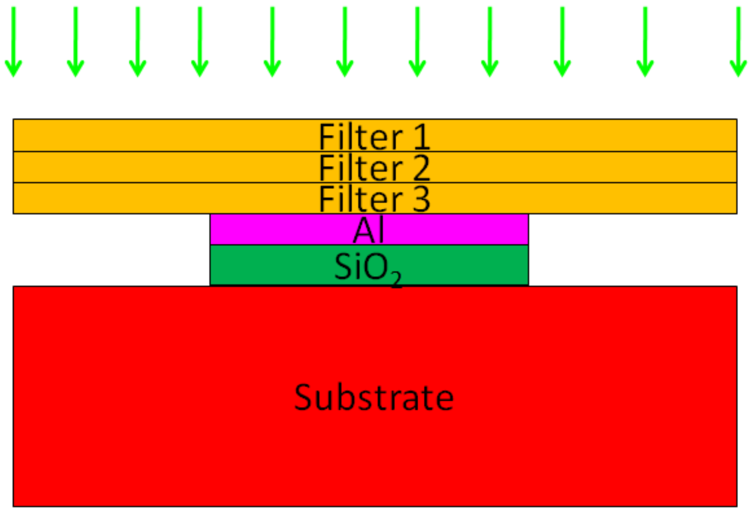

Figure 2.3: Three filters placed on the gate of the MOSFET. The incident of the irradiation beam is perpendicular to the filters.

2. 3 Results and discussion

2.3.1 *Energy response of the MOSFET with and without an epoxy bubble*

Figure 2.4 shows the absorbed doses deposited inside the sensitive volume in an aluminium gate of the MOSFET and in the 1 µm-thick layer of substrate immediately below the sensitive volume. The results clearly demonstrate the build-up effects of the dose, while the difference in the doses deposited in different layers is small. The dose deposited in the aluminium gate was always the lowest, whereas the dose deposited in the layer of silicon substrate was always the highest.

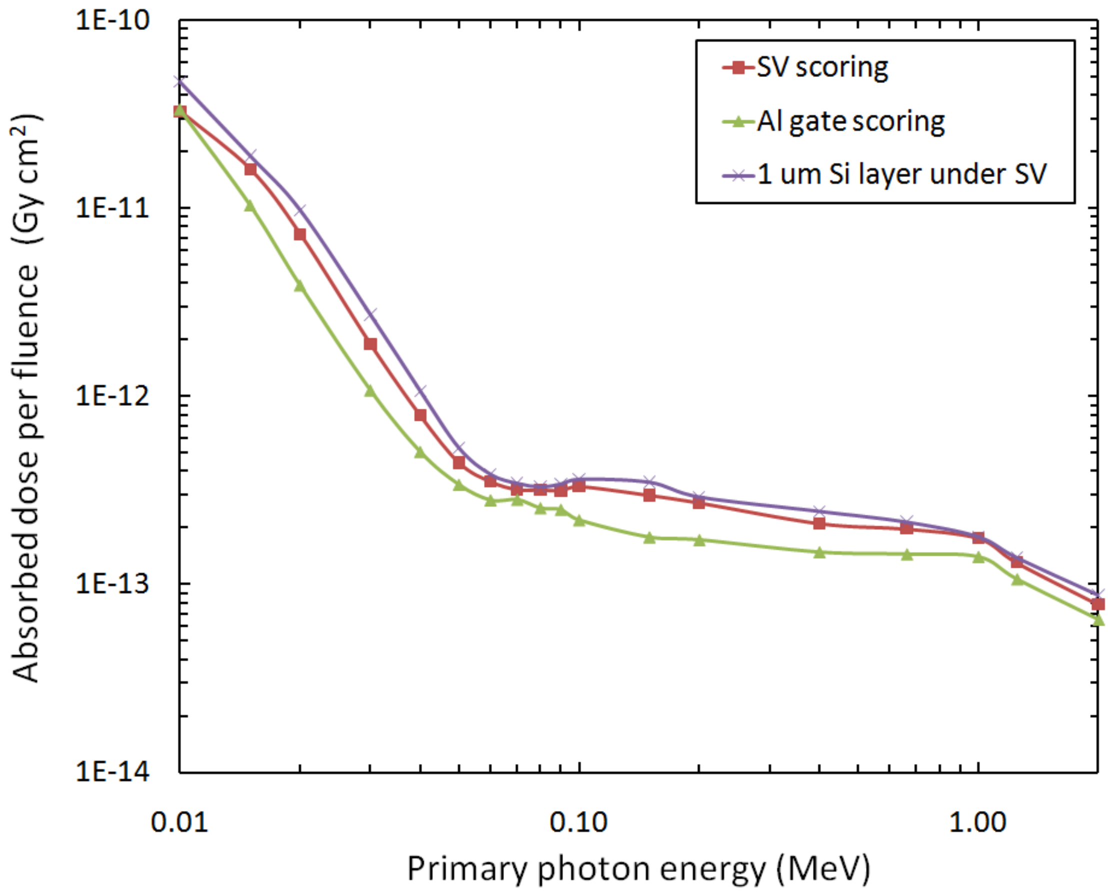

Figure 2.4: The MOSFET energy response without an epoxy bubble. The doses were measured in the sensitive volume (SV), the aluminium gate and the 1 µm-thick layer of substrate.

The epoxy, water and Kapton materials of the semi-spherical bubble have an equivalent effect under photon irradiation (Figure 2.5). The energy response of the epoxy bubble was closer to water at energy > 400 keV than to Kapton. With all the energy responses, the epoxy bubble and Kapton bubble showed the highest discrepancies with the response of the water bubble, at 60 keV (17.5%) and 1.25 MeV (24.6%), respectively. The response of the water bubble was higher than the other materials for energies from 20 keV to 90 keV. Without the semi-spherical bubble, the response of the MOSFET at energy > 100 keV would show a decreasing trend, because there was not enough material for dose build-up (Figure 2.4). The use of a semi-spherical bubble with 1 mm radius provided a sufficient build-up for photons with energy up to 400 keV, and drove a greater energy response than did to the bare

MOSFET. An additional simulation with a 0.9 mm-radius epoxy bubble showed the same energy response as a 1 mm-radius, except where the photons energies were > 400 keV, when it exhibited a lower response.

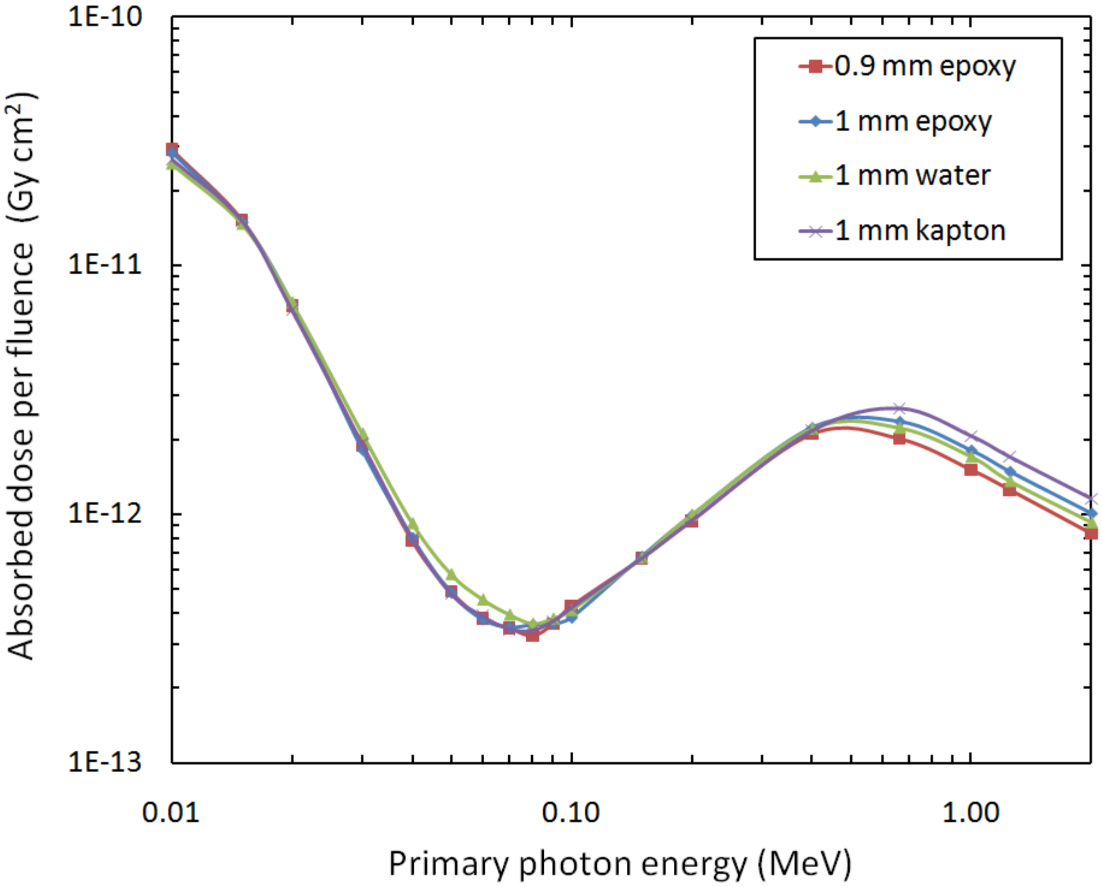

Figure 2.5: The MOSFET energy responses covered with a semi-spherical bubble made of epoxy, water and Kapton. The result with a 0.9 mm-radius epoxy bubble is also shown.

2.3.2 *Effects of photon angle of incidence*

MOSFET energy responses are influenced by the packaging under irradiation in free-air geometry. Figure 2.6 shows that the MOSFET response changed as the photon angles of incidence went from 0^o to 45^o, 90^o, 135^o and 180^o. The MOSFET semi-spherical epoxy bubble can provide an identical energy response to normally incident photons with less than 30% discrepancy (occurring at 40 keV) for the whole energy range of photon incidence angles under 45°. Photon-beam incidents at angles larger than 45° on the MOSFET cause an over- or under-response, depending on the energy of the photons, with a discrepancy of more than 30%.

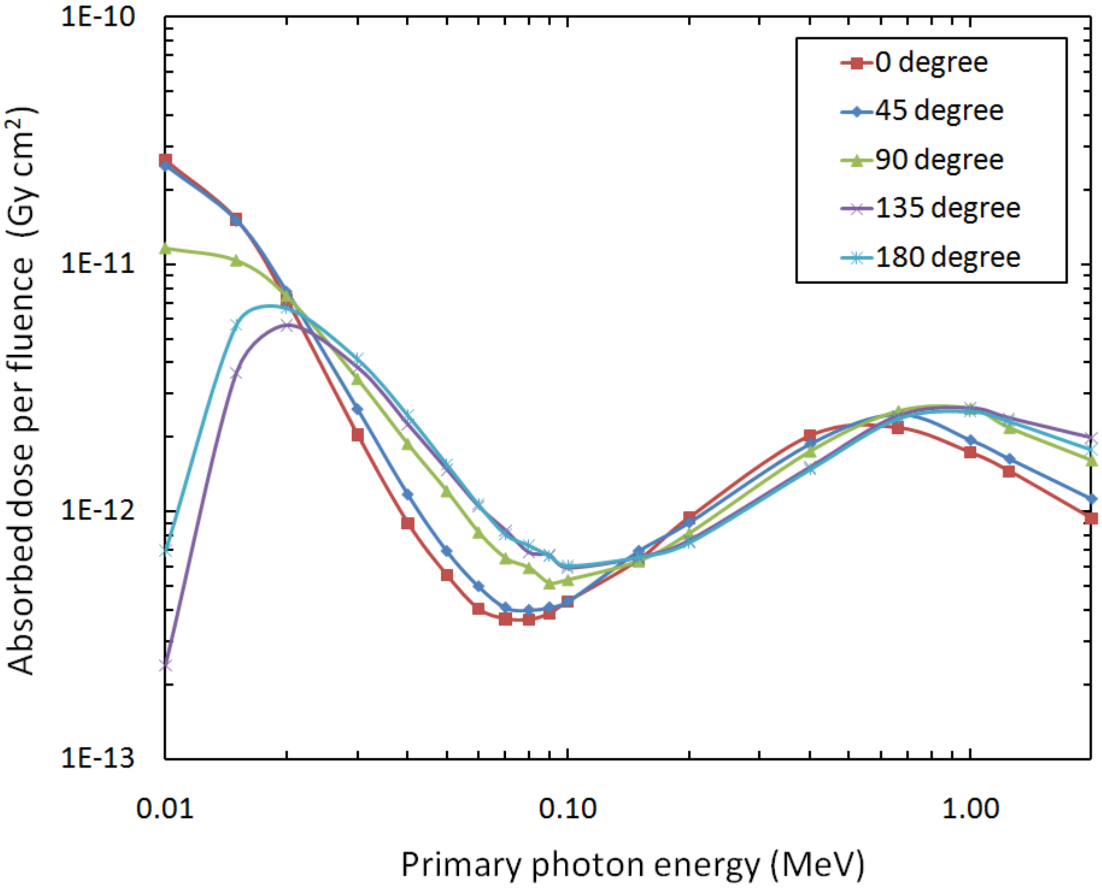

Figure 2.6: The MOSFET energy responses under angled-incident photon beams.

At photon energies < 25 keV, the angular response was determined by a strong photoelectric absorption in the packaging layers of the MOSFET. For an angle of 135°, the length of the attenuation path was maximal, and mostly driven by the silicon substrate, which explained the reduced response of the MOSFET at angles of 135° and 180°. The energy deposited into the sensitive volume of the MOSFET by scattered electrons due to the Compton-effect was minimal for this range of photon energy, while their range was short enough. The continuous slowing down approximation (CSDA) ranges of secondary electrons with energy < 20 keV in an epoxy bubble and silicon substrate were less than 8 µm and 5 µm, respectively, which are notably short. At a higher energy range of photons – from 25 to 100 keV – the response of angled incidents was generally higher than at 0^o. This can be explained by the increase of the Compton-effect contribution and the CSDA range of secondary electrons, which resulted in a larger deposited energy in the sensitive volume at bigger incidence angles.

With an energy range of 150 to 500 keV, the response from the angled incidences decreased compared to normal photon incidence. This behaviour can be explained by the role of backscattered electrons in increasing energy from the photons. Backscattered electrons from the silicon substrate (at 0^o incidence) clearly contributed more than those from the epoxy bubble (at 135^o and 180^o incidence) due to a silicon's higher atomic number.

A further increase in the energy of photons above 662 keV leads to the inverse effect. The increase in the response for larger angles of incidence is similar to the region 25 to 100 keV. This is related to dose enhancement due to scattered secondary electrons, which is stronger for these energies than the electron backscattering effect that leads to the energy responses in Figure 2.6.

These results agree with the findings of Wang *et al.* [60], who modelled the response of the commercial MOSFET with an epoxy bubble used for radiotherapy dosimetry. Even though their simulations were under CPE conditions, they did not use any build-up material in their simulation of MOSFET response for energies below 200 keV. Their results for photon incident normally on the epoxy side (0^o) and the Kapton side (180^o) showed the same energy response for energy up to 200 keV (Figure 2.6).

Figure 2.7 shows the angular responses of the MOSFET at three mono-energetic photons of 70 keV, 200 keV, and 1.25 MeV. All the responses were normalised to a 0^o incident angle. The responses for 70 keV and 1.25 MeV increased with an increase in the incident angle of the beam, whereas at 200 keV the response decreased at incident angles > 45^o. The results in Figure 2.7 concur with the results in Figure 2.6. Additionally, at incident angles below 45^o the discrepancies are < 30%, as mentioned above. The results also agree with Wang *et al.* [60], except for 1.25 MeV (Wang's result was plotted inversely) as they used build-up material for their simulations.

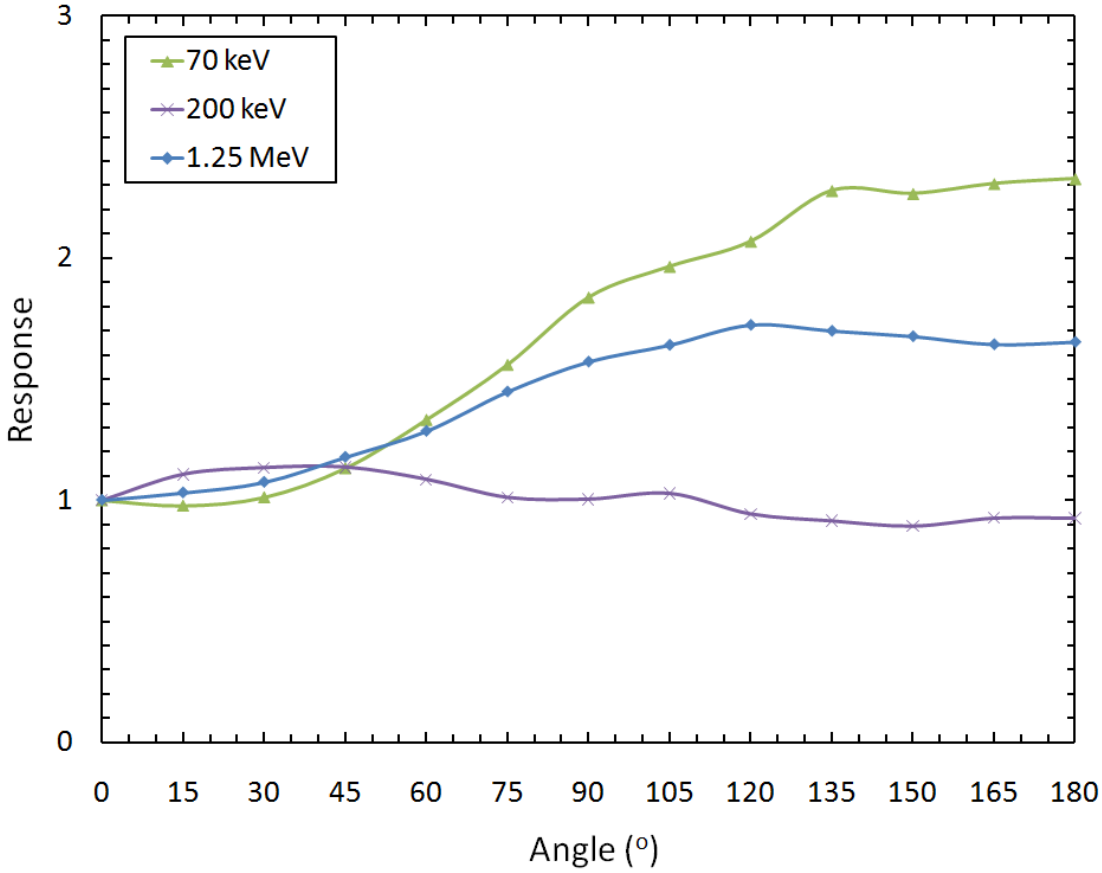

Figure 2.7: Angular responses of MOSFET for three photon energies normalised to 0^{o} incidence.

2.3.3 *The particle and dose origin regions*

The origin of particles that deposit their energy in the MOSFET sensitive volume depends on two of the most important interactions of photons: photoelectric absorption and Compton scattering. Hence the discussion in this section will be around those interactions considering the normal incidence (at 0^{o} incidence angle) of photons to the MOSFET with an epoxy bubble.

As shown in Figure 2.8, where the photoelectric absorption is a dominant interaction and the secondary Compton electrons are short-range (about 3 µm in silicon at 15 keV), the most significant quantity of secondary electrons originates from the sensitive volume for energies of photon from 15 to 50 keV. Likewise, more than 50% of the secondary electrons originates in the SiO_2 layer for low-energy photons up to 30 keV.

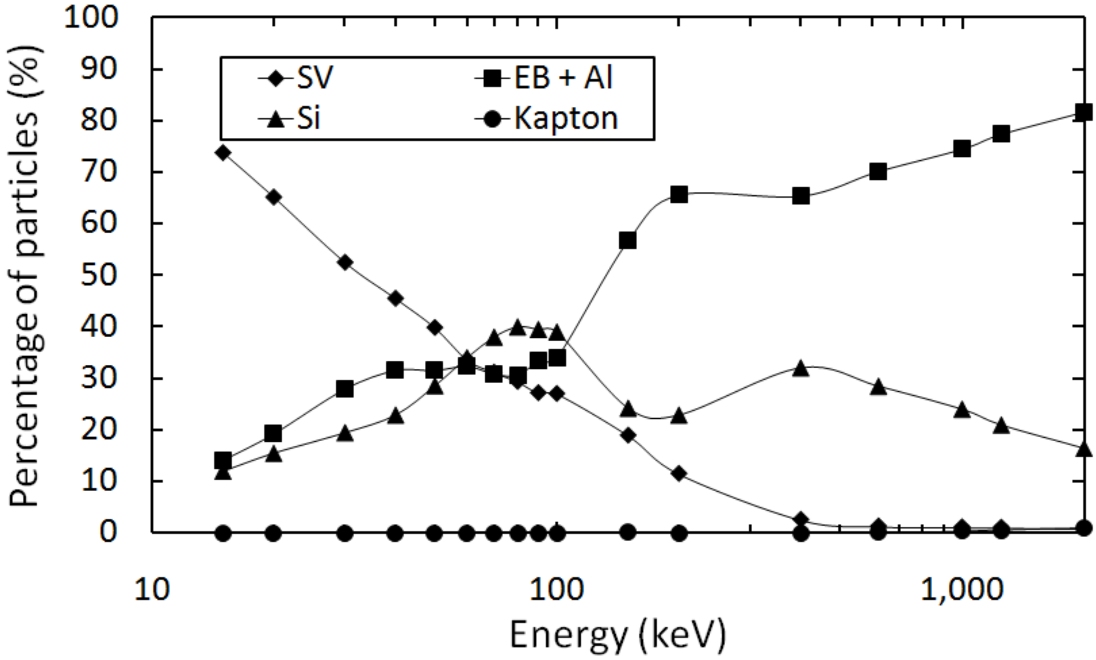

Figure 2.8: The partial contributions to a total number of secondary electrons depositing doses in the sensitive volume that originated from the sensitive volume (SV), silicon substrate, Kapton carrier and epoxy bubble plus the aluminium gate.

When the energy of the photons increases, more secondary electrons arrive at the MOSFET sensitive volume and deposit their energy. For the whole energy range considered in this study, the contribution of backscatter electrons from the silicon substrate and Kapton layers is < 50% of the total number of secondary electrons. The number of secondary electrons originating from the epoxy bubble and aluminium gate increases with photon energy. As the photon energy increases, the SiO_2 layer becomes more transparent because it is very thin, and eventually, as the photon energy reaches 2 MeV, the number of secondary electrons originating from the SiO_2 layer decreases to close to 0%. This finding is supported by the Bragg-Gray cavity theory, which confirms that the response of the MOSFET is driven by surrounding materials.

The partial contributions of different origins of secondary electrons to the dose deposited in the sensitive volume are presented in Figure 2.9; they match the result in the Figure 2.8 except for the silicon substrate. For incident photon energies > 400 keV, most of the secondary electrons originating from the epoxy bubble (Figure 2.8) have high energy, while their LET is decreasing as the energy is increasing. This is reflecting that their partial contribution to the dose in the sensitive volume is decreasing for photon energies > 400 keV, even though their number is increasing.

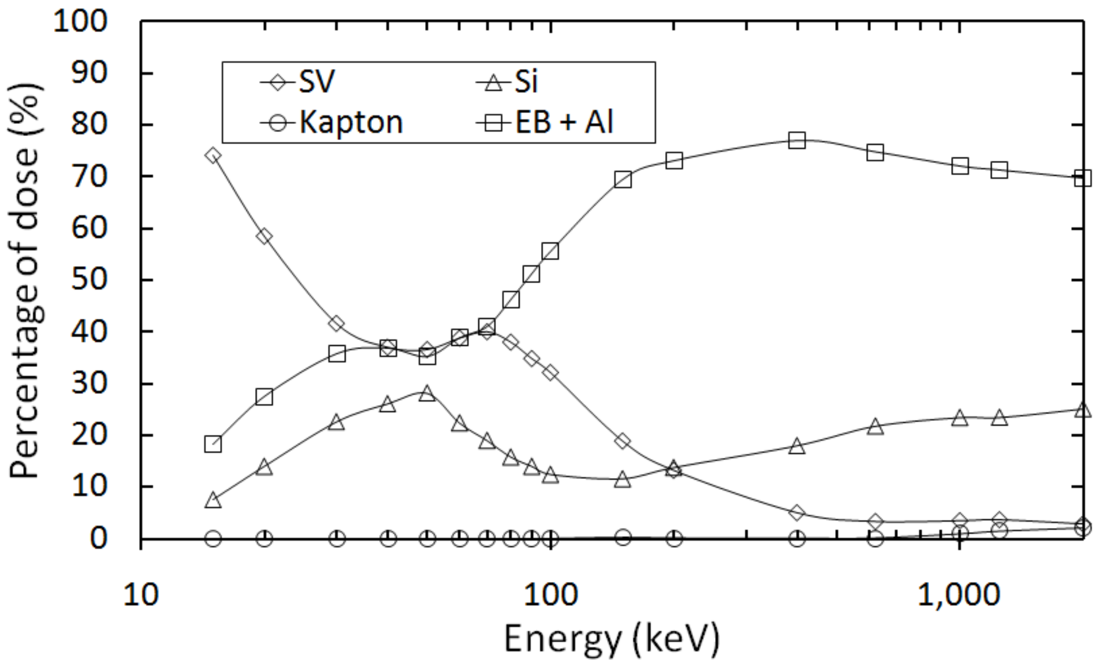

Figure 2.9: The partial contribution to a total dose deposited in sensitive volume from the secondary electrons that originated from the sensitive volume (SV), silicon substrate, Kapton carrier and epoxy bubble plus the aluminium gate.

It is important to mention that tracking the secondary electrons in Monte Carlo simulation shows that at intermediate and high photon energies where Compton scattering dominates, the proportion of secondary electrons that deposit a dose in the MOSFET sensitive volume are not from primary secondary electrons. These events are due to multiple scatterings (three or more) in the material or from delta electrons with long range. Thus, the direction of secondary electrons does not necessarily reflect the direction of the primary beam. In the silicon substrate, the delta electrons may be produced from knocked-out ionisation from the other high-energy secondary electrons which are then scattered backwards to the SiO_2 layer even with normal incidence of photon beams. This complicates the LET distribution of the secondary electrons that originated from the silicon substrate. As a result, the partial numbers of secondary electrons (Figure 2.8) from the silicon substrate for photon energies of 50 to 100 keV only match loosely with the partial contribution to the deposited dose in the sensitive volume (Figure 2.9), compared to the SiO_2 layer and epoxy bubble plus aluminium gate. The Kapton layer maintains the lowest number of secondary electrons and its contribution to the dose deposited in the MOSFET sensitive volume is due to its relatively large distance from the SiO_2 layer.

These results agree with the finding of Wang *et al.* [60], showing a trend of an increasing number toward secondary electrons originating from the epoxy bubble as the photon energy increases. Our results also show an increase in the transparency of the SiO_2 layer to the photons with increases in energy, again matching the Bragg-Gray theory.

2.3.4 *MOSFET responses under filtration*

The energy response of the MOSFET covered with a combination of filters on top of the gate was simulated. Figure 2.10 shows the energy responses under a combination of a single copper filter or multi-layered filter. The application of a single layer of 30 µm-thick copper attenuates the photons at energy < 20 keV in comparison with an unfiltered response (covered with epoxy bubble only). At energies from 20 keV to about 200 keV the response is higher than an unfiltered MOSFET, with a pronounce peak at 30 keV. This is due to increase in the energy of the secondary electrons produced from the photoelectric effect, and in the partial contribution of Compton scattering from the filter compared to the photoelectric effect alone.

The results in Figure 2.10 show that a combination of filters (from top to bottom as shown in Figure 2.3) of copper, aluminium and graphite with thicknesses of 30 µm, 30 µm and 50 µm, respectively, provide a lower response of the MOSFET at energies < 40 keV compared to an unfiltered MOSFET. This combination of filters with lower-atomic-number material such as aluminium and graphite also helps stop the secondary electrons that originated from the copper layer from reaching the sensitive volume for photon energy below 100 keV. An even lower energy response in comparison with an unfiltered MOSFET for photon with an energy range below 50 keV was achieved with a combination of filters of copper, aluminium and graphite, with thickness of 40 µm, 30 µm and 200 µm, respectively. The use of thicker low-atomic-number material, such as 30 µm-thick aluminium and 200 µm-thick graphite, stops the secondary electrons more effectively than the copper layer at even higher photon energies. This makes the filtered MOSFET match the energy response of an unfiltered MOSFET for higher-energy photons. For photons at higher energy > 662 keV, the range of secondary electrons is relatively larger than the thicknesses of the lower-atomic-number materials used, which creates a build-up effect from the filtered MOSFET; this, in turn, leads to a higher response than an unfiltered epoxy-bubble MOSFET.

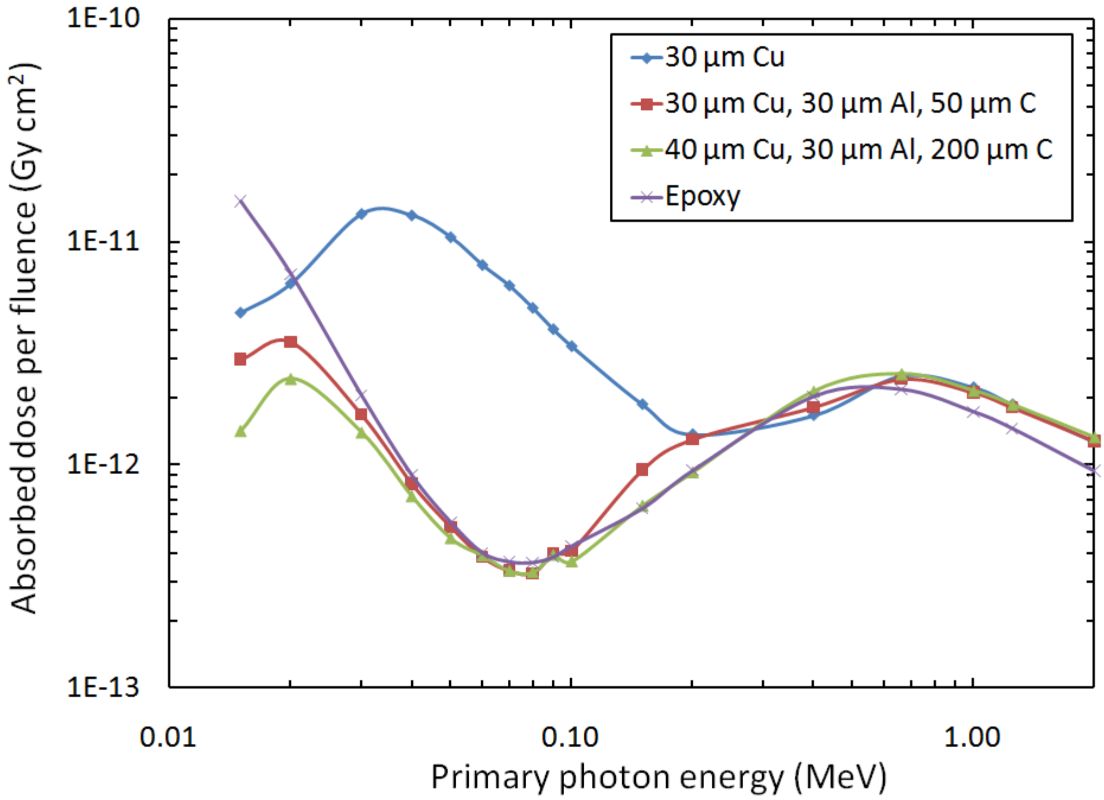

Figure 2.10: The energy response of the MOSFET with a combination of filters on top of the aluminium gate compared to the response of an unfiltered MOSFET covered with an epoxy bubble.

The results for MOSFET energy responses under a combination of lead, aluminium and graphite filters (from top to bottom as shown in Figure 2.3) are shown in Figure 2.11. Generally, the response of the MOSFET at photon energy < 40 keV decreases in proportion to the thickness of lead relative to the unfiltered MOSFET. The application of low-atomic-number materials helps stop the secondary electrons from the lead up to energy of 70 keV. The over-response of the MOSFET for the thinner layer of lead and thicker layers of low-atomic-number materials for a photon-energy range from 70 to 662 keV was reduced accordingly. At a higher photon energy (> 662 keV), the same effect was observed (Figure 2.11), and where the response of the filtered MOSFET were generally larger than the unfiltered MOSFET (Figure 2.10).

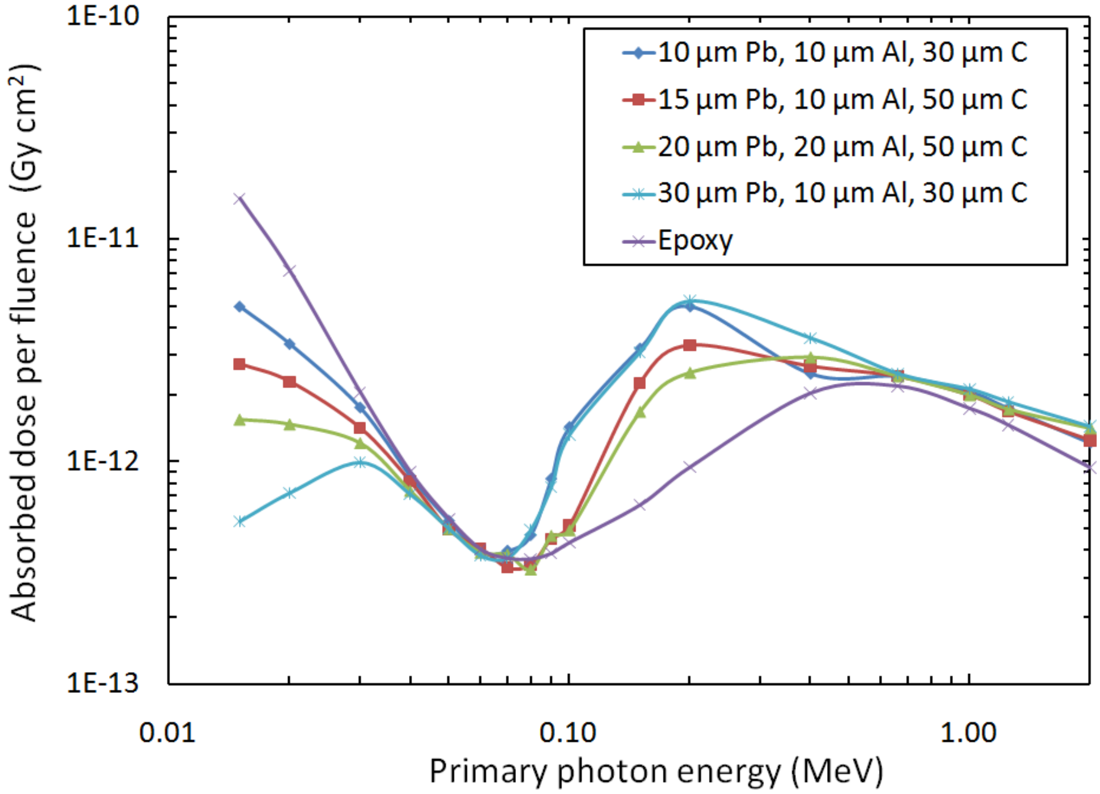

Figure 2.11: The energy responses of the MOSFET for a combination of filters on top of the aluminium gate. The MOSFET with the energy response of the epoxy bubble without a filter is shown for comparison.

2. 4 Conclusion

This chapter discussed the simulation study of the energy response for conventional MOSFET in free-air geometry approximated by a vacuum. The energy responses of the MOSFET depended strongly on how it was packaged, including the use of different filters and an epoxy bubble.

It was demonstrated that a combination of different filters increased the possibility of engineering the energy response of the MOSFET. The use of high-atomic-number filtering helped reduce the energy response for lower photon energies (< 30 keV). With higher photon energies, high-atomic-number filters are a source of secondary electrons, which can essentially increase the response of the MOSFET compared to a MOSFET with only an epoxy bubble. This excessive effect of secondary electrons from high-atomic-number filters can be compensated for by low-atomic-number filters, which stop more electrons than they generate their own (Figure 2.10 and Figure 2.11), in an intermediate range of photon energy. For higher photon energies, the high-atomic-number filters lead to dose-enhancement phenomena when low-atomic-number filters do not stop higher-energy secondary electrons as effectively. This was observed for photon energies more than 662 keV.

These studies demonstrate that to effectively engineer the energy response of the MOSFET in free-air geometry, a combination of high- and low-atomic-number filters is important. As was demonstrated, the problem became even more complicated when considering an angular response that also depends on the packaging of the MOSFET.

The effects of the epoxy bubble and filtration on the energy responses of the MOSFET set out in this chapter have paved the way for future simulations to develop MOSFET packaging that lead to an energy-independent, water-equivalent personal dosimeter that can be used in free-air geometry, as described in Chapter 3 and Chapter 4.

CHAPTER 3

OPTIMISING SINGLE-CHIP MOSFET PACKAGING TO IMPROVE ENERGY RESPONSE

3. 1 Introduction

Monte Carlo simulations of the energy responses in terms of ionising energy deposited in the sensitive volume per single photon of a conventionally packaged and filtered single MOSFET detector were performed in Chapter 2. Based on those results, this and the following chapters aim to optimise the MOSFET detector packaging to improve its energy responses for personnel accident or military dosimetry. Two different CMRP "*drop-in*" design packages for a single MOSFET detector were modelled and optimised using the GEANT4 Monte Carlo toolkit. Simulations of photon absorbed dose in the sensitive volume of the MOSFET dosimeter placed in free air, that correspond to the absorbed doses at depths of 0.07 mm ($D_w(0.07)$) and 10 mm ($D_w(10)$) in a water-equivalent phantom of 30 x 30 x 30 cm^3 for photon energies of 0.015 to 2 MeV, were performed.

Simulations were performed to optimise the MOSFET design and packaging to minimise its over-response to low-energy photons up to 15 keV while retaining its tissue-equivalent dosimetry of high-energy photons. Normalisation to water and 2 MeV mono-energetic photons to obtain the response *R*, was performed according to the following equation.

$$R = \frac{\left(\frac{D_{MOSFET}}{D_w}\right)_E}{\left(\frac{D_{MOSFET}}{D_w}\right)_{2\ MeV}} \qquad (3.1)$$

where D_{MOSFET} is the absorbed dose in SiO_2, D_w is the absorbed dose at particular depth in water phantom, and *E* is the photon energy.

Previously, the response of the MOSFET with TO-8 packaging in a mixed gamma neutron field was simulated using the Monte Carlo code (MCNP4A) [34]. The thickness of the SiO_2 layer was intentionally increased to yield reasonable statistics with the computing power of that time; additionally, MCNP4A had not been specialised to model small sensitive volumes such as the gate oxide of the MOSFET. Another attempt was made to simulate full MOSFET packaging using MCNP 4C code [58-60]; however, the authors admitted that standard tallies in MCNP did not accurately determine the absorbed dose in a sensitive volume. They applied an “electron track-length dose estimator”, first calculating a dose response function for a specific material, and then using it as a modifier to tally F4 (the track-length estimator used in MCNP to determine the average particle influence in a volume). Other studies have been performed that modelled the full MOSFET packaging geometry, using codes such as PENELOPE and GEANT4 [52, 57, 68, 144].

For this study, the GEANT4 version 9.1 toolkits were used to model a conventional MOSFET geometry, including the sensitive volume of SiO_2. The dimensions of the sensitive volume did not need to be modified to acquire an absorbed dose of sufficient statistical accuracy in the SiO_2 because the GEANT4 can track particles down to 250 eV (as described in Section 1.5.1) in very small volumes; it is thus feasible to directly tally energies deposited inside the sensitive volume. This study simulated the energy response of MOSFET to various normally incident mono-energetic photon fields, with the goal of optimising the packaging over-layers above the sensitive volume of the single chip MOSFET to engineer an energy-independent TE gamma dosimeter. Neither the effects of *electron-hole* pair recombination in the SiO_2 nor the nonlinearity of the response associated with radiation damage of the MOSFET were taken into account.

3. 2 Methods

3.2.1 *Optimisation of MOSFET packaging for $D_w(0.07)$ and $D_w(10)$ for $E > 200$ keV*

The first consideration in optimising the MOSFET packaging for a wide spectrum of photon energies is to match its responses to that of water at depths of 0.07 mm and 10 mm for photon energies above 200 keV. Three models of MOSFET packaging geometry were simulated (Figure 3.1): conventionally packaged, $D_w(0.07)$ optimised packaging (OP-007) and $D_w(10)$ optimised packaging (OP-10). A conventionally packaged MOSFET consists of a 180 x 270 x 1 μm^3 SiO_2 (sensitive volume) gate layer on top of a 1000 x 1000 x 500 μm^3 silicon substrate, which corresponds to the commonly used MOSFET or RADFET chip. This MOSFET chip is mounted on top of a 228 µm-thick Kapton carrier, or a thin 0.2 mm PC board [144]. A semi-spherical epoxy bubble covers the whole MOSFET, the structure of which is shown in Figure 3.1a.

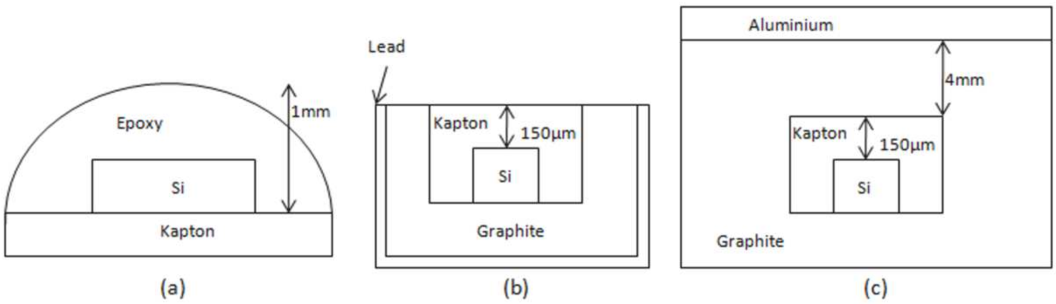

Figure 3.1: Cross-sections of three different MOSFET packaging configurations used in this study: a) conventional packaging, b) OP-007 and c) OP-10.

For an OP-007 MOSFET, silicon substrates 400 x 400 x 375 μm^3 are embedded inside the Kapton carrier to a thickness of 0.525 mm; this is referred to as the CMRP MO*Skin* drop-in design [63], the dimensions of which are 1 x 1 x 0.525 mm^3. The silicon substrates are positioned such that the distance from the surface of the gate to the surface of the Kapton box is approximately 150 µm above the SiO_2 gate. The Kapton is placed inside a 1.4 x 1.4 x 0.75 mm^3 graphite box, which in turn is encased in a 20 µm-thick lead sheet apart from the top surface (Figure 3.1b). The OP-10 MOSFET uses the same MOSFET chip and CMRP "drop-in" packaging in the Kapton box as per the OP-007 MOSFET. However, the Kapton carrier is placed 4 mm deep inside a 10 x 10 x 7.5 mm^3 graphite box. A 500 µm-thick sheet of aluminium is placed on top surface of the graphite box. All MOSFETs used in this study have identical sensitive-volume dimensions and a 1 µm-thick aluminium gate layer on top of the SiO_2 gate (Figure 3.2).

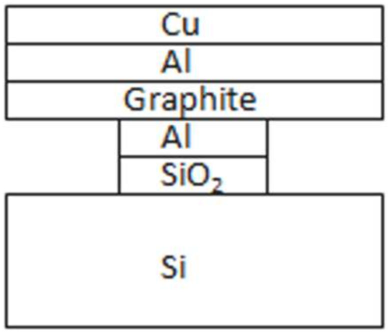

Figure 3.2: Filter layers on the MOSFET chip in OP-007 and OP-10.

3.2.2 *Optimisation of MOSFET packaging for $D_w(0.07)$ and $D_w(10)$ for $E < 200$ keV*

To optimise the filter for low-energy photons, two arrangements were modelled. First, a 30 µm-thick layer of copper was placed on top of the aluminium gate of the MOSFET, and then a combination of filters (30 µm copper, 20 µm aluminium and 50 µm graphite) replaced the 30 µm copper-only layer. This configuration, shown in Figure 3.2, was used to package the OP-007 and OP-10.

3.2.3 *The GEANT4 simulations*

A large number of histories, up to 10^{11}, were required to consider the full geometry of a 100 mm^2 cross-section for OP-10, compared to the 0.0504mm^2 cross-section of the sensitive volume. This study used a larger field than either Wang *et al.* [60] or Beck *et al.* [68], and thus required more events to achieve the same statistical certainty. Panettieri *et al.* [57], reported the largest area of radiation field (10 x 10 cm^2) for a MOSFET simulation at depth in a water phantom, and at most 7 x 10^{10} particles were required. However, some modifications were made, particularly the use of variance-reduction techniques and a SiO_2 sensitive volume 50 times thicker than that used in this study. In this study the energy of the photons was below 2 MeV. As such only the photoelectric effect, multiple scattering, Bremsstrahlung production, Rayleigh scattering, Compton scattering, low-energy ionisation and pair-production were considered in the physics interaction processes.

To simulate the energy response of the MOSFET with the above packaging, as in Figure 3.1b and Figure 3.1c, the average absorbed dose in the SiO_2 was compared to the doses in the water phantom at 0.07 mm and at 10.0 mm depth, respectively, per primary photon fluence. The simulated water phantom of 30 x 30 x 30 cm^3 was irradiated with a 10 x 10 cm^2 parallel beam of photons with incidence perpendicular to the surface. The dose scoring volumes were water cuboids 10 x 10 x 0.01 mm^3 at depths of 0.07 mm and 10.0 mm, placed in the centre of the field. For the MOSFET simulations, each packaged MOSFET OP-007 and OP-10 was irradiated in free-air geometry, approximated by a vacuum with a parallel beam incident to the front face of the MOSFET.

The error was estimated from tallying energy deposition from each event into total energy deposited E_{total} and total squared energy deposited, E^2_{total}. Then energy tallying was averaged to the photon fluence Φ_p, used in the simulation as $< E_{total} > = E_{total}/\Phi_\mathrm{p}$ and $<E^2_{total} > = E^2_{total}/\Phi_\mathrm{p}$. The calculation for one standard deviation σ is given by $\sigma = \sqrt{< E^2_{total} > - < E_{total} >^2}$. The energy-deposition error for 2σ was $E_{error} = 2\sigma/\sqrt{\Phi_\mathrm{p}}$.

3. 3 Results

3.3.1 *Optimisation of MOSFET packaging for $D_w(0.07)$ and $D_w(10)$ for E > 200 keV*

Figure 3.3 shows the average absorbed dose per fluence primary photon simulated for incident mono-energetic photons with an energy range 15 keV to 2 MeV for different MOSFET configurations, and in water at depths of 0.07 mm and 10 mm. For convenience of comparison, each curve was scaled to the dose per fluence primary photon at 200 keV in the case of the water medium. The errors in simulated doses were within ± 5%. The energy dependence of the absorbed dose per fluence primary photon at depths of 0.07 mm and 10 mm in the water phantom was visible. At low photon energy the absorbed dose at 0.07 mm deep was higher than at 10 mm deep because the lower-energy photons deposited their dose at shallower depths. For higher-energy photons above 200 keV, the dose at 0.07 mm was less than at 10 mm deep due to a lack of CPE in the build-up region.

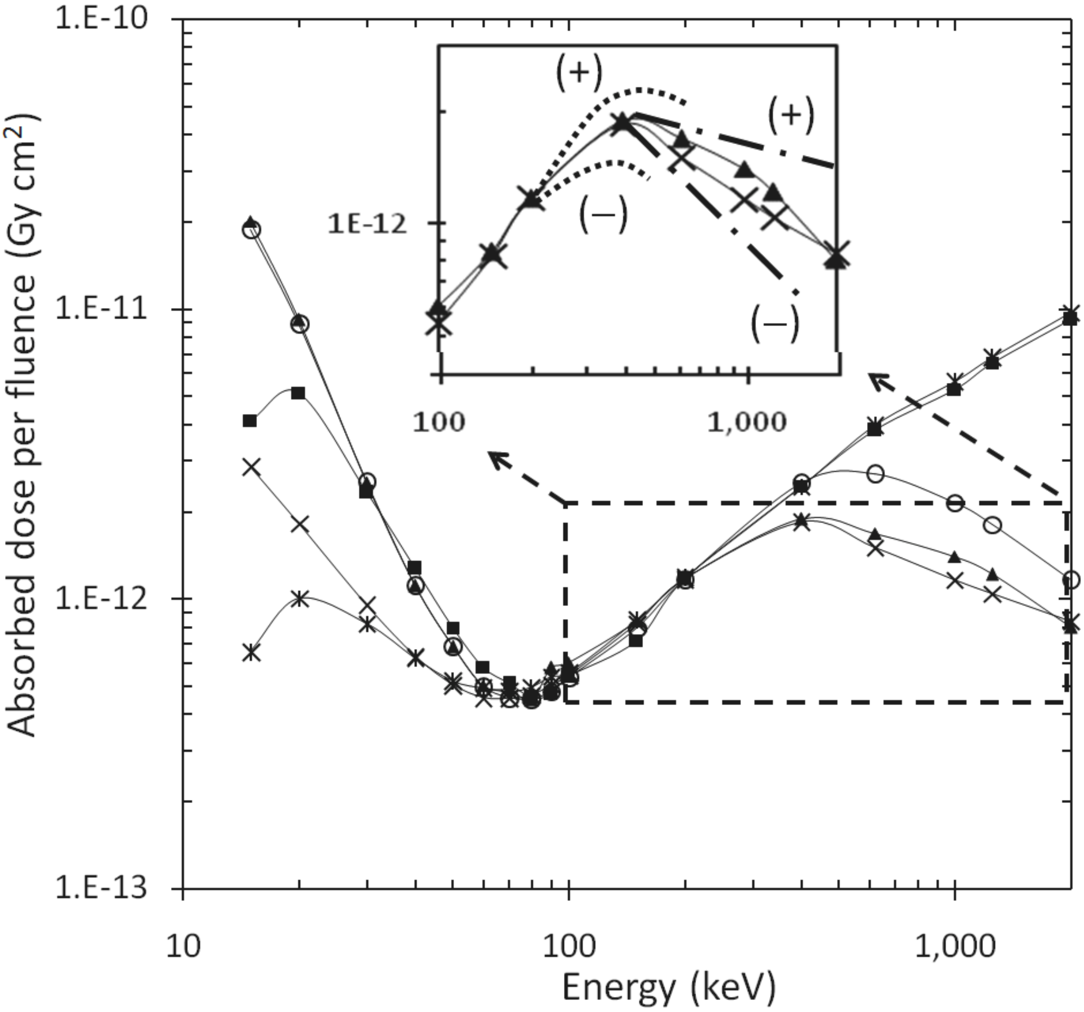

Figure 3.3: Absorbed dose per primary photon fluence in the sensitive volume of the MOSFET for conventional MOSFET packaging, OP-007 and OP-10, as well as dose in water at depths 0.07 mm and 10 mm. Shown inset are the effects of the thicknesses of Kapton and lead coating on the OP-007 response at the peak and the tail region, respectively. O – conventional MOSFET (x 0.81); ▲– OP-007 MOSFET (x 0.81); ■ – OP-10 MOSFET (x 0.8); X – water dose at depth 0.07 mm; Ж– water dose at depth 10 mm; ····· – peak region, ─ · ─ · – tail region

Conventional MOSFET packaging shows an over-response for photon energies E < 100 keV and E > 200 keV compared to the dose at 0.07 mm deep in water, due to a build-up effect produced by the 500 µm-thick epoxy bubble above the SiO_2, in contrast to the 0.07 mm build-up of water. Both the epoxy bubble in the conventional MOSFET and the 150 µm-thick layer of Kapton in the OP-007 provided CPE to the SiO_2 layer for energies up to 400 keV and 200 keV, respectively (Figure 3.3). This finding for the conventional MOSFET was greater than Wang *et al.*'s [60] finding of 200 keV. In comparison to the dose deposited 10 mm deep in water, the conventional MOSFET essentially overestimated the dose for photon energies by less than about 70 keV, due to a lack of filtration of low-energy photons, whereas it mostly agreed at the energy intervals of 70 to 400 keV. As expected, higher photon energies, the conventional MOSFET packaging underestimated the dose compared to the dose in water 10 mm deep, due to a lack of build-up.

Figure 3.4 shows the relative energy response *R* for the conventional MOSFET and OP-007 to a dose in water 0.07 mm deep, and normalised to the ratio of the MOSFET response to a dose in water at the same depth for 2 MeV photons, as per Equation (3.1), as well as for the OP-10 MOSFET to a dose in water 10 mm deep. While the responses of the OP-007 and OP-10 for energies above 100 keV were almost constant, there was a tendency for all the packages described above towards an increased sensitivity for energy below 100 keV. The highest over-response of the conventional MOSFET in this study was 4.74 for 15 keV photons, which was lower than that found by Wang *et al.* [60] (5.9), where they used normalisation to reference exposure with the CPE condition valid. The highest over-responses of the OP-007 and OP-10 were 7.36 and 6.62, respectively. A conventional MOSFET response could not match dose in water for both 0.07 and 10 mm depth for energy < 70 keV and > 400 keV (Figure 3.3).

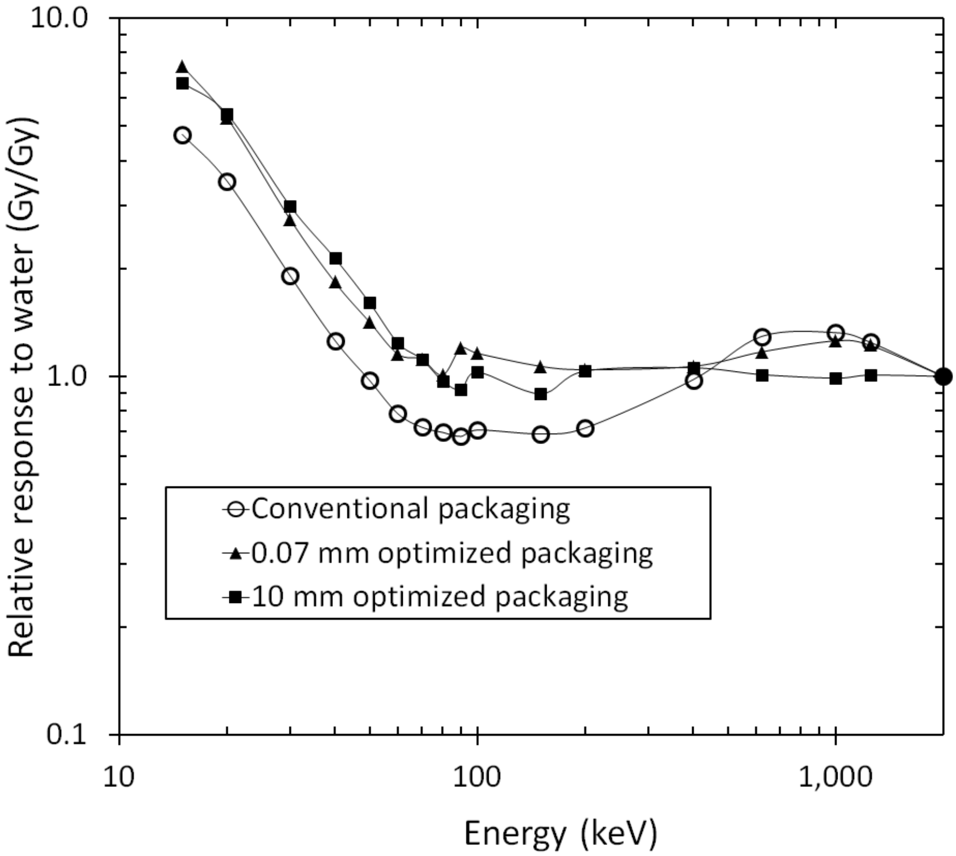

Figure 3.4: Energy response of a single MOSFET with conventional packaging and OP-007 relative to a dose 0.07 mm deep in water, and OP-10 MOSFET relative to a dose 10 mm deep in water. All were normalised to a ratio of responses at 2 MeV photon energy.

3.3.2 *Optimisation of MOSFET packaging for $D_w(0.07)$ and $D_w(10)$ for $E < 200$ keV*

Figure 3.5 shows the average absorbed dose per fluence primary particle for both the OP-007 and OP-10 MOSFET with two filtering configurations scaled at 200 keV photon energy. For the OP-007, filtration with a single layer of copper initially lowered the absorbed dose in the sensitive-volume response of 15 keV photons, close to that of water. But as the energy of the photons increased (> 15 keV), more secondary electrons created inside the copper could reach the sensitive volume and deposited dose. Single filtration caused the over-response peak to shift to the higher-energy photons, creating more over-response (16.61) than with the unfiltered OP-007 (7.36).

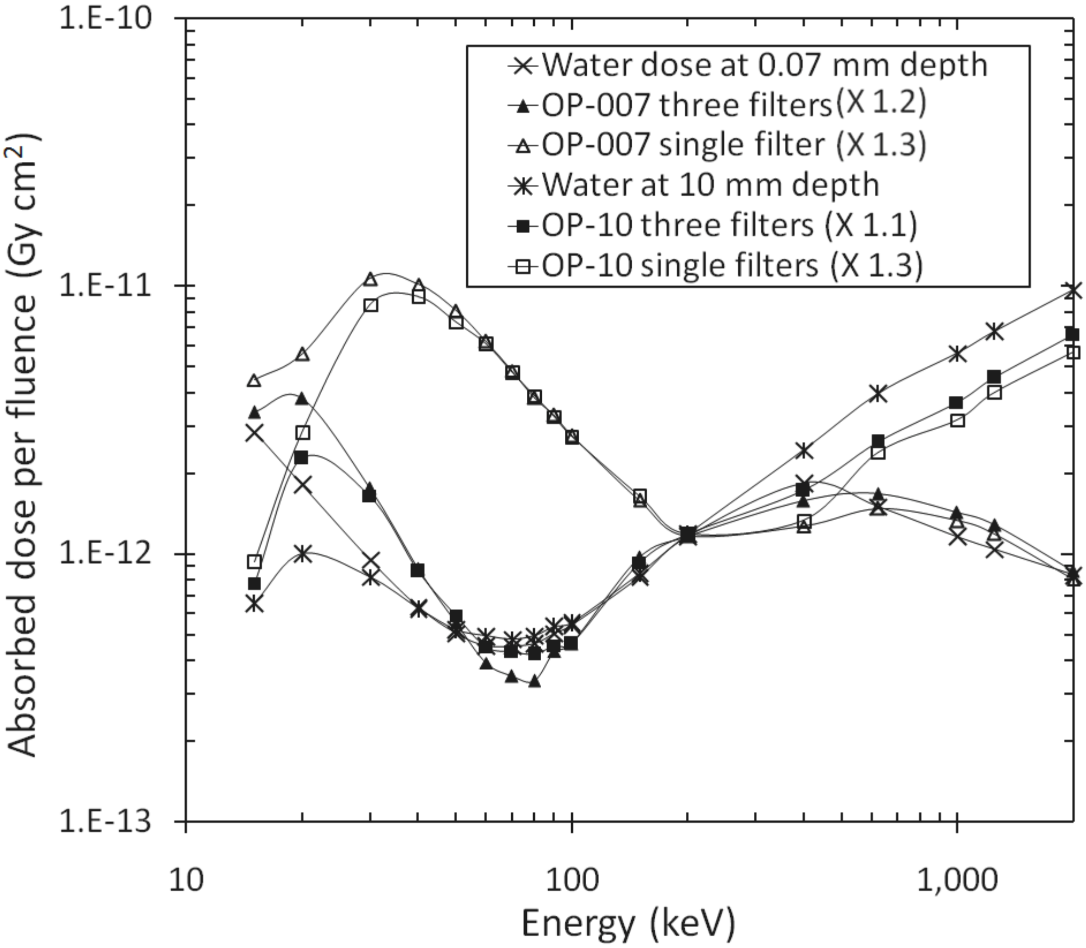

Figure 3.5: Response of OP-007 and OP-10 MOSFETs with two filtering methods. The doses to water 0.07 mm and 10 mm deep are shown for comparison.

In the three-layer filtration method using low-atomic-number materials, the excess secondary electrons created by the intermediate energy photons were stopped, which resulted in a finer-shaped response of dose to water. With the OP-10, the single copper filter again gave too high a dose for 30 to 40 keV photons, whereas the three-layer filtration responded better to dose in water. At energies above 200 keV, the filtered OP-10 resulted in a lower absorbed dose than dose in water compared to the unfiltered (Figure 3.3), a result of the thicker filter experienced by secondary electrons generated inside OP-10 packaging that scattered downwards. A larger portion of the absorbed dose in the MOSFET chip inside the OP-10 (due to satisfying CPE) was from scattered secondary electrons.

The relative response to water of both optimised packaging methods is shown in Figure 3.6. The OP-007 had an over-response peak (2.03) at 20 keV and the lowest under-response (0.70) at 80 keV, whereas the OP-10 had an over-response peak (3.32) at 20 keV and the lowest under-response (0.98) at 662 keV for mono-energetic photon energy.

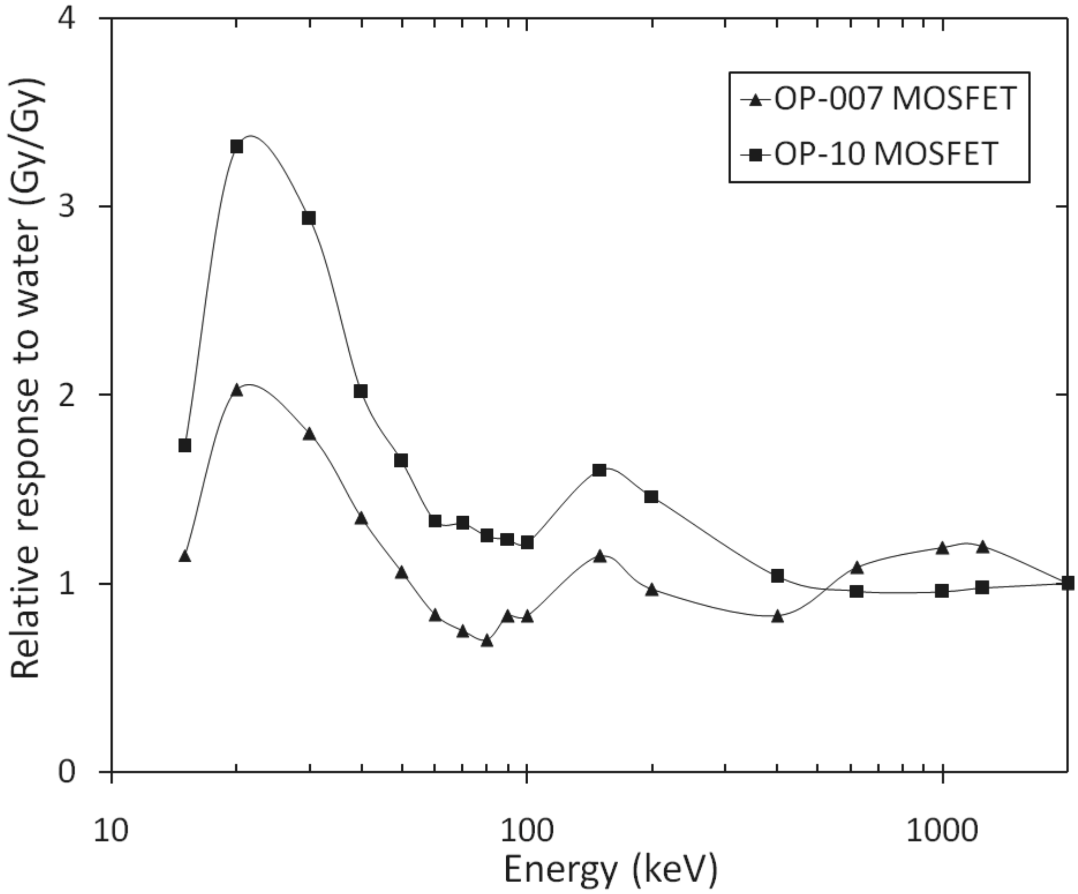

Figure 3.6: Relative response to water for OP-007 and OP-10 with multilayer filters normalised to 2 MeV photon energy.

3. 4 Discussion

3.4.1 *Optimisation of MOSFET packaging for* $D_w(0.07)$ *and* $D_w(10)$ *for E > 200 keV*

The principle of the MOSFET packaging design is a multi-step process. We have developed a technologically suitable and reproducible drop-in packaging for the MOSFET chip in a Kapton carrier [63] that avoids high-atomic-number wire bonding of the chip and the use of an epoxy bubble. This design improves skin dosimetry by allowing a reproducible water-equivalent depth (WED) of 0.07 mm. Considering that our dosimeter is designed for free-air geometry application, the polyamide build-up of 0.07 mm, as was adapted for the MO*Skin*, is not valid for $D_w(0.07)$ skin dosimetry in a photon field, due to the absence of backscattering; this is in contrast to a MO*Skin* on the surface of a patient body or a phantom. For photons with energies above 200 keV, the thickness of the Kapton over-layer was chosen to be 150 µm. When the Kapton thickness was increased, the peak (inset of Figure 3.3) increased (the plus sign); while conversely, the peak decreased (as shown by the minus sign). To account for the backscattering radiation as the photon energy increased, we modelled an optimal combination of graphite and lead coating on the back of the Kapton strip holding the MOSFET chip. If the Kapton was kept to 150 µm-thick and the thickness of the lead coating increased, the high-energy response increased (shown in the inset of Figure 3.3 as a plus sign), while conversely, the high-energy response decreased (as shown by the minus sign). All these factors make the OP-007 design much more complicated than the OP-10. These results show an almost independent response of the OP-007 MOSFET to photon energy above 200 keV (Figure 3.4). However, for conventional MOSFET, under-response was obvious due to the lack of backscattering.

With the OP-10 MOSFET, it was found that 500 µm-thick aluminium plus 4 mm-thick graphite above the sensitive volume provided an almost independent response for photons with energy above 100 keV compared to $D_w(10)$ in water, while having minimal thickness of total packaging. In this design we simply needed to meet CPE and attenuation effects at a depth of 10 mm in water. The combination of these thicknesses of aluminium and graphite meet both physics requirements under consideration in this study.

The attenuation effect was calculated approximately from the *mass attenuation coefficient, μ/ρ* for water, aluminium and graphite from reference [145]. The percentage of photons transmitted through the single material was per Equation (3.2).

$$Transmission = e^{-\left(\frac{\mu}{\rho}\right)\rho t} \times 100\% \tag{3.2}$$

where $\mu\ /\rho$ is the *mass attenuation coefficient* of the material, ρ is the density of the material and t is the thickness of the material. For dual layers of material, Equation (3.3) was used.

$$Multilayers\, Trans = \prod_{i=1}^{2} e^{-\left(\frac{\mu}{\rho}\right)_i \rho_i t_i} \times 100\% \tag{3.3}$$

where $(\mu\ /\rho)_i$ is the *mass attenuation coefficient* of the material-*i*, ρ_i is density of the material-*i* and t_i is the thickness of the material-*i*. Figure 3.7 shows the results of Equations (3.2) and (3.3) when applied to 10 mm-thick water and a combination of aluminium and graphite, respectively.

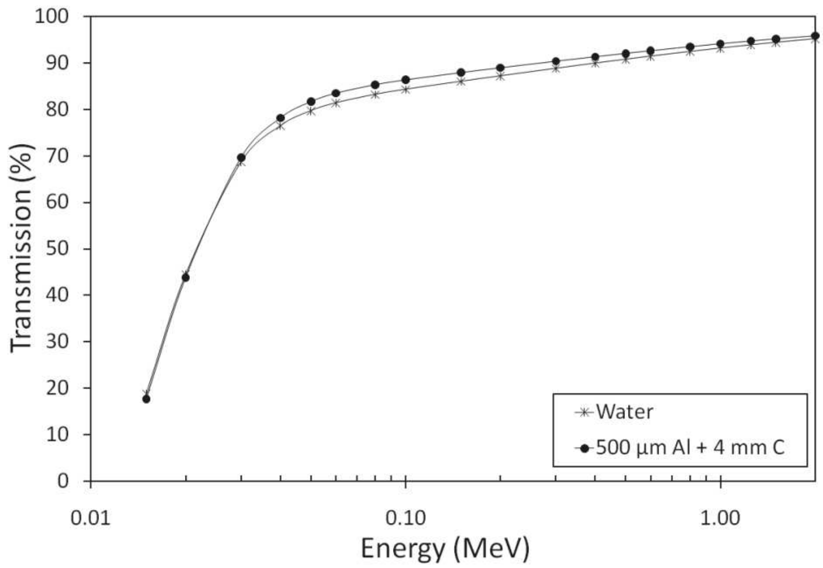

Figure 3.7: Transmission of the photon-energy fluence through 10 mm-thick water and the best combination of thicknesses of aluminium and graphite to match the transmission in water.

3.4.2 *Optimisation of MOSFET packaging for* $D_w(0.07)$ *and* $D_w(10)$ *for* $E < 200$ *keV*

The packaging was further improved with the removal of the over-response of the single MOSFET for $D_w(0.07)$ dosimetry for photons with energy less than 100 keV by optimising the filters above the aluminium electrode gate of the MOSFET. Figure 3.5 shows the effect of two different filters applied to the OP-007 MOSFET when irradiated with mono-energetic photon beams from 15 keV to 2 MeV. The MOSFET filtered by 30 μm copper alone showed an increase in the relative response over that of water for energies below 200 keV. This dose enhancement was due to an increase in photoelectrons generated within the copper layer. Modelling with Monte Carlo demonstrated that optimising the energy response is impossible with a single high-atomic-number filter because the dose is enhanced at intermediate photon energies. The effect of dose enhancement in MOSFET dosimetric response using high-atomic-number material filters was observed previously by Rosenfeld *et al.* [34], who found that a high-atomic-number Kovar encapsulation enhanced the measured MOSFET dose in a 6 MV photon beam near a water phantom surface. Brucker *et al.* [82] found that they could reduce the dose enhancement due to a high-atomic-number Kovar encapsulation material by using grease between the Kovar encapsulation and the MOSFET. However, filtering a MOSFET with a single layer still cannot give a constant response over the range of 15 keV to 100 keV.

Multiple over-layers with a variety of atomic-number materials and their thicknesses have been modelled to optimise the energy response for photons above 15 keV. The first layer effectively attenuates low-energy photons, while the second stops secondary electrons, reducing the dose enhancement for higher photon energies. We found that optimising the energy response of the MOSFET for $D_w(0.07)$ and $D_w(10)$ measurements can be achieved by having three over-layers above the MOSFET gate Cu-Al-C (Figure 3.2). This may be achieved using a Cu-C filter at thicker than 150 μm, while a combination of three filters provides a thinner option.

In addition, we expected that the detectors would have some angular dependence to incident radiation; this will be the subject of future study with prototype detectors.

3. 5 Conclusion

These results have demonstrated the possibility of optimising the packaging of a single-chip MOSFET (OP-007 and OP-10) for measurements of $D_w(0.07)$ and $D_w(10)$ for photons with energies > 15 keV. Both filtered packages OP-007 and OP-10 allow an almost independent energy response in the single MOSFET for $D_w(0.07)$ and $D_w(10)$ respectively, for photon energies > 100 keV within 20% for OP-007 and 60% for OP-10. The response of both packages would be more consistent in practice because the small over- and under-response would compensate each other in the broad spectrum of photon beams. Without optimising the packaging, a conventional MOSFET would be incapable of measuring a dose $D_w(0.07)$ and $D_w(10)$ for an energy range from 15 keV to 2 MeV in free-air geometry.

In Chapter 4, dual-chips MOSFET designs are used to further improve the energy response by comparing the measurement between the filtered and unfiltered MOSFET chips.

CHAPTER 4

OPTIMISING DUAL-CHIP MOSFET PACKAGING TO IMPROVE ENERGY RESPONSE

4. 1 Introduction

The solution using the dual-MOSFET detector was proposed and optimised using the GEANT4 Monte Carlo toolkits to correct its response in photon field measurements. The responses of the detector should be independent of photon energies from 0.015 to 2 MeV in free-air geometry for $D_w(0.07)$ and $D_w(10)$. Correction factors that depended on the photon energy of the detector were determined through a set of ratios simulated from the responses of dual MOSFETs while different filters were placed in the same package.

The approach to dual-MOSFET dosimetry has already been used in medical dosimetry for different purposes. Rosenfeld *et al.* [146, 147] demonstrated that a dual-MOSFET configuration could be used to obtain the neutron fluence in a phantom for a Boron Neutron Capture Therapy (BNCT) epithermal neutron beam by subtracting the response of two MOSFETs, one of which was covered by a ^{10}B converter. Soubra *et al.* [49] used dual MOSFETs for temperature compensation by subtracting the response of two MOSFETs irradiated with different bias voltages. The advantages of a dual-MOSFET configuration manufactured onto the same chip are their close proximity, as well as they response in the same degree to electrical characteristics, temperature, radiation and fading when they have been irradiated with the same bias voltage; and simultaneous readout. The aim here is to combine the advantages of a dual MOSFET with the proposed method for correcting the energy response for use as military-personnel dosimeter. An unknown photon field is expected in this application; therefore, this is an attempt to yield photon-energy-independent dosimetry for the relative response of a MOSFET in free-air geometry to an absorbed dose in water at particular depths of interest.

Low-energy photons, where the photoelectric effect is dominant, increases the dose deposited in the sensitive volume of the MOSFET relative to that deposited in water. Another approach was proposed in this study to reduce the over-response of the MOSFET at low-energy photons in addition to passive filtering, as described in Chapter 3 for a single chip MOSFET. This method uses the active combination of two MOSFET responses. The dual MOSFETs used in this study were placed inside an optimised package (OP) to obtain a dose equivalent to $H_p(0.07)$ and $H_p(10)$, defined in this case as the doses deposited at depths of 0.07 mm ($D_w(0.07)$) and 10 mm ($D_w(10)$) in a water phantom.

The active-correction approach uses dual MOSFETs on the same chip; unfiltered and filtered MOSFETs with the responses R_1 and R_2, respectively, as shown in Figure 4.1. Further details of the filter geometries are presented in Figure 4.2. A filter made from material with a high-atomic-number for photon attenuation was coupled with two materials with a low-atomic-number to filter excess secondary electrons generated in close proximity to the sensitive volume, as discussed in Chapter 2. The current study does not consider electron-hole recombination effect in the gate oxide (sensitive volume) of the MOSFET.

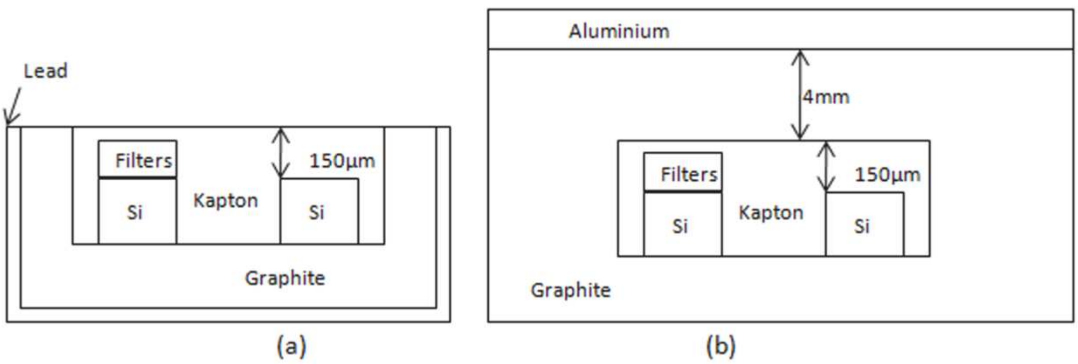

Figure 4.1: Dual MOSFETs inside optimised packages for measuring (a) $D_w(0.07)$ (OP-007) and (b) $D_w(10)$ (OP-10).

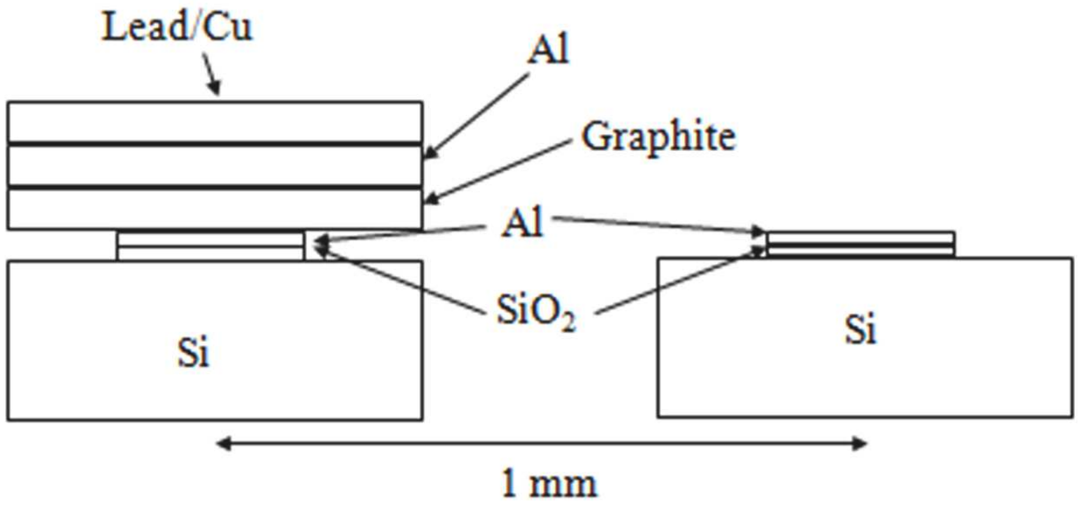

Figure 4.2: Dual MOSFET configurations in OP-007 and OP-10 packages. The unfiltered chip on the right and the filtered one on the left give readings denoted as R_1 and R_2, respectively.

This approach uses CMRP-developed MOSFET drop-in Kapton packaging [63], with an electrical connection of the MOSFET detector achieved with a surface layer of reproducible thickness. The copper filter above the gate of the R_2 MOSFET used in Chapter 3 was replaced with lead to give a multilayer-filter thinner than the 150 µm of Kapton (see Figure 4.1 and Figure 4.2). Over-filtration of the filtered MOSFET (R_2) combined with an unfiltered MOSFET (R_1) is a key feature in achieving an independent response to photon energy down to 15 keV. Furthermore, the dual-MOSFET approach can retain the uniform independent response to photon energy from the unfiltered MOSFET above 100 keV.

4. 2 Methods

4.2.1 *MOSFET geometries*

Two MOSFET packaging geometries, OP-007 and OP-10, developed as described in Chapter 3, were used here. OP-007 packaging is an optimised geometry to provide a measurement response equivalent to an absorbed dose at a depth of 0.07 mm in water. Two silicon substrates measuring 400 x 400 x 375 μm^3 were embedded inside a 1 x 2 x 0.525 mm^3 Kapton carrier (a so-called CMRP MO*Skin* drop-in design [63]) of OP-007 packaging. This gave the unfiltered MOSFET a 150 µm-thick Kapton over-layer. The dual-MOSFETs were embedded in a 1.4 x 2.4 x 0.75 mm^3 graphite casing. Apart from the top surface, the graphite casing was wrapped in a 20 µm-thick layer of lead. The OP-007 dual-MOSFET detector is shown in Figure 4.1a.

The OP-10 MOSFET was designed to provide measurement response equivalent to an absorbed dose at depth of 10 mm in water. The OP-10 packaging used the same arrangement of dual MOSFETs embedded on a Kapton carrier and placed inside a graphite casing, as per the OP-007 packaging. With the OP-10 MOSFET, however, the Kapton carrier was placed 4 mm deep into a 10 x 10 x 7.5 mm^3 graphite casing. A 500 µm-thick aluminium coating was placed on the top surface of the graphite casing (Figure 4.1b).

All the MOSFETs used in this study have an identical 180 x 270 x 1 μm^3 of layer gate oxide with a 1 µm-thick aluminium layer on top, as shown in Figure 4.2. Filtering was achieved by placing three over-layers on top of the aluminium gate of the MOSFET. The filters were made from a combination of lead, aluminium and graphite layers (Figure 4.2). The thickness and combination of the filters resulted from optimising the response of dual-active MOSFETs with Monte Carlo simulations.

4.2.2 *GEANT4 simulation*

The cutoff range (which is equivalent to cutoff energy) was set to millimetres for a region away from the sensitive volume down to 0.1 µm in the sensitive volume. This was done to speed up the computation times while maintaining accuracy. The highest number of histories required to get a 95% statistical confidence level at two standard deviations was 10^{11} particles. GEANT4.9.1 was used in this study.

As in Chapter 3, the photon-energy response of the dual-MOSFETs was studied for photons with energy 15 keV to 2 MeV. The photoelectric effect, multiple scattering, Bremsstrahlung production, Rayleigh scattering, Compton scattering, low-energy ionisation and pair-production were considered in the physics interaction processes.

A simulation of irradiation with mono-energetic photons was done for a parallel beam incident normally on top of the detector. The energy responses of the detector were compared to the simulated doses in a water phantom at depths of 0.07 mm and 10 mm. For the water-phantom simulations, a 30 x 30 x 30 cm^3 water phantom was irradiated with a 10 x 10 cm^2 parallel beam of photons incident normally onto the centre of the water-phantom surface. The dose scoring volumes were 10 x 10 x 0.01 mm^3 water cuboids at depths of 0.07 mm and 10.0 mm, placed at the centre of the field. The relative energy response of the dual MOSFETs to water was normalised to the response at 2 MeV photons.

To study the dual-MOSFETs detector's relative response to water, photon spectra were used. These photon energies were selected from different Bremsstrahlung spectra simulated by Xcomp5r software [148]. A generic LINAC 6 MV photon spectrum with an average energy of about 2 MeV was also used. Xcomp5r is a program for calculating X-ray spectra based on a semi-empirical model. The properties of the X-ray spectra generated by Xcomp5r for a tungsten target are shown in Table 4-1, and the spectra plots are shown in Figure 4.3. The dual-MOSFET response in X-ray spectra relative to water was normalised to a 6 MV LINAC spectrum.

Table 4-1: The properties of X-rays used in this study

Voltage (kV_p)	**Inclination** (^{o})	**Filtration** (*mm*)	**Average energy** (*keV*)
30	14	0.5(Be)+1.2(Al)	21.6
50	22	2.2(Be)+4(Al)+0.2(Cu)	38.2
80	12	1(Be)+2.5(Al)	43.4
100	22	2.2(Be)+4(Al)+0.2(Cu)	58.0
150	22	2.2(Be)+4(Al)+1.2(Sn)	106.8

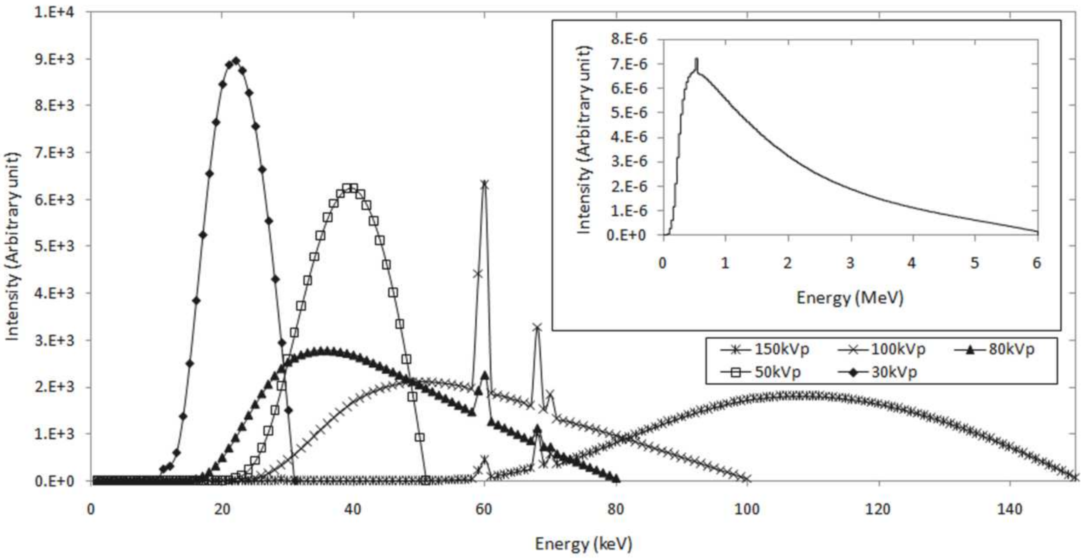

Figure 4.3: X-ray photon spectra generated from Xcomp5r. The inset shows the generic LINAC 6 MV spectrum used to normalise the detector response.

4. 3 Results

Figure 4.4 and Figure 4.5 show the response of dual MOSFETs for OP-007 and OP-10 packaging geometries respectively, when simulated with mono-energetic photon beams of various energies. The doses at depths of 0.07 and 10mm in water are shown for comparison, although they are not to scale. At photon energies $\leq$ 60 keV, the R_1 MOSFET detector showed an over-response compared to the absorbed dose in water. For photon energies $\leq$ 30 keV, the R_2 detector showed an under-response compared to the absorbed dose in water. These are the cases for both the OP-007 and OP-10 packaging geometries.

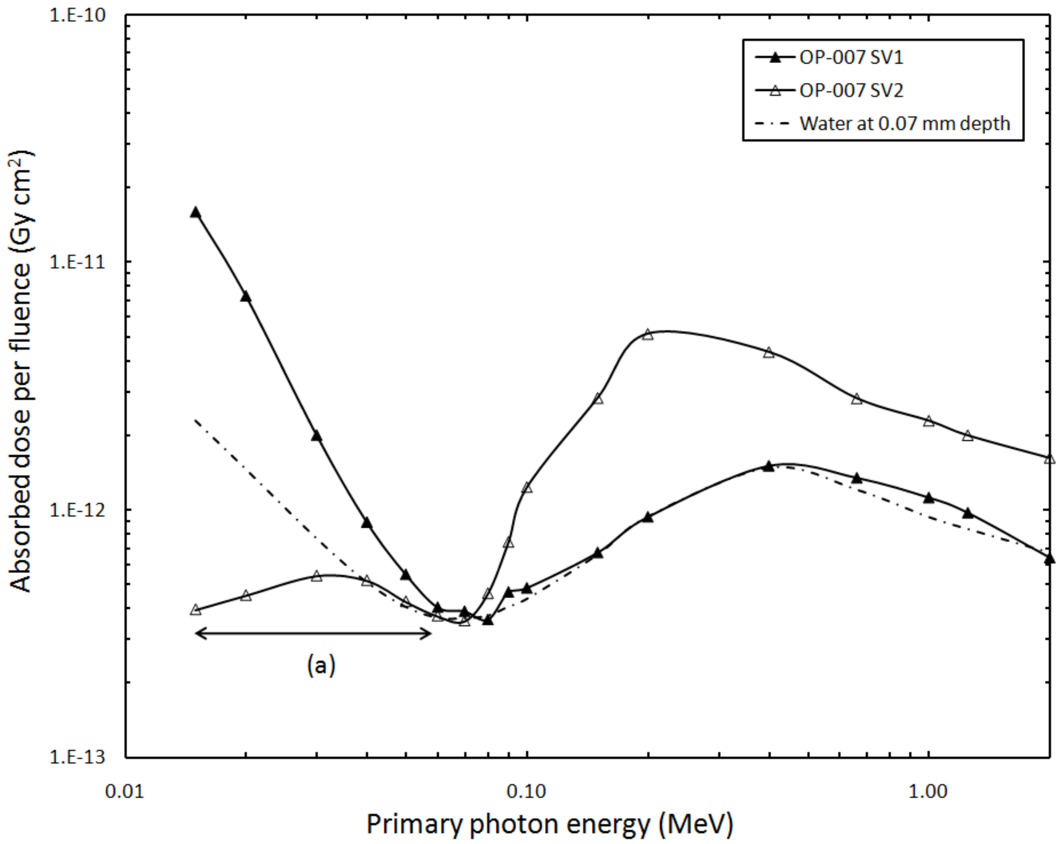

Figure 4.4: The response of OP-007 dual-MOSFETs R_1 and R_2 to mono-energetic photons. The water-absorbed dose at depth of 0.07 mm in a water phantom is also shown, but not to scale. (SV1 and SV2 correspond to MOSFETs R1 and R2, respectively.)

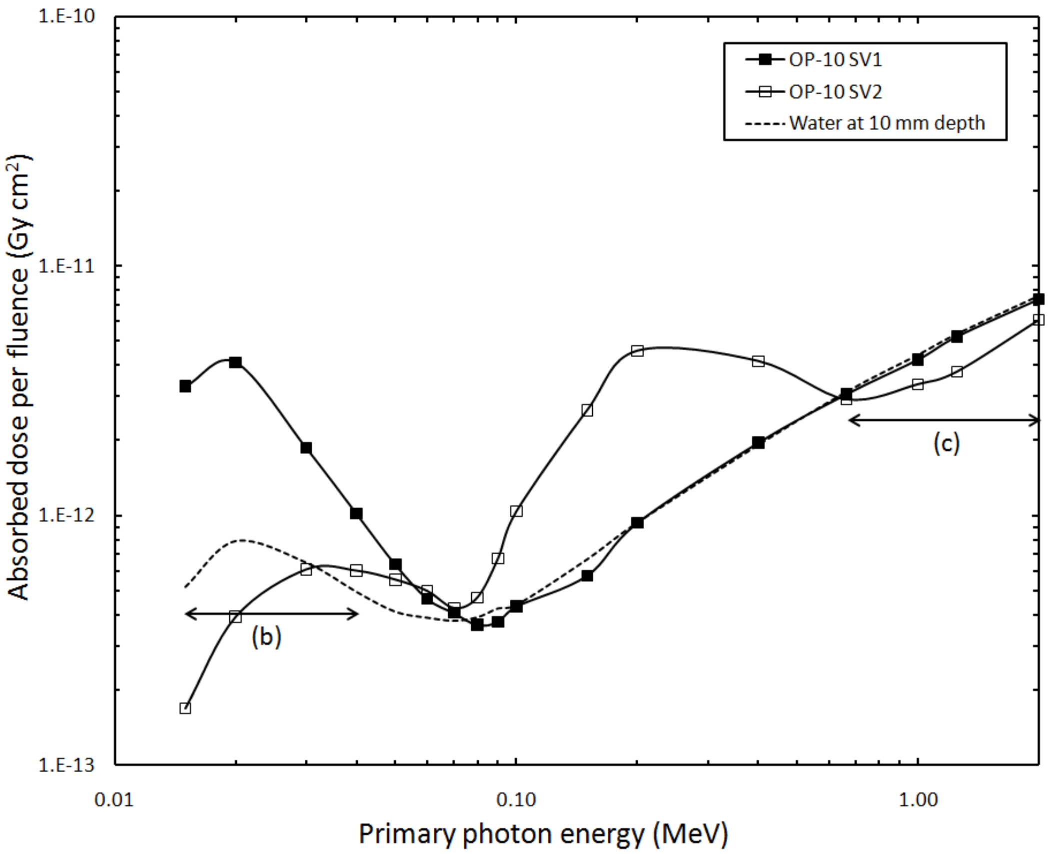

Figure 4.5: The response of OP-10 dual-MOSFETs R_1 and R_2 to mono-energetic photons. The water absorbed dose at depth of 10 mm in a water phantom is also shown, but not to scale. (SV1 and SV2 correspond to MOSFETs R1 and R2 respectively.)

The responses of both configurations of MOSFET packaging are split into two distinct regions: – low-energy photons (where $R_2 < R_1$) and high-energy photons (where $R_2 \geq R_1$). For OP-007, as shown in Figure 4.4, $R_2 < R_1$ for photon energies of 15 keV to 60 keV. For OP-10, as shown in Figure 4.5, $R_2 < R_1$, for photon energies of 15 keV to 50 keV. With OP-10, at photon energies > 600 keV, R_2 was again < R_1. This was due to the secondary electrons scattering downwards from the 500 µm aluminium layer being stopped by the graphite packaging, whereas there were fewer secondary electrons created in the 4 mm-wide graphite gap between the aluminium layer and the MOSFETs. For photon energies above 60 keV, $R_2 \geq R_1$ for both detectors (apart from the previously mentioned > 600 keV region for the OP-10 geometry), the response of detector R_1 matches that of water. Thus the response of the detector requires correction only for energies ≤ 60 keV.

The dual-MOSFET detector provided an incident photon spectra analysis based on a comparison of the responses of R_1 and R_2, while allowing for a correction algorithm in the form of a Heaviside function to be used. A correction factor was introduced to correct the over-response of the R_1 detector relative to water at a particular depth that occurred when R_2 is lower than R_1, $R_2 / R_1 < 1$, as shown in Figure 4.4 and Figure 4.5. In particular, for detector OP-007, shown in Figure 4.4 (a), $R_2 / R_1 < 1$ for energies 15 to 60 keV; in ratio values these are 0.025 (15 keV) < R_2 / R_1 < 0.923 (60 keV). Therefore, for OP-007 measurement with values of $R_2 / R_1 < 0.923$, the correction factor will be applied to R_1. For OP-10, however, as shown in Figure 4.5 (c), there are two intervals of photon energy where the ratio $R_2 / R_1 < 1$. This occurs for photon energies 15 to 50 keV, as shown in Figure 4.5b (0.051 < R_2 / R_1 < 0.87) and for 600 to 2000 keV, as shown in Figure 4.5c (0.72 < R_2/R_1 < 1). A correction factor was required for the former energy ranges, but not for the latter. Therefore, for the OP-007 and OP-10 geometries, the viable ranges for R_2 / R_1 ratio to be used in the correction algorithm were 0.025 (15 keV) < R_2 / R_1 < 0.923 (60 keV) and 0.051 (15 keV) < R_2 / R_1 < 0.590 (40 keV), respectively. This is summarised in Table 4-2 below.

Table 4-2: A summary of viable ratio range of R_2 / R_1 for the detector-reading correction factor to be applied to R_1

Detector	Energy range where $R_2 < R_1$	The lowest ratio values of R_2 / R_1 in the energy range	The highest ratio values of R_2 / R_1 in the energy range	Viable ratio range for correction at low-energy part of Figure 4.4a and Figure 4.5b
OP-007	15 – 60 keV (Figure 4.4a)	**0.025** at 15 keV	**0.923** at 60 keV	**0.025 – 0.923**
OP-10	15 – 50 keV (Figure 4.5b) and 600 – 2000 keV (Figure 4.5c)	**0.051** at 15 keV and **0.72** at 1250 keV	**0.87** at 50 keV and **1.0** at 600 keV	**0.051 – 0.590**

The R_2 / R_1 ratio is plotted against the photon energy in Figure 4.6a. The R_2 / R_1 ratio increases monotonically with energy, allowing for correction of the R_1 response. We associated a correction factor (CF) for the R_1 to the corresponding photon energy for a given ratio, as shown in Figure 4.6b. The correction factor was defined as the multiplier required to calculate the dose in water from the value of R_1. The correction factor is therefore a function of the ratio R_2 / R_1, which is in itself a function of photon energy. The correction factor was plotted as a function of the ratio R_2 / R_1 and up to a fourth-order polynomial was fitted. The agreement of the ratio plot with the polynomial is shown by the R^2 value in Figure 4.6c.

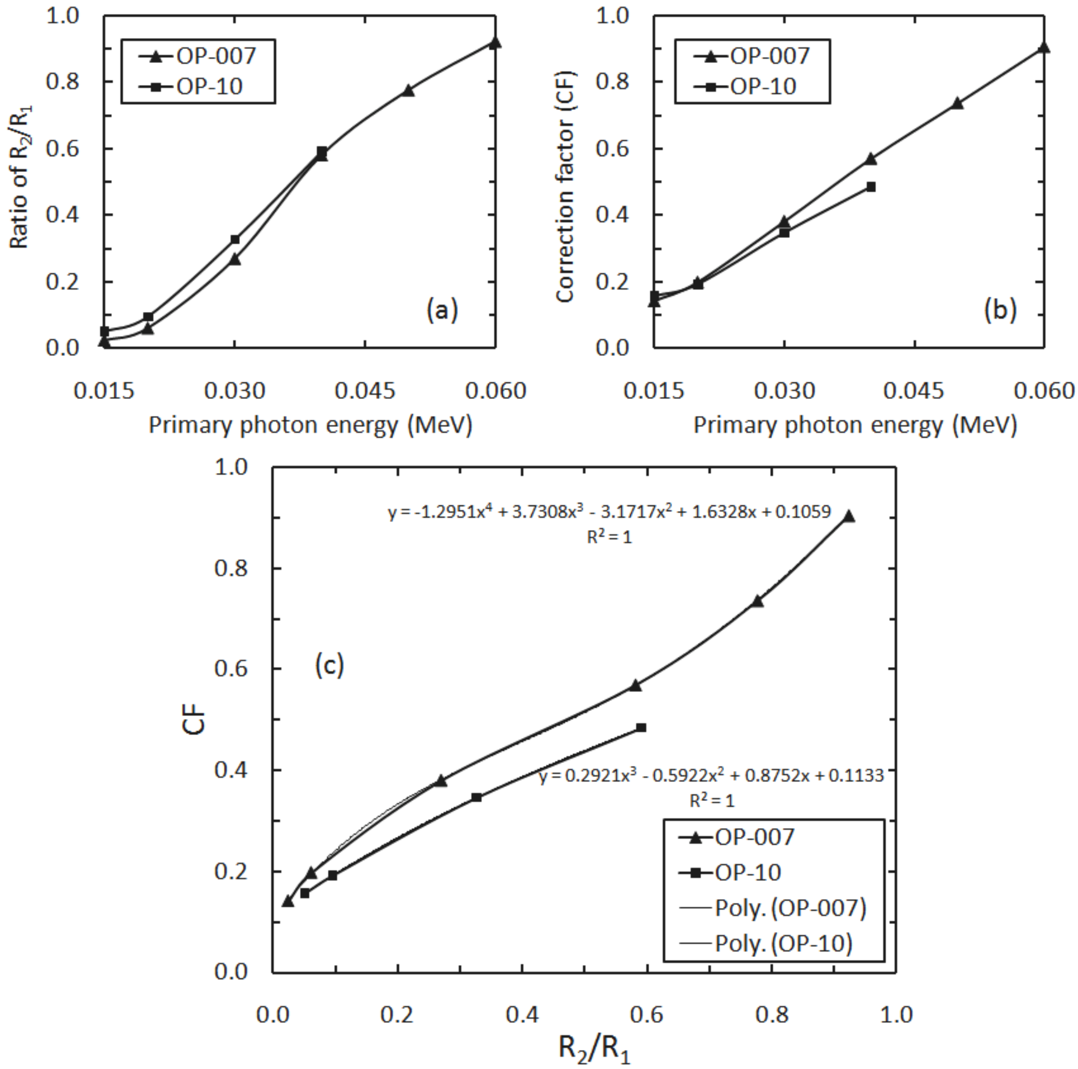

Figure 4.6: (a) The ratio of R_2 over R_1 for possible photon energies for correcting OP-007 and OP-10, and (b) the correction factor for correcting the R_1 associated with each ratio. Shown in (c) is the polynomial fit for correction factor versus R_2/R_1.

Therefore one can take the measured ratio R_2 / R_1, calculate the correction factor and then multiply the correction factor by the response of R_1 and a calibration factor for the 6 MV photon beam to obtain the dose to water. This process is summarised in Figure 4.7.

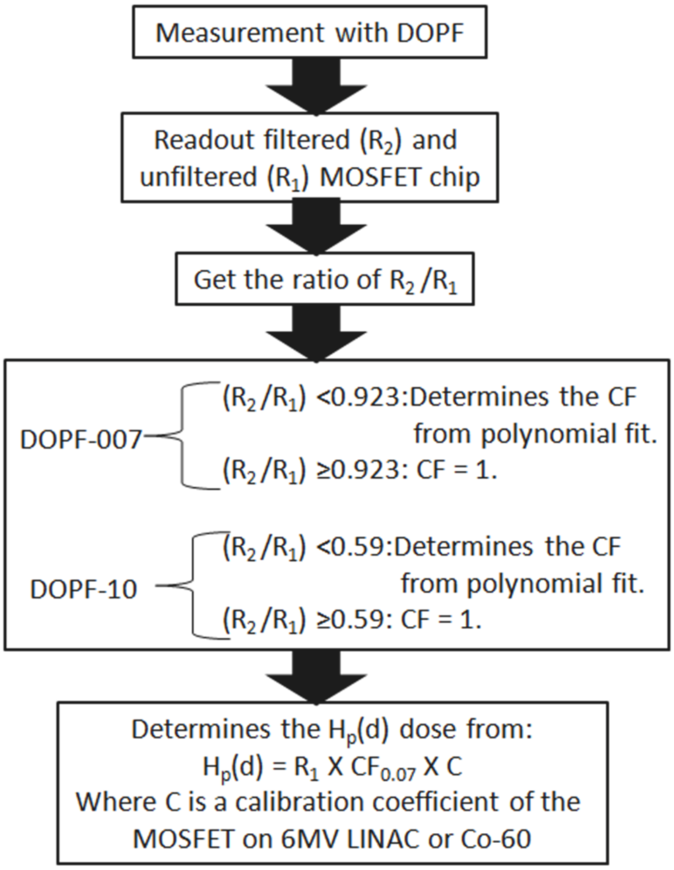

Figure 4.7: Algorithm for a newly developed method for correcting the energy response of the MOSFET for DOPF-007.This is also applicable to DOPF-10.

The correction algorithm was then tested in poly-energetic beam spectra (Figure 4.3) for both detector packages. The same irradiation setups were simulated with the poly-energetic beams, and the correction algorithm was applied to the detector measurements. The corrected and uncorrected detector measurements for the quality of each beam were then normalised to the dose in water. The results are shown in Figure 4.8. As expected, the uncorrected R_1 reading over-responded to the lower X-ray voltage peak energy spectra. Once the correction algorithm was applied to the R_1, the over-response was removed and both detectors provided a response equivalent to the absorbed dose in water. For 100 kV_p X-ray, the OP-10 response could not be fully corrected because the R_2 / R_1 gave a value is 0.72, which is outside the viable ratio as discussed above. However, because the over-response of R_1 in the OP-10 was small for 100 kV_p X-ray spectrum, the observed OP-10 over-response was likewise small. The problem could be even less pronounced in ionising-radiation accidents and military situations, where the photon spectra are smoother and have a broader energy range.

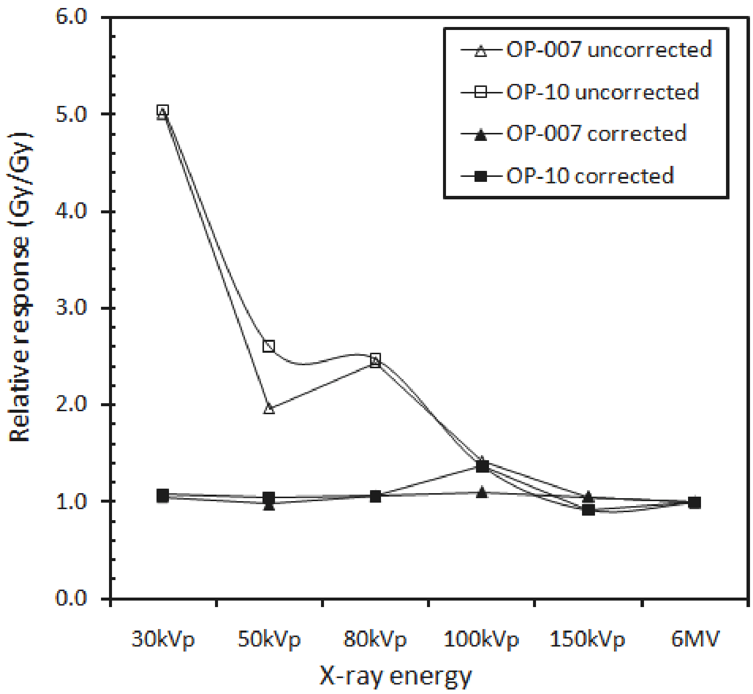

Figure 4.8: The relative response to water for corrected and uncorrected readings of OP-007 and OP-10 packaging after normalisation to a 6 MV spectrum.

4. 4 Discussion

The ratio of the responses of the two chips (one filtered, the other unfiltered) in a dual-MOSFET chips depends on the photon spectra. This allows for correction of the R_1 over-response to low-energy photons based on the ratio of the response of the two MOSFETs. The application of a correction factor derived from mono-energetic photon energy to poly-energetic photon spectra yielded promising results.

It must be stressed that this is purely a theoretical simulation of the MOSFET response, and does not take into account the characteristics of the detectors' readout electronics, the absolute sensitivity of the MOSFET affecting by frequency of readout and calibration measurements or the effects of electron-hole recombination [149]. Also, the dependence of the new packaging to the orientation of the incident photons will be investigated in a future study. It is expected that these results will be validated using a prototype dosimeter on different static and pulsed photon sources.

4. 5 Conclusion

This study presents a novel packaging of MOSFET detector based on a CMRP "*drop-in*" packaging design of radiation sensors and a correction algorithm, to make the response of MOSFET dosimeters in free-air geometry equivalent to absorbed dose in water and energy-independent for a photon-energy range of 15 keV to 2 MeV. Construction of the MOSFET-based photon dosimeter consists of dual-MOSFET chips embedded in a Kapton and graphite casing, with lead, aluminium and graphite filters on one MOSFET chip: dual-MOSFET optimised package filtered (DOPF) dosimeter. This approach was used for skin dosimetry at an equivalent depth of water at 0.07 mm (DOPF-007) and 10 mm (DOPF-10). Filtering one of the chips provides two distinctive photon-energy regions in the energy responses of both filtered and unfiltered dual-MOSFETs in DOPF packages.

This approach is in contrast to passively filtering a single MOSFET (Chapter 3), which enabled spectroscopy probing of incident photon radiation based on a comparison of the responses of both MOSFETs in DOPF packages, and to introduce an algorithm for correcting the response of unfiltered MOSFET that makes an energy-independent DOPF dosimeter in a photon-energy range of 15 keV to 2 MeV.

Both the DOPF-007 and DOPF-10 dosimeters responded in free-air geometry under normal incidence of photon radiation proportional to $D_w(0.07)$ and $D_w(10)$, respectively.

In an effort to prove the validity of the developed approach and algorithm, a MOSFET response was simulated for the energy spectrum of photons from an X-ray machine and a medical LINAC. The X-ray energy spectra chosen here were from 30 kV_p to 150 kV_p, the photon-energy range where the greatest over-response of MOSFET is observed. Response to a 6 MV medical LINAC spectrum was also simulated as a reference point for normalisation of the response for the field just mentioned. The correction algorithm was used to simulated the responses of the dual-MOSFETs in these spectral photon fields and demonstrated an almost energy-independent response for the DOPF-007 and DOPF-10 dosimeters relative to corresponding doses in water on the 6 MV LINAC.

These packages of dual-MOSFET detector were small and gave an energy-independent response to poly-energetic photon spectra. They are ideal for personnel accident and military dosimeters with applications in an unknown photon-spectrum field. Their advantage is that they can work in passive or active mode and can be read in real time without deterioration of information on accumulated static- or pulsed-photon doses.

Most accident or military scenarios involve a mixed gamma–neutron radiation field where dosimetry of neutron components from a mixed-radiation field is important. In Chapter 5, a pixelated silicon detector is studied with aim of developing a fast-neutron dosimeter whose response is independent of the energy of incident neutrons, and is gamma-insensitive.

CHAPTER 5

MEDIPIX2 AS A NEUTRON DOSIMETER

5. 1 Introduction to methods

This chapter presents the application of the Medipix2 for fast-neutron dosimetry using a newly developed segmented, multiple-thickness, polyethylene converter. This system has the ability to provide an energy-independent response to measure a dose equivalent of fast neutrons in a range of neutron energy from 0.3 to 15 MeV. The application of partial weighting factors to the response of a detector driven by a polyethylene converter of a particular thickness enables the total response of the detector system for fast-neutron dosimetry to be flattened. Six segments of polyethylene converter having their thicknesses and weighting factors optimised, is used to obtain the required response for an energy-independent detector. A GEANT4 suitability study for neutron dosimetry with respect to a previously published work was performed first.

This study presented a solution to the limitations encountered by single readout detector with a polyethylene converter, as described in Section 1.4.4. The configuration of a fragment of multi-thickness polyethylene converter placed above the Medipix2 detector is shown in Figure 5.1. The advantage of this detector system for neutron dosimetry lies in its ability to independently read out different segments of pixels corresponding to different thicknesses of PE. The areas of *i*-th segment of the Medipix2 detector that has a polyethylene over-layer are denoted by R_i. A segment of bare silicon is denoted by R_0.

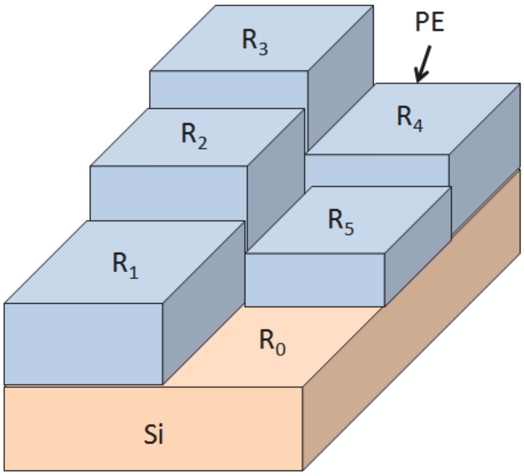

Figure 5.1: Fragment of the segmented silicon detector with polyethylene convectors of different thickness. Multiple thicknesses of polyethylene on a silicon surface provide the freedom to adjust the energy response of the silicon detector as required and to achieve an independent response to the energy of the neutron-dose equivalent. R_i is a segment with the converter thickness-*i*, and the uncovered segment is denoted by R_0.

Detecting lower energy neutrons at ~ 0.3 MeV means that the discriminator value of the threshold must be lowered, which in turn increases the relative contribution from inelastic neutron interaction and gamma background events in silicon, as discussed in Section 1.4.3. This means avoiding the events associated with direct interaction of gamma and neutron with silicon (background response), and only counting true events of the elastically scattered protons from the polyethylene convertor. This was achieved by subtracting the scaled background response of segment R_o (denoted as $R_{\Phi,0}$) from the response of each of the segments R_i (denoted as $R'_{\Phi,i}$) to obtain only the recoil-proton component. This allows for the counts produced by the gamma-ray component of the field and *Si(n,alpha)* and *Si(n,proton)* interactions to be eliminated. The recoil-proton counts can be expressed as in Equation (5.1).

$$R_{\Phi,i} = \left(R'_{\Phi,i} - \left(\frac{A_i}{A_0}\right) R_{\Phi,0}\right) / \Phi_{\mathrm{n}} \tag{5.1}$$

where $R_{\Phi,i}$ is the proton counts per neutron fluence, $R'_{\Phi,i}$ is the readout counts from a segment with a polyethylene thickness i, $R_{\Phi,0}$ is the readout counts from the uncovered segment, A_i is the area of the segment with a thickness i and A_0 is the area of the uncovered segment. Φ_n is the primary neutron fluence.

A GEANT4 9.2.p01 release was used in this study, and the QGSP_BIC_HP physics list provided within this release was adopted. A GEANT4 application was developed to characterise the neutron dosimeter.

5.1.1 *Verification of GEANT4 and simulations with a uniform polyethylene converter*

First, a GEANT4 study addressed to reproduce the Eisen *et al.* work [117] discussed in Section 1.4.4, was performed to benchmark GEANT4 for neutron dosimetry [150] as a part of an ongoing validation of GEANT4 with respect to in-house experimental measurements, in order to quantify its accuracy for neutron dosimetry. The word "verify" in our case is to check the agreement between a Monte Carlo simulation and analytical calculation.

A simple simulation to verify methods describing Equation (5.1) was performed using a 300 µm-thick silicon slab irradiated with a mono-energetic neutron beam with an energy of 0.3 to 15 MeV, as shown in Figure 5.2. The parallel primary mono-energetic neutron beam of 10^8 incident neutrons was simulated. The secondary production threshold was set to 0.01 MeV. The simulation was first run to get the total number of interactions from the 1 cm^2 cross-section of bare silicon slab. Then a series of simulations was conducted for the silicon slab covered with 0.01, 0.1, and 1 mm-thick polyethylene over-layers to simultaneously find the total number of interaction in the silicon slab and the counts of recoil protons for each thickness of PE. The number of counts in a detector due to the recoil protons only was then derived by the subtraction method as described in Equation (5.1), and from tracking the recoil protons produced in the polyethylene converter that entered the silicon slab.

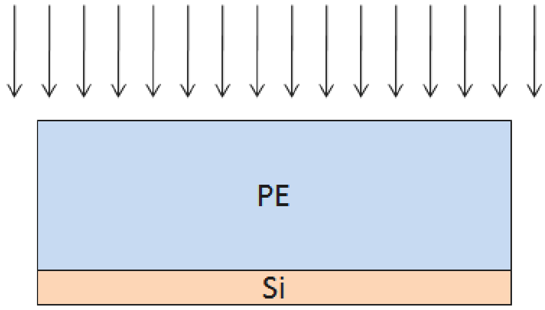

Figure 5.2: The polyethylene convertor (PE)-silicon detector setup used to verify the simulation by comparing the subtraction method and direct recoil proton tracking in GEANT4 code.

5.1.2 *Simulation with a structured polyethylene converter*

Medipix2 was modelled as a silicon substrate with a thickness equal to 300 μm and an area equal to 14 x 14 mm^2. 256 x 256 sensitive volume cells were defined across the surface area corresponding to the design of the Medipix2 system. The pixels were clustered into 25 segments, each with ~ 3 x 3 mm^2 cross-sectional areas. A dead layer on the surface of the silicon detector of several microns was not modelled in the simulation because there was no detailed technical information available. The polyethylene layer consisted of six different thicknesses occupying four of the segments, with different areas, as depicted in Figure 5.3. Parallel mono-energetic neutron beams with energy from 0.3 to 15 MeV normally incident on the detector surface, were simulated. Whenever an energy-deposition event occurred in a segment with energy greater than 6 keV, it was counted as a single event. To reduce the cross-talk between adjacent segments, each readout area was defined as smaller than the total segment area, as shown in Figure 5.3. The proton count per neutron fluence was obtained using Equation (5.1).

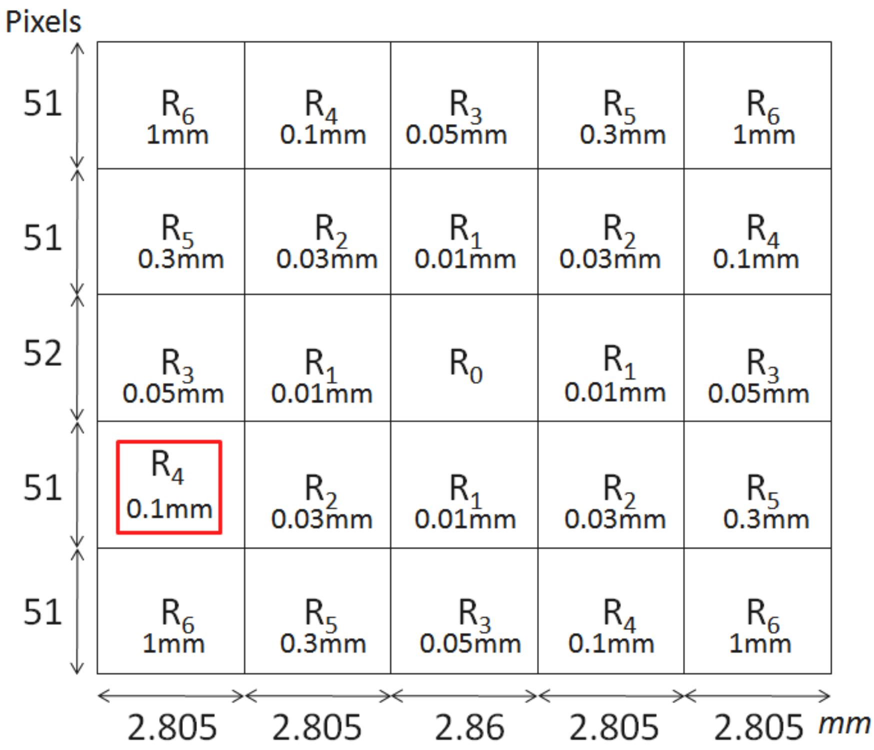

Figure 5.3: Arrangement of different thicknesses of polyethylene converter on the Medipix2 surface. Polyethylene thicknesses of 0.01, 0.03, 0.05, 0.1, 0.3 and 1 mm were used, and labelled as R_1, R_2, R_3, R_4, R_5 and R_6 respectively. R_0 was the uncovered area used to subtract background events associated with gamma-rays and direct neutron interactions with the silicon nuclei. The red box shows the possibility of scaling the readout segment area to reduce cross-talk between the segments.

5. 2 Results and discussions

5.2.1 *Verification of GEANT4 and results of simulation with a uniform polyethylene converter*

Figure 5.4 shows the analytically simulated response of the single silicon detector covered by different thicknesses of polyethylene in terms of the number of recoil protons per mSv of neutrons detected in an energy range 1 MeV to 15 MeV by Eisen *et al.* [150]. The NCRP fluence-to-dose equivalent conversion coefficient [151] was used here by the authors. Eisen *et al.*'s data were extracted from a figure in their paper using *xyExtract* graph digitiser software version 4.1. Simulated responses of the same silicon detector – a uniform polyethylene converter setup using the GEANT4 tool kit – confirmed the GEANT4 model for such simulations.

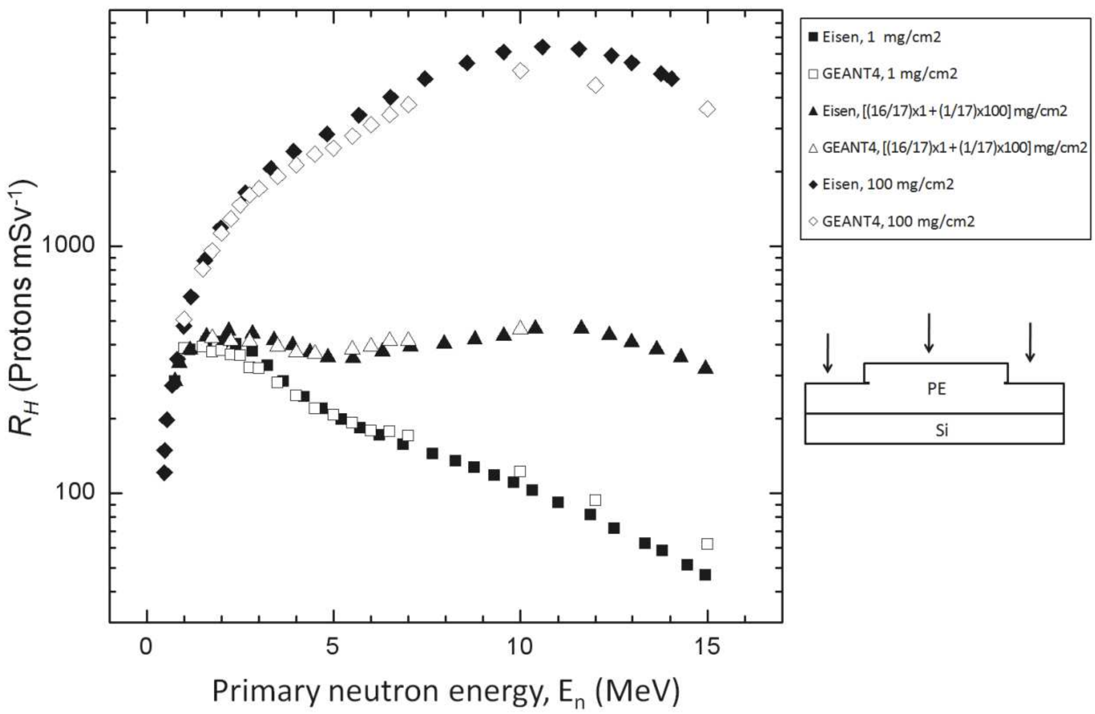

Figure 5.4: A previous study by Eisen *et al.*, using two different thicknesses of polyethylene converter of different areas on a silicon detector showed how the energy response R_H flattened in comparison to a single thickness of the converter [150]. The results were in good agreement with the GEANT4 simulations.

Figure 5.5 shows the simulated count response of a silicon detector covered by polyethylene with different thicknesses using the subtraction method as in Equation (5.1). Very good agreement in absolute count response for each thickness of polyethylene for a wide neutron-energy range provides confidence in the subtraction method for obtaining counts associated with recoil protons only.

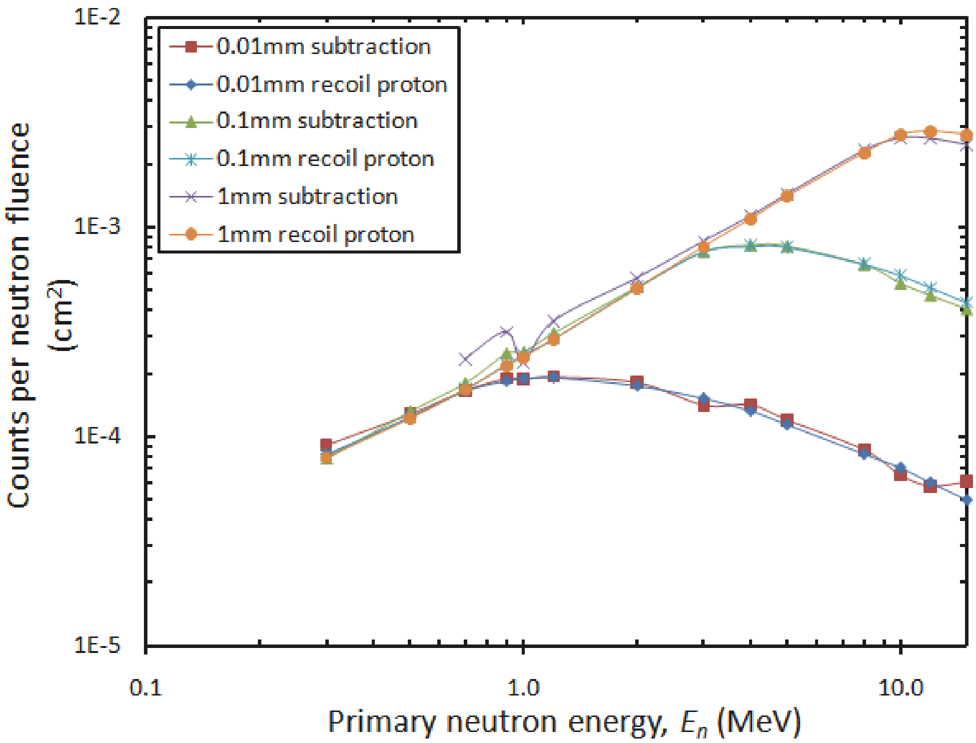

Figure 5.5: The comparisons between counts from the subtraction method and from tracking the proton recoils for different mono-energetic neutron energies.

5.2.2 *Results of simulation with a structured polyethylene converter*

Figure 5.6 shows the response of the detector, including a direct interaction of neutrons with silicon in counts per unit neutron fluence as a function of neutron energy for each thickness of polyethylene segment (Figure 5.3). The results in Figure 5.6 were for a defined gap of 16 pixels between adjacent segments, which corresponds to a gap 0.88 mm-wide for a Medipix2 detector. The introduced gap reduced the total polyethylene covered segmented area of 198 mm^2 to 141 mm^2. The response of the detector in the absence of the polyethylene-converter layer, the R_o, was not subtracted from the response of the detector for segments with a polyethylene-converter layer, R_i. For neutron energies below 1 MeV the response of the detector for polyethylene-converter segments was dominated by the background counts: i.e., direct neutron interactions with the silicon nuclei. At neutron energies from 1 to 15 MeV, and the thicknesses of converter layer from 0.01 to 0.1 mm, there was a non-negligible contribution of background counts. Only for neutron energies above 5 MeV and thicknesses of the converter greater than 0.3 mm did the number of counts begin to exceed the background component.

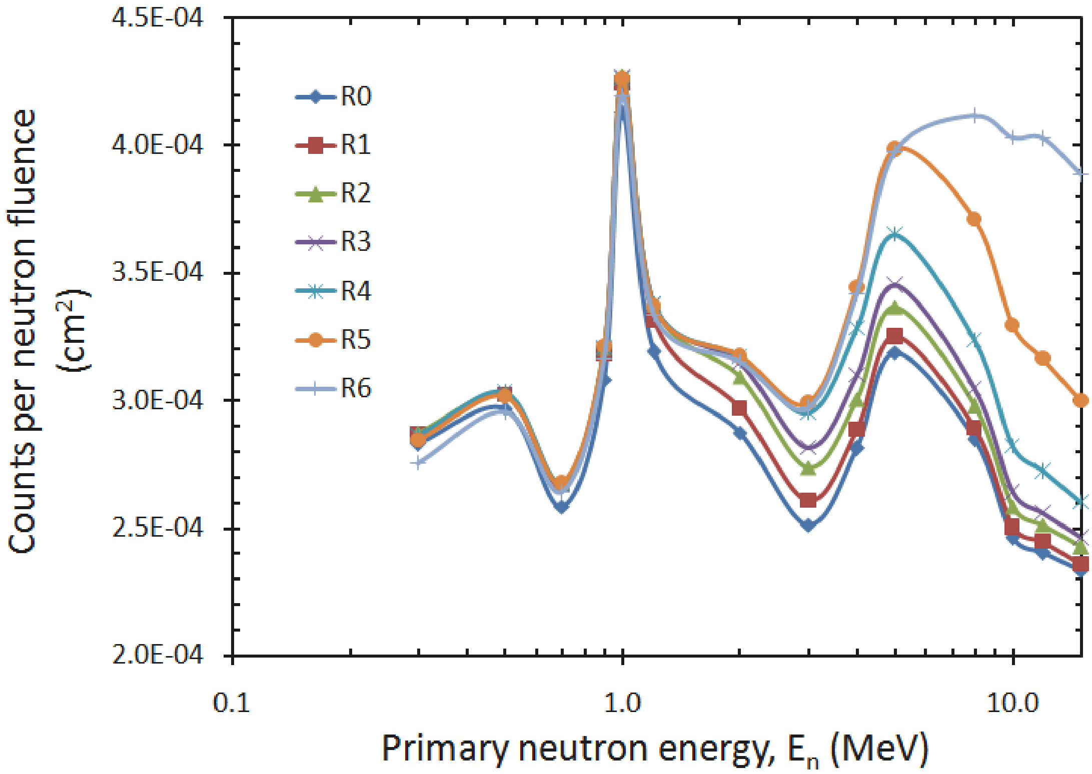

Figure 5.6: Counts per unit neutron fluence for each thickness of polyethylene converter as a function of neutron energy. The response of uncovered pixel R_0 is also shown. The results are for a gap of 0.88 mm between the segments.

Figure 5.7 shows the response of the detector for structured segments of polyethylene converter with different thicknesses from only those recoil-proton events that resulted in direct interaction of neutrons with the converter. This was achieved by subtracting background events due to inelastic interaction of neutrons with silicon according to Equation (5.1). For the 1 mm-thick polyethylene converter, the proton counts per fluence yielded a negative value (not shown in the logarithmic axis of Figure 5.7) after applying Equation (5.1) for energy below 0.7 MeV; this agrees with the results in Figure 5.6, which show a significant absorption for the lower-energy neutrons. Also shown in Figure 5.7 is the ICRP 74 [3] fluence-to-dose equivalent conversion coefficients (black line). As shown, the response of any single detector segment does not adequately fit the ICRP 74 dose-conversion coefficients; this confirms that no single thickness of polyethylene converter can be used to achieve an energy-independent neutron-dose equivalent detector based on silicon.

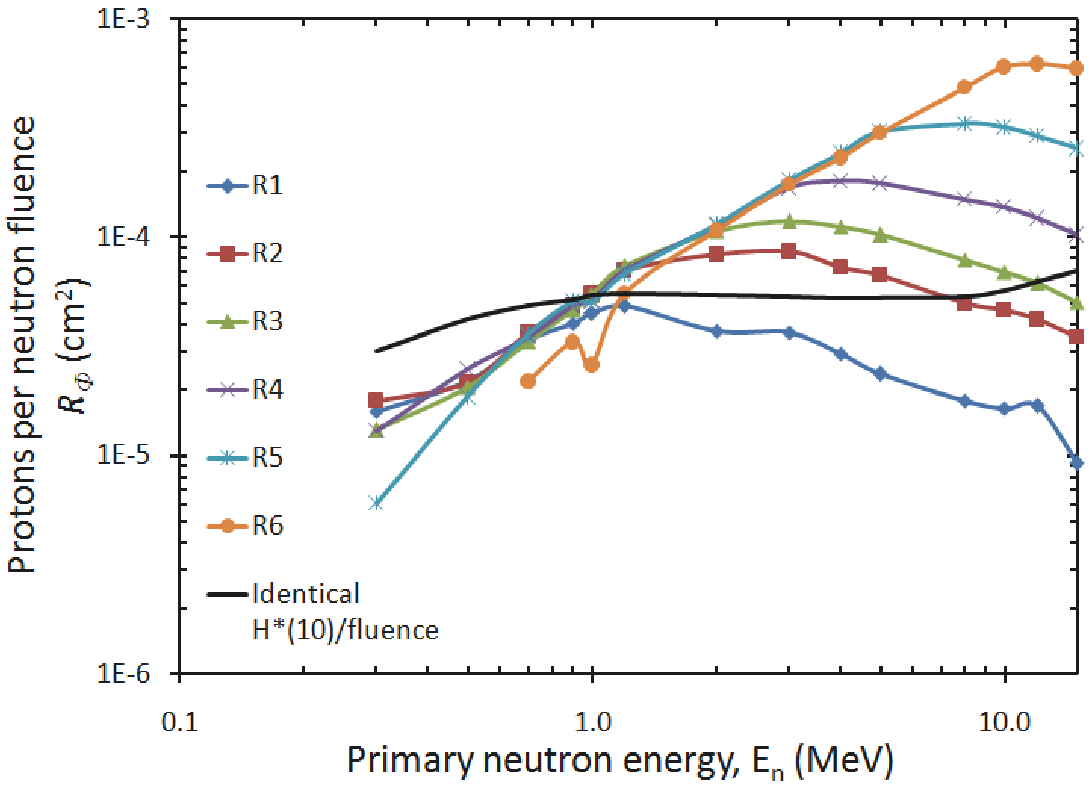

Figure 5.7: The proton-event counts per unit neutron fluence for different thicknesses of polyethylene converter as a function of neutron energy after using the subtraction method. The black line shows the fluence-dose equivalent conversion coefficients taken from ICRP 74, but not to scale. The results are for a gap of 0.88 mm between the segments.

Figure 5.8 shows the detailed response for each thickness of polyethylene after applying Equation (5.1) for the gap between the segments, which varied from 0 to 0.88

mm. It is obvious that increasing the gap between detector segments R_i reduces the readout area, and therefore the number of counts due to recoil protons.

It is worth mentioning that the net response of the particular segment not only depends on the area of the readout region, but also on the cross-talk from neighbouring segments. Additionally, cross-talk depends on the polyethylene thickness of a neighbouring segment and should be taken into account when optimising the readout region. The possibility of electronically reducing the readout region is a very convenient design feature of the pixelated-detector approach, and can be used to avoid cross-talk.

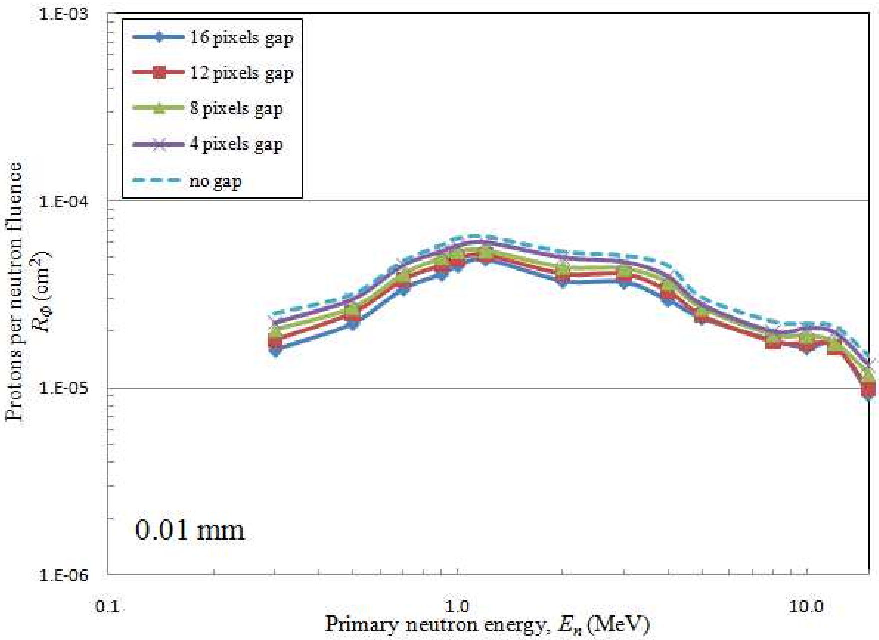

(a)

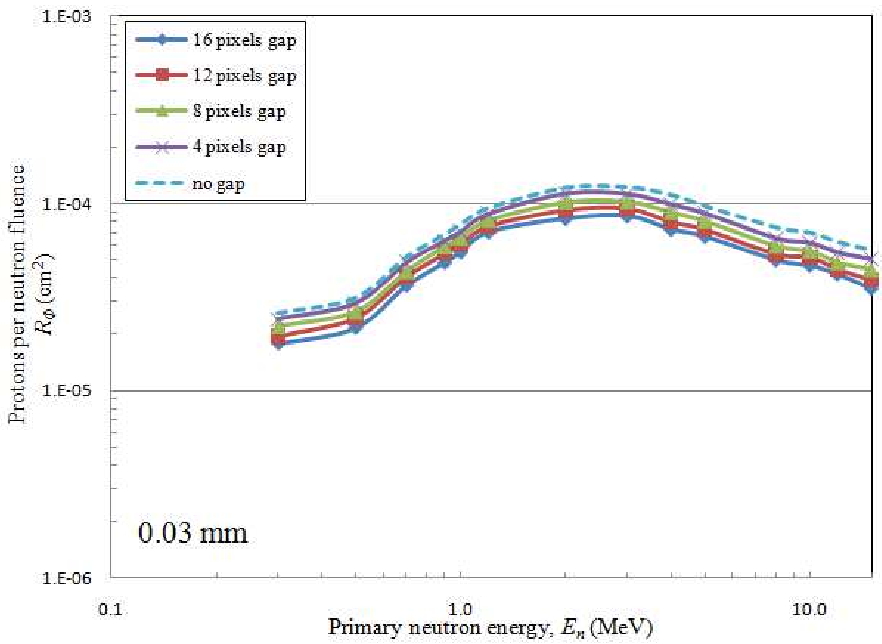
1.E-03
1.E-04
1.E-05
1.E-06
0.1
1.0
10.0
16 pixels gap
12 pixels gap
8 pixels gap
4 pixels gap
no gap
0.03 mm
Protons per neutron fluence
R_ϕ (cm^2)
Primary neutron energy, E_n (MeV)

(b)

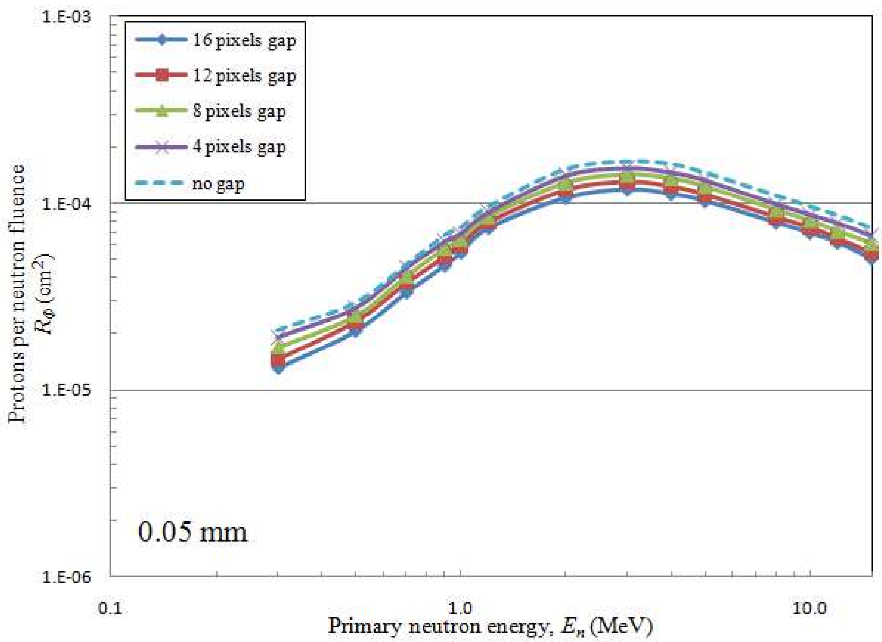
1.E-03
1.E-04
1.E-05
1.E-06
0.1
1.0
10.0
16 pixels gap
12 pixels gap
8 pixels gap
4 pixels gap
no gap
0.05 mm
Protons per neutron fluence
R_ϕ (cm^2)
Primary neutron energy, E_n (MeV)

(c)

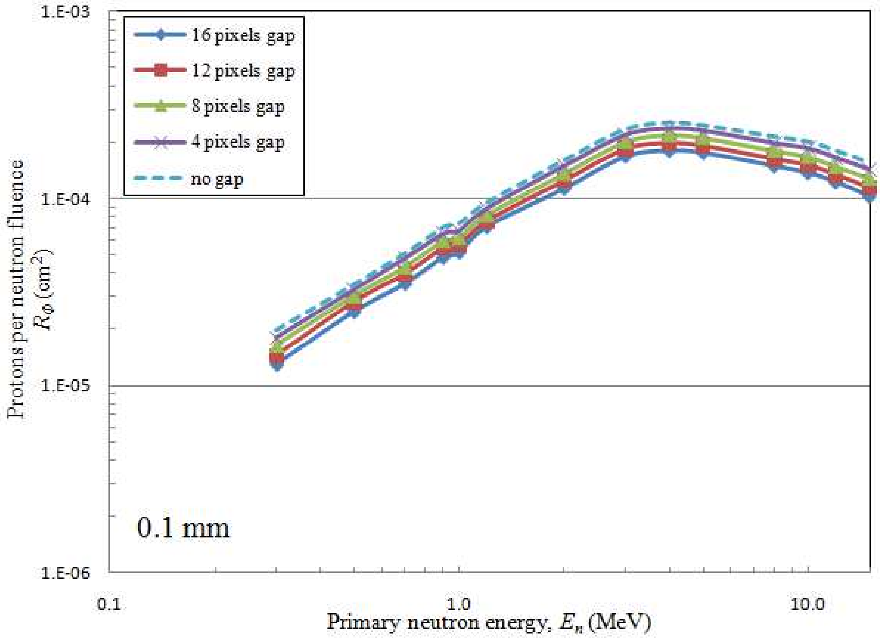

1.E-03
1.E-04
1.E-05
1.E-06
0.1
1.0
10.0
16 pixels gap
12 pixels gap
8 pixels gap
4 pixels gap
no gap
0.1 mm
Protons per neutron fluence
R_ϕ (cm^2)
Primary neutron energy, E_n (MeV)

(d)

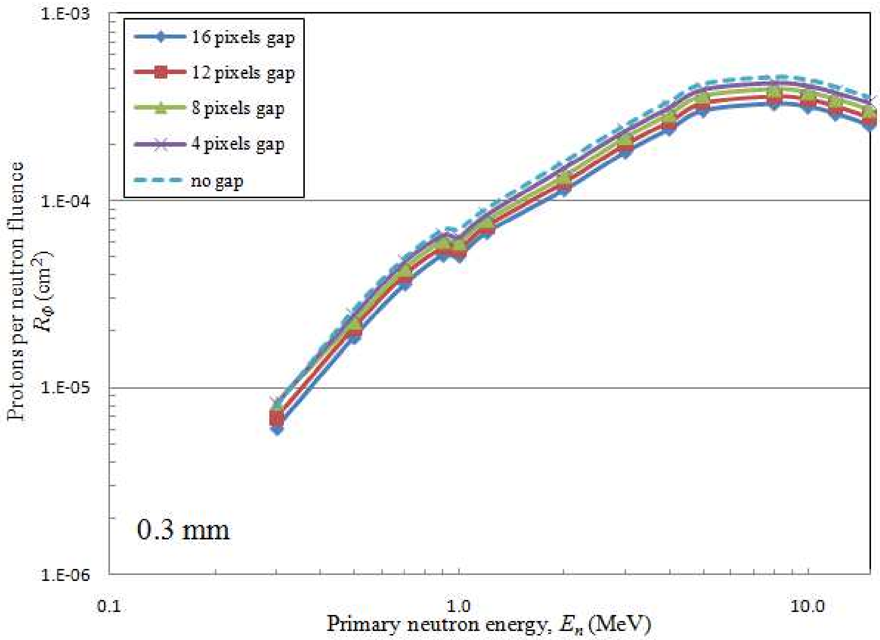

1.E-03
1.E-04
1.E-05
1.E-06
0.1
1.0
10.0
16 pixels gap
12 pixels gap
8 pixels gap
4 pixels gap
no gap
0.3 mm
Protons per neutron fluence
R_ϕ (cm^2)
Primary neutron energy, E_n (MeV)

(e)

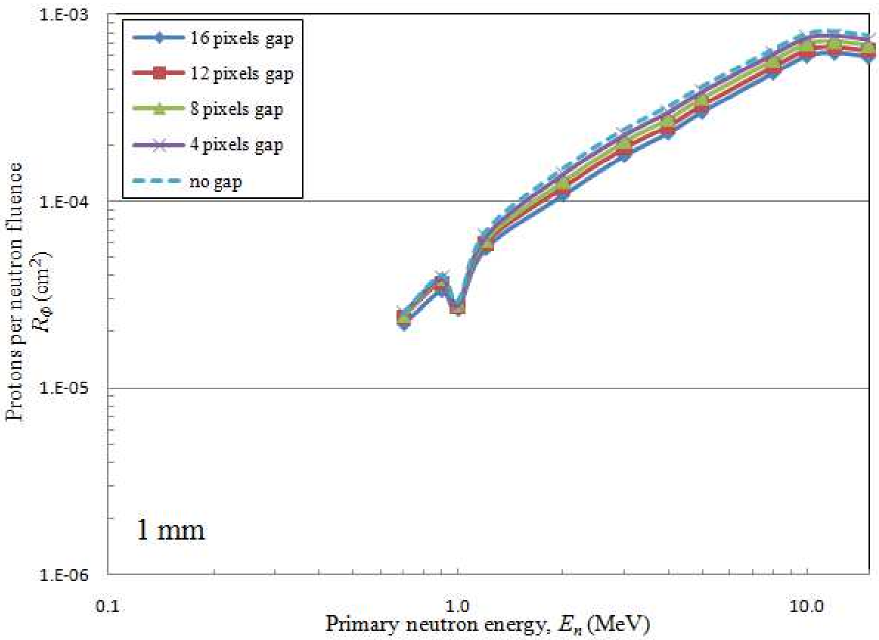

(f)

Figure 5.8: The net response of segments per unit neutron fluence for each thickness of polyethylene converter under different specified gaps between the adjacent segments. The thicknesses of polyethylene are: (a) 0.01 mm, (b) 0.03 mm, (c) 0.05, (d) 0.1 mm, (e) 0.3 mm and (f) 1 mm.

Optimisation was performed by taking into account the total response, $R_{\Phi,total}$, from all polyethylene thicknesses such that the $R_{\Phi,total}$ response was proportional with the ICRP 74 fluence to ambient dose equivalent conversion coefficients, H^*/Φ . The optimisation function for $R_{\Phi,total}$ is defined in Equation (5.2).

$$R_{\Phi,total}(E) = \sum_{i=1}^{9} \beta_{\Phi,i} R_{\Phi,i}(E) \tag{5.2}$$

where $R_{\Phi,1}$ to $R_{\Phi,6}$ are the responses of the proton counts from pixels covered by polyethylene of different thickness (shown in Figure 5.7) and $R_{\Phi,7}$ to $R_{\Phi,9}$ are the virtual responses given by Equation (5.3).

$$R_{\Phi,7} = \left(\frac{R_{\Phi,5}}{R_{\Phi,4}}\right) R_{\Phi,1}\,, R_{\Phi,8} = \left(\frac{R_{\Phi,4}}{R_{\Phi,3}}\right) R_{\Phi,2}\,, R_{\Phi,9} = \left(\frac{R_{\Phi,2}}{R_{\Phi,3}}\right) R_{\Phi,6} \qquad (5.3)$$

The $\beta_{\Phi,i}$ are the weighting factors for each partial response. Nine $\beta_{\Phi,i}$ can be found, giving $R_{\Phi,total}$ (E) $\propto$ $[H^*/\Phi](E)$ by solving nine simultaneous linear equations at nine neutron energies. The energies selected were 0.3, 0.7, 1, 2, 3, 4, 5, 8 and 15 MeV. The optimisation of $\beta_{\Phi,i}$ results are 5.984, -6.652, 4.826, -2.437, 0.598, -0.593, -2.89, 1.938 and 0.898 for i from 1 to 9 respectively, as shown in Equation (5.4).

$$\begin{aligned} R_{\Phi,total}(E) = {} & 5.984R_{\Phi,1}(E) - 6.652R_{\Phi,2}(E) + 4.826R_{\Phi,3}(E) \\ & - 2.437R_{\Phi,4}(E) + 0.598R_{\Phi,5}(E) - 0.593R_{\Phi,6}(E) \\ & - 2.89R_{\Phi,7}(E) + 1.938R_{\Phi,8}(E) + 0.898R_{\Phi,9}(E) \end{aligned} \qquad (5.4)$$

Hence, the recoil-proton response per mSv was obtained from Equation (5.5).

$$R_H = \frac{R_{\Phi,total}(E)}{[H^*/\Phi](E)} \qquad (5.5)$$

Figure 5.9 shows that the final response of the detector as a function of neutron energy is reasonably uniform from 0.3 to 15 MeV, as desired. The average response of the detector in terms of the proton count rate was found to be 115±10 per mSv of ambient dose equivalent of neutron.

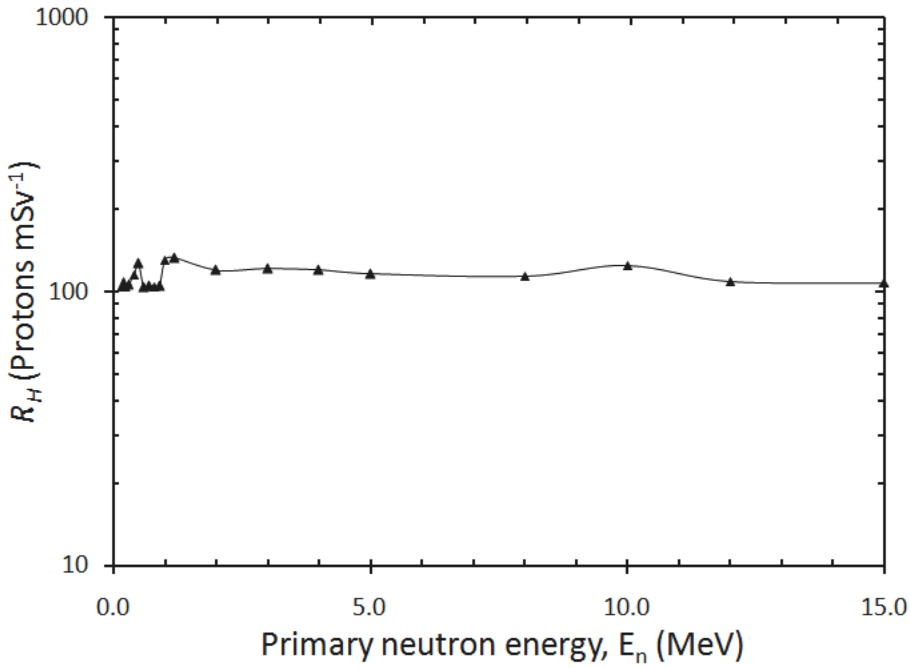

Figure 5.9: The response of the Medipix2 detector to the ambient dose equivalent of neutrons, using a multi-thickness layered converter as a function of neutron energy, was reasonably uniform from 0.3 to 15 MeV.

5. 3 Conclusion

A GEANT4 simulation study was performed to investigate a novel approach to neutron dosimetry using a multi-thickness polyethylene converter and a multi-channel readout detector. The suitability of GEANT4 for neutron dosimetry was verified with respect to previously published data. This study showed that this novel device can be used to produce an energy-independent response over a range of neutron energies from 0.3 MeV to 15 MeV. The improved response of this detector was within 115±10 counts per mSv of the ambient-dose equivalent of neutron for energy considered here.

Chapter 6, describes the experiments conducted on fast neutrons to validate this simulation study of the novel neutron dosimeter based on the Medipix2. There were two experiments: one validating the subtraction methods of Equation (5.1) and the other validating the optimisation method described by Equation (5.2).

CHAPTER 6

EXPERIMENTAL VALIDATION OF THE NOVEL MEDIPIX2 NEUTRON DOSIMETER

6. 1 Introduction

This chapter describes the experimental validation of the novel Medipix2 neutron dosimeter. Two experiments were performed to validate the simulation concepts introduced in Chapter 5. The word "validate" in our case involved comparing the Monte Carlo simulation and the proposed subtraction method for fast-neutron dosimeter to a set of experimental data.

The first experiment was to validate the subtraction method described in Section 5. 1 and used to get the number of proton recoils. In that section the subtraction method was initially verified by a simulated tracking of the proton recoils from the polyethylene over-layer (Figure 5.5).

There are reports on the possibility of directly counting the charged particles through the Medipix2 image output by looking at the shape of the pixel clusters [2, 99, 152-157]. A cluster of pixels in the Medipix2 detector is a pattern of charge collection in neighbouring pixels that depends on the LET and type of charged particle, and charge-sharing between pixels. Each particle has its own signature; for example, protons can simultaneously affect three to five pixels, alpha and heavy charged particles produce high-density ionisation that spreads to form a larger cluster and Compton electrons, which produce lower-density ionisation, can deposite energy in many pixels to form a cluster resembling a curly line. This method was believed to be able to differentiate the type of incident charged particles, but there were some ambiguities in determining the exact types of particles by referring to the shapes of the cluster. To get a good statistical confidence level with this method would require analysing a higher number of events compared to using the subtraction method, because the shapes of the clusters depend on many factors such as bias voltage, shutter time, sensor thickness, threshold setting, particle types, incident angle, overlapping clusters and dead pixels. Additionally, the data-processing time increases for a large number of events and when cluster shapes are complex (thus the algorithm for analysing cluster shapes). Analysing the shapes of the clusters increases the detector dead time considerably for real-time dosimetry applications. Thus the subtraction method is favoured in this fast-neutron dosimetry study because it depends less on cluster shapes.

The second experiment was aimed at a more realistic validation of the multi-thickness polyethylene converter on the Medipix2 sensor. The exact experimental setup of the detector geometry was modelled in GEANT4, and the results of the simulation were compared to the experimental results.

6. 2 Validating the subtraction method

For validation purposes, the response of a simplified detector set up with a uniform polyethylene converter to neutrons, exposed to a D-T generator and an Am-Be sources, was modelled through a GEANT4 simulation.

Figure 6.1 shows the experimental set-up of the Medipix2 detector. A significant issue for a neutron dosimeter is the evaluation of the neutron events while separating the background radiation generated, for example, by recoil products of inelastic reactions, silicon atoms, alphas, gammas and electrons. The use of a large-area and high-density pixelated detector such as a Medipix2 (with a cross-section equal to 14 x 14 mm^2 and 65536 pixels) addresses this issue by enabling the separate examination of two distinct portions of the sensitive areas. Thus the Medipix2 detector is only partially covered with a uniform layer of polyethylene converter, noted as SV1 (the proton window), with the remainder left uncovered, noted as SV2 (the background window). This structure was modelled in the GEANT4 simulations.

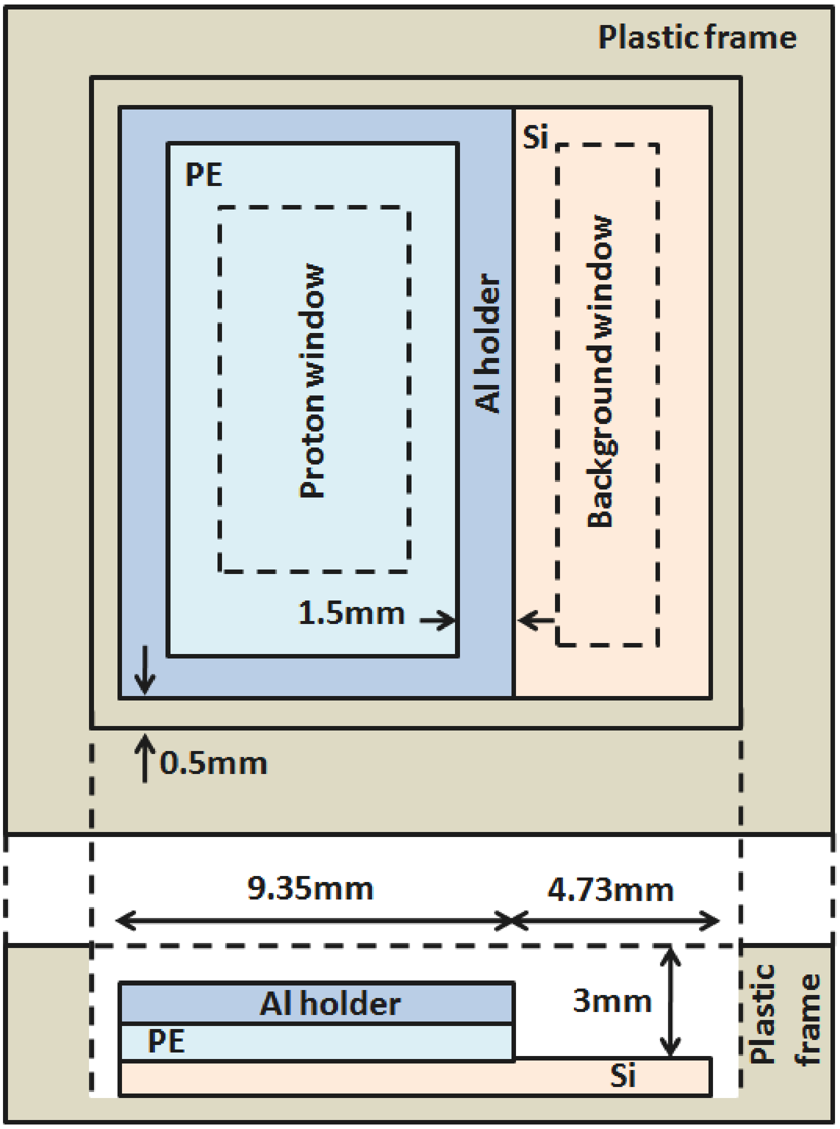

Figure 6.1: The Medipix2 with a partial polyethylene converter on top of the silicon sensor and an uncovered area modelled with GEANT4 (front and side views).

Experiments were carried out on 14 MeV D-T and Am-Be neutron sources at Australia's Commonwealth Scientific and Industrial Research Organisation (CSIRO) in collaboration with Dr. Marco Petasecca and Dr. Joseph Uher. The device was irradiated with 14 MeV neutrons from a D-T generator Thermo A-3062. The distance between the D-T generator and the detector was 55 cm. The emission rate of the D-T generator was 8.6 x 10^7 n/s into the full solid angle, thus the intensity of the neutron at the tested detector (area of 1.4 x 1.4 cm^2) was calculated at 2100 n/s. The emission rate of the D-T generator was estimated using a 2 x 2 x 2 cm^3 plastic scintillator (EJ 204) attached to a photomultiplier (Photonis XP2020). A detection efficiency of 3.9% of the scintillator for 14 MeV neutrons was approximated by an analytical calculation. The measured neutron flux was in good agreement with the calculated figure.

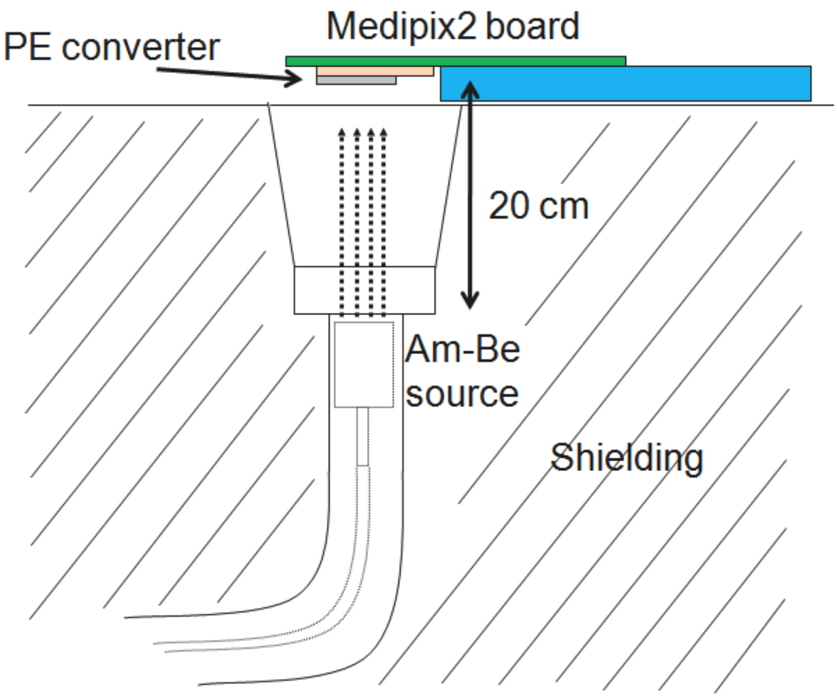

Figure 6.2: Irradiation setup on an Am-Be neutron source.

Figure 6.2 shows the irradiation set up on the Am-Be neutron source. The Medipix2 detector was placed on top of the collimator of the Am-Be neutron source container, but 20 cm away from the source when in the irradiation position. The polyethylene converter attached to the silicon sensor was faced down normally to the neutron beam. The emission of neutrons in 4π was 9.3 x 10^6 n/s calculated based on the activity of the source on the day of the experiment. When not in use the neutron source was kept in boronated paraffin shielding.

The physical construction of the layers of the polyethylene converter on the Medipix2 detector was as shown in Figure 6.1. The polyethylene converter occupied two-thirds of the active area of the detector, while the remainder was left uncovered to enable the background to be estimated. A 9 x 14 x 1 mm^3 square aluminium frame was used to hold the polyethylene layer attached to the surface of the detector to minimise the air gap and any misalignment between the converter and the silicon substrate. Four thicknesses of polyethylene were used during irradiation with the neutron sources. The polyethylene converters were 0.1, 0.25, 0.5 and 1 mm-thick.

The detector was placed immediately in front of the neutron source window for both fields, with the neutrons normally incident to the sensor surface. The experiment was repeated for each thickness of polyethylene using the same Medipix2 detector with the same neutron fluence and geometry of experiment. The data acquisition was based on a USB interface readout by the Pixelman software developed by the Medipix collaboration; this software provides several analyses and setting tools for use during data acquisition and post-processing. During the acquisition, the parameters were set to retrieve all data from the entire sensitive area of the chip. The data were later analysed using a C++ programming code that extracted the counts for the two defined readout regions.

The Medipix2 detector was modelled as a 14.08 x 14.08 x 0.3 mm^3 silicon sensor with 256 x 256 sensitive volumes, each with size of 0.055 x 0.055 x 0.3 mm^3. The ASIC chip beneath the silicon sensor was modelled as a 14.08 x 14.08 x 1.5 mm^3 silicon slab. The polyethylene converter was modelled as a polyethylene slab 0.1, 0.25, 0.5 and 1 mm-thick, each with a cross-section of 9.35 x 14.08 mm^2. The aluminium holder surrounding the polyethylene converter was engineered to ensure that the converter was rigid and flat, and to minimise air gaps between the polyethylene converter and the silicon surface.

The neutrons were generated as a parallel beam incident normally to the detector. The energy of the neutrons from a simulated D-T source was modelled with a Gaussian distribution, with a mean value of 14 MeV and one standard deviation of 0.01 MeV and 0.5 MeV. The energy of the neutrons of the Am-Be-source was modelled with the energy spectrum recommended in [158].

The QGSP_BIC_HP physics list that came with the GEANT4 version 9.2 patch p01 was used. The threshold of production of secondary particles was fixed equal to 5 μm in range within the sensitive regions SV1 and SV2. To reduce the execution times of the simulation without affecting the accuracy of the simulation results, the threshold was set higher outside regions SV1 and SV2.

6. 3 Results and discussion of the subtraction method

Figure 6.3 shows events from a particular frame under D-T neutron irradiation: events from proton recoils and inelastic reactions that created a rounded cluster with pixels > 7. The energetic secondary electrons also have pixels with a cluster > 7, but the electron tracks are thin lines. Figure 6.4 shows ambiguous events of proton recoils and two events overlapping. The overlapping events were easily detected using the subtraction method of analysis by looking at the output data: the pixels that were overlapped had a logic number of 2, instead of 0 for no event or 1 for one event.

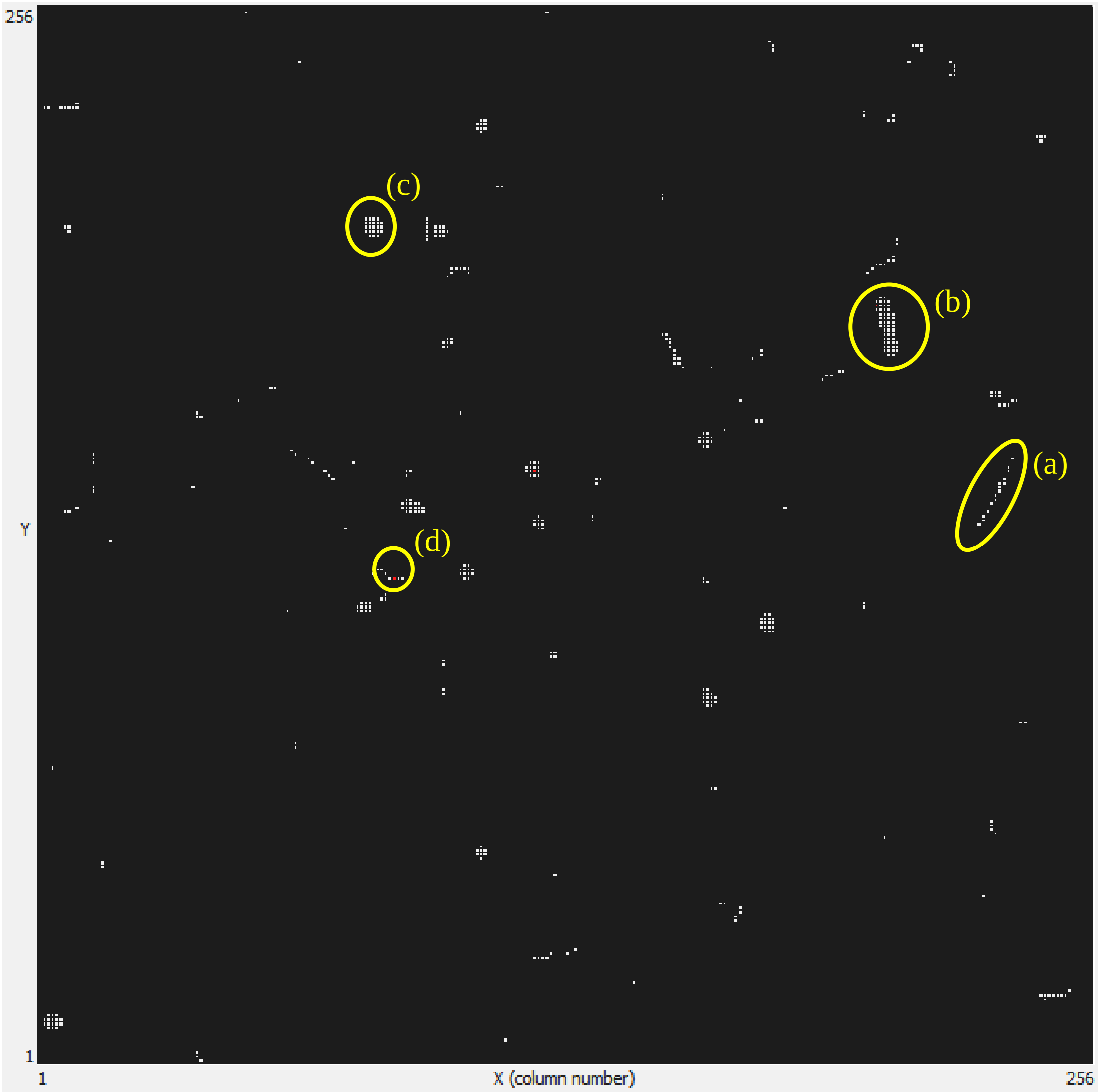

Figure 6.3: Events from a particular frame under D-T neutron irradiation. Small dots or a small cluster of pixels (< 7 pixels) are the low-energy gamma interactions, (a) is a high-energy secondary electron, (b) is a proton recoil that entered the silicon sensor at some angle, (c) is an inelastic reaction and (d) is low-energy secondary electrons (short, curly lines).

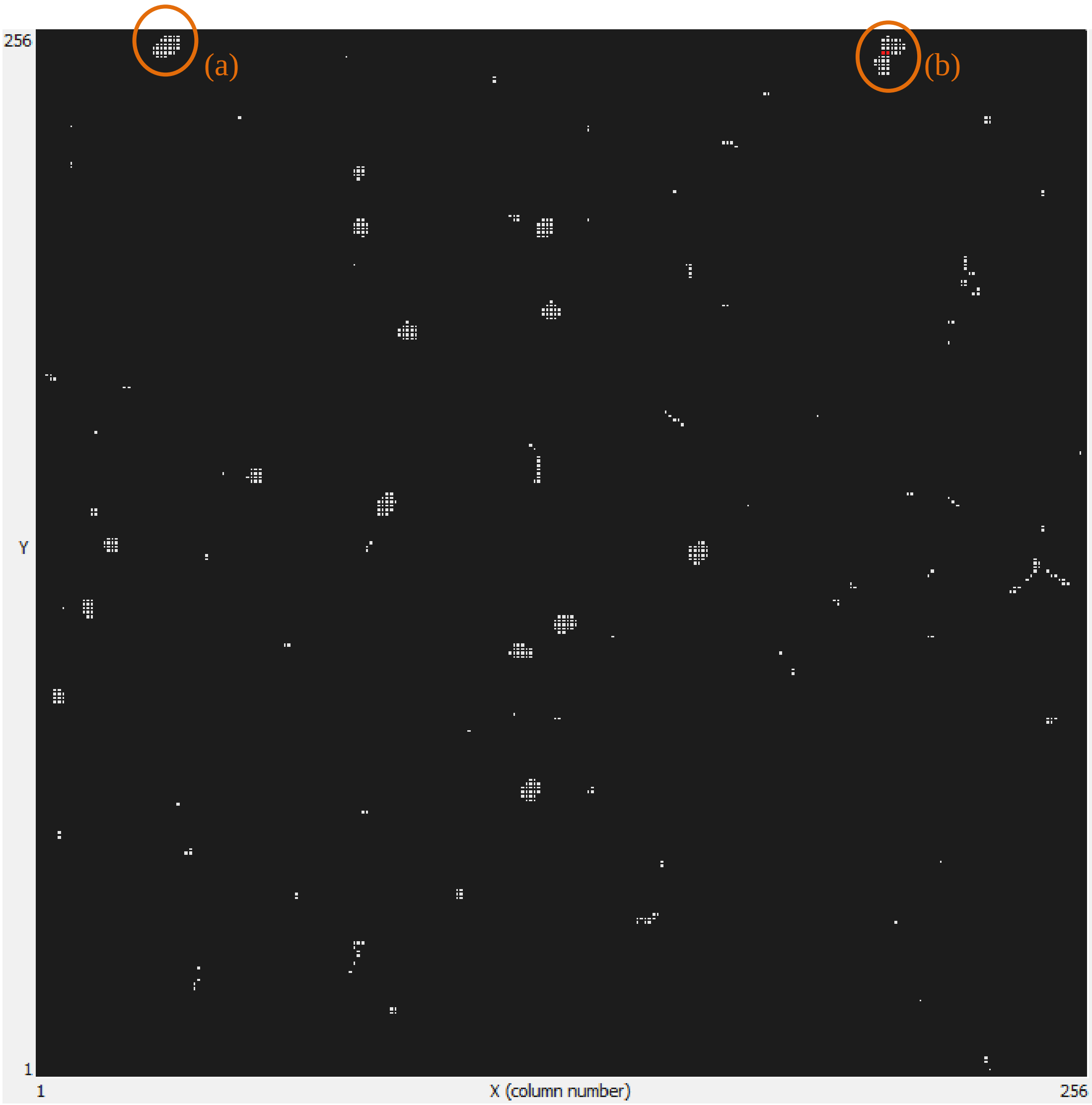

Figure 6.4: Events from another frame under D-T neutron irradiation: (a) shows ambiguously a proton-recoil event entering the silicon sensor at an angle smaller than in Figure 6.3, or possibly a distorted inelastic interaction; and (b) shows overlapping events of inelastic interactions.

Figure 6.5 shows a screenshot generated by Pixelman software, representing a greyscale modulated image of accumulated events in the Medipix2 detector within the SV1 and SV2 areas. There is a clear difference between the number of events in those regions of the detector covered by polyethylene (recoil protons and background) and uncovered (background only). Proton and background windows, which were also used in the simulations, are represented in Figure 6.5 with a broken red outline. Using these regions inside SV1 and SV2 inhibits cross-talk, where scattering events from one region are counted in another; this improves the evaluation of the neutron response.

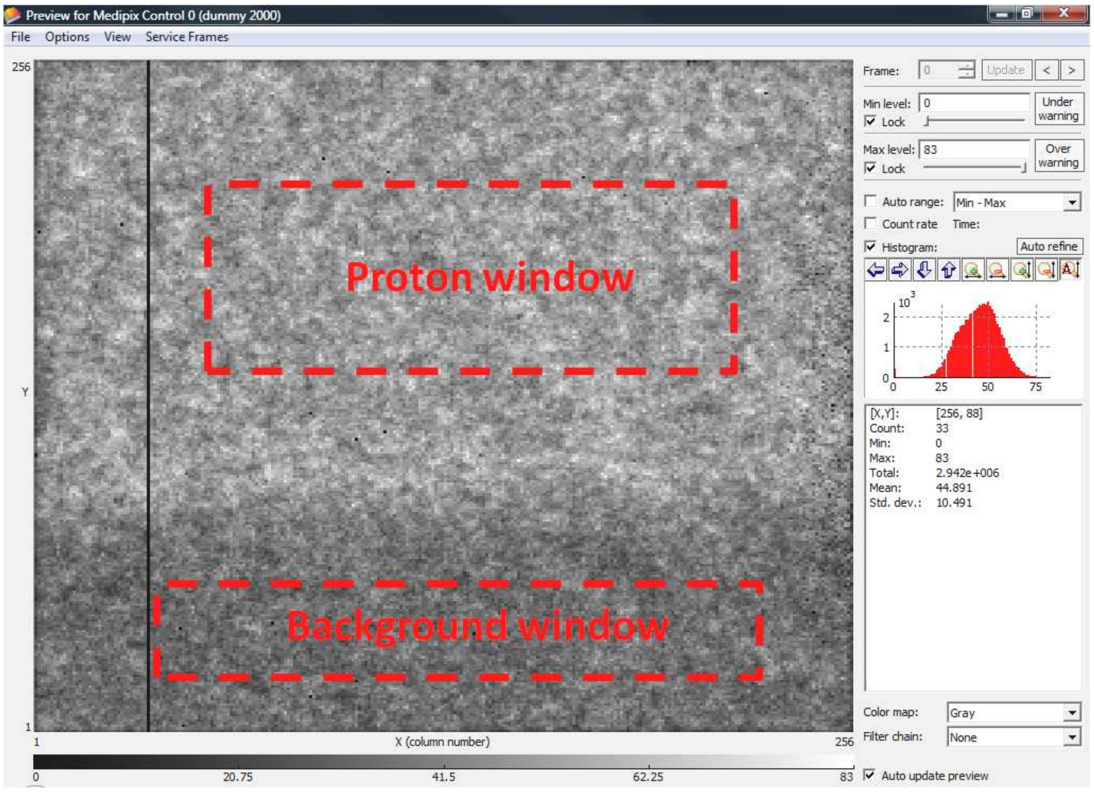

Figure 6.5: The accumulated events from all frames from fast-neutron irradiation. The black line shows the dead pixels. The counting windows under the layer of polyethylene and in the uncovered area are a proton window and a background window, respectively.

Figure 6.6 shows a comparison of the event images for different thicknesses of polyethylene converters irradiated with D-T and Am-Be neutrons. The gain in efficiency with polyethylene converters of different thicknesses is clearly visible, particularly when the thickness is increased for exposures with high-energy 14 MeV neutrons (Figure 6.6(a)).

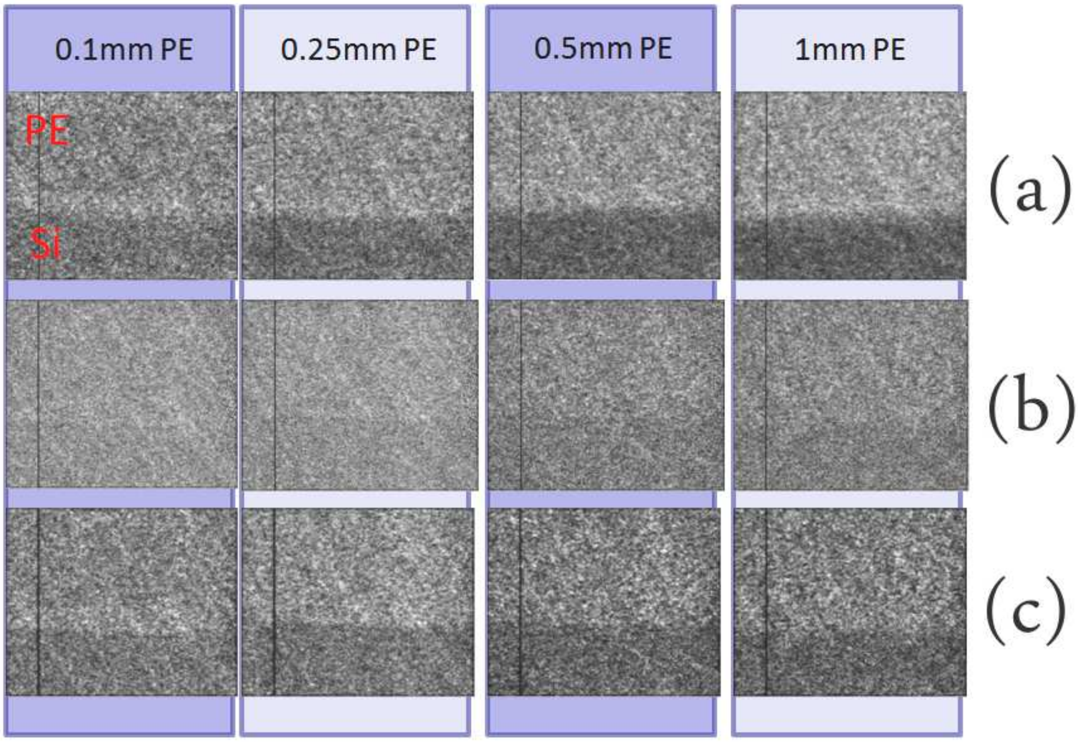

Figure 6.6: The total events are represented in the greyscale modulated image, as in Figure 6.5. The bright areas show high event counts under the polyethylene layer: (a) is the results from a 14 MeV D-T meutron source; (b) is the results from an Am-Be neutron source; and (c) corresponds to events in (b), after filtering out the events with a cluster size of less than seven pixels.

Figure 6.6 (b) and (c) shows the event images for the same thicknesses of polyethylene converters, but irradiated with neutrons from an Am-Be source, which has a lower average neutron energy (~ 4.2 MeV) than the D-T source and a higher gamma background. This can be seen in Figure 6.6b, where due to the larger gamma background the boundary between the SV1 and SV2 regions is not as clear.

In the mixed-radiation fields of these experimental setups there were other contributions to the event counts in both counting windows; these contributions were associated with backscattered neutrons, secondary charged particles and a gamma background (Figure 6.6). Secondary charged particles, like alphas, had the least effect on the counts because they were easily stopped in air. The backscattered neutrons had an almost equal effect on both counting windows because the back of the Medipix2 detector has uniform layers of material.

It is possible to improve the contrast in Figure 6.6b using those features of the Pixelman software that allow events to be filtered depending on size of the pixel cluster, which is related to the LET of the incident particle. Gamma radiation with low-energy photons will deposit energy within a single pixel, whereas higher-energy photons will create long tracks due to the higher energy of secondary electrons, which results in energy depositions within more than one pixel [155]. This allows for the removal of events corresponding to photons with low energy, for example, which only deposit energy in a single pixel. Figure 6.6c shows the events in Figure 6.6b after filtering out those with a cluster size of less than seven pixels. In this case the contribution of recoil protons becomes more obvious, which is a further advantage of this dosimeter. Thus the application of cluster-size filtration to the experimental data, in addition to the background-window subtraction method, improved the response of the Medipix2 to neutrons only.

In this study the net proton counts were calculated by subtracting the background counts according to Equation (5.1) after preliminary cluster-size filtration, allowing for a comparison of the counts produced by recoil protons only, for each partial converter. Thus, the data from both neutron field experiments were analysed further to filter out clusters below seven pixels, which as discussed, removes the background contribution from gammas that was not included in the GEANT4 simulations. The response of each converter was normalised to the total number of counts of all converters for the same neutron-fluence irradiations, as presented in Equation (6.1) below. This equation was used for both the GEANT4 simulations and experiments with the D-T and Am-Be sources.

$$R_{\Phi,total} = \sum_{i=1}^{4} R_{\Phi,i} \quad (6.1)$$

Figure 6.7 and Figure 6.8 present the variation in the normalised responses of recoil protons of the Medipix2 detector with different thicknesses of polyethylene converter, showing a direct comparison of the simulation and experiment results for irradiation with the D-T and Am-Be neutron sources, respectively.

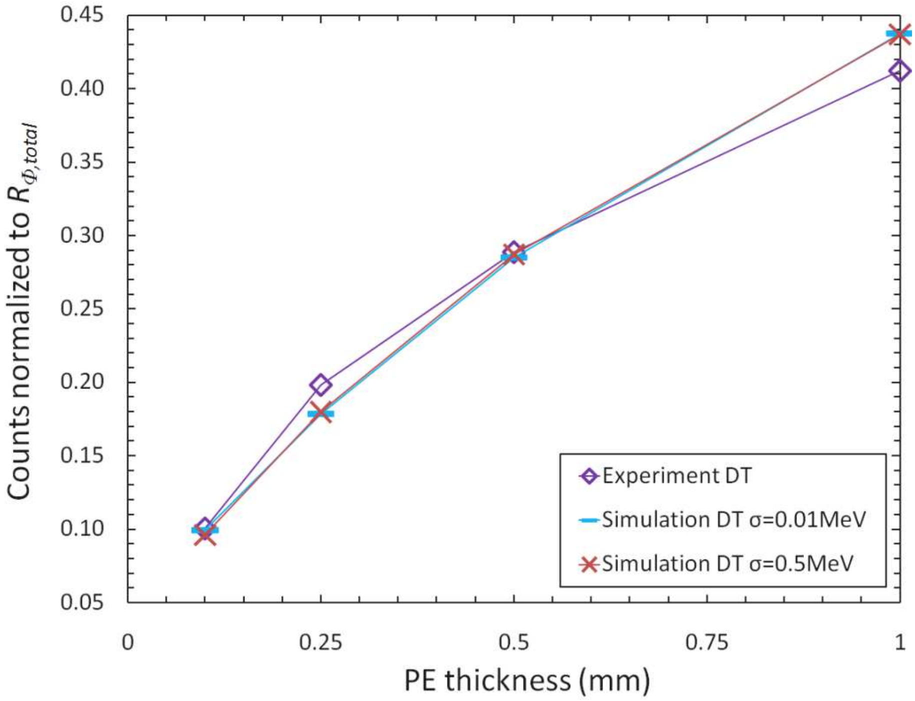

Figure 6.7: A comparison of the experimental result of the 14 MeV D-T neutron to the simulations, using a Gaussian spectrum of mean 14 MeV and σ of 0.01 and 0.5 MeV.

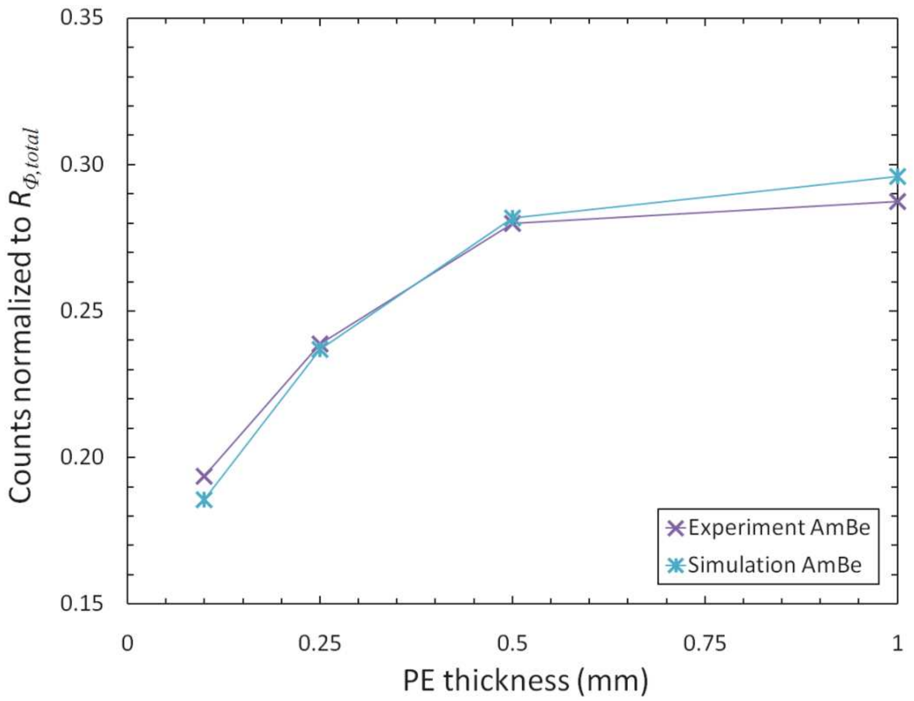

Figure 6.8: A comparison of the experimental result of the Am-Be neutron to the simulation.

For both neutron-source experiments, agreement with GEANT4 simulations was within 10%. Error bars for experimental results were estimated from the standard deviation of Poisson statistic $\sigma_\lambda = \sqrt{N}$, where N was number of counts. Error bars for experimental results were less than 1%, resulting from the large number of counts from recoil protons. The detector responses for polyethylene converters in Figure 6.8 with thicknesses of 1 mm and 0.5 mm were not significantly different due to the low average range of the recoil protons produced by neutrons from the Am-Be source. This is in contrast with the response of the detector with 14 MeV neutrons from the D-T source.

The observed agreement between the experimental and simulated results of the dosimeter responses for four polyethylene converters with distinct thicknesses demonstrates the validity of the GEANT4 simulations and the implementation of the subtraction model of Medipix2 with polyethylene converters. This lends confidence to the optimisation procedure described in Chapter 5, and demonstrates that applying a structured polyethylene converter to a pixelated detector can produce a neutron dosimeter with an independent response to neutron energy to within 10% variation in an energy range 0.3–15 MeV.

6. 4 Validating the optimisation method

This section describes the validation of the experiment results using the Medipix2 detector with a structured polyethylene converter. A D-T neutron source was used to provide two different neutron spectra: non-moderated and moderated fields. The moderation was performed with a poly-methyl-methacrylate (PMMA) moderator. The validation simulations were performed using GEANT4 version 9.2.p01.

6.4.1 *Simulation methods of a moderated D-T neutron source*

The neutron-dose equivalent of the moderated neutrons was estimated through GEANT4 Monte Carlo simulations. This simulation was done to obtain information from the neutron spectrum after being moderated by a 6 cm-thick PMMA moderator. The simulation geometry setup is shown in Figure 6.9. An additional 0.9 mm-thick layer of aluminium used in both the simulation and the experiment were to stop recoil protons originating from the moderator. The neutron source was a parallel beam with 14 MeV mono-energetic normally incident on the moderator. The beam had a 5 x 5 cm^2 cross-section. The physics library was the QGSP_BIC_HP that came with the GEANT4 installation. The secondary particle production threshold was assigned to 0.5 mm inside the moderator geometry.

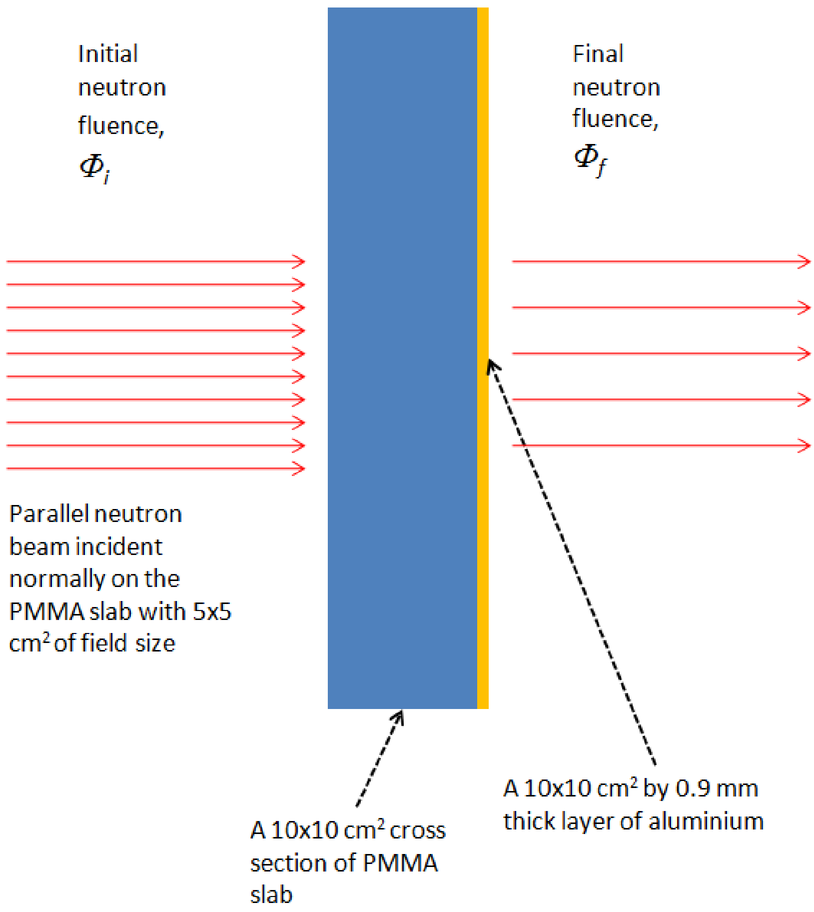

Figure 6.9: The geometry setup for the simulation of the neutron spectrum after moderation by the PMMA slab.

For each simulation event, the particles that exited from the side with the layer of aluminium were counted. The energy associated with each type of particle was stored in 0.002 MeV bins of energy that spanning 50 eV to 20 MeV. The types of particles for which the energy spectra were investigated were gamma, neutron, proton, electron and alpha.

6.4.2 *Simulation methods of a structured polyethylene converter on the Medipix2*

GEANT4 was used to simulate Medipix2 geometry with a structured polyethylene converter on top of the active area of Medipix2. The views of the simulated geometry are shown in Figure 6.10, Figure 6.11 and Figure 6.12. The threshold for secondary particle production was assigned to 5 µm at the Medipix2 readout pixels, and gradually increased at the region further away from the pixels.

The readout areas were divided into seven segments: 0.01, 0.03, 0.05, 0.1, 0.3 and 1 mm-thick, which were represented by R_1, R_2, R_3, R_4, R_5 and R_6, respectively, while the uncovered area for the background readout was denoted as R_0 in Figure 6.10. The remaining area in Figure 6.10 was covered by a 0.5 mm-thick polyethylene frame supporting the structured converter.

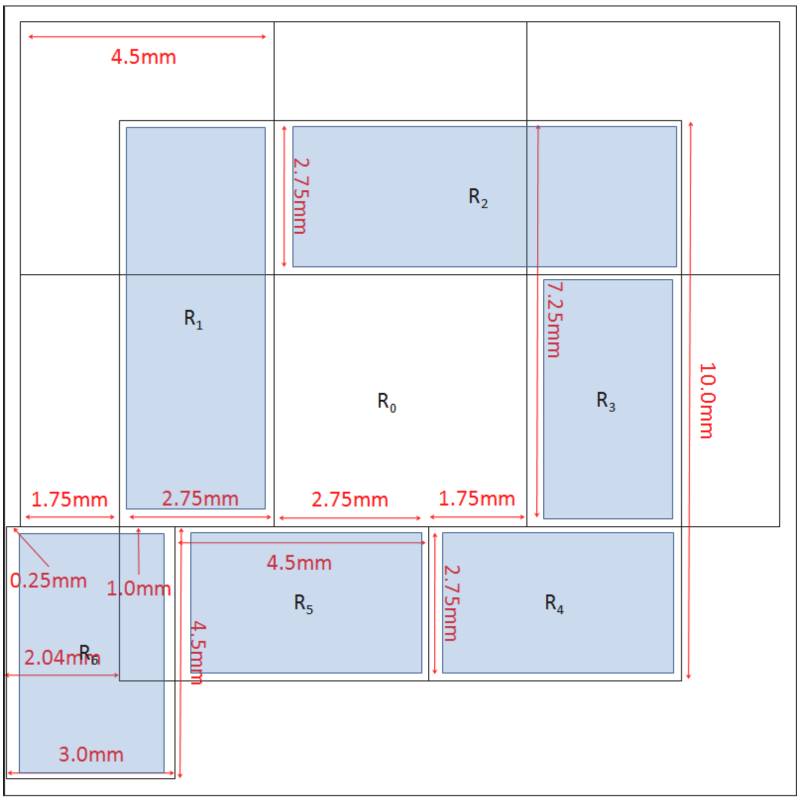

Figure 6.10: Plan view of the structured converter on the Medipix2 active area. The areas highlighted in blue show where the polyethylene converter was placed.

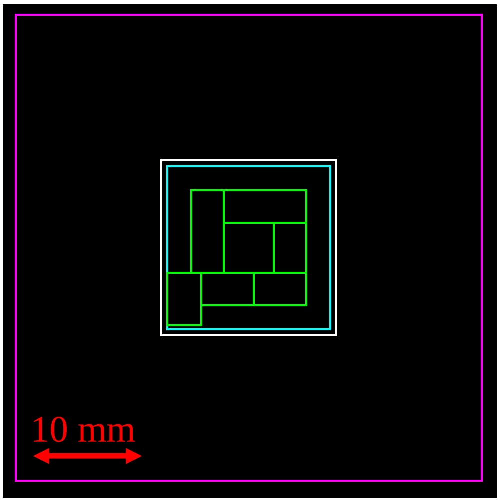

Figure 6.11: A view of the detector geometry in the simulation. The green lines represent the structured polyethylene converters. The light-blue line denotes the periphery of the active area of Medipix2, and the area between the white line and the magenta indicates the plastic frame on the Medipix2 board.

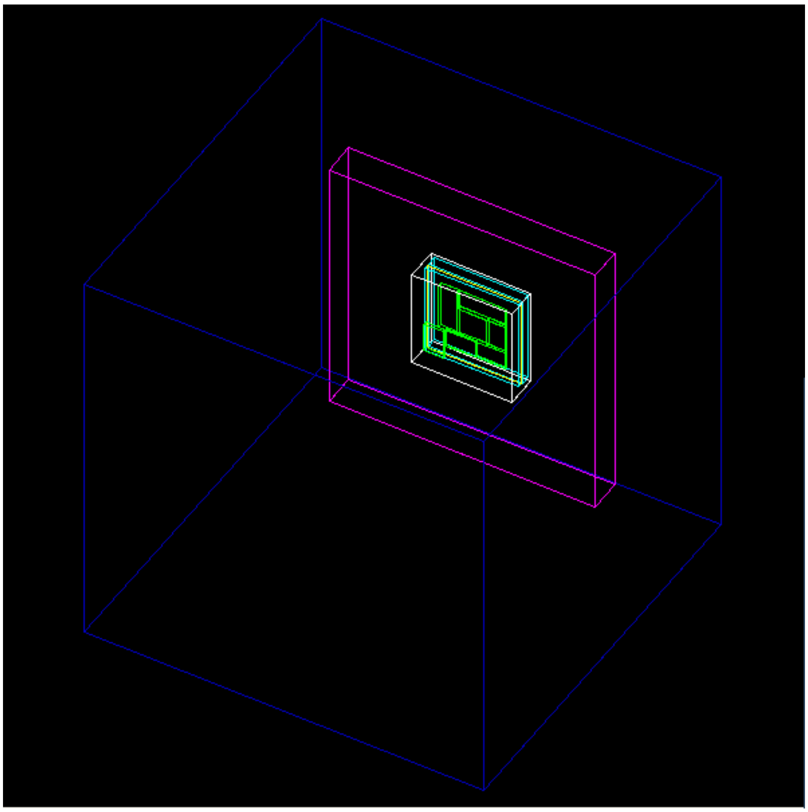

Figure 6.12: An angled view of the geometry in the simulation. The cubicle world geometry is shown by the blue line.

The mono-energetic neutron source was from 0.3 to 15 MeV of energy. The parallel neutron beam incidents were normally on the front of the detector. Every primary neutron event that deposited energy above 10 keV in the segments was counted as one, and tallied over a run. The size of the neutron beam field was 4 cm^2.

6.4.3 *Experiment methods for a structured polyethylene converter on the Medipix2*

A structured polyethylene converter was prepared using layers of high-density polyethylene (HDPE), as shown in Figure 6.13. The layers of different segments were glued together such that the converter measured 14 x 14 mm^2. This structured converter was placed onto the Medipix2 sensor and held in place with thin aluminium tape, as shown in Figure 6.14. The pixel equalisation was performed before the Medipix2 was used in the experiments by covering it with black fabric during equalisation, as shown in Figure 6.15.

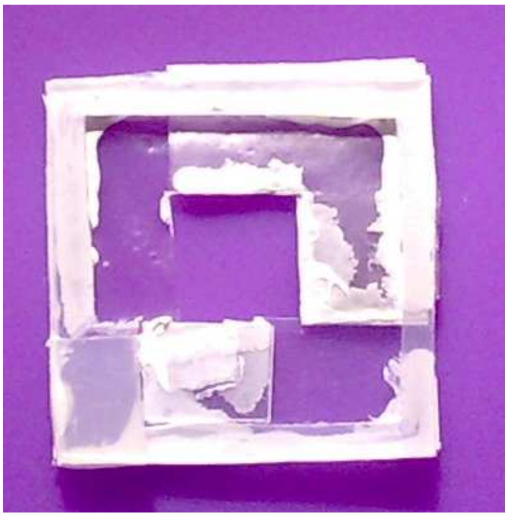

Figure 6.13: The structured polyethylene converter as described in Figure 6.10. The white region is the thin layer of hydrogen-free glue; protons generated from the glue can be neglected.

Figure 6.14: Medipix2 with a structured converter attached onto the sensor. A small twist on the converter, which occurred when it was being installed on the Medipix2, may have uncovered the periphery of the sensor (as indicated by the red circles).

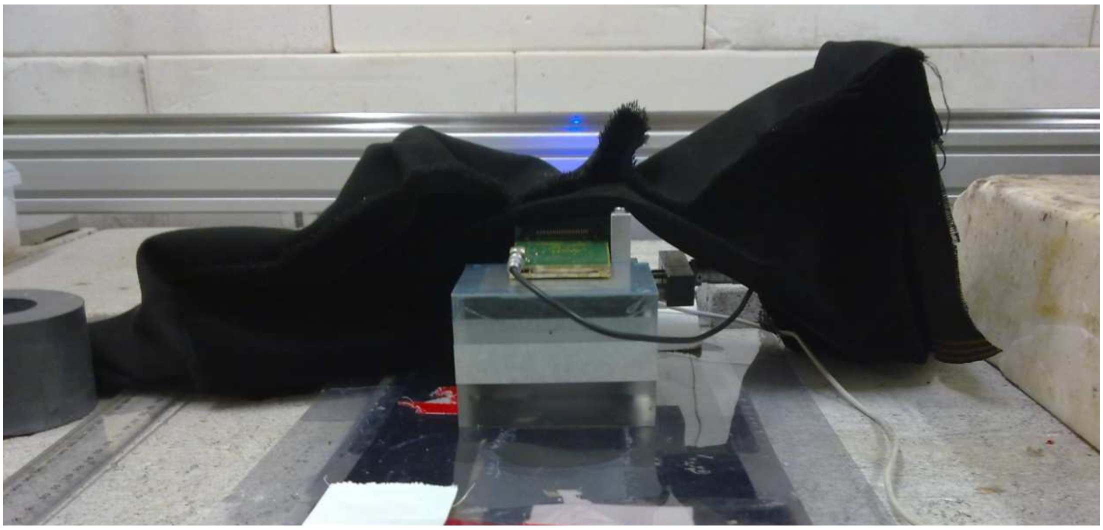

Figure 6.15: Setup for pixel equalisation.

The neutron-dose equivalent on the D-T exit window with and without a 6 cm PMMA moderator was measured by an ALNOR 2202D remmeter. The remmeter sensor was made from a large moderator body of polyethylene, an inner cylinder of boronated plastic and a central counter tube filled with BF_3. It allows measurement of the dose equivalent for neutrons with an energy range of 0.0025 eV to 17 MeV. It is less sensitive to gamma, where it can discriminate about 10^{-6} times the gamma-dose rate, which in 2 Gy/h of gamma dose rate is equal to a neutron-dose equivalent < 5 μSv/h. The remmeter was placed upright on the neutron exit windows, as shown in Figure 6.16. The dose rate was given in μSv/h in log scale meter. The remmeter was calibrated on the 20 March 2010, according to ANSTO.

The D-T neutron source current was stable after 20 minutes' warmup at 0.063 ± 0.002 mA and a voltage of 74.3 ± 0.2 kV. The dose-rate measurements with and without a moderator are summarised in Table 6-1.

Table 6-1: Neutron dose rates

Neutron moderation	**Dose rate**
Yes	3.8±0.5 mSv/h
No	5.5±0.5 mSv/h

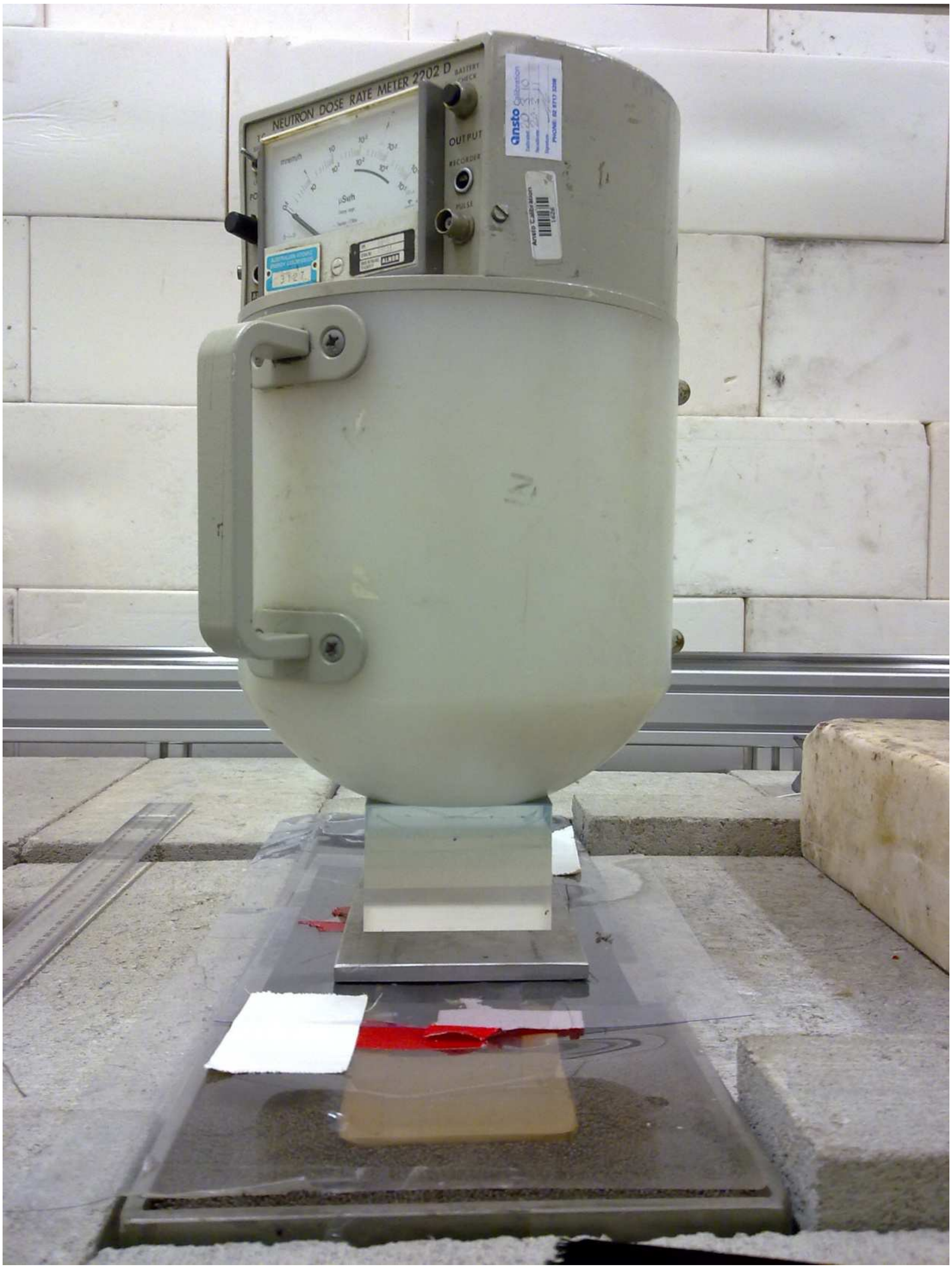

Figure 6.16: The remmeter standing on the moderator while the neutron-dose equivalent is being measured. To measure the dose without the moderator, the remmeter would stand on the aluminium plate.

While the measurement was taking place, the Medipix2 detector was placed as shown in Figure 6.17 and Figure 6.18. The moderator was placed between the Medipix2 sensor and the aluminium slab. The PMMA moderator was absent for non-moderated neutron experiments. The silicon sensor was biased at 7 V. Irradiation for a moderated neutron beam took an hour, whereas without a moderator it took 1.5 hours. The Pixelman data-acquisition frame period was set to 0.5 seconds per frame.

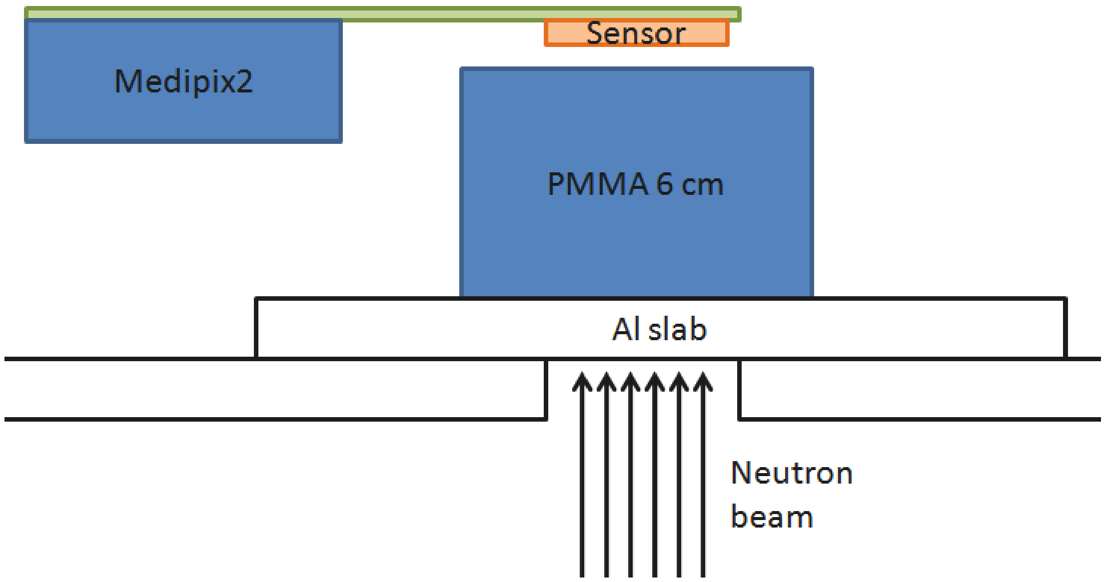

Figure 6.17: The experimental setups for the Medipix2 detector facing a moderated neutron beam.

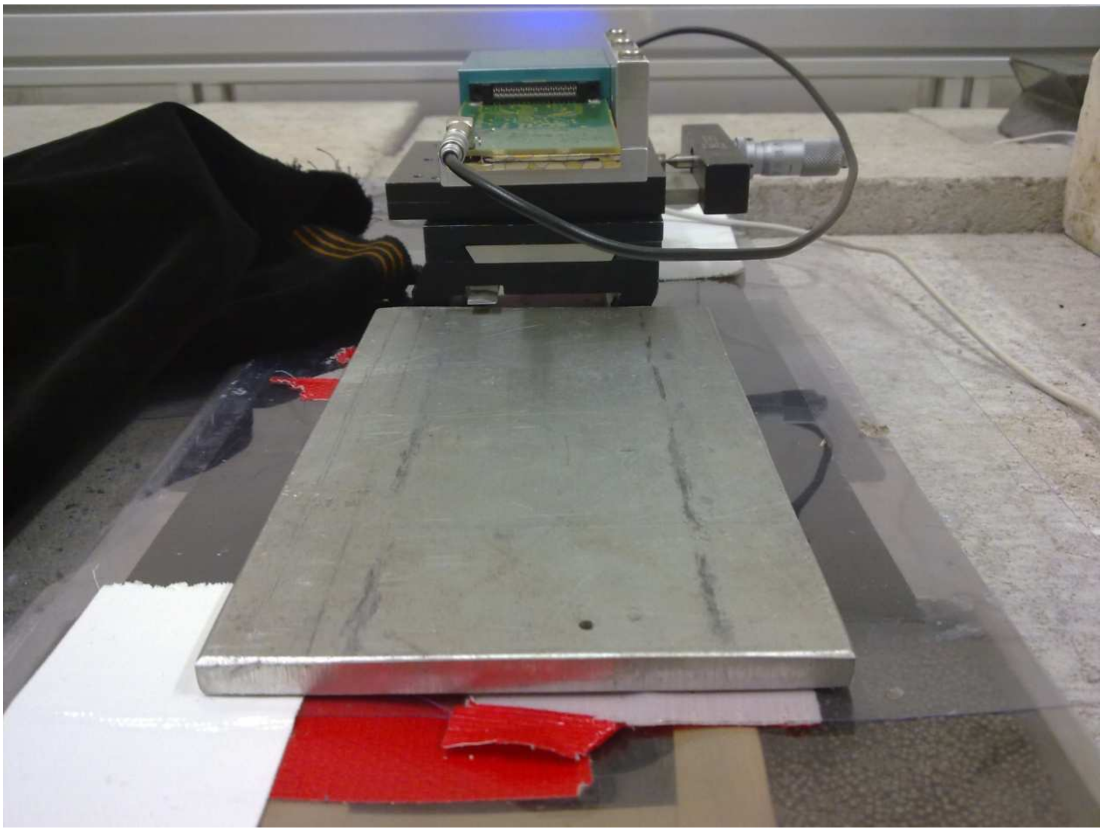

Figure 6.18: The experiment setup for the Medipix2 detector facing a non-moderated neutron beam.

6.4.4 *Simulation results for a moderated D-T neutron source*

Figure 6.19 shows the spectra from secondary particles and neutrons that were escaping the 6 cm moderator plus 0.9 mm layer of aluminium. The results show that the initial mono-energetic neutron energy is moderated, providing a continuous neutron spectrum below 14 MeV and dominated by a 14 MeV neutron peak. Table 6-2 shows the ratios of the final neutron fluence for full neutron spectra and for 14 MeV neutrons only to the initial 14 MeV neutron fluence for this moderation. This table shows that the moderated neutron fluence components were dominated by neutrons at 14 MeV energy with a fluence ratio of 3:1.

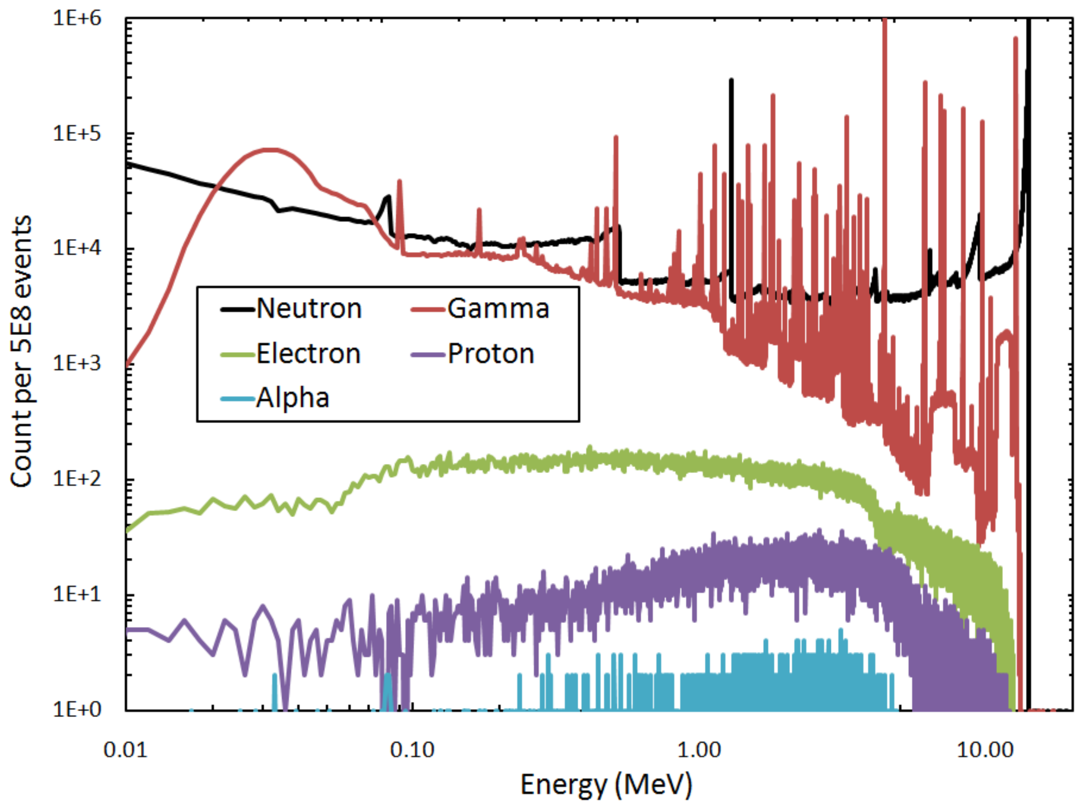

Figure 6.19: The spectra of secondary particles and neutrons that exit the moderator on the side with the aluminium layer.

Table 6-2: Neutron output fluence ratios

Ratios of final to initial fluence	
Full spectrum of exit neutron	$\Phi_f / \Phi_i = 0.68$
14 MeV only of exit neutron	$\Phi_{f,14MeV} / \Phi_i = 0.51$

Simulations were also carried out to investigate the effect of varying the thickness of the moderator on the output spectra of neutrons from the moderator. The PMMA moderator was set to two additional thicknesses, 3 and 20 cm, and an aluminium layer fixed at 0.9 mm. The results in Figure 6.20 show that altering the moderators to 3 and 6 cm-thick, resulted in almost equal quantities of lower-energy neutron components. The partial contribution of low-energy neutron components from the spectrum for the 6 cm-thick moderator was slightly higher than that for the 3 cm-thick moderator. The low-energy neutron components of fluence for the 20 cm-thick moderation were less than those for the 3 and 6 cm moderations. This could be explained by the neutrons having been scattered to the periphery of the PMMA and not emerging at the 5 x 5 cm^2 aluminium layer's side-exit field. Generally, the shapes of the neutron spectra from the three moderator thicknesses are identical.

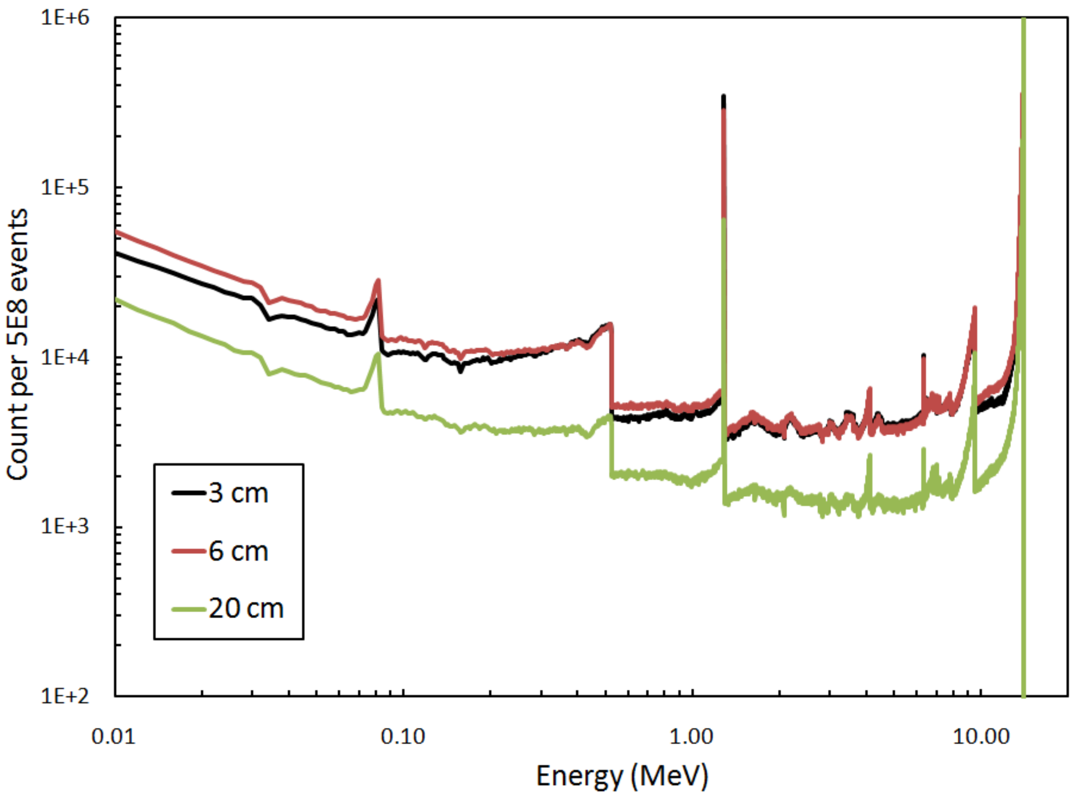

Figure 6.20: Neutron spectra after being moderated by 3, 6 and 20 cm-thick PMMA.

An estimation of the fluence-to-neutron ambient dose equivalent conversion factor was performed for the 6 cm-thick moderator. The fluence-to-ambient dose equivalent conversion factor for mono-energetic neutrons was adapted from the ICRP report 74 [3], *Conversion Coefficients for Use in Radiological Protection*. The ICRP 74 conversion table was interpolated into 0.002 MeV energy gaps to match the simulated energy bins. The spectrum in Figure 6.20 was normalised using Equation (6.2):

$$S_i = \frac{C_i}{\sum C_i} \tag{6.2}$$

where C_i is the count, as in Figure 6.20, for i^{th} - energy, S_i is the probability of neutrons at i^{th} -energy. Then the fluence-to-ambient dose equivalent conversion factor for the neutron spectrum moderated by the 6 cm PMMA is calculated using Equation (6.3):

$$H*(10)/\Phi = \sum S_i \cdot P_i \tag{6.3}$$

where P_i is the interpolated value of the ICRP 74 fluence to the neutron-dose equivalent conversion table for i^{th} -energy. Table 6-3 shows the results from this calculation.

Table 6-3: Neutron source conversion factors for the moderator with a 6 cm-thick PMMA and a 0.9 mm-thick aluminium plate

Neutron source moderation	**Conversion factor**	**Note**
Yes	5.06 x 10^{-7} mSv cm^2	For neutron energy 0.002-14 MeV
No	5.20 x 10^{-7} mSv cm^2	From ICRP Report 74 [3]

6.4.5 *Simulation results of a structured polyethylene converter on the Medipix2*

The energy responses for each defined segment on the Medipix2 active area are shown in Figure 6.21. Because the defined segments are different in their cross-sectional areas, the energy responses are exclusive to the design of this geometry. The results shown in Figure 6.21 are after background subtraction using Equation (5.1). The optimised response function $R_{\Phi,total}$ was calculated from Equation (5.2). The nine values of $\beta_{\Phi,i}$ were optimised to give results $R_{\Phi,total}$ (E) ∝ [H*/Φ](E).

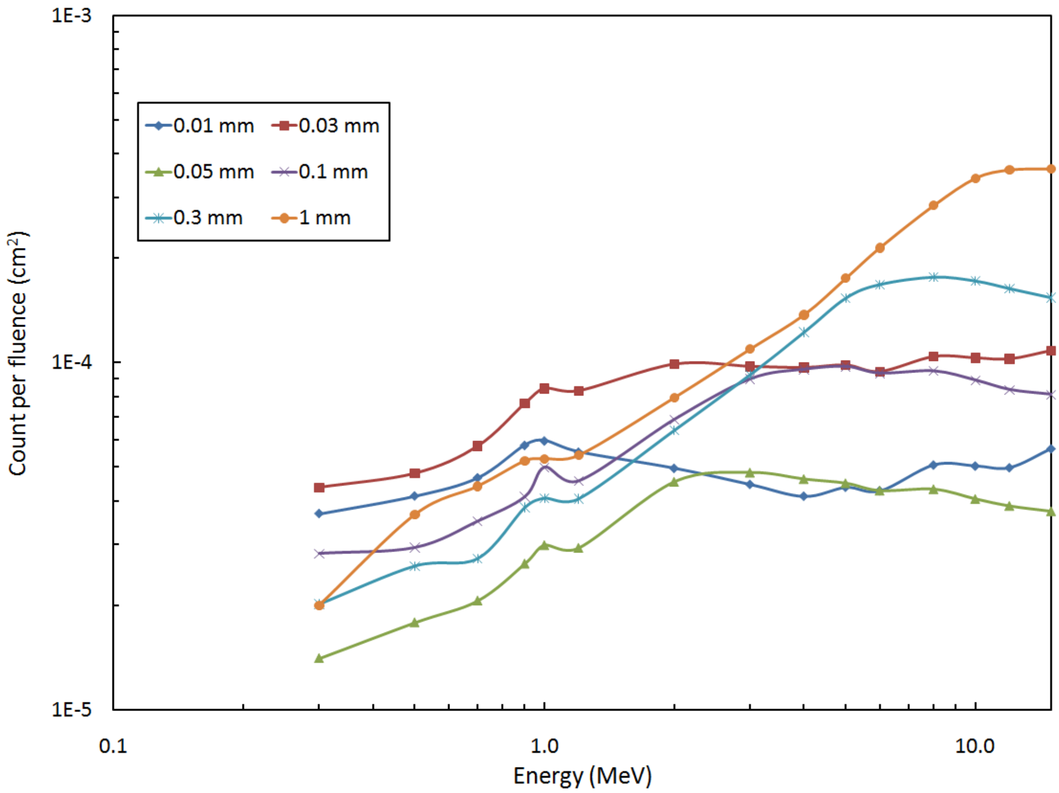

Figure 6.21: The energy responses for each defined segment corresponding to different thicknesses of PE.

The final response of detector to the neutron-dose equivalent was calculated using Equation (5.5); the optimised response of the detector counts over the neutron dose was 116 counts per mSv ± 15%, as shown in Figure 6.22. This is very similar to the response of the neutron detector with a structured polyethylene converter simulated in Chapter 5, 115 counts per mSv ± 9%, apart from a flatter response. This shows flexibility in designing a possible structure for a polyethylene converter to achieve an energy response for the neutron detector that is reasonably flat using the silicon pixelated detector proposed here.

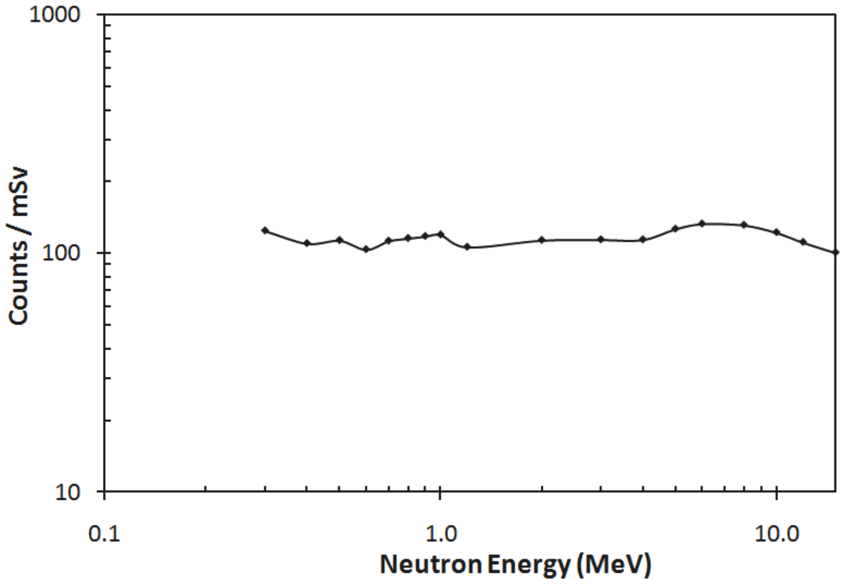

Figure 6.22: The total energy response of the detector shows good flattening of count per neutron-dose equivalent.

6.4.6 *Experiment results and discussion of a structured polyethylene converter on the Medipix2*

The Medipix2 detector with a structured polyethylene converter, as in the simulation above, was placed above a 6 cm PMMA moderator plus the 0.9 mm-thick aluminium layer (Figure 6.17). The images of event distribution on a 14 × 14 mm^2 sensitive area of the Medipix2 with and without a moderator are shown in Figure 6.23 and Figure 6.24, respectively. The green lines in both figures are the dead pixels. The number of registered counts in each segments of polyethylene converter, as marked, corresponding to the recoil protons, is reduced with introduction of a moderator. Raw C++ programming code was used to extract the counts from the assigned readout areas. The code was specified to read clusters with a size ≥ 7. The events on the perimeter of the sensitive area of the Medipix2 correspond to the polyethylene frame, as described earlier, and were not considered in the calculation of the detector response under both simulation and experimental works.

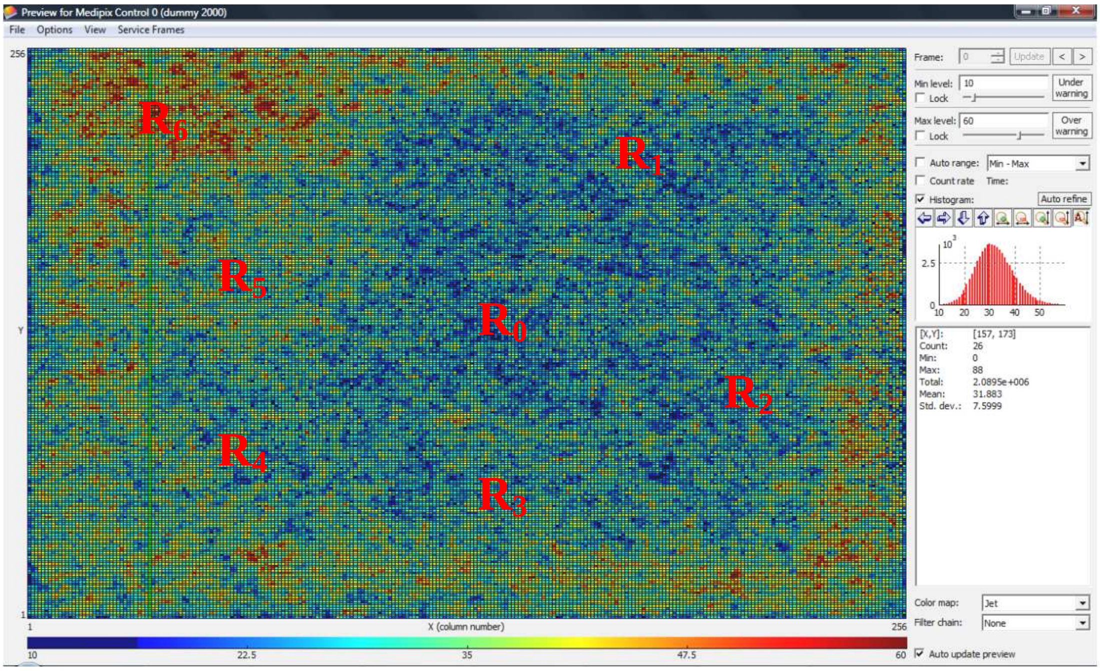

Figure 6.23: Counts on a sensitive area of the Medipix2 from the non-moderated neutron beam. The counts on the Medipix2 active area are given by the colour scale. The locations of assigned readout segments R_i are approximately as shown by the red text.

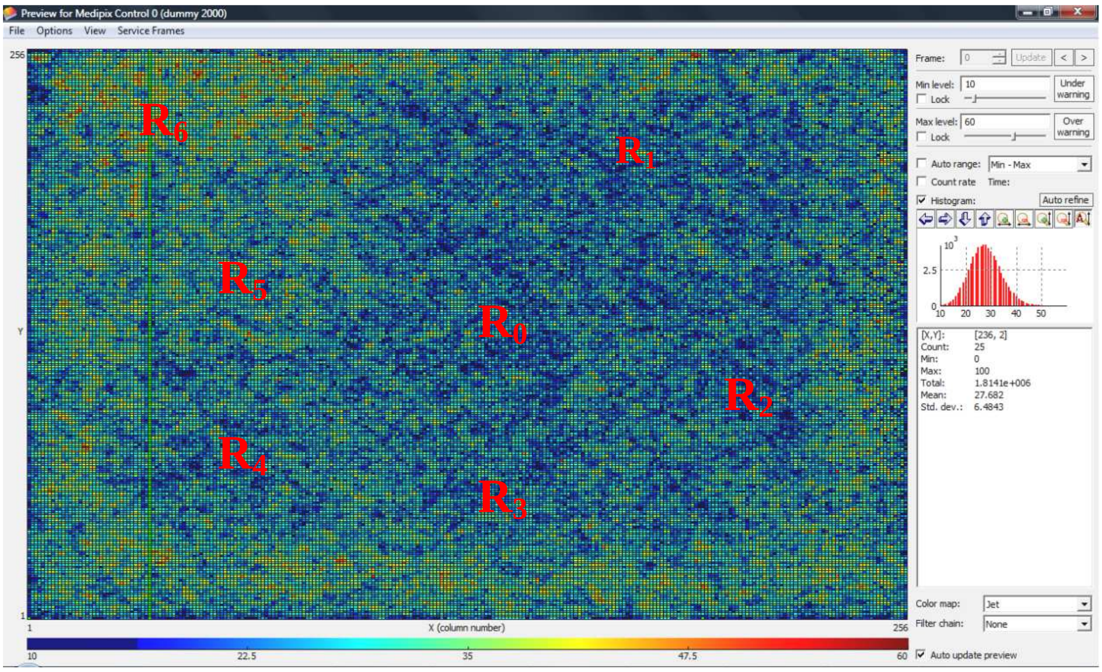

Figure 6.24: Counts the image of counts on a sensitive area of the Medipix2 from the moderated neutron beam. The counts on the Medipix2 active area are given by the colour scale. The locations of assigned readout segments R_i are approximately as shown by the red text.

To calculate the experimental response of the detector, the readout areas were first defined for each thickness of the segments, which include R_o. The size of each area had to have an equal size, as in the simulation. Then, the count of recoil protons was calculated based on Equation (5.1), as shown below.

$$R_i = \left(R'_i - \left(\frac{A_i}{A_0}\right) R_0\right) \tag{6.4}$$

where R'_i is the counts in segment-i^{th}, R_o is the uncovered segments counts, A_i and A_o are areas of a segment-i^{th} and an uncovered segment, respectively, and R_i is the recoil-proton counts per irradiation. Then, Equation (5.2) was used to calculate the R_{total} in term of counts per irradiation using the same $\beta_{\Phi,i}$ obtained from the simulation results in Section 6.4.5. The calculated experimental counts per measured neutron-dose equivalent, as shown in Table 6-4 were obtained from Equation (6.5).

$$Counts/mSv = \frac{R_{total}\ (counts)}{Dose\ rate\ (mSv/h) \times Time(hour)} \tag{6.5}$$

Table 6-4: Summaries of the final detector counts/mSv

Neutron-source moderation	Experimental response (counts/mSv)	Theoretical response (counts/mSv)
Yes	69.5 ± 13%	116 ± 15%
No	67.9 ± 9%	116 ± 15%

Moderation with a 6 cm-thick PMMA and 0.9 mm-thick aluminium decreased the 14 MeV neutron fluence to about half of its initial value. Total fluence of moderated neutrons was decreased to 68% of the initial fluence of 14 MeV neutrons, as shown in Table 6-2, in which the 14 MeV neutron fluence had a population ratio of 3:1 to the rest fluence of the moderated neutron.

Partial contributions to the neutron-dose equivalent per unit neutron fluence were calculated for energy ranges of 0.002-0.2 MeV (W_L) and 0.2-14 MeV (W_H) in the spectrum of neutron moderated by a 6 cm-thick PMMA moderator and 0.9 mm-thick aluminium layer as in Figure 6.9, and the results presented in a Table 6-5. Because of the total fluence of neutrons within W_L is much lower than W_H, as in Figure 6.20, as well as the calculated fluence conversion coefficient for W_L is only 11% of W_H, it is possible to conclude that major contribution to the neutron-dose equivalent will be from neutrons > 0.2 MeV.

Table 6-5: The ratio of the neutron-dose equivalent conversion of W_L to W_H

No	Neutron-energy range	***H*(10)/Φ* (mSv cm^2)**	Ratio
1	14 MeV mono-energy	5.2 x 10^{-7}	No 2 to No 1 = 0.98
2	0.2 – 14 MeV (W_H)	5.08 x 10^{-7}	No 3 to No 2 = 0.11
3	0.002 – 0.2 MeV (W_L)	0.58 x 10^{-7}	
4	0.002 – 14 MeV (full spectrum)	5.06 x 10^{-7}	No 4 to No 1 = 0.97

This is proved by the experimental values for counts/mSv (Table 6-4) for moderated and non-moderated neutron beams, which vary within 2%, which is an excellent agreement; this, again, suggests that the contribution of W_L neutrons to the response of this detector was negligible while this the detector was simulated and optimised for neutron energy > 0.3 MeV.

To further investigate this assumption, a detailed GEANT4 simulation of the response of a structured polyethylene converter on the Medipix2 neutron-detector geometry described in Section 6.4.2 was carried out. Table 6-6 shows the response of this detector, calculated from the simulation for W_L, full-moderated spectrum, and 14 MeV mono-energetic neutrons.

Table 6-6: Results from simulation of a structured Medipix2 detector for W_L, full moderated spectrum and 14 MeV mono-energetic neutrons. R_1, R_2, R_3, R_4, R_5 and R_6 are the 0.01, 0.03, 0.05, 0.1, 0.3 and 1 mm-thick polyethylene converters, respectively. R_7, R_8 and R_9 are the virtual thicknesses. β_i is the optimised weighting factor for each thickness for this geometry

Thickness	**<0.2 MeV**	**Full spectrum**	**14 MeV**	β_i	**<0.2 MeV**	**Full spectrum**	**14 MeV**
	Count/fluence				**Weighted count/fluence**		
R_1	9.52E-6	5.51E-5	5.65E-5	1.977	1.88E-5	1.09E-4	1.12E-4
R_2	1.03E-5	1.02E-4	1.08E-4	0.088	9.08E-7	8.99E-6	9.58E-6
R_3	4.85E-6	3.56E-5	3.72E-5	-0.089	-4.32E-7	-3.17E-6	-3.31E-6
R_4	5.17E-6	7.96E-5	8.09E-5	0.478	2.47E-6	3.80E-5	3.87E-5
R_5	2.84E-6	1.59E-4	1.54E-4	0.663	1.88E-6	1.05E-4	1.02E-4
R_6	-3.67E-6	3.54E-4	3.62E-4	-0.289	1.06E-6	-1.02E-4	-1.05E-4
R_7	5.23E-6	1.10E-4	1.07E-4	-1.049	-5.49E-6	-1.15E-4	-1.13E-4
R_8	1.09E-5	2.27E-4	2.36E-4	-0.548	-5.99E-6	-1.25E-4	-1.29E-4
R_9	-7.76E-6	1.01E-3	1.05E-3	0.135	-1.05E-6	1.37E-4	1.42E-4
				Total C/F	1.22E-5	5.24E-5	5.45E-5
				mSv/F	0.58E-7	5.06E-7	5.20E-7
				C/mSv	208.0	103.5	104.7
Variation to the value 116 C/mSv ±15% of averaged response of this detector				⟶	+79%	-11%	-10%

The recoil-proton simulated response of the Medipix2 neutron detector for W_L neutrons is 208 counts/mSv that is twice more that for full moderated neutron spectra and 14 MeV neutrons. It is not in contradiction with obtained results because partial fluence of W_L neutrons is as low as ~ 0.6% of the fluence from W_H neutrons that is leading to < 2 counts contribution to the 103 counts/mSv from full moderated spectrum that is within error of the detector response. The simulated value of counts/mSv for the full moderated spectra and 14 MeV mono-energetic neutrons showed that the developed optimisation of the response of the neutron detector with structured polyethylene on top of the pixelated silicon detector, even though was derived based on mono-energetic neutrons from an energy range of 0.3 MeV to 14 MeV, is also applicable to continues spectra of neutrons.

The dose equivalent rates measured by the ALNOR 2202D remmeter for moderated neutron beam had 31% lower rates of dose equivalent than the non-moderated 14 MeV D-T neutron beam as shown in Table 6-1. This result agrees with the results of the simulation which showed about 32% reduction in neutron fluence after being moderated by a 6 cm-thick PMMA, as shown in Table 6-2 which is again confirming the domination of 14 MeV neutrons in the moderated spectrum.

Table 6-7 shows experimental measurement of neutron-dose equivalent when assuming R_{total}= 116 counts/mSv as simulated for this Medipix2 neutron detector in comparison to measured value with ALNOR 2202D remmeter. While Medipix2 and ALNOR 2202D have about 40% difference for the moderated and non-moderated neutrons dose equivalents rate, the ratio of moderated to non-moderated dose rate is about the same for the value of 0.72 (Medipix2) and 0.69 (ALNOR 2202D) corresponding to 4% difference that again in good agreement with previous results.

Table 6-7: A comparison of the readout dose

Neutron-dose moderation	**Time of irradiation**	**Medipix2 neutron dose**	**ALNOR 2202D neutron dose**	**Different to ALNOR 2202D**
Yes	1 hour	2.3 mSv (or 2.3 mSv/h)	3.8 mSv (or 3.8 mSv/h)	39%
No	1.5 hour	4.8 mSv (or 3.2 mSv/h)	8.3 mSv (or 5.5 mSv/h)	42%
Ratio of moderated to non-moderated		0.72	0.69	4%

Almost twice the disagreement in absolute values of neutron-dose equivalent measured by these detectors is understandable, as the ALNOR 2202D remmeter was designed and calibrated for measurements of isotropic uniform neutron fields larger than the diameter of the remmeter. In present experiment the neutron field was a collimated beam with 5 × 5 cm^2 aperture, less than the 20 cm-diameter of the ALNOR 2202D's polyethylene cylindrical body (Figure 6.16), in contrast to the Medipix2 detector's sensitive area, which was smaller than the neutron field. This led to the ALNOR 2202D displaying higher values for ambient-dose equivalent due to the volumetric effect, while the Medipix2 was irradiated with uniform neutron fluence. For a more accurate comparison of these detectors, future experiments should be done in an isotropic, large and uniform neutron field.

6. 5 Conclusion

The results from both experimental validations verified the simulation concepts for subtraction and the optimisation methods for development of an energy-independent fast-neutron dosimeter introduced in Chapter 5. A semiconductor neutron-dose equivalent dosimeter with a neutron-energy-independent response can be produce based on a pixelated silicon detector with a structured polyethylene converter that includes a bare segment. These experimental results offer valuable insight for the future engineering of a fast-neutron dosimeter based on a structured polyethylene converter on a Medipix2 detector. The initial validation of the optimisation method showed the detectors's almost energy-independent response to the moderated and non-moderated fast-neutron sources. The experimental results would have agreed better with the simulation results if the experiments had been carried out in a wide, uniform isotropic neutron field. A better verification of the flatness of the response can be done by moderating the spectral neutron sources rather than using a mono-energetic 14 MeV source; this will avoid domination of a particular energy line in the moderated spectra. Strong ^{252}Cf and Pu-Be sources providing neutron spectra that can allow essential moderation while preserving reasonable dose rate were not available during this project. Future experiments will required a better-machined, structured polyethylene converter, as well as the introduction of a dead layer in the Medipix detector in GEANT4 simulations that can influence the detector response at the low-energy part of the considered spectra.

CHAPTER 7

CONCLUSION

This study has successfully used GEANT4 Monte Carlo simulations to show that MOSFET and Medipix2 semiconductor detectors can be used for personnel accident dosimetry in a mixed gamma-neutron field, in or near free-air geometry with an ambient dose equivalent response as prescribed by ICRU and ICRP for dosimetry on a standard phantom. The importance of developed dosimeters is in accident and military dosimetry, when detectors can be placed in free-air geometry for dose monitoring or, for example, on a wrist where CPE is not achieved. The main goal in this work was to improve the detectors' energy response for gamma and fast-neutron radiation fields while making a neutron dosimeter that is also insensitive to gamma. Engineering the energy response of those dosimeters was achieved by optimising the detector packaging using Monte Carlo simulations.

The version of the GEANT4 simulation toolkit used in this study was the updated version at the time of each individual study, and was stated in each chapter. The GEANT4 toolkit helped optimise detector packaging in three-dimensional and asymmetry geometry, tasks that are difficult to carry out through an analytical calculation. In this study, GEANT4 provided all the necessary tools for tracking particles in complex geometry, and for constructing complex geometry, while offering a variety of relevant physics modelling, add-in software to analyse output data and visualisation tools.

The detector's packaging imposes notable effects on its energy response due to the attenuation of primary radiation and the production of secondary charged particles and the backscattering effect; these were used to adjust energy response of the detector.

As a result of the optimisation of the MOSFET packaging, two new packaging models were proposed. The new packaging was intended for use in free-air dosimetric MOSFET applications. This packaging made the response of the MOSFET independent of the photon energy, and made it match the detector responses in terms of absorbed doses at depths of 0.07 mm and 10 mm in a water phantom. New packaging, the OP-007 and OP-10, led to a MOSFET response proportional to absorbed doses at depths of 0.07 and 10 mm in a water phantom, respectively. Both packaging designs were based on multiple layers of a copper-aluminium-graphite filter placed on the gate of the MOSFET. Proposed packaging optimisation using a single-chip MOSFET reduced the over-response for photon energies of 15 to 60 keV to 200% for $D_w(0.07)$ and 330% for $D_w(10)$. The MOSFET response was within ± 60% for photon energies between 0.06 and 2 MeV for both $D_w(0.07)$ and $D_w(10)$. The obtained energy response was improved in comparison to conventionally packaged MOSFET detectors, which usually exhibit a 500% to 700% over-response at photon energies < 100 keV when used in free-air geometry.

The second optimised MOSFET packaging used two MOSFET chips in the OP-007 and OP-10 designs. One of the chips was heavily filtered over-layers of lead-aluminium-graphite, while the other one was unfiltered. At photon energies of < 100 keV, the heavily filtered MOSFET chip had a lower response than the unfiltered one. The R_2 / R_1 ratio of those two MOSFET chips gives information on the average energy of the photons, which means that a correction can be applied to an unfiltered MOSFET according to the ratio given. The results of the simulation show how the two chips packaging method provides a better energy response than the single filtered MOSFET chip for both the OP-007 and OP-10 packaging designs. The proposed algorithm for the dual-MOSFET OP-007 and OP-10 was modelled in X-ray spectral fields with an energy range of 30 kV_p to 150 kV_p and a 6 MV spectrum of medical LINAC. The energy-response variation of the dual-MOSFET packages DOPF-007 and DOPF-10 for average photon energy in a range of 22 keV to 2 MeV was ± 10% and ± 40%, respectively. To our knowledge, they offer the best energy-response flatness for personnel accident dosimeter application in free-air geometry.

A new approach to design of a fast-neutron personnel dosimeter with a flat energy response was proposed and validated by Monte Carlo simulations and experiments. This approach was based on a silicon pixelated detector with a structured polyethylene converter as a source of elastically recoil-protons and was realised on a Medipix2 detector with 65,000 pixels. The GEANT4 optimisation of the response of the neutron-dose equivalent meter working in count recoil-proton mode allowed a ± 9% flatness in the energy response for neutrons with an energy range of 0.3 to 15 MeV.

This was achived by using a combination of the 0.01, 0.03, 0.05, 0.1, 0.3 and 1 mm-thick segments of structured polyethylene converter. Algorithms behind the proposed approach use different weighting factors ($\beta_{\Phi,i}$) for the count response from the different polyethylene segments (R_i) to produce an almost neuron-energy-independent combined sensitivity of $R_{\Phi,total}$ = 115 ± 10 counts per mSv of ambient neutron-dose equivalent.

The GEANT4 Monte Carlo simulations were benchmarked to the experiments in a mixed gamma-neutron spectral source of Am-Be and D-T generator with 14 MeV neutron energy. Monte Carlo simulated recoil protons from 0.1, 0.25, 0.5 and 1 mm-thick polyethylene converters partially covering the Medipix2 detector were experimentally validated, justifying the proposed subtraction method. An agreement within ± 10% was demonstrated for both neutron sources.

Finally, a fully assembled Medipix2 fast-neutron detector with an optimised structured polyethylene converter of six different thicknesses and areas of polyethylene segments including an uncovered segment was modelled with GEANT4; it demonstrated a response of 116 ± 17 counts/mSv for neutrons with an energy range of 0.3 to 15 MeV. The simulated response was verified on moderated and non-moderated neutrons from a D-T generator with a 5 × 5 cm^2 collimated 14 MeV neutron beam. The moderation was achieved using a 5 × 5 cm^2 by 6 cm-thick PMMA slab plus a 0.9 mm aluminium layer to stop recoil protons generated in the PMMA slab from reaching the Medipix2 detector. Response of the neutron dosimeter in terms of ambient neutron-dose equivalent was simulated with GEANT4 for both beam qualities. Independent measurement of the neutron-dose equivalent conducted by a team member of this project was made with an ALNOR 2202D remmeter. The neutron dosimeter based on the Medipix2 showed a dose rate about 40% lower than the remmeter; however, the ratio of the dose equivalents for both beams measured by the Medipix2 and the remmeter was within 4%. This proved the concept and accuracy of this design. Discrepancies in absolute dose values between this detector and the remmeter were justified due to the volumetric effect of the remmeter to the collimated beam and possible error in knowledge of an absolute fluence of 14 MeV neutrons entering the structured moderator of this detector.

An advantage of the dosimeter developed in this study compared to existing dosimeters is its high degree of flexibility in adjusting the energy response by varying the readout segments. This is done using Pixelman software along with the weighting factors applied to each segment. This can allow the dosimeter to self-calibrate when being irradiated in the fields of several calibrated-neutron-sources spectral in terms of neutron-dose equivalent. The dosimeter can also be used for space applications, as it is immune to background counts due not only to gamma radiation but to any charged particles (protons and heavy ions) typical in the space environment. In conjunction with the DOPF MOSFET dosimeter design, it can be used for independent dose measurement in a mixed gamma-neutron field, and can be incorporated in a wrist device.

Future work on MOSFET and Medipix2 personnel dosimeters

The DOPF MOSFET detector was optimised for normal incidence of photons, and does not consider radiation effects in the MOSFET, particularly the recombination effect of electron-hole pairs in the SiO_2 gate. Future simulations aimed at optimising the angular response of the MOSFET packaging in photon fields are underway for both single and dual-MOSFET chip packaging. A new simulation tool that incorporates kinetics of charge accumulation and recombination in SiO_2 gate into GEANT4 for photons with different energies will be developed for a better optimisation of a MOSFET personnel dosimeter.

Other studies have demonstrated some applications of the dual-MOSFET detector for thermal neutron dosimetry [147] and single-MOSFET detector for mixed gamma and fast-neutron dosimetry [159]. A new MOSFET simulation study will be proposed to optimise the fast-neutron response of the MOSFET package incorporating a polyethylene converter. It will use the future combined simulation tool, as in the current study, to model a response of the MOSFET to recoil protons that is LET-dependent [160, 161].

In this study, the verification of the approach and optimisation of the neutron dosimeter response was done for a neutron-energy range of 0.3 to 14 MeV. Further studies to optimise this Medipix2 dosimeter to a wider energy range can be extended down to the thermal-neutron range. It will demand modelling the response of the pixelated detector with ^{10}B or ^{6}LiF [102] converter segments, in conjunction with a structured polyethylene converter. The Medipix2 detector is an ideal candidate for this extension due to its flexibility in assigning readout areas. Angular response, as with the MOSFET dosimeter, should also be investigated, but optimisation of the angular response in personal electronic neutron dosimeters is not an easy task. New add-on software for self-calibration based on the Pixelman program is another area for development using this neutron detector.

REFERENCES

[1] Medipix2. *The Medipix2 collaboration*. [Web page] [cited 1/9/2010, 2010]; Available from: http://medipix.web.cern.ch/MEDIPIX/Medipix2/indexMPIX2.html.

[2] D. Greiffenberg, *et al. Detection efficiency of ATLAS-MPX detectors with respect to neutrons.* Nucl. Instrum. Methods in Phys. Res. A: Accel. Spectrom. Detect. Assoc. Equip, 2009. **607**(1): p. 38-40.

[3] ICRP. *Conversion Coefficients for Use in Radiological Protection.* Ann. ICRP, 1996. **26**(3-4): p. 1-205.

[4] ICRU. *Fundamental quantities and units for ionizing radiation.* Journal of the ICRU, 2011. **11**(1): p. 1-33.

[5] F.H. Attix. *Introduction to Radiological Physics and Radiation Dosimetry*. 1986: Wiley-VCH. 607.

[6] NIST. *XCOM: Photon cross sections database*. [cited from, 2007-2012]; Available from: http://www.nist.gov/pml/data/xcom/index.cfm.

[7] E.B. Podgoršak. *Radiation physics for medical physicists*. 2006, Berlin Heidleberg: Springer-Verlag 745.

[8] IAEA-NDS. *Evaluated nuclear data file (ENDF)*. [Web page] [cited 30th January, 2012]; Available from: http://www-nds.iaea.org/exfor/endf.htm.

[9] M.B. Chadwick, *et al. A consistent set of neutron kerma coefficients from thermal to 150 MeV for biologically important materials.* Med. Phys., 1999. **26**(6): p. 974-991.

[10] G.F. Knoll. *Radiation Detection and Measurement*. 3rd ed. 2000: John Wiley & Sons.

[11] J.R. Cassata, M. Moscovitch, J.E. Rotunda, K.J. Velbeck. *A new paradigm in personal dosimetry using LiF:Mg,Cu,P*. Radiat. Prot. Dosim., 2002. **101**(1-4): p. 27-42.

[12] J.N. Bradford. *Clusters in ionization tracks of electrons in silicon dioxide*. IEEE Trans. Nucl. Sci, 1986. **NS-33**(6): p. 1271-1275.

[13] G.A. Ausman, F.B. McLean. *Electron−hole pair creation energy in* SiO_2. Appl. Phys. Lett., 1975. **26**(4): p. 173-175.

[14] J.M. Benedetto, H.E. Boesch. *The Relationship between 60Co and 10-keV X-Ray Damage in MOS Devices*. IEEE Trans. Nucl. Sci, 1986. **33**(6): p. 1317-1323.

[15] Wikipedia. *Radiation protection*. [Web page] [cited 2nd December, 2011]; Available from: http://en.wikipedia.org/wiki/Radiation_protection.

[16] ICRU. *International Commission on Radiation Units & Measurements*. [Web page] [cited 3rd June, 2010]; Available from: http://www.icru.org/.

[17] ICRP. *International Commission on Radiological Protection*. [Web page] [cited 3rd June, 2010]; Available from: http://www.icrp.org/.

[18] ISO. *International Organization for Standardization, ISO/TC 85/SC 2/WG*. [Web page] [cited 3rd June, 2010]; Available from: http://www.iso.org/iso/standards_development/technical_committees/list_of_iso_technical_committees/iso_technical_committee.htm?commid=50280.

[19] J. Böhm, W.G. Alberts, K.L. Swinth, C.G. Soares, J.C. McDonald, I.M.G. Thompson, H.-M. Kramer. *ISO recommended reference radiations for the*

calibration and proficiency testing of dosemeters and dose rate meters used in radiation protection. Radiat. Prot. Dosim., 1999. **86**(2): p. 87-105.

[20] ICRP. *The 2007 Recommendations of the International Commission on Radiological Protection.* Ann. ICRP, 2007. **37**(2-4): p. 1-332.

[21] ICRU. *Measurement of dose equivalents from external photon and electron radiations.* Journal of the ICRU, 1992. **Report 47**.

[22] D.A. Schauer, J.R. Cassata, J.J. King. *A comparison of measured and calculated photon backscatter from dosemeter calibration phantoms.* Radiat. Prot. Dosim., 2000. **88**(4): p. 319-321.

[23] R.J. Traub, J.C. McDonald, M.K. Murphy. *Determination of photon backscatter from several calibration phantoms.* Radiat. Prot. Dosim., 1997. **74**(1/2): p. 13-20.

[24] R. Kramer, J.W. Vieira, H.J. Khoury, F.R.A. Lima, D. Fuelle. *All about MAX: a male adult voxel phantom for Monte Carlo calculations in radiation protection dosimetry.* Phys. Med. Biol., 2003. **48**: p. 1239-1262.

[25] P. Ferrari, G. Gualdrini. *An improved MCNP version of the NORMAN voxel phantom for dosimetry studies.* Phys. Med. Biol., 2005. **50**: p. 4299-4316.

[26] T.C. Chao, A. Bozkurt, X.G. Xu. *Conversion coefficients based on the VIP-Man anatomical model and EGS4-VLSI code for external monoenergetic photons from 10 keV to 10 MeV.* Health Phys., 2001. **81**(2): p. 163-183.

[27] ICRP. *1990 Recommendations the International Radiological of Commission Protection.* Ann. ICRP, 1991. **21**(1-3): p. 1-201.

[28] A.S. Pradhan. *Letter to the Editor.* Radiat. Prot. Dosim., 1992. **42**(2): p. 133-134.

[29] G. Busuoli, A. Cavallini, V. Klamert, F. Monteventi. *Preliminary results of some tests on the use of the dose equivalent operational quantities for some dosimetric systems.* Radiat. Prot. Dosim., 1989. **28**(1/2): p. 97-100.

[30] A. Holmes-Siedle. *The space charge dosimeter.* Nucl. Instrum. Methods, 1974. **121**: p. 169-179.

[31] Z.-Y. Qi, X.-W. Deng, S.-M. Huang, J. Lu, M. Lerch, D. Cutajar, A. Rosenfeld. *Verification of the plan dosimetry for high dose rate brachytherapy using metal--oxide--semiconductor field effect transistor detectors.* Med. Phys., 2007. **34**(6): p. 2007-2013.

[32] E. Brauer-Krish, A. Bravin, M.L.F. Lerch, A.B. Rosenfeld, J. Stepanek, M.D. Michael, J.A. Laissue. *MOSFET dosimetry for microbeam radiation therapy at the European Synchrotron Radiation Facility.* Med. Phys., 2003. **30**(4): p. 583-589.

[33] J.E. Cygler, A. Saoudi, G. Perry, C. Morash, E. Choan. *Feasibility study of using MOSFET detectors for in vivo dosimetry during permanent low-dose-rate prostate implants.* Radiother. Oncol., 2006. **80**(3): p. 296-301.

[34] A.B. Rosenfeld, M.G. Carolan, G.I. Kaplan, B.J. Allen, V.I. Khivrich. *MOSFET dosimeters: The role of encapsulation on dosimetric characteristics in mixed gamma-neutron and megavoltage x-ray fields.* IEEE Trans. Nucl. Sci, 1995. **42**(6): p. 1870-1877.

[35] F. Ravotti, M. Glaser, A.B. Rosenfeld, M.L.F. Lerch, A.G. Holmes-Siedle, G. Sarrabayrouse. *Radiation monitoring in mixed environments at CERN: From the IRRAD6 facility to the LHC experiments.* IEEE Trans. Nucl. Sci, 2007. **54**(4): p. 1170-1177.

[36] L. Adams, A. Holmes-Siedle. *The development of an MOS dosimetry unit for use in space.* IEEE Trans. Nucl. Sci, 1978. **25**(6): p. 1607-1612.

[37] J.R. Schwank, S.B. Roeske, D.E. Beutler, D.J. Moreno, M.R. Shaneyfelt. *A dose rate independent pMOS dosimeter for space applications.* IEEE Trans. Nucl. Sci, 1996. **43**(6): p. 2671-2678.

[38] A. Holmes-Siedle. *Calibration and flight testing of a low-field pMOS dosimeter.* IEEE Trans. Nucl. Sci, 1985. **32**(6): p. 4425-4429.

[39] C. Benson, R.A. Price, J. Silvie, A. Jaksic, M.J. Joyce. *Radiation-induced statistical uncertainty in the threshold voltage measurement of MOSFET dosimeters.* Phys. Med. Biol., 2004. **49**: p. 3145-3159.

[40] B. Camanzi, M. Glaser, E. Tsesmelis, L. Adams. *A study on the applicability of solid state, real-time dosimeters to the CMS experiment at the large hadron collider.* Nucl. Instrum. Methods in Phys. Res. A: Accel. Spectrom. Detect. Assoc. Equip, 2003. **500**(1-3): p. 431-440.

[41] M. Ciocca, *et al. Real-time in vivo dosimetry using micro-MOSFET detectors during intraoperative electron beam radiation therapy in early-stage breast cancer.* Radiother. Oncol., 2006. **78**(2): p. 213-216.

[42] R. Ramaseshan, K.S. Kohli, T.J. Zhang, T. Lam, B. Norlinger, A. Hallil, M. Islam. *Performance characteristics of a microMOSFET as an in vivo dosimeter in radiation therapy.* Phys. Med. Biol., 2004. **49**: p. 4031-4048.

[43] C. Ehringfeld, S. Schmid, K. Poljanc, C. Kirisits, H. Aiginger, D. Georg. *Application of commercial MOSFET detectors for in vivo dosimetry in the therapeutic x-ray range from 80 kV to 250 kV.* Phys. Med. Biol., 2005. **50**: p. 289-303.

[44] T.M. Briere, J. Lii, K. Prado, M.T. Gillin, A.S. Beddar. *Single-use MOSFET radiation dosimeters for the quality assurance of megavoltage photon beams.* Phys. Med. Biol., 2006. **51**: p. 1139-1144.

[45] A.S. Beddar, M. Salehpour, T.M. Briere, H. Hamidian, M.T. Gillin. *Preliminary evaluation of implantable MOSFET radiation dosimeters.* Phys. Med. Biol., 2005. **50**: p. 141-149.

[46] T.P. Ma, P.V. Dressendorfer. *Ionizing radiation effects in MOS devices and circuits*. 1989, New York: Wiley.

[47] A. Holmes-Siedle. *The space-charge dosimeter: General principles of a new method of radiation detection.* Nucl. Instrum. Methods, 1974. **121**(1): p. 169-179.

[48] A.B. Rosenfeld. *Mosfet dosimetry on modern radiation oncology modalities.* Radiat. Prot. Dosim., 2002. **101**: p. 6.

[49] M. Soubra, J. Cygler, G. Mackay. *Evaluation of a dual bias dual metal oxide-silicon semiconductor field effect transsitor detector as radiation dosimeter.* Med. Phys., 1994. **21**(4): p. 6.

[50] A. Holmes-Siedle. *RADFET Probes, Readers, Applications*. [Web page] [cited 6th June, 2010]; Available from: http://www.radfet.com/id4.html.

[51] R.C. Hughes. *Theory of response of radiation sensing field effect transistors.* J. Appl. Phys., 1985. **58**(3): p. 1375-1379.

[52] J. Mekki, L. Dusseau, M. Glaser, S. Guatelli, M. Moll, M.G. Pia, F. Ravotti. *Packaging effects on RadFET sensors for high energy physics experiments.* IEEE Trans. Nucl. Sci, 2009. **56**(4): p. 2061-2069.

[53] Best. *Best Medical Canada mobileMOSFET On-line Wireless Dosimetry*. [Web page] [cited 6th June, 2010]; Available from: http://www.mosfet.ca/products/mobilemosfet.htm.

[54] Best. *Best Medical Canada Portable Dosimeter TN-RD-90*. [Web page] [cited 6th June, 2010]; Available from: http://www.mosfet.ca/products/portable.htm.

[55] R. Kohno, T. Nishio, T. Miyagishi, E. Hirano, K. Hotta, M. Kawashima, T. Ogino. *Experimental evaluation of a MOSFET dosimeter for proton dose measurements.* Phys. Med. Biol., 2006. **51**(23): p. 6077-6086.

[56] G.A. Pablo Cirrone, *et al*. *Preliminary investigation on the use of the MOSFET dosimeter in proton beams.* Phys. Med., 2006. **22**(1): p. 29-32.

[57] V. Panettieri, M.A. Duch, N. Jornet, M. Ginjaume, P. Carrasco, A. Badal, X. Ortega, M. Ribas. *Monte Carlo simulation of MOSFET detectors for high-energy photon beams using the PENELOPE code.* Phys. Med. Biol., 2007. **52**: p. 303-316.

[58] B. Wang, C.H. Kim, X.G. Xu. *Monte Carlo modeling of the MOSFET dosimeter and its application.* Trans. Am. Nucl. Soc., 2003. **88**: p. 218-220.

[59] B. Wang, C.H. Kim, X.G. Xu. *Monte Carlo modeling of a High-Sensitivity MOSFET dosimeter for low- and medium-energy photon sources.* Med. Phys., 2004. **31**(5): p. 1003-1008.

[60] B. Wang, X.G. Xu, C.H. Kim. *Monte carlo study of MOSFET dosemeter characteristics: Dose dependence on photon energy, direction and dosemeter composition.* Radiat. Prot. Dosim., 2005. **113**(1): p. 40-46.

[61] J.C.L. Chow, M.K.K. Leung. *Monte Carlo simulation of MOSFET dosimeter for electron backscatter using the GEANT4 code.* Med. Phys., 2008. **35**(6): p. 2383-2390.

[62] A. Jaksic, Y. Kimoto, A. Mohammadzadeh, W. Hajdas. *RADFET response to proton irradiation under different biasing configurations.* IEEE Trans. Nucl. Sci, 2006. **53**(4): p. 2004-2007.

[63] I.S. Kwan, *et al. Skin dosimetry with new MOSFET detectors.* Radiat. Meas., 2008. **43**(2-6): p. 929-932.

[64] I.S. Kwan. *Characterization of the performance of the new MOSkin dosimeter as a quality assurance tool for pulsed dose-rate (PDR) prostate brachytherapy, and the effect of rectal heterogeneity on the dose delivered to the rectal wall*, in *School of Engineering Physics*. 2009, University of Wollongong: Wollongong. p. 227.

[65] I.S. Kwan, D. Wilkinson, M. Butson, D.L. Cutajar, M. Lerch, A.B. Rosenfeld. *Suitability of the MOSkin detector for skin dosimetry.* Australas. Phys. Eng. Sci. Med., 2007. **30**(4): p. 369-370.

[66] A.B. Rosenfeld, M.L.F. Lerch, T. Kron, E. Brauer-Krish, A. Bravin, A. Holmes-Siedle, B.J. Allen. *Feasibility study of online high-spatial-resolution MOSFET dosimetry in static and pulsed x-ray radiation fields.* IEEE Trans. Nucl. Sci, 2001. **48**(6): p. 8.

[67] R.L. Pease, M. Simons, P. Marshall. *Comparison of pMOSFET total dose response for Co-60 gammas and high-energy protons.* IEEE Trans. Nucl. Sci, 2001. **48**(3): p. 908-912.

[68] P. Beck, F. Bock, H. Böck, M. Latocha, R.A. Price, S. Rollet, M. Wind. *Investigations on photon energy response of RadFET using Monte Carlo simulations.* IEEE Trans. Nucl. Sci, 2007. **54**(4): p. 1151-1157.

[69] R.A. Kinhikar, P.K. Sharma, C.M. Tambe, D.D. Deshpande. *Dosimetric evaluation of a new OneDose MOSFET for Ir-192 energy.* Phys. Med. Biol., 2006. **51**: p. 1261-1268.

[70] J.M. McGarrity. *Considerations for Hardening MOS Devices and Circuits for Low Radiation Doses.* IEEE Trans. Nucl. Sci, 1980. **27**(6): p. 1739-1744.

[71] G. Ensell, A. Holmes-Siedle, L. Adams. *Thick oxide pMOSFET dosimeters for high energy radiation.* Nucl. Instrum. Methods in Phys. Res. A: Accel. Spectrom. Detect. Assoc. Equip, 1988. **269**(3): p. 655-658.

[72] D.J. Peet, M.D. Pryor. *Evaluation of a MOSFET radiation sensor for the measurement of entrance surface dose in diagnostic radiology.* Br. J. Radiol., 1999. **72**(858): p. 562-8.

[73] P.M. Lenahan, P.V. Dressendorfer. *An electron spin resonance study of radiation-induced electrically active paramagnetic centers at the Si/SiO_2 interface.* J. Appl. Phys., 1983. **54**(3): p. 1457-1460.

[74] T.R. Oldham. *Ionizing radiation effects in MOS oxides*. 1999, Singapore: World Scientific Publishing Co. Pte. Ltd. 171.

[75] C.W. Scarantino, D.M. Ruslander, C.J. Rini, G.G. Mann, H.T. Nagle, R.D. Black. *An implantable radiation dosimeter for use in external beam radiation therapy.* Med. Phys., 2004. **31**(9): p. 2658-2671.

[76] D.B. Brown. *Photoelectron Effects on the Dose Deposited in MOS Devices by Low Energy X-Ray Sources.* IEEE Trans. Nucl. Sci, 1980. **27**(6): p. 1465-1468.

[77] A. Kelleher, W. Lane, L. Adams. *A design solution to increasing the sensitivity of pMOS dosimeters: The stacked RADFET approach.* IEEE Trans. Nucl. Sci, 1995. **42**(1): p. 48-51.

[78] B. O'Connell, A. Kelleher, W. Lane, L. Adams. *Stacked RADFETs for increased radiation sensitivity.* IEEE Trans. Nucl. Sci, 1996. **43**(3): p. 985-990.

[79] R.E. Swaja, R. Oyan, C.S. Sims, M.A. Dooley. *Evaluation of the U.S. army DT-236 battlefield personnel dosimetry system.* Oak Ridge National Laboratory, 1986. **ORNL-6265**: p. 1-52.

[80] TM-11-6665-364-12. *Operator's and unit maintenance manual: Radiac set AN/UDR-13.* 1998.

[81] M.J. Butson, A. Rozenfeld, J.N. Mathur, M. Carolan, T.P.Y. Wong, P.E. Metcalfe. *A new radiotherapy surface dose detector: The MOSFET.* Med. Phys., 1996. **23**(5): p. 655-658.

[82] G.J. Brucker, S. Kronenberg, F. Gentner. *Effects of package geometry, materials, and die design on energy dependence of pMOS dosimeters.* IEEE Trans. Nucl. Sci, 1995. **42**(1): p. 33-40.

[83] G.J. Brucker, S. Kronenberg, T. Jordan. *Tactical army dosimeter based on p-MOS single and dual gate insulators,* in *Radiation and its Effects on Components and Systems, 1993.* 1993, IEEE: St. Malo, France. p. 56-62.

[84] C.M. Dozier, D.B. Brown. *Photon energy dependence of radiation effects in MOS structures.* IEEE Trans. Nucl. Sci, 1980. **26**(6): p. 1694-1699.

[85] T. Kron, L. Duggan, T. Smith, A.B. Rosenfeld, M. Butson, G. Kaplan, S. Howlett, K. Hyodo. *Dose response of various radiation detectors to synchrotron radiation.* Phys. Med. Biol., 1998. **43**: p. 3235-3259.

[86] C.R. Edwards, S. Green, J.E. Palethorpe, P.J. Mountford. *The response of a MOSFET, p-type semiconductor and LiF TLD to quasi-monoenergetic x-rays.* Phys. Med. Biol., 1997. **42**: p. 2383-2391.

[87] J.G. Alves. *Developments in standards and other guidance for individual monitoring.* Radiat. Meas., 2008. **43**(2-6): p. 558-564.

[88] M. Campbell. *10 years of the Medipix2 collaboration.* Nucl. Instrum. Methods in Phys. Res. A: Accel. Spectrom. Detect. Assoc. Equip, 2010.

[89] X. Llopart, M. Campbell, R. Dinapoli, D. San Segundo, E. Pernigotti. *Medipix2: a 64-k pixel readout chip with 55-μm square elements working in single photon counting mode.* IEEE Trans. Nucl. Sci, 2002. **49**(5): p. 2279-2283.

[90] X. Llopart, M. Campbell. *First test measurements of a 64k pixel readout chip working in single photon counting mode.* Nucl. Instrum. Methods in Phys. Res. A: Accel. Spectrom. Detect. Assoc. Equip, 2003. **509**(1-3): p. 157-163.

[91] B. Mikulec, M. Campbell, E. Heijne, X. Llopart, L. Tlustos. *X-ray imaging using single photon processing with semiconductor pixel detectors.* Nucl. Instrum. Methods in Phys. Res. A: Accel. Spectrom. Detect. Assoc. Equip, 2003. **511**(1-2): p. 282-286.

[92] G. McMullan, D.M. Cattermole, S. Chen, R. Henderson, X. Llopart, C. Summerfield, L. Tlustos, A.R. Faruqi. *Electron imaging with Medipix2 hybrid pixel detector.* Ultramicroscopy, 2007. **107**(4-5): p. 401-413.

[93] G. McMullan, A.R. Faruqi. *Electron microscope imaging of single particles using the Medipix2 detector.* Nucl. Instrum. Methods in Phys. Res. A: Accel. Spectrom. Detect. Assoc. Equip, 2008. **591**(1): p. 129-133.

[94] J. Jakubek, T. Holy, E. Lehmann, S. Pospisil, J. Uher, J. Vacik, D. Vavrik. *Spatial resolution of Medipix-2 device as neutron pixel detector.* Nucl. Instrum. Methods in Phys. Res. A: Accel. Spectrom. Detect. Assoc. Equip, 2005. **546**(1-2): p. 164-169.

[95] J. Jakubek, G. Mettivier, M.C. Montesi, S. Pospisil, P. Russo, J. Vacik. *CdTe hybrid pixel detector for imaging with thermal neutrons.* Nucl. Instrum. Methods in Phys. Res. A: Accel. Spectrom. Detect. Assoc. Equip, 2006. **563**(1): p. 238-241.

[96] J. Jakubek, *et al. Neutron imaging and tomography with Medipix2 and dental micro-roentgenography.* Nucl. Instrum. Methods in Phys. Res. A: Accel. Spectrom. Detect. Assoc. Equip, 2006. **569**(2): p. 205-209.

[97] O.H. Siegmund, J.V. Vallerga, A.S. Tremsin, J. McPhate, B. Feller. *High spatial resolution neutron sensing microchannel plate detectors.* Nucl. Instrum. Methods in Phys. Res. A: Accel. Spectrom. Detect. Assoc. Equip, 2007. **576**(1): p. 178-182.

[98] J. Vallerga, J. McPhate, A. Tremsin, O. Siegmund. *High-resolution UV, alpha and neutron imaging with the Timepix CMOS readout.* Nucl. Instrum. Methods in Phys. Res. A: Accel. Spectrom. Detect. Assoc. Equip, 2008. **591**(1): p. 151-154.

[99] J. Jakubek. *Data processing and image reconstruction methods for pixel detectors.* Nucl. Instrum. Methods in Phys. Res. A: Accel. Spectrom. Detect. Assoc. Equip, 2007. **576**(1): p. 223-234.

[100] M. Chmeissani, *et al. First experimental tests with a CdTe photon counting pixel detector hybridized with a Medipix2 readout chip.* IEEE Trans. Nucl. Sci, 2004. **51**(5): p. 2379-2385.

[101] X. Llopart. *Design and characterization of 64K pixels chips working in single photon processing mode*, in *Department of Information Technology and Media*. 2007, Mid Sweden University: Sundsvall. p. 255.

[102] Z. Vykydal, *et al. The Medipix2-based network for measurement of spectral characteristics and composition of radiation in ATLAS detector.* Nucl. Instrum.

Methods in Phys. Res. A: Accel. Spectrom. Detect. Assoc. Equip, 2009. **607**(1): p. 35-37.

[103] T. Holy, J. Jakubek, S. Pospisil, J. Uher, D. Vavrik, Z. Vykydal. *Data acquisition and processing software package for Medipix2.* Nucl. Instrum. Methods in Phys. Res. A: Accel. Spectrom. Detect. Assoc. Equip, 2006. **563**(1): p. 254-258.

[104] C. Carpentieri, C. Schwarz, J. Ludwig, A. Ashfaq, M. Fiederle. *Absolute dose calibration of an X-ray system and dead time investigations of photon-counting techniques.* Nucl. Instrum. Methods, 2002. **487**: p. 71-77.

[105] T. Michel, M. Bohnel, J. Durst, P. Sievers, G. Anton. *Low energy dosimetry with photon counting pixel detectors such as Medipix.* IEEE Trans. Nucl. Sci, 2009. **56**(2): p. 417-423.

[106] IAEA. *Dosimetry in diagnostic radiology: An international code of practice.* IAEA Technical Report Series 457, 2007.

[107] S. Agosteo, P. Colautti, A. Fazzi, D. Moro, A. Pola. *A solid state microdosimeter based on a monolithic silicon telescope.* Radiat. Prot. Dosim., 2006. **122**(1-4): p. 382-386.

[108] S. Agosteo, G. D'Angelo, A. Fazzi, A.F. Para, A. Pola, P. Zotto. *Neutron spectrometry with a monolithic silicon telescope.* Radiat. Prot. Dosim., 2007: p. 1-8.

[109] S. Agosteo, A. Pola. *Analytical model for a monolithic silicon telescope - Response fucntion of the E stage.* Radiat. Meas., 2008. **43**: p. 1487-1492.

[110] T. Nakamura, M. Horiguchi, T. Suzuki, T. Yamano. *A real time wide energy range personal neutron dosemeter with two silicon detectors.* Radiat. Prot. Dosim., 1989. **27**(3): p. 149-156.

[111] M. Sasaki, T. Nakamura, N. Tsujimura, O. Ueda, T. Suzuki. *Development and characterization of real-time personal neutron dosemeter with two silicon detectors*. Nucl. Instrum. Methods, 1998. **418**(2-3): p. 465-475.

[112] S. Agosteo, C. Birattari, G. D'Angelo, F.D. Corso, A.F. Para, I. Lippi, A. Pola, P. Zotto. *Neutron spectrometry with a recoil radiator-silicon detector device*. Nucl. Instrum. Methods, 2003. **515**: p. 589-604.

[113] B. Barelaud, D. Paul, B. Dubarry, L. Makovicka, J.L. Decossas, J.C. Vareille. *Principles of an electronic neutron dosemeter using a PIPS detector*. Radiat. Prot. Dosim., 1992. **44**(1/4): p. 363-366.

[114] I.M. Cornelius, A.B. Rosenfeld. *Verification of Monte Carlo calculations in fast neutron therapy using silicon microdosimetry*. IEEE Trans. Nucl. Sci, 2004. **51**(3): p. 873-877.

[115] J.R. Harvey. *The basis of a suggested instrumental approach to the surveying of neutron fields and the measurement of personal dose from neutrons*. Phys. Med. Biol., 1981. **26**(2): p. 253-267.

[116] C.R. Hirning, A.J. Waker. *Needs and performance requirements for neutron monitoring in the nuclear power industry*. Radiat. Prot. Dosim., 1997. **70**(1-4): p. 67-72.

[117] Y. Eisen, G. Engler, E. Ovadia, Y. Shamai, Z. Baum, Y. Levi. *A small size neutron and gamma dosemeter with a single silicon surface barrier detector*. Radiat. Prot. Dosim., 1986. **15**(1): p. 15-30.

[118] GEANT4. *Geant4 User's Documents: Introduction to Geant4*. [Web page] [cited 27th Dicember, 2011]; Available from: http://geant4.web.cern.ch/geant4/support/introductionToGeant4.shtml.

[119] S. Agostinelli, *et al. G4--a simulation toolkit.* Nucl. Instrum. Methods in Phys. Res. A: Accel. Spectrom. Detect. Assoc. Equip, 2003. **506**(3): p. 250-303.

[120] J. Allison, *et al. Geant4 developments and applications.* IEEE Trans. Nucl. Sci, 2006. **53**(1): p. 270-278.

[121] GEANT4. *GEANT4 collaboration*. [Web page] [cited 15th June, 2010]; Available from: http://geant4.cern.ch/collaboration/index.shtml.

[122] GEANT4. *GEANT4 homepage*. [Web page] [cited 15th June, 2010]; Available from: http://geant4.cern.ch/.

[123] CLHEP. *CLHEP homepage*. [Web page] [cited 15th June, 2010]; Available from: http://proj-clhep.web.cern.ch/proj-clhep/.

[124] F. James. *A review of pseudorandom number generators.* Computer Physics Communications, 1990. **60**(3): p. 329-344.

[125] D.E. Cullen, J.H. Hubbell, L. Kissel. *EPDL97: the evaluated photon data library, '97 version.* UCRL-50400, 1997. **6**(5): p. 1-28.

[126] S.T. Perkins, D.E. Cullen, S.M. Seltzer. *Tables and graphs of electron-interaction cross sections from 10 eV to 100 GeV derived from the LLNL Evaluated Electron Data Library (EEDL), Z = 1 to 100.* UCRL-50400, 1991. **31**.

[127] S.T. Perkins, M.H. Chen, D.E. Cullen, J.H. Hubbell, J. Rathkopf, J. Scofield. *Tables and graphs of atomic subshell and relaxation data derived from the LLNL Evaluated Atomic Data Library (EADL), Z=1-100.* UCRL-50400, 1991. **30**.

[128] H.H. Andersen, J.F. Ziegler. *The stopping and ranges of ions in matter*. Vol. 3. 1977, New York: Pergamon Press.

[129] J.F. Ziegler. *The stopping and ranges of ions in matter*. Vol. 4. 1977, New York: Pergamon Press.

[130] J.F. Ziegler, J.P. Biersack, U. Littmark. *The stopping and ranges of ions in solids*. Vol. 1. 1985, New York: Pergamon Press.

[131] ICRU. *Stopping Powers and Ranges for Protons and Alpha Particles.* Journal of the ICRU, 1993. **Report 49**.

[132] B. Crasemann. *Atomic inner-shell processes*. Vol. 2. 1975: Academic Press.

[133] IAEA. *Fusion Evaluated Nuclear Data Library*. [Web page] [cited 17th June, 2010]; Available from: http://www-nds.iaea.org/fendl/index.html.

[134] NNDC. *Evaluated Nuclear Data File*. [Web page] [cited 17th June, 2010]; Available from: http://www.nndc.bnl.gov/exfor/endf00.jsp.

[135] JAEA. *Japanese Evaluated Nuclear Data Library*. [Web page] [cited 17th June, 2010]; Available from: http://wwwndc.jaea.go.jp/jendl/jendl.html.

[136] CJD. *Russian Nuclear Data Center*. [Web page] [cited 17th June, 2010]; Available from: http://www.ippe.obninsk.ru/podr/cjd/.

[137] OECD. *NEA Joint Evaluated Fission and Fusion* [Web page] [cited 17th June, 2010]; Available from: http://www.nea.fr/dbdata/projects/nds_jef.htm.

[138] CENDL. *China Institute of Atomic Energy*. [Web page] [cited 17th June, 2010]; Available from: http://www.ciae.ac.cn/default.jsp.

[139] Y.N. Shubin, V.P. Lunev, A.Y. Konobeyev, A.I. Ditjuk. *Cross-section data library MENDL-2 to study activation as transmutation of materials irradiated*

by nucleons of intermediate energies. International Atomic Energy Agency, 1995. **IAEA-NDS-136**(Rev. 1).

[140] GEANT4. *GEANT4 user's guide for application developers*. Vol. 9.2.1. 2009. 1-317.

[141] GEANT4. *Physics reference manual*. Vol. 9.2. 2008. 1-533.

[142] NIST. *NIST meterial compostion*. [Web page] [cited from, 2008-2010]; Available from: http://physics.nist.gov/cgi-bin/Star/compos.pl?matno=223.

[143] NIST. *NIST atomic weights and isotopic composition*. [Web page] [cited from, 2008-2010]; Available from: http://www.nist.gov/physlab/data/comp.cfm.

[144] A.B. Rosenfeld, *et al. Edge-on Face-to-Face MOSFET for Synchrotron Microbeam Dosimetry: MC Modeling.* IEEE Trans. Nucl. Sci, 2005. **52**(6): p. 2562-2569.

[145] NIST. *Tables of X-ray mass attenuation coefficients and mass energy-absorption coefficients*. [Web page] [cited from, 2007-2010]; Available from: http://www.nist.gov/physlab/data/xraycoef/index.cfm.

[146] A.B. Rosenfeld, G.I. Kaplan, M.G. Carolan, B.J. Allen, R. Maughan, M. Yudelev, C. Kota, J. Coderre. *Simultaneous macro and micro dosimetry with MOSFETs.* IEEE Trans. Nucl. Sci, 1996. **43**(6): p. 2693-2700.

[147] G.I. Kaplan, A.B. Rosenfeld, B.J. Allen, J.A. Coderre, H.B. Liu. *Fission converter and metal--oxide--semiconductor field effect transistor study of thermal neutron flux distribution in an epithermal neutron therapy beam.* Med. Phys., 1999. **26**(9): p. 1989-1994.

[148] R. Nowotny, A. Hvfer. *Programm für die Berechnung von diagnostischen Roentgenspektren.* Fortschr Roentgenstr, 1985. **142**: p. 685-689.

[149] C.M. Dozier, D.B. Brown. *Effect of Photon Energy on the Response of MOS Devices.* IEEE Trans. Nucl. Sci, 1981. **28**(6): p. 4137-4141.

[150] D.G. Marinaro, M.A.R. Othman, S. Guatelli, J. Jakubek, S. Pospisil, A.B. Rosenfeld. *The application of pixelated detectors to neutron personnel dosimetry*, in *Joint 6th International Symposium on Protection Against Toxic Substances and 2nd International CBRE Ops Conference*. 2009: Singapore.

[151] NCRP. *National Council on Radiation Protection and Measurements: Protection againts neutron radiation.* NCRP Publications, 1971. **Report 38**.

[152] L. Pinsky, A. Ignatiev, R. Vilalta. *Development of a Medipix2-based space radiation dosimeter.* ISSO Annual Report, 2007: p. 27-32.

[153] L.S. Pinsky, J. Chancellor. *Development of a New Active Personal Dosimeter for Use in Space Radiation Environments*. in *Aerospace Conference, 2007 IEEE*. 2007.

[154] L.S. Pinsky, *et al. Heavy ion charge and velocity resolution with a Medipix-based active Space Radiation Dosimeter*. in *Aerospace Conference, 2010 IEEE*. 2010.

[155] T. Holy, E. Heijne, J. Jakubek, S. Pospisil, J. Uher, Z. Vykydal. *Pattern recognition of tracks induced by individual quanta of ionizing radiation in Medipix2 silicon detector.* Nucl. Instrum. Methods in Phys. Res. A: Accel. Spectrom. Detect. Assoc. Equip, 2008. **591**(1): p. 287-290.

[156] C. Teyssier, J. Bouchami, F. Dallaire, J. Ida´ rraga, C. Leroy, S. Pospısil, J. Solc, O. Scallon, Z. Vykydal. *Performance of the Medipix and Timepix devices for the recognition of electron-gamma radiation fields.* Nucl. Instrum. Methods, 2010.

[157] C. Granja, Z. Vykydal, Y. Kopatch, J. Jakubek, S. Pospísil, S.A. Telezhnikov. *Position-sensitive spectroscopy of 252Cf fission fragments.* Nucl. Instrum. Methods in Phys. Res. A: Accel. Spectrom. Detect. Assoc. Equip, 2007. **574**(3): p. 472-478.

[158] ISO. *Reference neutron radiations–Part 2: calibration fundamentals of radiation protection devices related to the basic quantities characterizing the radiation filed.* ISO 8529-2, 2000.

[159] A. Rosenfeld, G. Kaplan, M. Carolan, B. Allen, I. Anokhin, O. Zinets, V. Khivrich, P.G. Litovchenko. *Application of P-I-N diodes and mosfets for dosimetry in gamma and neutron radiation fields.* Radiat. Prot. Dosim., 1999. **84**(1-4): p. 349-352.

[160] P.G. Litovchenko, L.I. Barabash, V.I. Kuts, A.B. Rosenfeld, I.A. Marusan, M.B. Pinkovska, V.I. Khivrich. *P-channel MOS sensor for neasurement of emergency gamma and neutron irradiation.* Radiat. Prot. Dosim., 1996. **66**(1-4): p. 225-228.

[161] A.B. Rosenfeld, *et al. A new silicon detector for microdosimetry applications in proton therapy.* IEEE Trans. Nucl. Sci, 2000. **47**(4): p. 1386-1394.

APPENDIX

This section describes the contribution made by each author in the journal publications co-authored by the candidate.

1) First publication.

   M.A.R. Othman, D.L. Cutajar, N. Hardcastle, S. Guatelli, A.B. Rosenfeld. *Monte Carlo study of MOSFET packaging, optimised for improved energy response: Single MOSFET filtration.* Radiation Protection. Dosimetry, 141(1):10–17. 2010.

   In this publication candidate did the writing and the simulation, and provided the idea to use the multi-layer filter on the MOSFET sensitive volume. Dr. Cutajar and Dr. Hardcastle helped improve the writing. Dr. Guatelli helped supervising the simulation. Prof. Anatoly articulated the problem of how to flatten energy response of the MOSFET dosimeter using filters, and helped improve the writing.

2) Second publication.

   M.A.R. Othman, D.G. Marinaro, M. Petasecca, S. Guatelli, D.L. Cutajar, M.L.F. Lerch, D.A. Prokopovich, M.I. Reinhard, J. Uher, J. Jakubek, S. Pospisil, A.B. Rosenfeld. *From imaging to dosimetry: GEANT4-based study on the application of Medipix to neutron dosimetry*. Radiation Measurements 45(10): 1355-1358. 2010.

   In this publication candidate did the writing and simulation, constructed the practical geometry for the simulation study and developed the optimisation methods. Dr. Marinaro helped in the Eisen-verification simulation. Prof. Anatoly was the leader of this project, and gave a view of the problem to the candidate to carry out the simulation study. The other team members provided technical advice, writing advice and the Medipix2 for this publication project.

3) Third publication.

   Othman, M.A.R.; Petasecca, M.; Guatelli, S.; Uher, J.; Marinaro, D.G.; Prokopovich, D.A.; Reinhard, M.I.; Lerch, M.L.F.; Jakubek, J.; Pospisil, S.; Rosenfeld, A.B. *Neutron Dosimeter Development Based on Medipix2*. IEEE Transactions on Nuclear Science 57(6): 3456 – 3462. 2010.

   In this publication candidate did the writing and simulation, constructed the practical geometry for simulation and devised the experimental study and the optimisation methods. The candidate prepared the structured polyethylene converter and was actively involved in the experimental discussion. Prof. Anatoly was the leader of this project, and gave a view of the problem to the candidate to carry out the simulation study. Dr. Petasecca and Dr. Uher performed the experimental parts of this publication. The other team members helped by giving technical advice, writing advice and preparation of experimental devices.

Each article is reproduced below.

Radiation Protection Dosimetry (2010), Vol. 141, No. 1, pp. 10–17
Advance Access publication 11 May 2010

doi:10.1093/rpd/ncq144

MONTE CARLO STUDY OF MOSFET PACKAGING, OPTIMISED FOR IMPROVED ENERGY RESPONSE: SINGLE MOSFET FILTRATION

M. A. R. Othman[1,2], D. L. Cutajar[1], N. Hardcastle[1], S. Guatelli[1] and A. B. Rosenfeld[1,*]
[1]Centre for Medical Radiation Physics, University of Wollongong, Northfields Avenue, Wollongong, NSW 2522, Australia
[2]School of Applied Physics, Faculty of Science and Technology, National University of Malaysia, 43600 Bangi, Selangor, Malaysia

*Corresponding author: anatoly@uow.edu.au

Received October 7 2009, revised March 16 2010, accepted April 8 2010

Monte Carlo simulations of the energy response of a conventionally packaged single metal-oxide field effect transistors (MOSFET) detector were performed with the goal of improving MOSFET energy dependence for personal accident or military dosimetry. The MOSFET detector packaging was optimised. Two different 'drop-in' design packages for a single MOSFET detector were modelled and optimised using the GEANT4 Monte Carlo toolkit. Absorbed photon dose simulations of the MOSFET dosemeter placed in free-air response, corresponding to the absorbed doses at depths of 0.07 mm (D_w(0.07)) and 10 mm (D_w(10)) in a water equivalent phantom of size 30 × 30 × 30 cm^3 for photon energies of 0.015–2 MeV were performed. Energy dependence was reduced to within ±60 % for photon energies 0.06–2 MeV for both D_w(0.07) and D_w(10). Variations in the response for photon energies of 15–60 keV were 200 and 330 % for D_w(0.07) and D_w(10), respectively. The obtained energy dependence was reduced compared with that for conventionally packaged MOSFET detectors, which usually exhibit a 500–700 % over-response when used in free-air geometry.

INTRODUCTION

The utility of metal-oxide field effect transistors (MOSFET) as radiation dosemeters was first recognised in 1974 by Holmes-Siedle for applications in space dosimetry(1). This recognition was followed by the successful application of MOSFET dosemeter in radiotherapy(2–4), radiation monitoring in mixed gamma and neutron fields(5, 6) and space radiation monitoring(7–9).

MOSFETs consist of a drain, source and gate on a silicon (Si) substrate, as shown in Figure 1. The thin layer of silicon oxide (SiO_2) is grown on the top surface of the Si substrate. Metal such as aluminium is deposited on top of the SiO_2 forming the gate. As a dosemeter, the MOSFET operates with either no applied gate voltage (passive mode) or with a bias voltage applied to the gate (active mode). Active mode with positive bias on the gate offers greater sensitivity in radiation detection than passive mode(10). MOSFETs record ionising radiation dose in the SiO_2 in the manner of charge trapping in the SiO_2 and interface charge build-up. When ionising radiation interacts with the SiO_2 gate oxide, electron-hole (e-h) pairs are formed. For the MOSFET in passive mode or active mode when positive bias on the gate, holes produced by ionising radiation are swept towards the Si–SiO_2 interface, where they are captured on traps producing a positive sheet of charge. This charge leads to a negative shift in the gate voltage (ΔV_{th}) required to maintain a fixed current in a MOSFET channel. The threshold voltage shift is proportional to the absorbed dose in the SiO_2. More detailed theory of MOSFET dosimetry can be found in ref. (11). The change in threshold voltage (ΔV_{th}) in a MOSFET is almost linear with low accumulated absorbed dose, D, and can be described as $\Delta V_{th} = \alpha \bullet D$, where α are experimental parameters.

The small size of the MOSFET dosemeter sensitive volume (SV), the ability to work in either passive or active mode, real-time or off-line readout make the MOSFET an ideal dosemeter for *in vivo* mini-dosimetry in radiation therapy and radiation diagnostics(4, 12, 13). Additionally, the MOSFET is an excellent candidate for personal dosimetry, in particular for instantaneous gamma dose assessment in accident and military dosimetry where radiation can be of a pulsed nature. The challenges in utilising the MOSFET for personal dosimetry are the low sensitivity in comparison with TLD detectors and energy dependence relative to tissue dose response. The former problem can be addressed with stacked MOSFETs(14) and is not as important for accident and military dosimetry, where the absorbed doses of interest are >0.01 Gy. Regarding the latter, MOSFET dosemeters have been successfully used

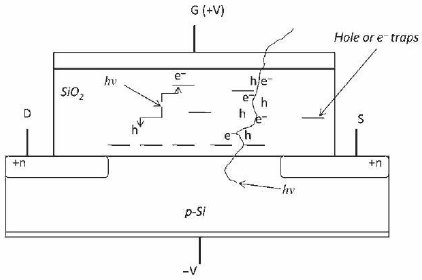

Figure 1. MOSFET structure, showing energy deposition directly by photons or indirectly through secondary electrons.

for military dosimetry, for example, in the USA army wrist watch dosemeter RADIACS AN/PDR-75[15] and in conjunction with a p-i-n diode neutron dosemeter in RADIACS AN/UDR-13[16]. In these applications, the MOSFET dosemeter is being used in close to free-air geometry, as it can be worn on a belt, wrist, 'tie-clip' or placed in free air around nuclear facilities. Optimisation of the energy response of the MOSFET dosemeter suitable for operational quantities for personal monitoring of $H_s(007)$ and $H_p(10)$ in a photon field in such applications is not a trivial task.

In previous work, MOSFET chips were packed in commercially available microelectronic packages DIL, TO-5, TO-8, which are not optimal and less suitable in the achievement of tissue-equivalent (TE) penetrating dose response being irradiated in free-air geometry. An early attempt to characterise the MOSFET energy response for use as a military personal dosemeter, which should be photon-energy independent over the range of 80 keV–1 MeV, was undertaken by Brucker *et al.*[17] In order for MOSFETs to be viable as personal accidents dosemeters, particularly in detecting skin absorbed dose from low-energy photons, the minimum photon energy should be 15 keV, as in radiation fields a large proportion of scattered photons have a lower energy than 80 keV. Thus, 15-keV minimum photon energy should be considered in designing of the MOSFET package and simulating its energy response.

MOSFET detectors have been shown to exhibit an over-response for low-energy photons in free-air geometry, particularly <100 keV[18]. This over-response is an effect of the dose enhancement due to a high atomic number packaging and stronger photoelectric interactions in SiO_2 compared with tissue. This over-response has been ascertained previously either experimentally[19–21] or with Monte Carlo simulation[18, 22]. Initial experimental results by Rosenfeld *et al.*[5] and Brucker *et al.*[17, 23] showed a correlation between the packaging of MOSFET detectors and energy response for effective X-ray energies (average energies in the X-ray spectrum) <250 keV. The observed essential dose enhancement effect was related to excessive creation of secondary electrons from high atomic number materials of the commercial packages and at the aluminium gate electrode of the MOSFET. The experimental attempt of characterisation and adjustment of the energy response of the MOSFET in free-air geometry for photon fields was undertaken for TO-5 packed n-MOSFETs with removed kovar lead and MOSFET chip covered with epoxy[5]. In all previous work, the comparison of the response of the MOSFET was performed relative to TE dose in the case of full electronic equilibrium. Additionally, the response of the MOSFET for lower X-ray energies was also affected by LET-dependent recombination of e-h pairs in a plasma track produced by electrons with reduced energies[24].

The aim of this work is to develop a MOSFET personal accident dosemeter for operation in free-air (approximated with a vacuum) geometry, that is, not in a phantom, with tissue response in terms of personal dose equivalent[25] for a large dynamic range of photon energies. The $H_s(0.07)$ and $H_p(10)$ quantities referred to in this study are as recommended by ICRP report 60[26] for external dose protection. The special case of $H_p(d)$, where d is the depth in tissue from the surface in millimetres, is the measured dose equivalent to d millimetres below the point where the dosemeter is worn. Thus, the absolute value of $H_p(d)$ depends on the individual, the particular location on human body, the scoring volume cross-sectional size for measuring $H_p(d)$ as compared with body surface cross section, the size of the incident radiation field and the angle of incident radiation. The standard procedures to derive $H_s(0.07)$ and $H_p(10)$ use conversion factors to convert the air kerma or exposure measured at the surface of the phantom at the point of interest to dose equivalent at particular depth and specified phantom. These conversion factors take into account build-up dose and attenuation. For normally incident photon beams with energies >30 keV, the dose difference between $H_s(0.07)$ and $H_p(10)$ is less than 10 % while for low-energy photons $H_s(0.07)$ can be essentially larger than $H_p(10)$[27].

Previously, measurement of operational quantities for area monitoring of $H'(0.07)$ and $H'(10)$ by Busuoli *et al.*[28] was performed using a $20 \times 20 \times 15\ cm^3$ slab of polymethyl methacrylate (PMMA). This was because a standard phantom for measuring these quantities was unavailable until 1992[29]. To avoid uncertainty in $H_s(0.07)$ and $H_p(10)$ related to different phantom geometry and kerma approximation issues for $H_s(0.07)$[30–32], these were substituted with $D_w(0.07)$ and $D_w(10)$, respectively. These quantities conservatively represent the absorbed photon dose at depth of 0.07 and 10 mm in the $30 \times 30 \times 30$ cm^3 water phantom (close to that recommended in ICRU Report 47[29] of $30 \times 30 \times 15$ cm^3), respectively. Although the quantities $D_w(0.07)$ and $D_w(10)$ as surrogates of $H_s(0.07)$ and $H_p(10)$, respectively, are used, they are still a close approximation.

Simulations have been performed to optimise the MOSFET design and packaging to minimise over-response to low-energy photons up to 15 keV while retaining MOSFET TE dosimetry at high-energy photons. Normalisation both to water and 2 MeV monoenergetic photons to obtain the response, R, was performed according to the following equation.

$$R = \frac{(D_{\mathrm{MOSFET}}/D_{\mathrm{w}})_E}{(D_{\mathrm{MOSFET}}/D_{\mathrm{w}})_{2\mathrm{MeV}}},$$

where D_{MOSFET} is the absorbed dose in SiO_2, D_w is the absorbed dose at depth in water phantom and E is the photon energy.

Previously, the response of the MOSFET with TO-8 packaging in a mixed gamma neutron field has been simulated using the MC code (MCNP4A)[5]. The thickness of the SiO_2 layer was intentionally increased to yield reasonable statistics with computing power of that time; additionally MCNP4A has not been specialised in the modelling of small SV such as gate oxide of the MOSFET. Another attempt was made to simulate full MOSFET packaging using MCNP 4C code[18]; however, the authors admit that standards tallies in MCNP do not accurately determine the absorbed dose in SV. They apply an 'electron track-length dose estimator', in which they first calculated a dose response function for a specific material then used it as modifier to F4 tally (the track length estimator used to determine averaged particle fluence in a volume in MCNP). Other studies have been performed that model the full MOSFET packaging geometry, using codes such as PENELOPE and GEANT4[33–35]. For this study, the GEANT4 version 9.1 MC toolkits were used to model a conventional MOSFET geometry including the SiO_2 SV. No modification of the SV dimensions was required to acquire absorbed dose to sufficient statistical accuracy in the SiO_2, as the GEANT4 code is capable of tracking particles down to 250 eV in very small volumes thus direct tallying of energies deposited inside the SV is viable. The goal of this study was to simulate the MOSFET response to various normally incident monoenergetic photon fields for the optimisation of the packaging over layers above the SV of the single chip MOSFET to engineer an energy independent TE gamma dosemeter. No effects of e-h pair recombination in the SiO_2, or non-linearity of the response associated with radiation damage of the MOSFET were taken into account. This study will yield another new MOSFET packaging design from the centre for personal dosimetry after promising measurements in skin dosimetry with the MO*Skin*[36] in megavolt X-ray radiotherapy applications.

MATERIALS AND METHODS

Optimisation of MOSFET packaging for $D_w(0.07)$ and $D_w(10)$ for $E > 200$ keV

The first consideration in optimising the MOSFET packaging for a wide spectrum of photon energy is to match the MOSFET response to that of water at depth of 0.07 and 10 mm for photon energies >200 keV. Three models of MOSFET packaging geometry have been simulated (shown in Figure 2), conventionally packaged $D_w(0.07)$ optimised packaging (OP-007) and $D_w(10)$ optimised packaging (OP-10). The conventionally packaged MOSFET consists of a $180 \times 270 \times 1$ µm^3 SiO_2 gate layer (SV) on top of a $1000 \times 1000 \times 500$ µm^3 Si substrate, corresponding to the commonly used MOSFET or RADFET chip. This MOSFET chip is mounted on top of a Kapton carrier with thickness of 228 µm, or a thinness of 0.2-mm PC board[33].

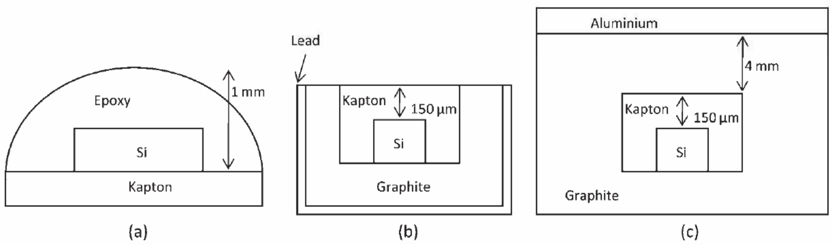

Figure 2. The cross section of three different MOSFET packaging configurations used in this study (**a**) conventional packaging, (**b**) OP-007 and (**c**) OP-10.

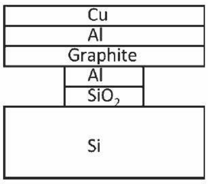

Figure 3. Filter layers on the MOSFET chip in OP-007 and OP-10.

An epoxy bubble semi-sphere covers the whole MOSFET, the structure of which is shown in Figure 2a. For the OP-007 MOSFET, Si substrates of dimension $400 \times 400 \times 375\ \mu m^3$ are embedded inside of the Kapton carrier with thickness of 0.525 mm, named the CMRP MO*Skin* drop-in design(36), the dimensions of which are $1 \times 1 \times 0.525\ mm^3$. The Si substrates are positioned such that distance from the surface of the gate to the Kapton box is approximately 150 μm above the SiO_2 gate. The Kapton is placed inside a graphite box with dimensions of $1.4 \times 1.4 \times 0.75\ mm^3$. A thin lead layer of 20 μm encases the graphite box with the exception of the top surface, see Figure 2b. The OP-10 MOSFET uses the same MOSFET chip and 'drop-in' packaging in the Kapton box as per the OP-007 MOSFET. However, the Kapton carrier is embedded at 4 mm depth within the graphite box of dimensions $10 \times 10 \times 7.5\ mm^3$. An aluminium metal layer with thickness of 500 μm is placed on the top surface of the graphite box. All MOSFETs used in this study have identical SV dimensions and a 1-μm thick aluminium gate layer on top of the SiO_2 gate as shown in Figure 3.

Optimisation of MOSFET packaging for $D_w(0.07)$ and $D_w(10)$ for $E < 200$ keV

To optimise the filter for low-energy photons, two arrangements were modelled. First, a layer of 30-μm thick copper was placed on top of the aluminium gate of the MOSFET, and second, a combination of filters of 30-μm copper, 20-μm aluminium and 50-μm graphite replaced the 30-μm copper layer alone. This configuration, shown in Figure 3, was used additionally to the packaging of the OP-007 and OP-10 as mentioned above.

The GEANT4 simulations

GEANT4 (GEometry ANd Tracking) is a collection of library extensions to the C++ programming language that allows simulation of ionising radiation transport and tracking through complex geometry(37, 38). For this study, the physics processes in the low-energy electromagnetic package were implemented, as they cover particles with energy from 250 eV to 100 GeV. This minimum energy cut is adequate for providing an electron range cut-off, representing the threshold for secondary particle production and particle tracking, down to 0.1 μm range in the SiO_2 SV. Particle cut values were set based on the position and region in the simulation geometry. The closer the region to the SV, the shorter the cut value, down to 0.1 μm range in the SV. This method aimed to reduce computational time while maintaining accuracy of the simulation. The number of histories required to give statistical uncertainties less than 5 % was up to 10^{11} particles. This large number of histories was required as there is a large radiation field to be simulated, which is $100\ mm^2$ cross section (for OP-10) as compared with $0.0504\ mm^2$ cross section of the SV. This study used a larger field than that used by Wang *et al.*(18) and Beck *et al.*(34), thus required more events to achieve the same statistical uncertainty. Panettieri *et al.*(35) reported the largest area of radiation field size ($10 \times 10\ cm^2$) for MOSFET simulation at depth in a water phantom, and at most 7×10^{10} particles were required. However, some modifications were made, particularly the use of variance reduction techniques and a SiO_2 SV 50 times thicker than that used in this study. In this study, the energy of the photons was <2 MeV. As such only the photoelectric effect, multiple scattering, bremsstrahlung production, Rayleigh scattering, Compton scattering, low-energy ionisation and pair production were considered in the physics interaction processes.

For energy response simulations of the MOSFET with the above packaging as on Figure 2b and c, the average absorbed dose in the SiO_2 was compared with both the dose in the water phantom at 0.07 and 10.0 mm depth per primary photon, respectively. For the water phantom simulations, a water phantom with dimensions $30 \times 30 \times 30\ cm^3$ was irradiated with a $10 \times 10\ cm^2$ parallel beam of photons incident perpendicularly to the water surface. The dose scoring volumes were water cuboids with dimensions $10 \times 10 \times 0.01\ mm^3$ at depth of 0.07 and 10.0 mm, placed at the centre of the field. For the MOSFET simulations, each packaged MOSFET OP-007 and OP-10 was irradiated in free-air geometry, approximated with a vacuum with a parallel beam incident on the front face.

RESULTS

Optimisation of MOSFET packaging for $D_w(0.07)$ and $D_w(10)$ for $E > 200$ keV

Figure 4 shows the average absorbed dose per fluence primary photon simulated for incident monoenergetic photons with energy range of 15 keV–2 MeV for different MOSFET configurations and in water at the

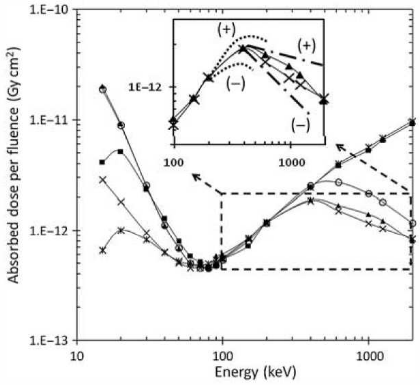

Figure 4. Absorbed dose per primary photon fluence in the sensitive volume of the MOSFET for conventional MOSFET packaging, OP-007 and OP-10, as well as dose in water at depth 0.07 mm and 10 mm. Shown inset are the affects of Kapton thickness and lead coating thickness on the OP-007 response at the peak region and the tail region respectively. (O - conventional MOSFET (x 0.081); ▲- OP-007 MOSFET (x 8.05); ■ - OP-10 MOSFET (x 0.8); X - water dose at depth 0.07 mm; Ж- water dose at depth 10 mm; ..... peak region; — · — · - tail region)

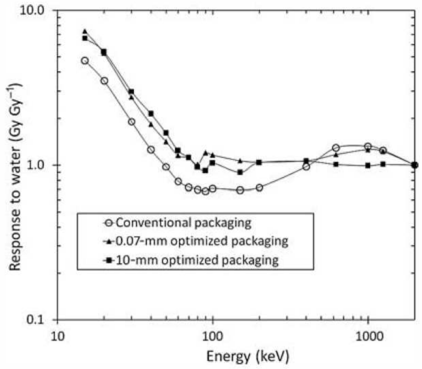

Figure 5. Energy response of the single MOSFET with conventional packaging and OP-007 relative to dose at 0.07 mm depth in water and OP-10 MOSFET relative to dose at 10 mm depth in water. All normalised to ratio of responses at 2 MeV photon energy.

depth of 0.07 and 10 mm. For convenience of comparison, each curve was scaled to the dose per fluence primary photon at 200 keV in the case of water medium for comparison. The errors in simulated doses were within ±5 %. The energy dependence of the absorbed dose per fluence primary photon at depths 0.07 and 10 mm in the water phantom is visible. At low photon energy, the absorbed dose at 0.07 mm depth is higher than at 10 mm depth as lower energy photons deposit their dose at shallower depths. For higher energy photons >200 keV, dose at 0.07 mm less than at 10 mm depth due to lack of charge particle equilibrium (CPE) in the build-up region. Conventional MOSFET packaging shows an over-response for photon energies $E < 100$ keV and >200 keV compared with the dose at 0.07 mm depth in water due to a build-up effect produced by 500-µm thick epoxy bubble above the SiO_2, in contrast to 0.07 mm build-up of water. Both the epoxy bubble in the conventional MOSFET and the 150-µm thick Kapton layer in the OP-007 provide CPE to the SiO_2 layer for energies up to 400 keV and 200 keV, respectively, as shown in Figure 4. In the case of the conventional MOSFET, it is greater than the finding of Wang *et al.*[18], of 200 keV. In comparison to dose deposited at 10 mm depth in water, the conventional MOSFET essentially overestimates dose for photon energies less than about 70 keV due to lack of filtration of low-energy photons while in reasonable agreement for the energy interval of 70–400 keV. For higher photon energies, the response of the conventional MOSFET packaging underestimated the dose in comparison with dose in water at 10 mm depth due to a lack of build up as expected.

Figure 5 shows the relative energy response, *R*, of the conventional MOSFET and OP-007 to water at a depth of 0.07 mm and normalised to the ratio of the MOSFET response to dose in water at the same depth for 2 MeV photons as in the above equation, as well as for the OP-10 MOSFET to water at a depth of 10 mm. While the responses for OP-007 and OP-10 for energies >100 keV are quite constant, for all packages as described above, a similar tendency of increased sensitivity for energy <100 keV has been observed. The highest over-response of the conventional MOSFET in this study is 4.74 for 15 keV photons, which is lower than Wang *et al.*[18] (5.9), due to the different normalisation, where they used normalisation for the reference of free-air exposure with the valid CPE condition. The highest over-response of the OP-007 and OP-10 are 7.36 and 6.62, respectively. The conventional MOSFET could not satisfy both the depth dose in water for energies <70 keV and >400 keV.

Optimisation of MOSFET packaging for $D_w(0.07)$ and $D_w(10)$ for $E < 200$ keV

Figure 6 shows averaged absorbed dose per fluence primary particle for both OP-007 and OP-10 MOSFET with two filtering configurations scaled at 200 keV photon energy. For OP-007, filtration with

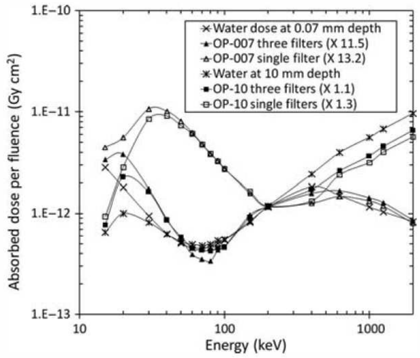

Figure 6. Response of OP-007 and OP-10 MOSFETs with two filtering methods. Shown again the dose to water at depth 0.07 and 10 mm for comparison.

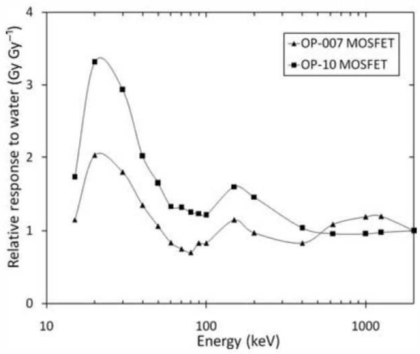

Figure 7. Relative response to water for OP-007 and OP-10 with multilayer filters normalised to 2 MeV photon energy.

a single copper layer initially lowered the absorbed dose in the SV response of 15 keV photons near to that of water. But as the energy of photons increases (>15 keV), more secondary electrons created inside of the copper can reach the SV and deposited dose. Single filtration causes the over-response peak to shift to the higher energy photons, giving a greater over-response (16.61) as compared with unfiltered (7.36). In the three layers filtration method using low atomic number materials, the excess secondary electrons created by intermediate energy photons are stopped, resulting in a finer response shape of dose to water. For the OP-10, the response of the single copper filter again gives too high a dose for 30–40 keV photons, whereas the three layers filtration gives a better dose response to water. At energies >200 keV, the filtered OP-10 results in a lower absorbed dose than that in the water compared with unfiltered, a result of the thicker filter experienced by secondary electrons generated inside the OP-10 packaging that scatter downwards. A larger portion of the absorbed dose in MOSFET chip inside the OP-10 (due to satisfying CPE) is from scattered secondary electron. The relative response to that of water is shown in Figure 7 for both optimised packaging. The OP-007 has a peak over-response (2.03) at 20 keV and lowest under-response (0.70) at 80 keV, whereas, the OP-10 has a peak over-response (3.32) at 20 keV and lowest under-response (0.98) at 662 keV for monoenergetic photon energy.

DISCUSSION

Optimisation of MOSFET packaging for $D_w(0.07)$ and $D_w(10)$ for $E > 200$ keV

The principle of the MOSFET packaging design is a multi-step process. A technologically suitable and reproducible drop-in packaging of the MOSFET chip in a Kapton carrier was developed,[36] which avoids wire bonding of the chip and use of an epoxy bubble. This design improves skin dosimetry allowing a reproducible water equivalent depth of measurement of 0.07 mm. Taking into account that the dosemeter is designed for free-air application the polyamide build-up of 0.07 mm, as was adapted for MO*Skin* is not valid anymore for $D_w(0.07)$ skin dosimetry in a photon field due to the absence of backscattering in contrast to MO*Skin* on the surface of the patient body or phantom. For photons with energies >200 keV, the thickness of the Kapton over layer was chosen to be 150 µm. When the Kapton thickness is increased, the peak as shown in inset of Figure 4 is increased (the plus sign), inversely, the peak is decreased as shown by the minus sign. To account for the contribution of backscattering radiation with an increasing of the photon energy an optimal combination of graphite and lead coating have been modelled on the back of a Kapton strip holding the MOSFET chip. If the Kapton thickness is kept at 150 µm and the lead coating thickness increases, the high-energy response increase as shown in inset of Figure 4 as plus sign, conversely, the high-energy response experiences a decrease, as shown by minus sign. All of these factors make the OP-007 design much complicated as compared with the OP-10 design. These results show almost energy independent response of the OP-007 MOSFET for the photons with energy >200 keV (Figure 5). However, for the conventional MOSFET under-response is obvious due to lack of backscattering.

For the OP-10 MOSFET, it was found that 500 µm thickness of aluminium plus 4 mm of graphite above the SV provide a near-energy independent response for photons with energy >100 keV in comparison with $D_w(10)$ in water while have minimal total packaging thickness. In this design one simply need to meet CPE and attenuation effects at a depth of 10-mm water. The combination of above thicknesses of aluminium and graphite meet both physics requirements under consideration in this study.

Optimisation of MOSFET packaging for $D_w(0.07)$ and $D_w(10)$ for $E < 200$ keV

Further improvement of packaging to remove the over-response of the single MOSFET for $D_w(0.07)$ dosimetry for photons with energy <100 keV can be achieved by optimisation of filters above aluminium electrode gate of the MOSFET. Figure 6 shows the effect of two different filters applied to the OP-007 MOSFET when irradiated with monoenergetic photon beams from 15 keV to 2 MeV. The MOSFET filtered by 30-μm copper alone shows an increase in the relative response over that of water for energies <200 keV. This dose enhancement is due to an increase in photoelectrons generated within the copper layer. Modelling with Monte Carlo has demonstrated that optimisation of energy response is impossible with a single high atomic number filter, due to dose enhancement at intermediate photon energies. The effect of dose enhancement in MOSFET response using high atomic number material filters was observed previously by Rosenfeld *et al.*[5] who found a high atomic number kovar encapsulation enhanced the measured MOSFET dose in a 6 MV photon beam near a water phantom surface. Brucker *et al.*[23] found that they could reduce the dose enhancement due to a high atomic number kovar encapsulation material by using grease between the kovar encapsulation and the MOSFET. However, filtering a MOSFET with a single layer still cannot give a constant response over the range 15–100 keV.

Multiple over layers with a variety of atomic number materials and their thicknesses have been modelled to optimise the energy response for photons >15 keV. The first layer is effectively attenuating low-energy photons while the second is stopping secondary electrons to reduce the dose enhancement for higher photon energies. It has been found that the optimisation of the energy response of the MOSFET for $D_w(0.07)$ and $D_w(10)$ measurements can be achieved by three cover layers above the MOSFET gate Cu-Al-C as presented in Figure 3. This may be achieved using a Cu-C filter >150 μm thickness, although the combination of three filters is a thinner option.

In addition, it is expected that the detectors would have some angular dependence to incident radiation; this will be the subject of future study with prototype detectors.

CONCLUSION

Obtained results have demonstrated the possibility of optimisation of packaging of a single chip MOSFET (OP-007 and OP-10) for measurements of $D_w(0.07)$ and $D_w(10)$ for photons with energies >15 keV. Both filtered packages OP-007 and OP-10 allow an almost energy independent response of the single MOSFET for $D_w(0.07)$ and $D_w(10)$, respectively, for photon energies >100 keV within 20 % for OP-007 and 60 % for OP-10. The response of both packaging would be more consistent in practical use as the small over-response and under-response will compensate each other in the spectrum of photon beams. Whereas, without packaging optimisation, the conventional MOSFET would be incapable in measuring dose $D_w(0.07)$ and $D_w(10)$ for the energy range from 15 keV to 2 MeV in free-air geometry.

ACKNOWLEDGEMENTS

The authors would like to acknowledge Bradley Oborn for assistance with GEANT4 simulations.

FUNDING

One of the authors would like to acknowledge funding assistance from Australian Rotary Health (N. Hardcastle).

REFERENCES

1. Holmes-Siedle, A. *The space charge dosimeter.* Nucl. Instrum. Methods **121**, 169–179 (1974).
2. Qi, Z.-Y., Deng, X.-W., Huang, S.-M., Lu, J., Lerch, M., Cutajar, D. and Rosenfeld, A. *Verification of the plan dosimetry for high dose rate brachytherapy using metal oxide semiconductor field effect transistor detectors.* Med. Phys. **34**, 2007–2013 (2007).
3. Brauer-Krish, E., Bravin, A., Lerch, M. L. F., Rosenfeld, A. B., Stepanek, J., Michael, M. D. and Laissue, J. A. *MOSFET dosimetry for microbeam radiation therapy at the European Synchrotron Radiation Facility.* Med. Phys. **30**, 583–589 (2003).
4. Cygler, J. E., Saoudi, A., Perry, G., Morash, C. and Choan, E. *Feasibility study of using MOSFET detectors for in vivo dosimetry during permanent low-dose-rate prostate implants.* Radiother. Oncol. **80**, 296–301 (2006).
5. Rosenfeld, A. B., Carolan, M. G., Kaplan, G. I., Allen, B. J. and Khivrich, V. I. *MOSFET dosimeters: the role of encapsulation on dosimetric characteristics in mixed gamma-neutron and megavoltage x-ray fields.* IEEE Trans. Nucl. Sci. **42**, 1870–1877 (1995).
6. Ravotti, F., Glaser, M., Rosenfeld, A. B., Lerch, M. L. F., Holmes-Siedle, A. G. and Sarrabayrouse, G. *Radiation monitoring in mixed environments at CERN:*

from the IRRAD6 facility to the LHC experiments. IEEE Trans. Nucl. Sci. **54**, 1170–1177 (2007).
7. Adams, L. and Holmes-Siedle, A. *The development of an MOS dosimetry unit for use in space.* IEEE Trans. Nucl. Sci. **25**, 1607–1612 (1978).
8. Schwank, J. R., Roeske, S. B., Beutler, D. E., Moreno, D. J. and Shaneyfelt, M. R. *A dose rate independent pMOS dosimeter for space applications.* IEEE Trans. Nucl. Sci. **43**, 2671–2678 (1996).
9. Holmes-Siedle, A. *Calibration and flight testing of a low-field pMOS dosimeter.* IEEE Trans. Nucl. Sci. **32**, 4425–4429 (1985).
10. Benson, C., Price, R. A., Silvie, J., Jaksic, A. and Joyce, M. J. *Radiation-induced statistical uncertainty in the threshold voltage measurement of MOSFET dosimeters.* Phys. Med. Biol. **49**, 3145–3159 (2004).
11. Ma, T. P. and Dressendorfer, V. Ionizing Radiation Effects in Mos Devices and Circuits (New York: Wiley) (1989). ISBN: 978-0-471-84893-6.
12. Ramaseshan, R., Kohli, K. S., Zhang, T. J., Lam, T., Norlinger, B., Hallil, A. and Islam, M. *Performance characteristics of a microMOSFET as an in vivo dosimeter in radiation therapy.* Phys. Med. Biol. **49**, 4031–4048 (2004).
13. Ehringfeld, C., Schmid, S., Poljanc, K., Kirisits, C., Aiginger, H. and Georg, D. *Application of commercial MOSFET detectors for in vivo dosimetry in the therapeutic x-ray range from 80 kV to 250 kV.* Phys. Med. Biol. **50**, 289–303 (2005).
14. O'Connell, B., Kelleher, A., Lane, W. and Adams, L. *Stacked RADFETs for increased radiation sensitivity.* IEEE Trans. Nucl. Sci. **43**, 985–990 (1996).
15. Swaja, R. E., Oyan, R., Sims, C. S. and Dooley, M. A. Evaluation of the U.S. army DT-236 Battlefield Personnel Dosimetry System. Oak Ridge National Laboratory. **ORNL-6265**, 1–52 (1986).
16. *Operator's and unit maintenance manual: Radiac set AN/UDR-13.* TM-11-6665-364-12 (1998).
17. Brucker, G. J., Kronenberg, S. and Jordan, T. Tactical army dosimeter based on p-MOS single and dual gate insulators. Proceedings of Radiation and its Effects on Components and Systems, St. Malo, France, 56–62 (1993).
18. Wang, B., Xu, X. G. and Kim, C. H. *Monte carlo study of MOSFET dosemeter characteristics: dose dependence on photon energy, direction and dosemeter composition.* Radiat. Prot. Dosim. **113**, 40–46 (2005).
19. Dozier, C. M. and Brown, D. B. *Photon energy dependence of radiation effects in MOS structures.* IEEE Trans. Nucl. Sci. **26**, 1694–1699 (1980).
20. Kron, T., Duggan, L., Smith, T., Rosenfeld, A. B., Butson, M., Kaplan, G., Howlett, S. and Hyodo, K. *Dose response of various radiation detectors to synchrotron radiation.* Phys. Med. Biol. **43**, 3235–3259 (1998).
21. Edwards, C. R., Green, S., Palethorpe, J. E. and Mountford, P. J. *The response of a MOSFET, p-type semiconductor and LiF TLD to quasi-monoenergetic X-rays.* Phys. Med. Biol. **42**, 2383–2391 (1997).
22. Wang, B., Kim, C. H. and Xu, X. G. *Monte Carlo modeling of a high-sensitivity MOSFET dosimeter for low-and medium-energy photon sources.* Med. Phys. **31**, 1003–1008 (2004).
23. Brucker, G. J., Kronenberg, S. and Gentner, F. *Effects of package geometry, materials, and die design on energy dependence of pMOS dosimeters.* IEEE Trans. Nucl. Sci. **42**, 33–40 (1995).
24. Dozier, C. M. and Brown, D. B. *Effect of photon energy on the response of MOS devices.* IEEE Trans. Nucl. Sci. **28**, 4137–4141 (1981).
25. Alves, J. G. *Developments in standards and other guidance for individual monitoring.* Radiat. Meas. **43**, 558–564 (2008).
26. ICRP. *The system of protection for proposed and continuing practices.* Ann. ICRP. 21, 32–49 (1991).
27. Pradhan, A. S. *Letter to the editor.* Radiat. Prot. Dosim. **42**, 133–134 (1992).
28. Busuoli, G., Cavallini, A., Klamert, V. and Monteventi, F. *Preliminary results of some tests on the use of the dose equivalent operational quantities for some dosimetric systems.* Radiat. Prot. Dosim. **28**, 97–100 (1989).
29. ICRU. *ICRU measurement of dose equivalents from external photon and electron radiations.* ICRU Report 47 (1992).
30. Chao, T. C., Bozkurt, A. and Xu, X. G. *Conversion coefficients based on the VIP-Man anatomical model and EGS4-VLSI code for external monoenergetic photons from 10 keV to 10 MeV.* Health Phys. **81**, 163–183 (2001).
31. Kramer, R., Vieira, J. W., Khoury, H. J., Lima, F. R. A. and Fuelle, D. *All about MAX: a male adult voxel phantom for Monte Carlo calculations in radiation protection dosimetry.* Phys. Med. Biol. **48**, 1239–1262 (2003).
32. Ferrari, P. and Gualdrini, G. *An improved MCNP version of the NORMAN voxel phantom for dosimetry studies.* Phys. Med. Biol. **50**, 4299–4316 (2005).
33. Rosenfeld, A. B. *et al. Edge-on face-to-face MOSFET for synchrotron microbeam dosimetry: MC modeling.* IEEE Trans. Nucl. Sci. **52**, 2562–2569 (2005).
34. Beck, P., Bock, F., Böck, H., Latocha, M., Price, R. A., Rollet, S. and Wind, M. *Investigations on photon energy response of RadFET using Monte Carlo simulations.* IEEE Trans. Nucl. Sci. **54**, 1151–1157 (2007).
35. Panettieri, V., Duch, M. A., Jornet, N., Ginjaume, M., Carrasco, P., Badal, A., Ortega, X. and Ribas, M. *Monte Carlo simulation of MOSFET detectors for high-energy photon beams using the PENELOPE code.* Phys. Med. Biol. **52**, 303–316 (2007).
36. Kwan, I. S. *et al. Skin dosimetry with new MOSFET detectors.* Radiat. Meas. **43**, 929–932 (2008).
37. Agostinelli, S. *et al. G4—a simulation toolkit.* Nucl. Instrum. Methods Phys. Res. A Accel. Spectrom. Detect. Assoc. Equip. **506**, 250–303 (2003).
38. Allison, J. *et al. Geant4 developments and applications.* IEEE Trans. Nucl. Sci. **53**, 270–278 (2006).

Radiation Measurements 45 (2010) 1355–1358

Contents lists available at ScienceDirect

Radiation Measurements

journal homepage: www.elsevier.com/locate/radmeas

From imaging to dosimetry: GEANT4-based study on the application of Medipix to neutron dosimetry

M.A.R. Othman [a], D.G. Marinaro [b], M. Petasecca [a], S. Guatelli [a], D.L. Cutajar [a], M.L.F. Lerch [a], D.A. Prokopovich [a,c], M.I. Reinhard [a,c], J. Uher [d], J. Jakubek [e], S. Pospisil [e], A.B. Rosenfeld [a,*]

[a] *Centre for Medical Radiation Physics, University of Wollongong, Northfield Ave, Wollongong 2522, N.S.W., Australia*
[b] *Defence Science and Technology Organisation, 506 Lorimer St, Fishermans Bend, VIC 3207, Australia*
[c] *ANSTO, New Illawarra Road, Lucas Heights, NSW, Australia*
[d] *CSIRO Process Science and Engineering, New Illawarra Road, Lucas Heights, NSW 2234, Australia*
[e] *Institute of Experimental and Applied Physics, Czech Technical University in Prague, 12800 Prague 2, Czech Republic*

A R T I C L E I N F O

Article history:
Received 18 November 2009
Received in revised form
20 April 2010
Accepted 22 June 2010

Keywords:
Medipix2
Neutron dosimetry
GEANT4

A B S T R A C T

An application of Medipix2 using a newly developed segmented multiple thickness polyethylene (PE) converter for fast neutron detection is presented. The system has the ability to provide an energy independent response for the dose equivalent for fast neutrons. The application of weighting factors to each defined thickness of PE allows for a flattening of the response of the detector system for dosimetry applications. Six PE converter segments were applied, and their thicknesses and weighting factors were optimised to obtain the required energy independent detector response. The study performed by means of GEANT4. Its suitability for neutron dosimetry was studied with respect to a previously published work.

1. Introduction

An important need in neutron dosimetry for radiation protection is a dosimeter with an energy independent response over a broad energy range. Such dosimeters are of great importance for accident and military dosimetry. The dosimeter should be reliable and capable to provide dose rate and total neutron dose equivalent in a mixed gamma-neutron radiation field. Neutron detection with silicon detectors is usually performed indirectly with the assistance of a converter material that converts neutrons into charged particles. The material selected for the converter is usually dependant on the neutron energy under consideration. For thermal neutrons, B-10 can be used to convert thermal neutrons to alpha particles and recoil Li-7 nuclei. For fast neutrons, a hydrogenous material such as polyethylene (PE) can be used to convert fast neutrons to protons through elastic scattering reactions, where the energy of the scattered proton, E_p, is related to the incident neutron energy, E_n, and the scattering angle, θ, by $E_p = E_n \cos^2 \theta$.

There are two main constraints in designing a silicon-based neutron dosimeter for energy independent response; the dependence on neutron energy of both the dose equivalent conversion coefficient (ICRP, 1996) and the proton recoil yield within the PE. Previously, Eisen and co-workers (Eisen et al., 1986) demonstrated a neutron detector with a response variation of a factor of two over an energy range of 1–15 MeV (see Fig. 1). This was achieved by the introduction of a dual thickness PE converter layer on a silicon detector. In this case the response of the silicon detector is limited to single output readout, limiting the potential to apply separate weighting factors to the response of a specific PE thickness.

To discriminate the gamma dose contribution in a mixed gamma-neutron radiation field, the use of a silicon detector requires the application of a discriminator threshold, the value of which will depend on the thickness of the detector and the energy spectrum of the gamma radiation background. This value can be up to 1 MeV for a detector thickness of 350 μm with Co-60 gamma radiation. An even higher threshold value is required to discriminate charged particles produced by elastic and inelastic neutron reactions directly with the silicon nuclei, e.g. nuclei elastically scattered with an energy E_s=(0.133) $E_n \cos^2 \theta$ or inelastic Si(n,α) reactions. Simulated counts for a silicon detector of 300 μm thickness and 14 × 14 mm^2 cross section area in a Co-60 photon beam is shown in Fig. 2. The energy depositions show a significant count rate for energies below 0.4 MeV. For the purpose of military emergency response dosimetry applications, the typical radiation field expected is likely to compromise of a mixed field of neutrons, with maximum E_n = 14 MeV and moderate-to-low energy gamma-

* Corresponding author. Tel.: +61 2 42214574.
E-mail address: anatoly@uow.edu.au (A.B. Rosenfeld).

1350-4487/$ – see front matter © 2010 Elsevier Ltd. All rights reserved.
doi:10.1016/j.radmeas.2010.06.058

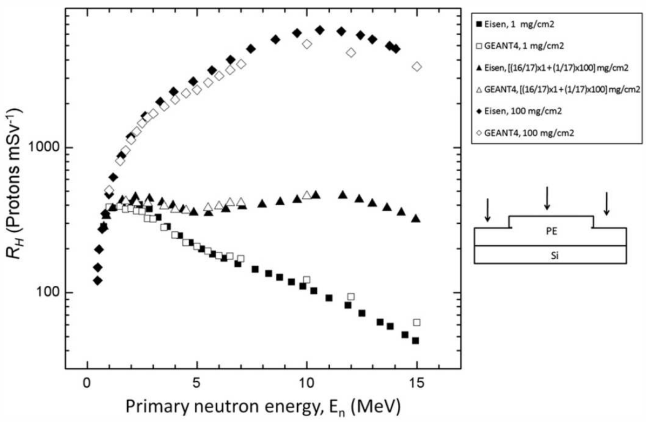

Fig. 1. A previous study (Eisen et al., 1986) using two different thicknesses of PE converter on a silicon detector which show a flattening of the response R_H compared to single thickness of converter. Simulated responses of this result using GEANT4 carried out in this paper show good agreement confirming the GEANT4 model and its implementation used here.

ray components, typical of radioisotopic sources. Low energy (<100 keV) gamma-rays have a higher ratio of photoelectric to Compton scattering cross section than for gamma-rays as simulated in Fig. 2, so a higher background count is anticipated.

2. Pixelated neutron dosimetry approach

The aim of this study is to design a neutron dosimeter that is energy independent to fast neutrons in the range of 0.3–15 MeV achieved through the use of a multiple PE thickness converter with multiple signal readout. In Fig. 3 the configuration of a multi-thickness PE converter placed above a pixelated silicon detector is shown. The particular area segments that have a PE layer are denoted by R_i. A region of bare silicon is denoted by R_0.

Detecting lower energy neutrons at ~0.3 MeV requires a lowering of the discriminator threshold value. Subtraction of the background response R_0 from the R_i segments (denoted as $R'_{\Phi,i}$) can instead be used to obtain the recoil proton only component as shown in Equation (1). This allows elimination of counts produced by the gamma-ray component of the field and Si(n,α) interactions. The recoil proton counts can be expressed as

$$R_{\Phi,i} = \left(R'_{\Phi,i} - (A_i/A_0)R_{\Phi,0}\right)\Big/\Phi_n, \quad (1)$$

where $R_{\Phi,i}$ is the proton counts per neutron fluence, $R'_{\Phi,i}$ is the readout counts from segment with thickness i, $R_{\Phi,0}$ is the readout counts from the uncovered segment, A_i is the area of the segment with thickness i and A_0 is the area of the uncovered segment area. Φ_n is the primary neutron fluence.

The proposed detector for use with the multiple thickness PE converter layer is a Medipix2 (Medipix2, 2009). Medipix2 is a pixelated silicon detector with a 256 × 256 pixel array. Each pixel

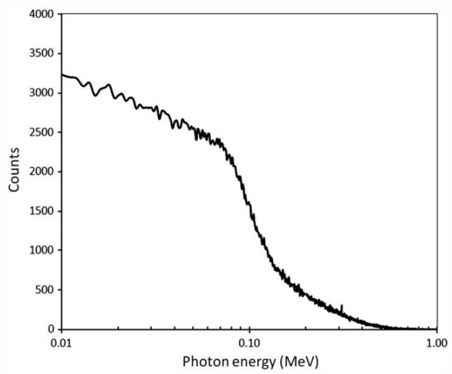

Fig. 2. A GEANT4 (Allison et al., 2006) simulated counts of the multi-channel analyzer in a silicon detector of dimensions 0.3 × 14 × 14 mm^3 for Co-60 energy gamma-ray photons. Energy bins of 1 keV width where employed.

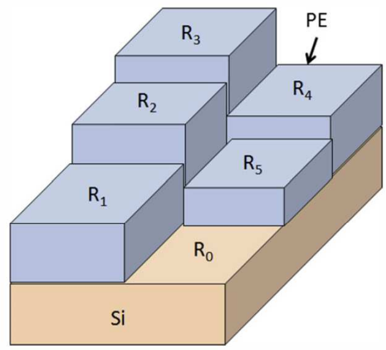

Fig. 3. Multiple PE thicknesses on a silicon surface provide the freedom to adjust the energy response of the silicon detector as required to achieve a neutron energy independent response. R_i is a segment with the converter thickness i, and the uncovered segment is denoted by R_0.

is read out independently by a bump-bounded readout application specific integrated circuit (ASIC) chip. The advantage of this detector system for the neutron dosimetry application is the ability to independently read out different pixels corresponding to different PE thicknesses. Small pixels of area 55 × 55 μm^2 promise high spatial resolution for correctly associating particular signals with the appropriate PE converter layer. Medipix2 is read out in a counting mode with a logic signal assignment to each event. A "1" state corresponds to events lying within a predetermined upper and lower threshold range and a "0" state for other events. The achievable count rate of Medipix2 is 1 GHz. The large active area of 14 × 14 mm^2 allows a high detection efficiency to be achieved as required for radiation protection related neutron dosimetry applications.

3. The GEANT4 application

GEANT4 (Allison et al., 2006) is a Monte Carlo Toolkit for radiation transport simulations. GEANT4 provides advance functionality in geometry modelling, important for a detailed detector description, complemented by a sophisticated physics component, crucial to model accurately the interactions of neutrons and its secondary particles in matter. GEANT4 9.2.p01 release was used in this study. The QGSP_BIC_HP physics list provided within the release was adopted.

A GEANT4 application was developed in this study to characterise the neutron dosimeter. Medipix2 was modelled as a silicon substrate with thickness equal to 300 μm and area equal to 14 × 14 mm^2. 256 × 256 sensitive volume cells were defined across the surface area corresponding with the physical pixels of the Medipix2 system. The pixels were clustered into 25 segments, each with ~3 × 3 mm^2 cross section areas. A dead layer of several microns on the surface of the silicon detector was not modelled in the simulation as there was no detailed technical information available. The PE layer consisted of six different thicknesses occupying four of the segments with different area as depicted in Fig. 4. Parallel mono-energetic neutron beams, with energy from 0.3 to 15 MeV, incident normally on the detector surface were simulated. When an energy deposition event occurred with energy greater than 6 keV in a segment, it was counted as a single event. To reduce the cross talk between adjacent segments, each readout area was defined to be smaller than the total segment area, as shown in Fig. 4. The proton count per neutron fluence was obtained using Equation (1).

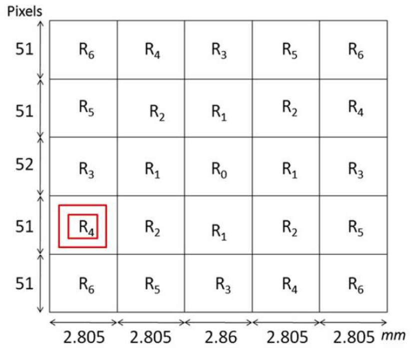

Fig. 4. Arrangement of different thicknesses of PE converter on the Medipix2 surface. PE thicknesses of 0.01, 0.03, 0.05, 0.1, 0.3 and 1 mm were used labelled as R_1, R_2, R_3, R_4, R_5 and R_6 respectively. The R_0 was the uncovered area used to subtract background events associated with gamma-rays and direct neutron interactions with the silicon nuclei. The red boxes show possibility of scaling of the readout segments area to reduce cross talk between segments.

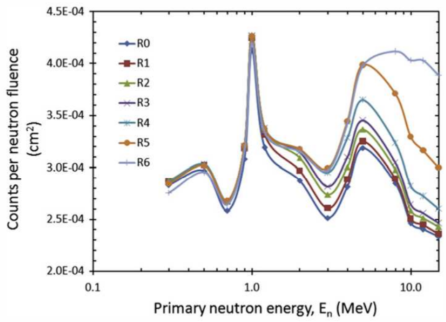

Fig. 5. Count per unit of neutron fluence for each thickness of PE converter as a function of neutron energy. Also shown is the counts from R_0 which corresponds to no converter layer.

A GEANT4 study, addressed to reproduce the Eisen et al. work (Eisen et al., 1986) discussed previously, was performed to check the suitability of GEANT4 for neutron dosimetry (Marinaro et al., 2009). This is integrated by the current on-going validation of GEANT4 with respect to in-house experimental measurements, to quantify the accuracy of GEANT4 for neutron dosimetry.

4. Results and discussions

The detector response in counts per unit neutron fluence as a function of neutron energy for each thickness of PE segment is shown in Fig. 5. The detector response in the absence of the PE converter layer has not been subtracted from the detector response for segments with the PE converter layer. For neutron energies below 1 MeV the detector response for PE converter segments was dominated by the background counts i.e. neutron interactions with the silicon nuclei. At neutron energies from 1 to 15 MeV, for converter layer thicknesses from 0.01 to 0.1 mm a non-negligible contribution of background counts is observed. Only at neutron

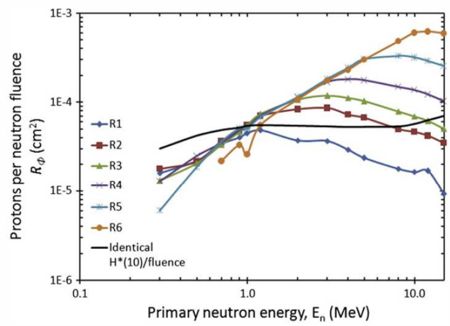

Fig. 6. The proton event counts per unit of neutron fluence for different PE thicknesses as a function of neutron energy after the application of the subtraction method. The black line is the fluence-dose equivalent conversion coefficients taken from ICRP 74.

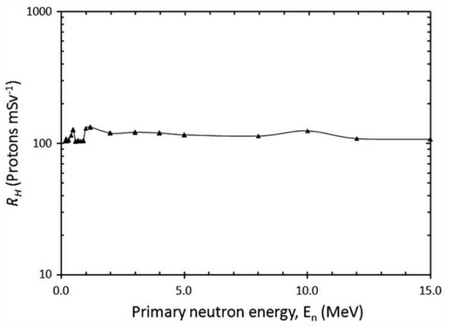

Fig. 7. The neutron ambient dose equivalent response of the Medipix2 detector using a multi-thickness converter layer as a function of neutron energy was found to be reasonable uniform from 0.3 to 15 MeV.

energies above 5 MeV and thicknesses of converter greater than 0.3 mm does the number of counts begin to exceed the background component.

After application of Equation (1), i.e. the subtraction of the area-weighted background counts, does the resulting proton recoil event become evident as shown in Fig. 6. Also shown in Fig. 6 is the ICRP 74 (ICRP, 1996) fluence to dose equivalent conversion coefficients. The response of any single detector segment does not adequately fit the ICRP 74 dose conversion coefficients. This indicates, as previously known, that no single thickness of PE converter can be used to achieve an energy independent detector based on silicon.

Optimisation was performed by taking into account the total response, $R_{\Phi,\mathrm{total}}$, from all PE thicknesses such that the $R_{\Phi,\mathrm{total}}$ response is proportional with the ICRP 74 fluence to ambient dose equivalent conversion coefficients, H^*/Φ. The optimisation function for $R_{\Phi,\mathrm{total}}$ is defined by Equation (2),

$$R_{\Phi,\mathrm{total}}(E) = \sum_{i=1}^{9} \beta_{\Phi,i} R_{\Phi,i}(E), \quad (2)$$

where $R_{\Phi,1}$ to $R_{\Phi,6}$ are the proton count responses from pixels covered by PE of different thickness (Fig. 6) and $R_{\Phi,7}$ to $R_{\Phi,9}$ are the virtual responses given by Equation (3),

$$R_{\Phi,7} = \left(\frac{R_{\Phi,5}}{R_{\Phi,4}}\right) R_{\Phi,1}, R_{\Phi,8} = \left(\frac{R_{\Phi,4}}{R_{\Phi,3}}\right) R_{\Phi,2}, R_{\Phi,9} = \left(\frac{R_{\Phi,2}}{R_{\Phi,3}}\right) R_{\Phi,6}. \quad (3)$$

The $\beta_{\Phi,i}$ are the weighting factors for each partial response. Nine $\beta_{\Phi,i}$ can be found, giving $R_{\Phi,\mathrm{total}}\,(E) \propto [H^*/\Phi](E)$ by solving nine simultaneous linear equations at nine neutron energies. The energies selected were 0.3, 0.7, 1, 2, 3, 4, 5, 8 and 15 MeV. The optimisation of $\beta_{\Phi,i}$ results are 5.984, −6.652, 4.826, −2.437, 0.598, −0.593, −2.89, 1.938 and 0.898 for i from 1 to 9 respectively. The recoil proton response per mSv was obtained from Equation (4),

$$R_H = \frac{R_{\Phi,\mathrm{total}}(E)}{[H^*/\Phi](E)}. \quad (4)$$

Fig. 7 shows that the final detector response as a function of neutron energy is reasonable uniform from 0.3 to 15 MeV as desired. The average response of the detector in terms of the proton count rate was found to be (115 ± 10) per mSv of neutron ambient dose equivalent.

5. Conclusion

A GEANT4 simulation study was performed to investigate a novel approach to neutron dosimetry using a multi-thickness PE converter and multi-channel readout detector. GEANT4 suitability for neutron dosimetry was verified with respect to previously published data and is currently on-going research at Centre for Medical Radiation Physics (CMRP), University of Wollongong. This study showed that the novel device can be used to produce an energy independent response over a range of neutron energies from 0.3 to 15 MeV. The lower energy limit of 0.3 MeV could potentially be reduced to access thermal neutrons with the addition of a B-10 or LiF (Vykydal et al., 2009) converter. This is achievable as the Medipix2 detector has the flexibility to add additional segments to the converter stage, thanks to its readout channel capacity. This new approach could allow the development of a true neutron energy independent detector for radiation protection applications involving neutron fields. The next step in the research will be to develop the multi-thickness PE converter and to conduct first experimental validation.

Acknowledgements

Authors want to acknowledge thanks to MEDIPIX Collaboration (Medipix2, 2009) for Medipix2 detector. This work was supported by funding from the Commonwealth of Australia.

References

Allison, J., Amako, K., Apostolakis, J., Araujo, H., Dubois, P.A., Asai, M., Barrand, G., Capra, R., Chauvie, S., Chytracek, R., et al., 2006. GEANT4 developments and applications. IEEE Trans. Nucl. Sci. 53, 270–278.

Eisen, Y., Engler, G., Ovadia, E., Shamai, Y., Baum, Z., Levi, Y., 1986. A small size neutron and gamma dosemeter with a single silicon surface barrier detector. Radiat. Prot. Dosimetry 15, 15–30.

ICRP, 1996. International Commission on Radiological Protection, ICRP 74. Ann. ICRP 26, 157–205.

Marinaro, D.G., Othman, M.A.R., Guatelli, S., Jakubek, J., Pospisil, S., Rosenfeld, A.B. The application of pixelated detectors to neutron personnel dosimetry. In: Proceedings of Joint sixth International Symposium on protection against Toxic Substances and second International CBRE Ops Conference, Singapore, 8th–11th December, 2009.

Medipix2, 2009. http://medipix.web.cern.ch/MEDIPIX/Medipix2/indexMPIX2.html.

Vykydal, Z., Bouchami, J., Campbell, M., Dolezal, Z., Fiederle, M., Greiffenberg, D., Gutierrez, A., Heijne, E., Holy, T., Idarraga, J., et al., 2009. The Medipix2-based network for measurement of spectral characteristics and composition of radiation in ATLAS detector. Nucl. Instrum. Methods Phys. Res. A 607, 35–37.

Neutron Dosimeter Development Based on Medipix2

Mohd A. R. Othman, M. Petasecca, *Member, IEEE*, S. Guatelli, J. Uher, Damian G. Marinaro, Dale A. Prokopovich, *Member, IEEE*, Mark I. Reinhard, *Member, IEEE*, Michael L. F. Lerch, *Member, IEEE*, J. Jakubek, *Member, IEEE*, S. Pospisil, *Member, IEEE*, and Anatoly B. Rosenfeld, *Senior Member, IEEE*

***Abstract*—A novel neutron dosimetry system for avionics and space applications is described. The new dosimetric system is based on Medipix2, a high density silicon based pixilated detector with integrated readout and digital interface circuitry. Real time dose equivalent response to fast neutron fields with flattened energy response is achieved through the coupling of a structured variable thickness polyethylene (PE) over layer with the high density pixilated detector. Experimental results obtained to 14 MeV D-T and Am-Be neutron fields are described along with a comparison to results obtained with GEANT4 simulations.**

***Index Terms*—GEANT4, Medipix2, neutron dosimetry.**

I. Introduction

EXPOSURE to ionizing radiation in space environments can increase the risk of morbidity and mortality. In addition, radiation damage to electronic components could compromise space mission success and put the wellbeing of the crew at risk. Improving the means to detect and quantify both risk and damage attributable to radiation is an important need.

The radiation environment of space is enhanced relative to that on Earth where the Earth's geomagnetic field and atmosphere provide protection from extra-terrestrial radiation sources. Space radiation is composed of a mix of high energy electrons, protons, and both light and heavy ions [1]. The particles originate from several sources including trapped radiation, galactic cosmic rays (GCR) and solar particle events (SPE). To some extent shielding can be employed to reduce the exposure of astronauts to the primary radiation field. Sufficient shielding to passively attenuate primary radiation to an acceptable level for humans is generally unacceptable from the point of view of spacecraft mass launch limitations. Multilayered shielding can be utilised to reduce the radiobiological effectiveness (RBE) and dose equivalent associated with the secondary radiation field, as well as to address spacecraft weight restrictions. However inadequate shielding design can result in the production of a secondary radiation field which can present greater risk than the primary radiation field on account of enhanced RBE. In an interplanetary mission a female astronaut at age 30 is projected to receive the prescribed limiting dose equivalent equating to a probability of 3% excess fatal cancer at 95% confidence in 54 days. The equivalent duration for a male to reach the same limit is 91 days [2], [3].

Until the early 1990s high-energy heavy ions, such as iron, were considered to be the major radiological hazard. However, Dicello and others [4] noted that secondary neutrons and charged particles of up to several hundred MeV are produced in abundance by the GCR and SPE, as well as the less abundant high energy heavy ions referred as high $-Z$, $-E$ (HZE), as these primary radiations pass through the spacecraft or the astronauts. It was further noted that secondary neutrons, produced from the highly abundant primary protons, could be one of the most biologically damaging radiations encountered in space, perhaps comparable in effect to that of the primary HZEs. There has been a lot of ongoing work towards evaluating the relative consequences of HZEs and secondary neutrons at the NASA Space Radiation Lab (NSRL) at Brookhaven National Laboratory and the Loma Linda Proton Therapy Facility during the past decade. These facilities offer heavy ions from 0.1 to 1 GeV/a.m.u. allowing radiobiological effects of space to be studied. An overview of space related radiobiological results obtained at these dedicated radiation beams are well reviewed in [5].

The importance of personnel dosimetry for astronauts is increasing with planned Lunar and Mars missions where the radiation background is less well known in comparison with low earth orbits (LEO). Given the significance of both neutrons and HZEs in determining the dose equivalent it is important that new methods and instrumentation be developed for determining the dose equivalent in real time. Uncertainties in the RBE of such radiations also need further attention.

One of the existing methods widely adapted for real time dose equivalent measurements in space environments is based on microdosimetry. Microdosimetric spectra convoluted with quality coefficients can provide the RBE of radiation and consequently the dose equivalent [6].

During the last decade efforts have been made to develop a solid state microdosimeter to replace bulky high voltage operated tissue equivalent proportional gas counters (TEPC). The detector is based on silicon-on-insulator (SOI) material with an array of sensitive volumes (SV) of individual size similar to that

Manuscript received July 16, 2010; revised September 06, 2010; accepted September 06, 2010. Date of publication October 07, 2010; date of current version December 15, 2010. This work was supported in part by funding from the Commonwealth Government of Australia.

M. A. R. Othman, M. Petasecca, S. Guatelli, M. L. F. Lerch and A. B. Rosenfeld are with the Centre for Medical Radiations Physics, University of Wollongong, NSW 2522, Australia (e-mail: anatoly@uow.edu.au).

J. Uher is with CSIRO Process Science and Engineering, Lucas Heights, NSW 2234, Australia.

D. A. Prokopovich and M. I. Reinhard are with the Australia Nuclear and Technology Organisation (ANSTO), NSW 2234, Australia and also with the Centre for Medical Radiations Physics, University of Wollongong, NSW 2522, Australia.

D. G. Marinaro is with the Defence Science and Technology Organisation, Fishermans Bend, VIC 3207, Australia.

J. Jakubek and S. Pospisil are with the Institute of Experimental and Applied Physics, Czech Technical University in Prague, 12800 Prague 2, Czech Republic.

Color versions of one or more of the figures in this paper are available online at http://ieeexplore.ieee.org.

Digital Object Identifier 10.1109/TNS.2010.2076837

of biological cells [7]–[12]. The principal advantage of the microdosimetric approach is its applicability to any mixed radiation field including those containing charged particles, neutrons and photons.

We have previously demonstrated good agreement of a SOI microdosimeter with TEPC in a standard neutron radiation field facility at CERN typical of high altitude avionic environments (20 to 25 km above sea level) [13]. This field is dominated by secondary neutrons, produced by interactions of GCRs with the atmosphere [14].

In this work we describe a new approach to dose equivalent neutron dosimetry suitable for mixed radiation field applications in avionics and space.

The novel detector has been realized by coupling an *ad-hoc* PE converter to pixilated detector. This detector was primarily developed for X-ray imaging [15], with more recent adoption to neutron imaging through use of suitable converters [16].

The novel detector measures the neutron dose equivalent by counting proton recoil events within the detector pixels which originate from neutron interactions within a variable thickness PE. The ratio of the detector response to the neutron tissue-equivalent dose is almost independent of the energy of the incident neutrons.

In a previous study [17] we demonstrated the possibility of optimizing the thicknesses of the PE segments by means of a GEANT4 simulation in order to obtain an energy-independent detector response proportional to neutron dose equivalent. This paper describes a complementary study consisting of the validation of the GEANT4 simulation with respect to experimental measurements.

II. Design of the Novel Dosimeter

The detection of fast neutrons using silicon radiation detectors and hydrogenous PE converters is well known based on the detection of the recoil protons resulting from the elastic scattering of neutrons with energy E_n on a stationary proton where the recoil proton is scattered under an angle θ with energy E_p given by, $E_p = E_n \cos^2 \theta$.

However the response of the silicon detector covered with a uniform hydrogenous converter has several shortcomings:

— First, it is a tradeoff between thickness of the converter (efficiency of the dosimeter) and the energy range of the detectable fast neutrons.

— Second, it is not possible to achieve an energy independent response in terms of dose equivalent.

— Third, the deposition of energy from Compton electrons (gamma radiation) and charged particles present within a mixed radiation field, as well as charged particles from $Si(n, x)$ reactions, produce background events which are undistinguishable from recoil proton events.

Attempts have been made to achieve an improvement in energy response of a single silicon detector by coupling a dual layered PE converter of 0.01 and 1 mm thicknesses in a ratio by area of 17:1 [18]. This led to a variation in the dosimeter response counts/Sv of approximately a factor of two within a neutron energy range of 1–15 MeV. Another approach for fast neutron dosimetry was based on a monolithic $\Delta E - E$ detector by Shiraishi [19] coupled with a PE converter. This system allows measurement of the proton energy E_p and angle of scattered proton θ followed by a determination of the neutron energy and dose equivalent using fluence to dose equivalent conversion factors [20]. This system is limited to relatively low neutron energies on account of the need to stop the recoiling proton within the E detector layer to obtain a full energy measurement. For example, for 0.5 mm silicon the sensitivity is limited to protons of energy less than 8 MeV.

Fig. 1. The Medipix2 board; the sensor can be read out through a USB interface by the software Pixelman.

Our approach is based on a pixilated silicon detector and a structured PE converter that allows independent readout of counts under each partial PE converter. Additionally, the uncovered active area of the pixilated detector is used for subtraction of the background events associated with gamma radiation, charged particles from the space radiation environment and products of direct neutron inelastic reactions within the silicon detector material. By optimizing the thicknesses and total area of particular PE segments it is possible to achieve an energy independent neutron dose equivalent response due to the high level of parameterization that is normally impossible with a single bulk silicon detector. With pixilated detectors it is possible to use an additional degree of adjustment by readout of only part of the area under a partial converter which is controllable by software.

The pixilated detector used in this study was the Medipix2 detector developed originally at CERN ([21] and references therein). Recently Medipix2 has been used for high resolution imaging [16] as well as for thermal and fast neutron fluence monitoring in the high energy physics (HEP) detector barrel as a Radiation Damage Monitoring (RDM) system by use of a partial cover of Medipix2 with ^{6}Li and PE converters [22].

The sensor is composed of a 300 μm thick high resistivity silicon substrate organized as a bi-dimensional array of pad diodes with a pitch of 55 μm and a total sensitive area of 14×14 mm^2 (Fig. 1). The array of diodes has been bump-bonded to a 0.25 μm CMOS ASIC with 65536 charge sensitive amplifiers (CSA), digital-to-analog converter (DAC), two discriminator thresholds, pixel configuration register (PCR), shift register and counter (SR/C) and double discriminator logic [23]. Each pixel is independently readout using Pixelman data acquisition software through an USB interface [24].

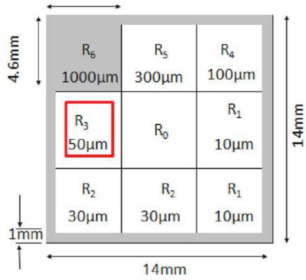

Fig. 2. A simplified arrangement of 3 × 3 segments of different thicknesses of PE converter on the Medipix2 14 × 14 mm^2 active surface area.

III. GEANT4 Simulation and Validation

A. The Simulation Application and Simulated Response

GEANT4 (GEometry ANd Tracking) [25], [26], was adopted as Monte Carlo Simulation Toolkit in this research. GEANT4 describes the interactions of particles with matter, providing advanced functionality in physics and geometry modeling. GEANT4 version 9.2.p01 was used. GEANT4 is a collection of C++ class libraries for radiation transport simulations.

The GEANT4 QGSP_BIC_HP physics list was adopted in this work to describe the electromagnetic and hadronic interactions of the particles involved in the experimental set-up. In particular this physics list uses evaluated cross section databases for neutrons, with energy lower than 20 MeV.

Medipix2 was modelled in GEANT4 with a silicon substrate thickness of 300 μm and a 14 × 14 mm^2 area. 256 × 256 sensitive volume cells were defined across the surface area corresponding with the physical pixels of the Medipix2 system. A dead layer of several microns on the surface of the silicon detector was not modelled in the simulation.

The partial PE converters were selected based on a preliminary analysis which lead to the selection of six different thicknesses of 0.01, 0.03, 0.05, 0.1, 0.3 and 1 mm labelled as R_1, R_2, R_3, R_4, R_5 and R_6 respectively. The layout is presented in Fig. 2. Region R_0 was the uncovered area used to subtract background events associated with gamma-rays, charged particles and products of inelastic neutron interactions with silicon nuclei. The Medipix2 silicon sensitive scoring volume was defined in GEANT4 simulations immediately under each partial PE converter. The red boxes show the possibility of scaling the readout area of each segment to reduce cross talk between segments. This is an additional degree of parameterization allowing adjustment of the energy response of the dosimeter.

Parallel beam primary mono-energetic neutrons with energies from 0.3 to 15 MeV at normal incidence to the detector surface were simulated using the GEANT4 code. Energy deposition events occurring with energies greater than 10 keV in the segments, which is a low energy threshold of the Medipix2 detector, were counted as a single event.

Optimization of the structured converter was performed by taking into account the total response, $R_{\Phi,\mathrm{total}}$, from all partial PE converters such that the $R_{\Phi,\mathrm{total}}$ response is proportional with the ICRP 74 fluence to ambient dose equivalent conversion coefficients, H^*/Φ. This infers that the total number of counts produced by recoil protons per unit dose equivalent in Medipix2 is independent of the neutron energy in the range 0.3–15 MeV. The optimization function for $R_{\Phi,\mathrm{total}}$ is defined by (1)

$$R_{\Phi,\mathrm{total}} = \sum_{i=1}^{9} \beta_{\Phi,i} R_{\Phi,i}(E) \quad (1)$$

$R_{\Phi,1}$ to $R_{\Phi,6}$ are the proton count responses from pixels covered by partial PE of different thickness (Fig. 2) and $R_{\Phi,7}$ to $R_{\Phi,9}$ are the virtual responses given by (2)

$$R_{\Phi,7} = \left(\frac{R_{\Phi,5}}{R_{\Phi,4}}\right) R_{\Phi,1}$$
$$R_{\Phi,8} = \left(\frac{R_{\Phi,4}}{R_{\Phi,3}}\right) R_{\Phi,2}$$
$$R_{\Phi,9} = \left(\frac{R_{\Phi,2}}{R_{\Phi,3}}\right) R_{\Phi,6} \quad (2)$$

$\beta_{\Phi,i}$ are the weighting factors for each partial response. The recoil proton counts can be expressed as in (3).

$$R_{\Phi,i} = (R'_{\Phi,i} - (A_i/A_0)R_{\Phi,0})/\Phi_n \quad (3)$$

$R_{\Phi,i}$ and $R'_{\Phi,i}$ are the proton counts and total event counts respectively per neutron fluence under a partial PE segment with thickness i. $R_{\Phi,0}$ is the readout counts from the uncovered segment, A_i is the area of the segment with thickness i and A_0 is the area of the uncovered segment area. Φ_n is the primary neutron fluence.

Virtual responses $R_{\Phi,7}$ to $R_{\Phi,9}$ were introduced for fine tuning of the low energy response (< 1 MeV) and can be neglected in most practical situations, leaving six terms in (1). The energy response of a neutron dosimeter based on Medipix2 with a structured PE converter optimized and modelled with GEANT4 is presented in Fig. 3. The flatness of the neutron energy response was $\pm 9\%$ in the energy range 0.3–15 MeV. This is a substantially better flatness than that achievable with known neutron dosimeters based on a single silicon detector and PE converter.

B. Validation of the GEANT4 Simulation Application and Radiation Setup

In order to quantify the accuracy of the results deriving from the GEANT4 simulation study adopted to optimize the design of the PE layer structure, we validated the GEANT4 application with respect to experimental measurements.

For testing purposes we modeled in the simulation the response of a simplified detector set up with a uniform PE converter to neutrons, exposed to a D-T generator and an Am-Be source.

Fig. 4 shows the experimental set-up of the Medipix2 detector. A significant issue for a neutron dosimeter is the evaluation of the neutron events while separating the background radiation generated, for example, by alphas, gammas and electrons. The use of a large area and high density pixilated detector such as the Medipix2 (with cross section equal to 14 × 14 mm^2 and

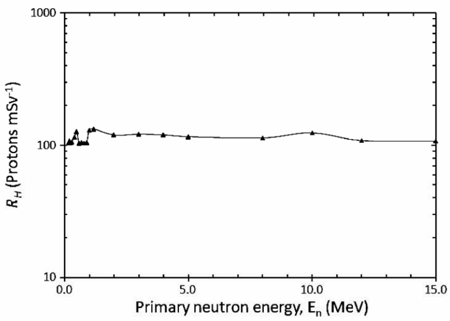

Fig. 3. Dose equivalent energy response of simulated neutron dosimeter with structured PE converter according to (1).

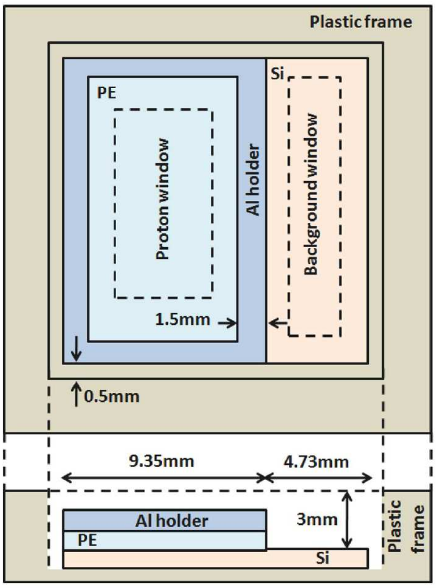

Fig. 4. The Medipix2 with partial PE converter on top of the silicon sensor and uncovered area modeled with GEANT4 (front and side views).

with 65536 pixels) enables the creation of two distinct portions of the sensitive areas to address this issue. Thus the Medipix2 detector is only partially covered with a uniform PE converter layer, noted as SV1 (the proton window), with the reminder left uncovered, noted as SV2 (the background window), and this structure was modeled in the GEANT4 simulation.

The Medipix2 was modeled as a $14.08 \times 14.08 \times 0.3$ mm^3 silicon sensor with 256×256 sensitive volumes, with size $0.055 \times 0.055 \times 0.3$ mm^3. The ASIC chip beneath the silicon sensor was modeled as a silicon slab of size $14.08 \times 14.08 \times 1.5$ mm^3. The PE converter was modeled as a polyethylene slab with thicknesses of 0.1, 0.25, 0.5 and 1 mm, each with a cross section of 9.35×14.08 mm^2. The aluminum holder surrounding the PE converter has been engineered to ensure the converter is rigid and flat, and to minimize air gaps between the PE converter and silicon surface (Fig. 4).

The neutrons are generated as a parallel beam incident normally to the detector. The energy of the neutrons from a simulated D-T source was modeled with a Gaussian distribution, with mean value of 14 MeV and σ of 0.01 MeV and 0.5 MeV. The energy of the neutrons of the Am-Be-source was modeled with the energy spectrum recommended in [27].

QGSP_BIC_HP physics list was used. The threshold of production of secondary particles was fixed equal to 5 μm in range within the sensitive regions SV1 and SV2. In order to reduce the execution times of the simulation without affecting the accuracy of the simulation results, the threshold was set higher outside regions SV1 and SV2.

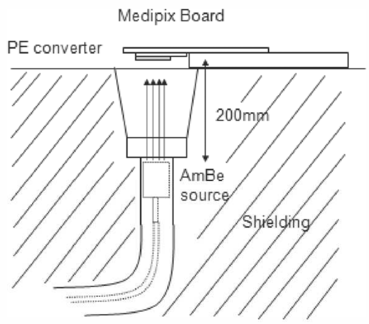

Fig. 5. Irradiation setup on Am-Be neutron source.

IV. Experimental Results and Discussion

A. Simplified Setup for GEANT4 Validation

Experiments were carried out on 14 MeV D-T and Am-Be neutron sources at Australia's Commonwealth Scientific and Industrial Research Organisation (CSIRO).

The device was irradiated with 14 MeV neutrons from a D-T generator Thermo A-3062. The distance between the D-T generator and the detector was 55 cm. The emission rate of the D-T generator was 8.6×10^7 n/s into the full solid angle, thus the neutron intensity at the tested detector (area of 1.4×1.4 cm^2) was calculated at 2100 n/s. The D-T generator emission rate was estimated using a $2 \times 2 \times 2$ cm^3 plastic scintillator (EJ 204) attached to a photomultiplier (Photonis XP2020). The detection efficiency of 3.9% of the scintillator for 14 MeV neutrons was approximated by an analytical calculation. The measured neutron flux was in good agreement with the calculated figure.

Fig. 5 shows the irradiation set up on the Am-Be neutron source. The Medipix2 detector was placed on top of the collimator of the Am-Be neutron source container at a distance of 20 cm from the source when in the irradiation position. The PE converter attached to the silicon sensor was faced down normally to the neutron beam. Neutron emission in 4π was 9.3×10^6

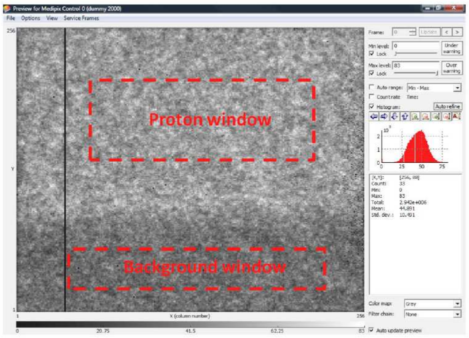

Fig. 6. The events results from fast neutron irradiation. The black line was the dead pixels. The counting windows under PE layer and uncovered area were denoted as proton windows and background windows, respectively.

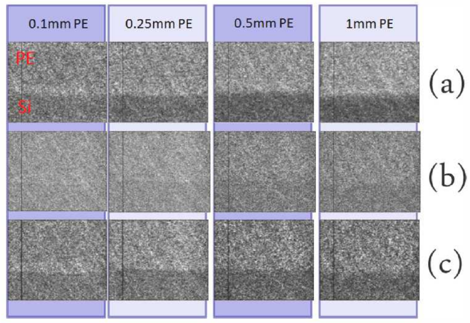

Fig. 7. The total event represented in grey scale modulated image as in Fig. 6. The bright areas show high event counts under PE layer.

n/s calculated based on the activity of the source on the day of the experiment. When not in use the neutron source was kept in boronated paraffin shielding.

The physical construction of the PE converter layer on the Medipix2 detector was as described in Section III.B. The PE converter occupied two-thirds of the active area of the detector, while the other area was uncovered for estimation of the background. A square aluminum frame of $9 \times 14 \times 1$ mm^3 has been used to hold the PE layer attached at the surface of the detector and to minimize the air gap and misalignment between the converter and the silicon substrate (Fig. 4). Four PE thicknesses as modeled in the GEANT4-based study described in Section III.B have been used during the irradiation with the neutron sources. The PE converters were 0.1, 0.25, 0.5 and 1 mm thick.

The detector was placed immediately in front of the neutron source window for both fields with neutrons normally incident to the sensor surface. The experiment was repeated for each thickness of PE using the same Medipix2 detector with the same neutron fluence and geometry of experiment. The data acquisition was based on a USB interface readout by the Pixelman software developed by the Medipix collaboration that provides several analyses and setting tools for use during data acquisition and for data post-processing. During the acquisition the parameters were set to retrieve all data out of the chip from the entire sensitive area.

Fig. 6 shows a screenshot generated by the Pixelman software, representing a grey-scale modulated image of the events in the Medipix2 detector within the SV1 and SV2 areas. A clear difference can be observed between the number of events in the regions of the detector covered by PE (recoil protons and background) and uncovered (background only). Proton and background windows, which were also used in the simulations, are represented in Fig. 6 with a broken red outline. Using these regions inside of SV1 and SV2 inhibits cross-talk, where scattering events from one region are counted in another, therefore improving the accuracy of the neutron response evaluation.

Fig. 7 shows a comparison of the event images for different thicknesses of PE converters irradiated with D-T and Am-Be neutrons. The difference in efficiency of the PE converters of different thicknesses is clearly visible, particularly the increase in efficiency with increased converter thickness observed for exposures with the high energy 14 MeV neutrons (Fig. 7(a)).

Fig. 7(b) and (c) show the event images for the same thicknesses of PE converters but irradiated with neutrons from an Am-Be source, which has a lower average neutron energy ($\sim$ 4.2 MeV) than the D-T source and higher gamma background. This is observed in Fig. 7(b), where due to the larger gamma background the boundary between the SV1 and SV2 regions is not as clear.

In the mixed radiation fields of these experimental setups there were other contributions to the event counts in both counting windows associated with backscattered neutrons, secondary charged particles and a gamma background (Fig. 7). Secondary charged particles, like alphas, contributed the least effect to the counts as they are easily stopped in air. The backscattered neutrons have an almost equal effect on both counting windows as the back of the Medipix2 detector has uniform layers of material.

It is possible to improve the contrast in Fig. 7(b) using features of the Pixelman software that allow filtering of events depending on pixel cluster sizing, which is related to LET of the incident particle. Gamma radiation with low energy photons will deposit energy within a single pixel, whereas higher energy photons will create long tracks due to the higher energy of secondary electrons resulting in energy depositions within more than one pixel [28]. This allows the removal of events corresponding to low energy photons for example which deposit energy in a single pixel only. Fig. 7(c) corresponds to the events of Fig. 7(b) after filtering out events with a cluster size less than 7 pixels. In this case the recoil proton contribution becomes more obvious, which is a further advantage of this dosimeter. Thus the application of cluster size filtration to the experimental data in addition to the background window subtraction method provides improved response of the Medipix2 to neutrons only.

In this study the net proton counts were calculated by subtracting the background counts according to (3) after preliminary cluster size filtration, allowing comparison of the counts produced by recoil protons only for each partial converter. The

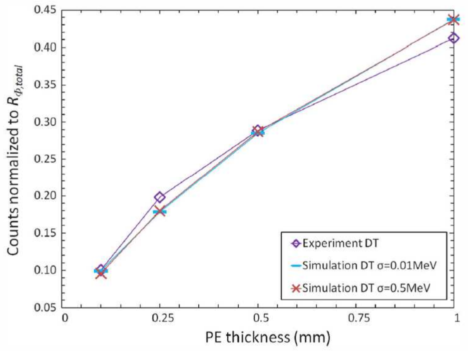

Fig. 8. The comparison of the experimental result of the 14 MeV D-T neutron to that of simulations using Gaussian spectrum of mean 14 MeV and σ of 0.01 and 0.5 MeV.

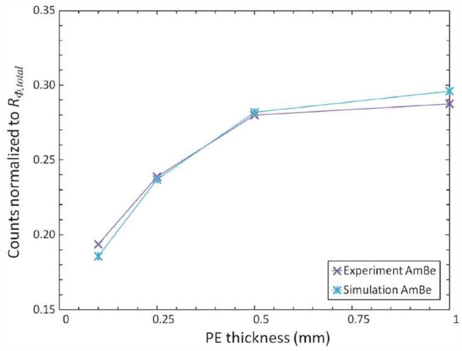

Fig. 9. The comparison of the experimental result of the Am-Be neutron to that of simulation.

response of each converter was normalized to the total number of counts of all converters for the same neutron fluence irradiation as presented in (4). It was used for both the GEANT4 simulations and experiments with D-T and Am-Be sources

$$R_{\Phi,\mathrm{total}} = \sum_{i=1}^{4} R_{\Phi,i}. \quad (4)$$

The data from both neutron field experiments was analyzed further to filter out clusters with a size below seven pixels, which as discussed, removes the background contribution due to the gamma beam that was not included in the GEANT4 simulations.

B. GEANT4 Validation Study Results

Figs. 8 and 9 present the variation of the normalized recoil proton response of the Medipix2 detector with different PE converter thicknesses, showing the direct comparison of the simulation and experiment results for the irradiation with D-T and Am-Be neutron sources, respectively.

For both neutron sources agreement with GEANT4 simulations was within 10%. Error bars for experimental results were too small to be presented resulting from the large number of counts from recoil protons. The detector responses for PE converters with thicknesses of 1 and 0.5 mm in Fig. 9 are not significantly different due to the low average range of the recoil protons produced by neutrons from the Am-Be source. This is in contrast to the behavior of the detector response for 14 MeV neutrons from the D-T source.

The observed agreement between the experimental and simulated results of the dosimeter responses for four PE converters with distinct thicknesses demonstrates the validity of the GEANT4 simulation and of the implemented model of Medipix2 with PE converters. This lends confidence to the optimization procedure, demonstrating that the application of a structured PE converter to a pixilated detector can produce a neutron dosimeter with an energy independent response in the energy range 0.3–15 MeV to within 10%.

A further strength of the application of a pixilated detector such as Medipix2 coupled to structured PE converter for neutron dosimetry is the potential for self-calibration. The optimization process described can be automated being run by an *add-on* software algorithm that automatically adjusts parameters based upon the results of calibration exposures. Several such calibration points would be acquired using a variety of neutron dose equivalent calibration fields, and could be tailored to suit specific radiation fields or neutron energy ranges. Calibrations for individual dosimeters could also allow for variations in commercial production batches. Such a function is not possible with single pad detector dosimeter, but is under development for a pixilated detector such as Medipix2.

Currently astronaut personal dosimetry at the ISS is relying upon on TEPC and some electronic active personal dosimeters. The active personal dosimeters are based on about 350 μm thick, 1×1 cm^2 silicon p-i-n diodes detectors like in LIULIN and DOSTEL [29] and thin silicon p-i-n diodes described in [30], [31] operating in a LET mode followed by conversion of their response to microdosimetry spectra and dose equivalent. These instruments do not providing neutron dose equivalent but rather total dose equivalent as a mixture of neutrons and charged particle fields. Additionally poor representation of micron size spherical or cylindrical type sensitive volumes, with associated variance in chord distributions, produce some distortion in dose equivalent determination. Thick silicon detectors with 350 μm thickness do not allow LET measurements for neutrons with energy below 3–4 MeV because recoil protons with energy below 3 MeV are stoppers in such detectors.

The presented device for neutron dose equivalent measurements for space application has the following potential advantages above currently used dosimeters: 1) measurement of the neutron dose equivalent in mixed neutron-photon-charged particle fields, 2) low neutron energy threshold for fast neutrons (0.25 MeV), and, 3) sophisticated readout techniques and data analysis allowing further development on the same detector for independent measurements of dose equivalent associated with heavy ions. The presented device is not commercially available at this point in time and will require angular dependence characterization as aspect of future research.

V. Conclusion

We have demonstrated the possibility to develop a real time energy independent fast neutron dosimeter for use in mixed radiation fields relevant to space radiation environments.

A pixilated detector, such as Medipix2, is ideally suited to this application due to the high degree of pixilation and parameterization of the response that can be achieved through coupling with a structured variable thickness polyethylene over layer. This approach allows the subtraction of any unwanted radiation background and to therefore estimate the dose due to neutrons only. The high flexibility in response adjustment of such a dosimeter also allows for self-calibration using neutron dose equivalent calibration sources.

Acknowledgment

Authors would like to thanks Medipix Collaboration for providing detectors and support during this project.

References

[1] *NRC, Managing Space Radiation Risk in the New Era of Space Exploration*. Washington, DC: The National Academies Press, 2008.

[2] F. A. Cucinotta *et al.*, "Space radiation cancer risks and uncertainties for Mars missions," *Radiat. Res.*, vol. 156, pp. 682–688, 2001.

[3] F. A. Cucinotta, M. H. Y. Kim, and L. Ren, "Managing lunar and mars mission radiation risks Part I: Cancer risks, uncertainties, and shielding effectiveness," NASA/TP-2005-213164, Houston, TX, 2005.

[4] J. F. Dicello, "HZE cosmic rays in space. Is it possible that they are not the major radiation hazard?," *Radiat. Prot. Dosim.*, vol. 44, no. 1–4, pp. 253–257, 1992.

[5] G. A. Nelson, "Fundamental space radiobiology," *Gravit. Space Biol. Bull.*, vol. 16, no. 2, pp. 29–36, 2003.

[6] ICRU, "The dosimetry of pulsed radiation," *J. ICRU*, vol. Report 34, 1983.

[7] P. D. Bradley, A. B. Rosenfeld, and M. Zaider, "Solid state microdosimetry," *Nucl. Intrum. Methods B*, vol. 184, no. 1–2, pp. 135–157, 2001.

[8] L. Pisacane *et al.*, "Microdosimeter instrument (MIDN) on Mid-STAR-I," *SAE Trans. J. Aero.*, vol. 2006-01-2146, 2006.

[9] Wroe *et al.*, "Solid state microdosimetry with heavy ions for space applications," *IEEE Trans. Nucl. Sci*, vol. 54, no. 6, pp. 2264–2271, 2007.

[10] A. L. Ziebell *et al.*, "A cylindrical silicon-on-insulator microdosimeter: Charge collection characteristics," *IEEE Trans. Nucl. Sci*, vol. 55, no. 6, pp. 3414–3420, 2008.

[11] W. H. Lim *et al.*, "Cylindrical silicon-on-insulator microdosimeter: Design, fabrication and TCAD modeling," *IEEE Trans. Nucl. Sci*, vol. 56, no. 2, pp. 424–428, 2009.

[12] L. N. Shyan *et al.*, "Development and fabrication of cylindrical silicon-on-insulator microdosimeter arrays," *IEEE Trans. Nucl. Sci*, vol. 56, no. 3, pp. 1637–1641, 2009.

[13] D. A. Prokopovich, M. I. Reinhard, G. C. Taylor, A. Hands, and A. B. Rosenfeld, "GEANT4 simulation of the CERN-EU high-energy reference field (CERF) facility," *Radiat. Prot. Dosim.*, vol. 141, no. 2, pp. 106–113, 2010.

[14] W. Heinrich, S. Roesler, and H. Schraube, "Physics of cosmic radiation fields," *Radiat. Prot. Dosim.*, vol. 86, no. 4, pp. 253–258, Dec. 1, 1999, 1999.

[15] Mikulec, M. Campbell, E. Heijne, X. Llopart, and L. Tlustos, "X-ray imaging using single photon processing with semiconductor pixel detectors," *Nucl. Instrum. Methods Phys. Res. A: Accel. Spectrom. Detect. Assoc. Equip.*, vol. 511, no. 1–2, pp. 282–286, 2003.

[16] J. Jakubek *et al.*, "Neutron imaging and tomography with Medipix2 and dental micro-roentgenography," *Nucl. Instrum. Methods Phys. Res. A: Accel. Spectrom. Detect. Assoc. Equip.*, vol. 569, no. 2, pp. 205–209, 2006.

[17] M. A. R. Othman *et al.*, "From imaging to dosimetry: GEANT4-based study on the application of Medipix to neutron dosimetry," *Radiat. Meas.*, 2010, doi:10.1016/j.radmeas.2010.06.058, to be published.

[18] Y. Eisen *et al.*, "A small size neutron and gamma dosemeter with a single silicon surface barrier detector," *Radiat. Prot. Dosim.*, vol. 15, no. 1, pp. 15–30, 1986.

[19] F. Shiraishi *et al.*, "A new fast neutron spectrometer made of epitaxial integrated dE-E Si detector," *IEEE Trans. Nucl. Sci*, vol. 32, no. 1, pp. 471–475, 1985.

[20] ICRP, "Conversion coefficients for use in radiological protection," *Ann. ICRP*, vol. 26, no. 3–4, pp. 1–205, 1996.

[21] Medipix2, "The Medipix2 collaboration," 2010, 1/9/2010, [Online]. Available: http://medipix.web.cern.ch/MEDIPIX/Medipix2/indexMPIX2.html

[22] Z. Vykydal *et al.*, "Evaluation of the ATLAS-MPX devices for neutron field spectral composition measurement in the ATLAS experiment," in *Proc. IEEE Nuclear Science Symp. Conf. Record, NSS'08*, pp. 2353–2357.

[23] X. Llopart, "Design and characterization of 64K pixels chips working in single photon processing mode," Department of Information Technology and Media, Mid Sweden Univ.. Sundsvall, Ph.D. dissertation, 2007.

[24] T. Holy *et al.*, "Data acquisition and processing software package for Medipix2," *Nucl. Instrum. Methods Phys. Res. A: Accel. Spectrom. Detect. Assoc. Equip.*, vol. 563, no. 1, pp. 254–258, 2006.

[25] S. Agostinelli *et al.*, "G4—A simulation toolkit," *Nucl. Instrum. Methods Phys. Res. A: Accel. Spectrom. Detect. Assoc. Equip.*, vol. 506, no. 3, pp. 250–303, 2003.

[26] J. Allison *et al.*, "GEANT4 developments and applications," *IEEE Trans. Nucl. Sci*, vol. 53, no. 1, pp. 270–278, 2006.

[27] ISO, "Reference neutron radiations–Part 2: calibration fundamentals of radiation protection devices related to the basic quantities characterizing the radiation filed," 2000, ISO 8529-2.

[28] T. Holy *et al.*, "Pattern recognition of tracks induced by individual quanta of ionizing radiation in Medipix2 silicon detector," *Nucl. Instrum. Methods Phys. Res. A: Accel. Spectrom. Detect. Assoc. Equip.*, vol. 591, no. 1, pp. 287–290, 2008.

[29] G. Reitz *et al.*, "Space radiation measurements on-board ISS—the DOSMAP experiment," *Radiat. Prot. Dosim.*, vol. 116, no. 1–4, pp. 374–379, 2005.

[30] M. Luszik-Bhadra, "Electronic personal neutron dosemeters for high energies: Measurements, new developments and further needs," *Radiat. Prot. Dosim.*, vol. 126, no. 1–4, pp. 487–490, 2007.

[31] M. Luszik-Bhadra, M. Nakhostin, K. Niita, and R. Nolte, "Electronic personal neutron dosemeters for energies up to 100 MeV: Calculations using the PHITS code," *Radiat. Meas.*, vol. 43, no. 2–6, pp. 1044–1048, 2008.